Modeling of Boundary Transport and Divertor Target Heat Flux - Implications for Advanced Divertor Concepts

by
Sean Bozkurt Ballinger
B.S. Applied Physics, Columbia University (2016)
Submitted to the Department of Nuclear Science and Engineering
in partial fulfillment of the requirements for the degree of
Doctor of Philosophy in Applied Plasma Physics
at the
MASSACHUSETTS INSTITUTE OF TECHNOLOGY
May 2022

Author .....
Department of Nuclear Science and Engineering
May 19, 2022

Certified by .....
James L. Terry
Principal Research Scientist, Plasma Science and Fusion Center
Thesis Supervisor

Certified by .....
Anne E. White
Professor and Head, Department of Nuclear Science and Engineering
Thesis Reader

Certified by .....
Brian L. LaBombard
Senior Research Scientist, Plasma Science and Fusion Center
Thesis Committee

Accepted by .....
Ju Li
Battelle Energy Alliance Professor of Nuclear Science and Engineering
Professor of Materials Science and Engineering
Chairman, Department Committee on Graduate Theses

Modeling of Boundary Transport and Divertor Target Heat Flux - Implications for Advanced Divertor Concepts

by

Sean Bozkurt Ballinger

Submitted to the Department of Nuclear Science and Engineering
on May 19, 2022, in partial fulfillment of the
requirements for the degree of
Doctor of Philosophy in Applied Plasma Physics

Abstract

Tokamaks are currently being designed and built to achieve net positive unharnessed fusion energy, an important milestone on the path to electricity production. Experimental trends predict an additional challenge in these upcoming devices: a decrease in the area of the metal wall on which the plasma deposits significant heat flux, increasing the likelihood of melting damage. The heat deposition area is proportional to a parameter called the heat flux width, which decreases with increasing poloidal magnetic field and average plasma pressure. In devices designed to achieve physics breakeven such as ITER and SPARC, the heat flux width is predicted by some estimates to be less than 1 millimeter. It is therefore crucial to develop methods to more accurately predict the heat flux width and to mitigate large heat fluxes. Data from the Alcator C-Mod tokamak are particularly relevant in the effort to predict conditions in SPARC, as both are designed to use a higher magnetic field than other major tokamak experiments. Before this work, the relationship between the heat flux width and edge profiles of plasma density and temperature in C-Mod was unknown. Studies with plasma edge simulation codes were limited to a small number of discharges at a time, with many model settings being ad-hoc and difficult to evaluate for general applicability. Simulations of C-Mod had a much shorter outer divertor leg compared to SPARC, making it difficult to use detachment studies in C-Mod to speculate on detachment in SPARC. Finally, there was only a rough idea of edge plasma conditions in SPARC, and it was not known whether detachment would even be feasible. This thesis uses data from Alcator C-Mod and simulations with the UEDGE code to investigate heat flux width scalings, detachment, and advanced divertor concepts to inform the design of next-generation tokamaks that can produce significant fusion energy while remaining safe against heat flux damage.

This thesis begins by augmenting a C-Mod heat flux width database (containing $\sim$300 discharges) with midplane density and temperature profile data. Detailed analysis finds that the outer target heat flux width depends on the edge plasma pressure, but fails to find a clear dependence on edge gradients. The scaling of the heat flux width with the edge pressure varies by confinement mode and is used to confirm

predictions of the heat flux width of 0.2–0.4 mm in SPARC and 0.4–0.6 mm in ITER H-mode scenarios.

The UEDGE code is then used to simulate the edge of Alcator C-Mod plasmas. 75 discharges from the heat flux width database are successfully modeled in UEDGE using a fully automated process that matches experimental midplane density and temperature profiles. The resulting heat flux width in UEDGE is then compared to experimental measurements, and it is found that the UEDGE and experimental values are correlated but that UEDGE overestimates the heat flux width by an average factor of 1.8. The UEDGE-modeled discharges are modified to include single-particle drift effects and (separately) to remove flux limits. These changes do not significantly improve the UEDGE heat flux width match to experiment but demonstrate the capability of this framework to evaluate which settings in the UEDGE model improve agreement with experiment over the large range of edge plasma conditions included in the C-Mod database.

One particular C-Mod attached H-mode discharge is then simulated in UEDGE, and a good match is achieved to experimental data at the midplane and outer target simultaneously with full drift effects included in the model. This discharge is also simulated with a ∼2x longer outer divertor leg, an important component of advanced divertor concepts that could enable better high heat flux handling. Detachment is found to occur when a nitrogen impurity is introduced at a fixed fraction of 3.5% of the main ion density in the real C-Mod geometry, while with the longer leg, detachment occurs at a significantly lower fraction of 2.4% nitrogen. This bodes well for the SPARC design, which features a long outer leg.

Finally, a full-power SPARC H-mode scenario is directly simulated with UEDGE. It is found that detachment is possible at the high heat fluxes and small heat flux width predicted for SPARC and that the heat flux at the targets can remain significantly reduced with a carbon impurity fraction around 1%. This value is not a prediction of the detachment threshold in SPARC due to the use of bifurcated attached and detached solutions obtained at low power, but is encouraging when compared to the detachment thresholds in C-Mod UEDGE simulations. This study confirms that detachment is a promising solution to mitigate high heat fluxes in the SPARC full-power scenario.

Thesis Supervisor: James L. Terry
Title: Principal Research Scientist, Plasma Science and Fusion Center

Thesis Supervisor: Anne E. White
Title: Professor and Head, Department of Nuclear Science and Engineering

Thesis Supervisor: Brian L. LaBombard
Title: Senior Research Scientist, Plasma Science and Fusion Center

Acknowledgments

These years at MIT have been truly wonderful. This thesis is dedicated to:

- Everyone who helped me accomplish the work in this thesis: Jim Terry, Adam Kuang, Maxim Umansky, Mike Wigram, Tom Rognlien, Jeremy Lore, John Canik, Seung Gyou Baek, Matthew Reinke, Anne White, Dan Brunner, Jerry Hughes, Amanda Hubbard, Ted Golfinopoulos, Martin Greenwald, Brian LaBombard, Dennis Whyte, Zach Hartwig.

- My professors at MIT: Jeff Freidberg, Anne White, Dennis Whyte, Nuno Loureiro.

- My friends and mentors at W7-X: Adrian von Stechow, Carsten Killer, Olaf Grulke, Marco Krause, Andrei Goriaev, Eric Edlund, Thomas Klinger, Thomas Sunn Pedersen.

- Bob Mumgaard and the SPARC team for starting an exciting new chapter in fusion at MIT.

- My fellow grad students: Kieran Dolan, Dan Segal, William McCarthy, Norman Cao, Abhi Mathews, Bodhi Biswas, Sam Frank, Lucio Milanese, Francesco Sciortino, Egon Coppens, Libby Tolman, Muni Zhou, Alex Sandberg, Raspberry Simpson, Bryan Linehan, Julian Picard, Aaron Rosenthal, Alex Tinguely, Alex Creely, Kevin Montes, Juan Ruiz Ruiz, Pablo Rodriguez-Fernandez, Leigh Ann Kesler, Sara Ferry, Guillaume Giudicelli, Rachel Bielajew, Sterling Harper, Isaac Meyer, Stephen Lam, Miriam Kreher, Sean Robertson, Rachel Connick, Lucas Rush, Mohammad Shahin, Steven Jepeal, Caroline Sorensen, Shikhar Kumar, Hannah Hoffmann, Charlie Hirst, Erica Salazar, Raymond Diab, Evan Leppink.

- Other amazing people at MIT and the PSFC: Andrew Birkel, Ryan Sweeney, Kevin Woller, Brandy Baker, Jessica Coco, Valerie Censabella, Paul Rivenberg, Marina Dang.

- My friends, if not mentioned earlier: Craig Mascarenhas, Ben Cameron, Emily Pond, Emre Anamur, Jordan Smith, Austin Mei, Raphi Zonis, Eli Karvelis, Jonas Lehmann, Steve Holcomb, James Penna, Josh Cabrera, Niger Little-Poole, Idris Sardharwala, Alex Roth, Fabio DeSousa, Bernhard Fasenfest.

- My professors and mentors before MIT: Jeannette, Susanne Torabi, John Bird, Clyfe Beckwith, Peter Watt, Patrick Farrell, Chris Odden, Fei Yao, Mika Latva-Kokko, Michael Mauel, Jeff Levesque, Patrick Byrne, Norman Christ, David Vallancourt, Cetin Kiris, Nick Eidietis, Dave Humphreys, Leora Brovman.

- Charlie the cat.

- The MIT Sailing Pavilion: nothing beats an afternoon windsurfing break on the Charles.

- Mom and Dad: you always encouraged me to follow this dream, and your love and delicious food helped me through all the stressful times.
- Ollie, I hope you'll drag me on more very long hikes.
- Anneanne, I've missed you so much and I can't wait to see you again.
- Dede, you left us too soon. We traveled to so many amazing places together. You were always excited about physics and my work. I'm sad that you won't be around to see me graduate.

Contents

List of Figures

List of Tables

List of publications

First-author publications

[1] S. B. Ballinger, J. L. Terry, S. G. Baek, K. Tang, A. von Stechow, C. Killer, D. Nicolai, G. Satheeswaran, P. Drews, and O. Grulke, "Fast camera imaging of plasmas in Alcator C-Mod and W7-X," *Nuclear Materials and Energy*, 2018.

[2] S. B. Ballinger, J. L. Terry, S. G. Baek, M. Beurskens, K. J. Brunner, G. Fuchert, J. Knauer, C. Killer, E. Pasch, K. Rahbarnia, J. Schilling, E. Scott, A. von Stechow, H. Thomsen, O. Grulke, G. Wurden, G. Kocsis, T. Szepesi, and L. Zsuga, "Dynamics and dependencies of the configuration-dependent 1–2 kHz fluctuation in W7-X," *Nuclear Materials and Energy*, vol. 27, p. 100 967, 2021.

[3] S. B. Ballinger, A. Q. Kuang, M. V. Umansky, D. Brunner, J. M. Canik, M. J. Greenwald, J. D. Lore, B. LaBombard, J. L. Terry, and M. Wigram, "Simulation of the SPARC plasma boundary with the UEDGE code," *Nuclear Fusion*, 2021.

[4] S. Ballinger, D. Brunner, A. Hubbard, J. Hughes, A. Kuang, B. LaBombard, J. Terry, and A. White, "Dependence of the boundary heat flux width on core and edge profiles in Alcator C-Mod," *Nuclear Fusion*, vol. 62, no. 7, p. 076 020, 2022.

[5] S. B. Ballinger, M. V. Umansky, A. Q. Kuang, J. L. Terry, and M. R. K. Wigram, "Automated UEDGE Modeling of the C-Mod Heat Flux Width Database," 2022.

Co-author publications

[1] J. L. Terry, S. Ballinger, D. Brunner, B. LaBombard, A. E. White, and S. J. Zweben, "Fast imaging of filaments in the X-point region of Alcator C-Mod," *Nuclear Materials and Energy*, Proceedings of the 22nd International Conference on Plasma Surface Interactions 2016, 22nd PSI, vol. 12, pp. 989–993, 2017.

[2] T. Klinger, T. Andreeva, S. Bozhenkov, C. Brandt, R. Burhenn, B. Buttenschön, G. Fuchert, B. Geiger, O. Grulke, H. Laqua, N. Pablant, K. Rahbarnia, T. Stange, A. Von Stechow, N. Tamura, H. Thomsen, Y. Turkin, T. Wegner, I. Abramovic, S. Akaslompolo, J. Alcuson, P. Aleynikov, K. Aleynikova, A. Ali, A. Alonso, G. Anda, E. Ascasibar, J. Bahner, S. Baek, M. Balden, J. Baldzuhn, M. Banduch, T. Barbui, W. Behr, C. Beidler, A. Benndorf, C. Biedermann, W. Biel, B. Blackwell, E. Blanco, M. Blatzheim, S. Ballinger, T. Bluhm, D. Böckenhoff, B. Böswirth, L.-G. Böttger, M. Borchardt, V. Borsuk, J. Boscary, H.-S. Bosch, M. Beurskens, R. Brakel, H. Brand, T. Brauer, H. Braune, S. Brezinsek, K.-J. Brunner, R. Bussiahn, V. Bykov, J. Cai, I. Calvo, B. Cannas, A. Cappa, A. Carls, D. Carralero, L. Carraro, B. Carvalho, F. Castejon, A. Charl, N. Chaudhary, D. Chauvin, F. Chernyshev, M. Cianciosa, R. Citarella, G. Claps, J. Coenen, M. Cole, M. Cole, F. Cordella, G. Cseh, A. Czarnecka, K. Czerski, M. Czerwinski, G. Czymek, A. Da Molin, A. Da Silva, H. Damm, A. De La Pena, S. Degenkolbe, C. Dhard, M. Dibon, A. Dinklage, T. Dittmar, M. Drevlak, P. Drewelow, P. Drews, F. Durodie, E. Edlund, P. Van Eeten, F. Effenberg, G. Ehrke, S. Elgeti, M. Endler, D. Ennis, H. Esteban, T. Estrada, J. Fellinger, Y. Feng, E. Flom, H. Fernandes, W. Fietz, W. Figacz, J. Fontdecaba, O. Ford, T. Fornal, H. Frerichs, A. Freund, T. Funaba, A. Galkowski, G. Gantenbein, Y. Gao, J. Garcia Regana, D. Gates, J. Geiger, V. Giannella, A. Gogoleva, B. Goncalves, A. Goriaev, D. Gradic, M. Grahl, J. Green, H. Greuner, A. Grosman, H. Grote, M. Gruca, C. Guerard, P. Hacker, X. Han, J. Harris, D. Hartmann, D. Hathiramani, B. Hein, B. Heinemann, P. Helander, S. Henneberg, M. Henkel, J. Hernandez Sanchez, C. Hidalgo, M. Hirsch, K. Hollfeld, U. Höfel, A. Hölting, D. Höschen, M. Houry, J. Howard, X. Huang, Z. Huang, M. Hubeny, M. Huber, H. Hunger, K. Ida, T. Ilkei, S. Illy, B. Israeli, S. Jablonski, M. Jakubowski, J. Jelonnek, H. Jenzsch, T. Jesche, M. Jia, P. Junghanns, J. Kacmarczyk, J.-P. Kallmeyer, U. Kamionka, H. Kasahara, W. Kasparek, Y. Kazakov, N. Kenmochi, C. Killer, A. Kirschner, R. Kleiber, J. Knauer, M. Knaup, A. Knieps, T. Kobarg, G. Kocsis, F. Köchl, Y. Kolesnichenko, A. Könies, R. König, P. Kornejew, J.-P. Koschinsky, F. Köster, M. Kramer, R. Krampitz, A. Kramer-Flecken, N. Krawczyk, T. Kremeyer, J. Krom, M. Krychowiak, I. Ksiazek, M. Kubkowska, G. Kühner, T. Kurki-Suonio, P. Kurz, S. Kwak, M. Landreman, P. Lang, R. Lang, A. Langenberg, S. Langish, H. Laqua, R. Laube, S. Lazerson, C. Lechte, M. Lennartz, W. Leonhardt, C. Li, C. Li, Y. Li, Y. Liang, C. Linsmeier, S. Liu, J.-F. Lobsien, D. Loesser, J. Loizu Cisquella, J. Lore, A. Lorenz, M. Losert, A. Lücke, A. Lumsdaine, V. Lutsenko, H. Maaßberg, O. Marchuk, J. Matthew, S. Marsen, M. Marushchenko, S. Masuzaki, D. Maurer, M. Mayer, K. McCarthy, P. McNeely, A. Meier, D. Mellein, B. Mendelevitch, P. Mertens, D. Mikkelsen, A. Mishchenko, B. Missal, J. Mittelstaedt, T. Mizuuchi, A. Mollen, V. Moncada, T. Mönnich, T. Morisaki, D. Moseev, S. Murakami, G. Náfrádi, M. Nagel, D. Naujoks, H. Neilson, R. Neu, O. Neubauer, U. Neuner, T. Ngo, D. Nicolai, S. Nielsen, H. Niemann, T. Nishizawa, R. Nocentini, C. Nührenberg, J. Nührenberg, S. Obermayer, G. Offermanns, K. Ogawa, J. Olmanns, J. On-

gena, J. Oosterbeek, G. Orozco, M. Otte, L. Pacios Rodriguez, N. Panadero, N. Panadero Alvarez, D. Papenfuß, S. Paqay, E. Pasch, A. Pavone, E. Pawelec, T. Pedersen, G. Pelka, V. Perseo, B. Peterson, D. Pilopp, S. Pingel, F. Pisano, B. Plaum, G. Plunk, P. Pölöskei, M. Porkolab, J. Proll, M.-E. Puiatti, A. Puig Sitjes, F. Purps, M. Rack, S. Récsei, A. Reiman, F. Reimold, D. Reiter, F. Remppel, S. Renard, R. Riedl, J. Riemann, K. Risse, V. Rohde, H. Röhlinger, M. Romé, D. Rondeshagen, P. Rong, B. Roth, L. Rudischhauser, K. Rummel, T. Rummel, A. Runov, N. Rust, L. Ryc, S. Ryosuke, R. Sakamoto, M. Salewski, A. Samartsev, E. Sanchez, F. Sano, S. Satake, J. Schacht, G. Satheeswaran, F. Schauer, T. Scherer, J. Schilling, A. Schlaich, G. Schlisio, F. Schluck, K.-H. Schlüter, J. Schmitt, H. Schmitz, O. Schmitz, S. Schmuck, M. Schneider, W. Schneider, P. Scholz, R. Schrittwieser, M. Schröder, T. Schröder, R. Schroeder, H. Schumacher, B. Schweer, E. Scott, S. Sereda, B. Shanahan, M. Sibilia, P. Sinha, S. Siplia, C. Slaby, M. Sleczka, H. Smith, W. Spiess, D. Spong, A. Spring, R. Stadler, M. Stejner, L. Stephey, U. Stridde, C. Suzuki, J. Svensson, V. Szabó, T. Szabolics, T. Szepesi, Z. Szökefalvi-Nagy, A. Tancetti, J. Terry, J. Thomas, M. Thumm, J. Travere, P. Traverso, J. Tretter, H. Trimino Mora, H. Tsuchiya, T. Tsujimura, S. Tulipán, B. Unterberg, I. Vakulchyk, S. Valet, L. Vano, B. Van Milligen, A. Van Vuuren, L. Vela, J.-L. Velasco, M. Vergote, M. Vervier, N. Vianello, H. Viebke, R. Vilbrandt, A. Vorköper, S. Wadle, F. Wagner, E. Wang, N. Wang, Z. Wang, F. Warmer, T. Wauters, L. Wegener, J. Weggen, Y. Wei, G. Weir, J. Wendorf, U. Wenzel, A. Werner, A. White, B. Wiegel, F. Wilde, T. Windisch, M. Winkler, A. Winter, V. Winters, S. Wolf, R. Wolf, A. Wright, G. Wurden, P. Xanthopoulos, H. Yamada, I. Yamada, R. Yasuhara, M. Yokoyama, M. Zanini, M. Zarnstorff, A. Zeitler, D. Zhang, H. Zhang, J. Zhu, M. Zilker, A. Zocco, S. Zoletnik, and M. Zuin, "Overview of first Wendelstein 7-X high-performance operation," *Nuclear Fusion*, vol. 59, no. 11, 2019.

[3] R. A. Tinguely, A. Rosenthal, R. Simpson, S. B. Ballinger, A. J. Creely, S. Frank, A. Q. Kuang, B. L. Linehan, W. McCarthy, L. M. Milanese, K. J. Montes, T. Mouratidis, J. F. Picard, P. Rodriguez-Fernandez, A. J. Sandberg, F. Sciortino, E. A. Tolman, M. Zhou, B. N. Sorbom, Z. S. Hartwig, and A. E. White, "Neutron diagnostics for the physics of a high-field, compact, Q≥1 tokamak," *Fusion Engineering and Design*, vol. 143, pp. 212–225, 2019.

[4] A. J. Creely, L. M. Milanese, E. A. Tolman, J. H. Irby, S. B. Ballinger, S. Frank, A. Q. Kuang, B. L. Linehan, W. McCarthy, K. J. Montes, T. Mouratidis, J. F. Picard, P. Rodriguez-Fernandez, A. M. Rosenthal, A. J. Sandberg, F. Sciortino, R. A. Simpson, R. A. Tinguely, M. Zhou, and A. E. White, "Design study of a combined interferometer and polarimeter for a high-field, compact tokamak," *Physics of Plasmas*, vol. 27, no. 4, p. 042 516, 2020.

[5] A. J. Creely, M. J. Greenwald, S. B. Ballinger, D. Brunner, J. Canik, J. Doody, T. Fülöp, D. T. Garnier, R. Granetz, T. K. Gray, C. Holland, N. T. Howard, J. W. Hughes, J. H. Irby, V. A. Izzo, G. J. Kramer, A. Q. Kuang, B. LaBombard, Y. Lin, B. Lipschultz, N. C. Logan, J. D. Lore, E. S. Marmar, K.

Montes, R. T. Mumgaard, C. Paz-Soldan, C. Rea, M. L. Reinke, P. Rodriguez-Fernandez, K. Särkimäki, F. Sciortino, S. D. Scott, A. Snicker, P. B. Snyder, B. N. Sorbom, R. Sweeney, R. A. Tinguely, E. A. Tolman, M. Umansky, O. Vallhagen, J. Varje, D. G. Whyte, J. C. Wright, S. J. Wukitch, J. Zhu, and t. S. Team, "Overview of the SPARC tokamak," *Journal of Plasma Physics*, vol. 86, no. 5, 2020.

[6] A. Q. Kuang, S. Ballinger, D. Brunner, J. Canik, A. J. Creely, T. Gray, M. Greenwald, J. W. Hughes, J. Irby, B. LaBombard, B. Lipschultz, J. D. Lore, M. L. Reinke, J. L. Terry, M. Umansky, D. G. Whyte, S. Wukitch, and the SPARC Team, "Divertor heat flux challenge and mitigation in SPARC," *Journal of Plasma Physics*, vol. 86, no. 5, p. 865 860 505, 2020.

[7] P. Rodriguez-Fernandez, A. J. Creely, M. J. Greenwald, D. Brunner, S. B. Ballinger, C. P. Chrobak, D. T. Garnier, R. Granetz, Z. S. Hartwig, N. T. Howard, J. W. Hughes, J. H. Irby, V. A. Izzo, A. Q. Kuang, Y. Lin, E. S. Marmar, R. T. Mumgaard, C. Rea, M. L. Reinke, V. Riccardo, J. E. Rice, S. D. Scott, B. N. Sorbom, J. A. Stillerman, R. Sweeney, R. A. Tinguely, D. G. Whyte, J. C. Wright, and D. V. Yuryev, "Overview of the SPARC physics basis towards the exploration of burning-plasma regimes in high-field, compact tokamaks," *Nuclear Fusion*, vol. 62, no. 4, p. 042 003, 2022.

Chapter 1

Introduction

1.1 The need for a new energy source

Global energy demand is rising, and climate change due to greenhouse gas emissions is one of the most pressing issues of our time [1]. In 2022, around 60% of the electricity generated in the United States was generated with coal and natural gas, while 40% was generated with nuclear, renewables, and hydropower. While the use of renewable energy such as solar and wind power is slowly increasing [2], renewables provide only intermittent power which cannot be stored for later use in large amounts. A long-term solution for clean production of base load electricity is required.

Fusion energy holds great promise as a source of energy due to the abundance of its required fuel, the lack of significant waste products, its carbon-free nature, and its safety. The fuels are deuterium and tritium, which are isotopes of hydrogen. Tritium can be created during operation, and deuterium can be extracted at low cost from seawater. Since fusion is a nuclear reaction, it produces an extreme amount of energy per gram of fuel consumed: "it would take only about a pickup truck full of deuterium laced ocean water (HDO rather than H_2O) to power Boston for a year" [1]. Rather than emitting CO_2, the main byproduct of fusion power would be a small amount of helium. Fusion also emits high-energy neutrons, which would be captured by materials surrounding the fusion device, and the structures through which these neutrons pass would become radioactive. They would only require careful storage,

however, for around 100 years, which is significantly shorter than the time required to store waste from nuclear fission. Finally, fusion would be a safe source of energy. There is no risk of an uncontrollable, runaway reaction: generating net fusion power requires precise control of vacuum pumping, gas fueling, magnetic fields, and input power. If any one of these systems fail, energy will quickly stop being produced, and the plasma will terminate without damaging anything other than the inside of the vessel [1]. The greatest risk would likely be an accidental release of a large quantity of tritium, which is radioactive and harmful when ingested, but this risk can be reduced in the design of a power plant [3]. These advantages of abundant fuel, little waste, and safety make fusion impossible to ignore, but achieving net fusion energy has so far been a challenge. Fusion energy is not likely to be achieved in time to lead the way in decarbonization, but could minimize the environmental impact of industrial society in the future.

1.2 Fusion energy

In fusion reactions, small nuclei combine to produce a larger nucleus and release energy equivalent to the difference in binding energy between the product and reactants. The most prominent example of fusion in our daily lives is the sun, inside which the dominant energy-producing reaction is the multi-step combination of four hydrogen nuclei into a helium-4 nucleus. Fusion was first harnessed on Earth in the 1950s to boost the destructive power of nuclear weapons. Since then, the challenge to use fusion to produce significant energy in a non-explosive manner has been ongoing. The most attractive fusion reaction for energy production is that between deuterium and tritium:

$$\mathrm{D} + \mathrm{T} \rightarrow \alpha + \mathrm{n} + 17.6\,\mathrm{MeV}. \tag{1.1}$$

In this reaction the hydrogen isotopes of deuterium (D or ${}^{2}_{1}\mathrm{H}$) and tritium (T or ${}^{3}_{1}\mathrm{H}$) fuse into an alpha particle (α or ${}^{4}_{2}\mathrm{He}$) and a neutron, which have a combined kinetic energy of 17.6 MeV, with 3.5 MeV being the alpha particle kinetic energy and 14.1 MeV being the neutron kinetic energy. Tritium is not naturally occurring, so a

fusion power plant would need to maintain its own supply. The most promising way to accomplish this is the reaction of neutrons with lithium:

$$^{6}_{3}\mathrm{Li} + \mathrm{n}\ (\mathrm{slow}) \rightarrow \alpha + \mathrm{T} + 4.8\,\mathrm{MeV}. \tag{1.2}$$

The known reserves of lithium on Earth would enable operation with these fuels for thousands of years, and future development of more challenging D-D fusion could eventually remove the dependence on lithium and tritium.

Fusion reactions are difficult to achieve because the positively charged nuclei (e.g. D and T) repel each other electrostatically. Very high temperatures and densities are therefore required for the reactions to occur with enough frequency to be harnessed for energy. Compared to other fusion reactions, the D-T reaction has the least demanding temperature requirement, with the peak in velocity-averaged cross section occurring around 60 keV (figure 1-1), or 700 000 000 °C. At these temperatures, matter is in the plasma state: particles have so much energy that atomic nuclei (ions) and electrons move independently, and their motion is dominated by electromagnetic forces. Getting the plasma to such high temperatures requires external heating power. The as-yet standing challenge of fusion is to produce more power through fusion reactions than is required to heat the plasma. The situation in which the input and output power are equal is commonly called "breakeven" and is a milestone that must be cleared on the way to net energy production. There are various definitions of breakeven that take into account the inefficiencies along the way to producing electricity: "engineering breakeven" is the most demanding, where the total power consumed by the fusion power plant must be equal to the power delivered to the grid; for "physics breakeven," which has yet to be achieved in a magnetically-confined plasma, the power entering the plasma must be equal to the power of the fusion reactions in the plasma.

The general power balance in a fusion plasma is

$$P_{\mathrm{net}} = P_{\mathrm{h}} + P_{\alpha} - P_{\mathrm{rad}} - P_{\mathrm{cond}} \tag{1.3}$$

where P_{h} is the external heating power supplied to the plasma, P_{α} is the plasma self-

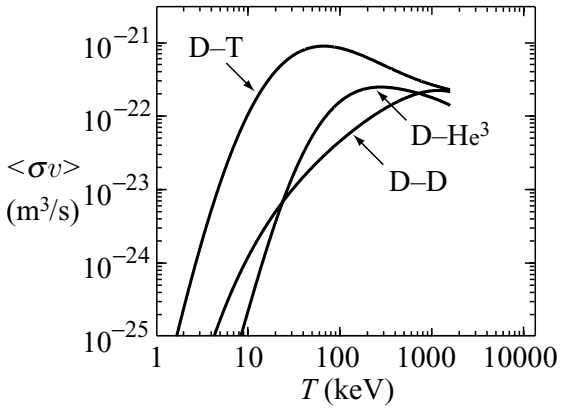

Figure 1-1: Velocity-averaged cross section for various fusion reactions as a function of temperature. Image reproduced from [1].

heating by the alpha particles produced in fusion reactions, and P_{rad} and P_{cond} are the power lost from the plasma due to electromagnetic radiation and heat conduction, respectively. When the alpha particles contribute enough power back to the plasma that no external source of power is required to keep particles at fusion-relevant temperatures, the plasma is said to have achieved "ignition," meaning that it is in some respects self-sustaining (deuterium and tritium fueling, magnetic fields, and plasma current drive must still be supplied). The power lost due to heat conduction can be characterized as

$$P_{\text{cond}} = \frac{3}{2}\frac{p}{\tau_{\text{E}}}, \tag{1.4}$$

where $p = nT$ is the plasma pressure and n and T are the plasma density and temperature, respectively. τ_{E} is the time required for the plasma energy to decay to $1/e$ of its starting value with no external heating [1]. Under certain assumptions, the condition to achieve ignition is

$$nT\tau_{\text{E}} > 3 \times 10^{21}\,\text{m}^{-3}\,\text{keV}\,\text{s}, \tag{1.5}$$

and $nT\tau_{\text{E}}$ is called the triple-product [4]. Net energy production is still possible before achieving ignition, but the ignition criterion gives a rough idea of the parameter ranges being targeted.

1.3 The tokamak

The basic requirement for fusion energy production is a high enough product of temperature, density, and energy confinement time. In the sun, this requirement is satisfied because the massive fusion plasma is confined by gravity. On Earth, gravitational confinement is not an option, so the plasma can be confined either by compression (inertial confinement fusion) or with a magnetic field, because charged particles gyrate around magnetic field lines. Plasmas in straight or purely toroidal magnetic fields suffer from issues with end losses, uncompensated drifts, and instabilities. The simplest magnetic configuration that can achieve net-energy-relevant confinement is called the tokamak (figure 1-2), in which external magnets create toroidal and poloidal magnetic fields inside the plasma chamber, but a large electric current is also made to run through the plasma itself in the toroidal direction, creating a poloidal magnetic field. In the device depicted in figure 1-2, the plasma current is induced by a transformer in the middle of the tokamak.

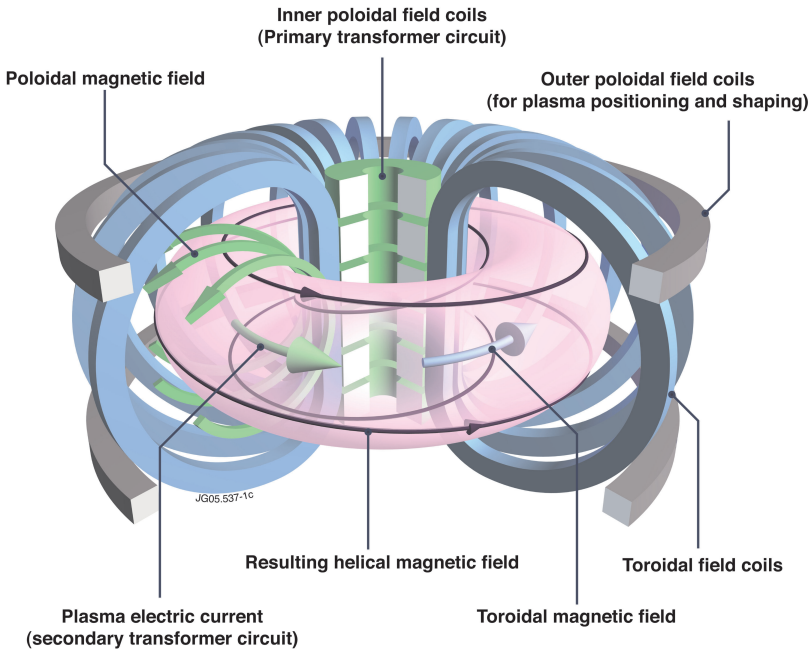

Figure 1-2: The tokamak configuration. Image courtesy of EUROfusion.

Tokamaks have achieved immense progress in triple-product value since the 1960s, but energy confinement times are still too short to generate net fusion power in present

devices. One solution to this problem is to build larger tokamaks, in which it would simply take longer for the heat and particles to diffuse out [1]. But large tokamaks are costly and require longer construction times: the most prominent example is the ITER tokamak, an international effort to achieve physics breakeven, which is projected to cost a total of $22 billion. Construction on ITER began in 2007 and physics breakeven experiments are expected to run in 2035 [5]. A potentially faster path to net fusion energy is being explored by the SPARC tokamak effort, in which new superconducting magnet technology is predicted to enable physics breakeven in a tokamak much smaller than ITER thanks to more powerful magnetic fields [6].

1.3.1 The tokamak power plant

The mechanism by which a tokamak could generate electricity is shown in figure 1-3. A crucial requirement is the "blanket" between the plasma vessel and magnets, which would be heated up by collisions from the fusion neutrons. The neutrons have no charge and high kinetic energy, and so can travel out of the magnetic confinement region and through the metal vessel (with collisions irradiating it and reducing its integrity over time). The neutron-heated blanket would heat water and drive a steam turbine to generate electricity. The blanket must also be able to contain lithium to create tritium for later use as fuel [1].

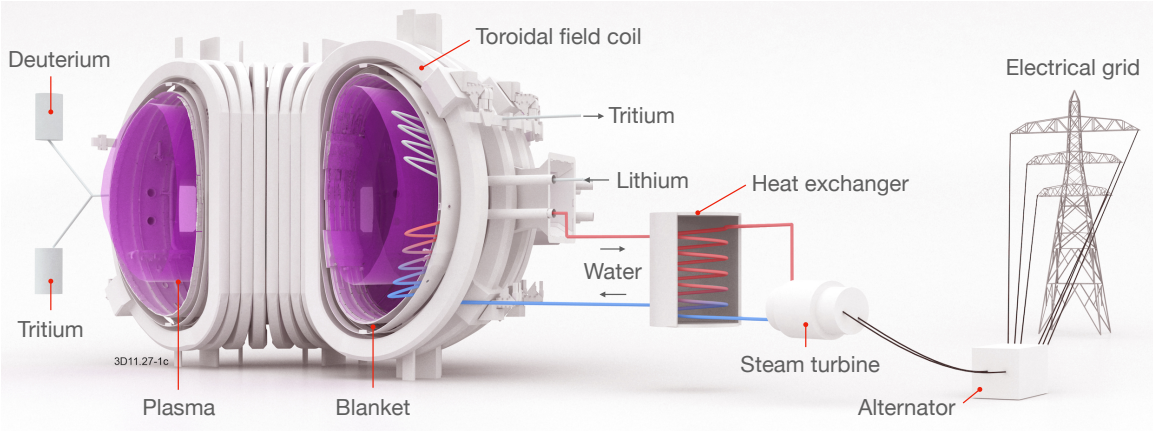

Figure 1-3: Conceptual overview of a tokamak fusion power plant. Figure adapted from image courtesy of EUROfusion.

1.3.2 The heat flux handling challenge

In addition to all the technological challenges of a fusion power plant, tokamaks have an Achilles' heel (not to imply that the rest of the tokamak is invulnerable) in the region where the high-temperature plasma's exhaust heat and particles are removed. At high heat fluxes, the metal plasma vessel can be in danger of eroding or melting, which ruins the tight tolerances needed for high-performance plasma operation and requires costly repairs. The width of the high heat flux region is described by the so-called heat flux width, and small heat flux widths make it more challenging to dissipate the exhaust heat. Predicting the heat flux width from fundamental theory is not yet possible, so experimental trends from existing tokamak experiments are used to predict it. Unfortunately, these experimental trends predict that the heat flux width shrinks to values smaller than 1 millimeter in tokamaks like ITER and SPARC that are expected to achieve physics breakeven [7, 8]. This motivates examining in greater detail the experimental factors that the heat flux width depends on and using advanced models of the tokamak edge plasma to study solutions to withstand high heat fluxes.

1.4 Thesis outline

This thesis uses experimental data and advanced models of the tokamak edge plasma to investigate the dependencies of the heat flux width in Alcator C-Mod and to evaluate promising solutions to handle large heat fluxes, including in the SPARC tokamak currently under development:

- Chapter 2 provides an introduction to physical processes in the plasma edge and the advanced UEDGE code used to model this region in this thesis.

- Chapter 3 examines a database of experimental heat flux width measurements from Alcator C-Mod, finding that some edge plasma quantities are correlated with the heat flux width.

- Chapter 4 presents a first-of-its-kind achievement of automated UEDGE models of 75 discharges in the C-Mod experimental database, assessing the generality of the setup and the suitability of UEDGE for heat flux width estimation using experimentally measured midplane profiles.

- Chapter 5 describes an advanced UEDGE model of a single C-Mod H-mode attached-divertor discharge which was then used to examine the impact of extending the outer divertor "leg" on the target heat flux and detachment threshold.

- Chapter 6 uses the UEDGE code and empirically-based predictions of the heat flux width in SPARC to study plasma conditions and the detachment process in this next-generation device with high heat flux handling requirements and an advanced divertor.

- Chapter 7 summarizes the conclusions of this thesis.

- Appendix A presents several useful utilities developed over the course of this study to increase productivity and enable deeper analysis when working with the UEDGE code.

- Appendix B details the workflows used to produce the results of this study.

Chapter 2

Tokamak edge plasma physics

2.1 Physical processes in the plasma edge

The plasma edge in tokamaks contains electrons, ions, neutral atoms, and molecules, including elements other than the isotopes of hydrogen commonly used for fueling. A large number of possible reactions exist between these particles, and some of the most important ones in the edge of fusion plasmas are summarized here:

- Ionization, usually due to electron impact, is most significant at temperatures above 10 eV.
- Recombination of ions and electrons into neutral atoms is significant at temperatures around and below 1 eV.
- Charge-exchange, in which a low-energy neutral atom and high-energy plasma ion collide, results in a neutral with the speed of the typically much hotter ion and therefore deeper penetration of the neutral into the plasma.
- Electron-impact dissociation of molecules into individual atoms or ions.
- Electromagnetic radiation due to de-excitation or bremsstrahlung is a mechanism of energy loss from the plasma.

The rates of these reactions depend on the plasma density, temperature, and elements involved.

Plasma-surface interactions also play an important role in the edge region of tokamaks. Ions incident on surfaces can recombine (regain electrons and be reintroduced to the plasma as neutral atoms, a process also known as recycling), become adsorbed, or sputter additional atoms from the surface into the plasma. The rates of these processes depend on the incident ion element, its kinetic energy, and the surface composition and atomic structure. Neutral atoms incident on surfaces are usually reflected. In tokamaks, the neutral atom population is influenced by a number of processes, including wall conditioning and recycling, gas puffing, neutral beam sources, and pumping [9].

2.1.1 Anomalous transport

Confining a plasma for the purpose of producing significant fusion energy requires limited rates of particle and energy diffusion out of the core, perpendicular to the magnetic field. These particle and energy fluxes can be predicted based on plasma collision mechanics and frequencies using classical and neoclassical theory. In experiments, however, these fluxes are observed to be much larger than those predicted by theory, resulting in their being termed "anomalous" transport. It is thought that fine-scale plasma turbulence is responsible for anomalous transport [9, 10].

In tokamaks, various degrees of confinement are observed. The main ones are L-mode, I-mode, and H-mode, corresponding to "low," "intermediate," and "high" confinement. In L-mode, density and temperature decline gradually from the core to the edge, and the particle and energy confinement times are short. H-mode plasmas have steep gradients (commonly called pedestals) in density and temperature near the separatrix due to a transport barrier near the edge [4]. In L-mode, such edge pedestals are not observed either in density or temperature, and the particle and energy confinement times are significantly shorter than in H-mode (L-mode density profiles can also be largely flat except for the gradient at the edge). I-mode plasmas have L-mode-like particle confinement and H-mode-like energy confinement [11].

2.2 The divertor configuration

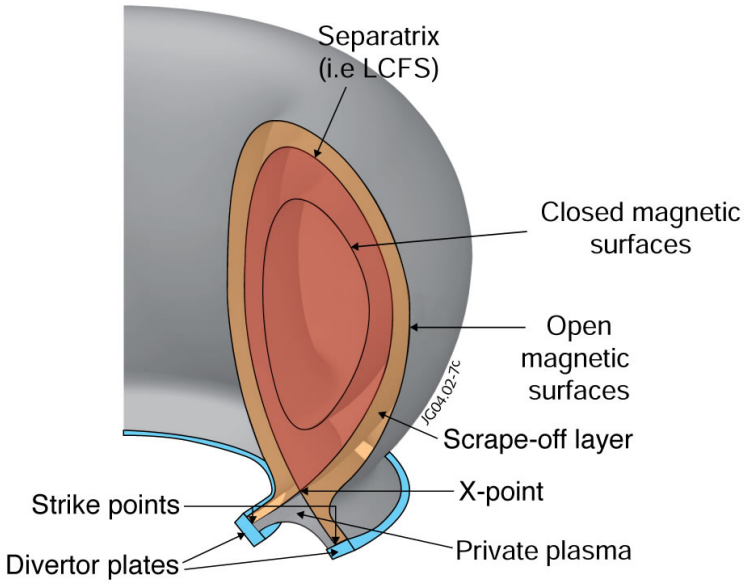

Figure 2-1: Diagram of the scrape-off layer and divertor in a tokamak. Figure courtesy of EUROfusion.

The simplest configuration for a tokamak plasma is the "limiter" configuration, in which the last closed flux surface (LCFS) is defined by the plasma intersecting a material surface. The limiter configuration makes it difficult to keep impurities and recycled neutral atoms from contaminating the core plasma and causing radiative power loss, degrading the maximum achievable core density, temperature, and fusion power.

An alternative to the limiter configuration is the "divertor" configuration (figure 2-1), in which the magnetic field coils are used to create a magnetic null in the poloidal field called an X-point, which lies on a flux surface called the separatrix that separates the plasma core and the scrape-off layer (SOL). In the "divertor" configuration the closed flux surfaces do not contact any material surfaces. Beyond the core and LCFS, in the SOL, the field-lines intersect material surfaces (divertor targets) that typically are far-removed from the LCFS. These SOL field-lines are called divertor "legs," and very high levels of exhaust heat and particles are transported along the legs to the targets in fusion-relevant plasmas. The intersection of the separatrix with a target is

called the strike-line, or the strike-point when viewed in a 2-dimensional plasma cross-section [9]. This greater separation between the LCFS and plasma-surface interactions provides a better path toward handling the exhaust heat and particles than that of the limiter configuration, but finding an acceptable solution to the power handling challenge remains one of the key areas of magnetic-confinement fusion research.

2.2.1 Parallel heat flux

The most important processes determining the heat flux to plasma surfaces are heat conduction and convection in the direction parallel to the magnetic field. The parallel convected heat flux, including electron and ion contributions, is

$$q_{\parallel \mathrm{conv}} = \left(5k_B T + \frac{1}{2} m_i v_\parallel^2\right) \Gamma_\parallel, \tag{2.1}$$

assuming $T_e = T_i$, where $\Gamma_\parallel = n v_\parallel$ is the electron and ion flux in the direction parallel to the magnetic field. The parallel conducted heat flux (also called the classical or Spitzer conducted heat flux) is

$$q_{\parallel \mathrm{cond}(e,i)} = -\kappa_{0(e,i)} T_{(e,i)}^{5/2} \frac{\mathrm{d}T_{(e,i)}}{\mathrm{d}s_\parallel}, \tag{2.2}$$

where $s_\parallel$ is the distance in the direction parallel to the magnetic field, and $\kappa_{0e} \approx 2000\,\mathrm{W\,eV^{-7/2}\,m^{-1}}$ for electrons and $\kappa_{0i} \approx 60\,\mathrm{W\,eV^{-7/2}\,m^{-1}}$ for ions in a purely hydrogenic plasma. Due to these coefficients, the electron parallel heat conduction is usually much larger than the ion parallel heat conduction. Another consequence of equation 2.2, specifically the $T^{5/2}$ term, is that the upstream temperature varies little depending on $q_\parallel$. Over a wide range of possible peak $q_\parallel$ values, tokamaks usually have an upstream separatrix temperature of $T_{e\,\mathrm{sep}} \approx 100\,\mathrm{eV}$, to within a factor of 3 [9].

2.2.2 The sheath

When a surface is in contact with a plasma, the highly mobile plasma electrons accumulate on it, resulting in a negative charge. Plasma ions are then drawn to the

negatively charged surfaces, forming a thin "sheath" region where $n_i > n_e$. The sheath has a thickness of

$$\lambda_{\text{Debye}} = \sqrt{\frac{\varepsilon_0 k_B T_e}{e^2 n}}. \tag{2.3}$$

The Bohm criterion specifies that charged particles at the sheath edge have a velocity greater than or equal to the sound speed:

$$v_{se} \geq c_s = \sqrt{\frac{k_B(T_e + T_i)}{m_i}}. \tag{2.4}$$

Due to the electric potential profile near the sheath, the heat fluxes due to incident ions and electrons are related to the respective particle fluxes by constant factors:

$$q_{se}^{(e,i)} = \gamma_{(e,i)} k_B T_{(e,i)} \Gamma_{se}^{(e,i)}, \tag{2.5}$$

where the subscript *se* denotes values at the sheath edge. In a simple treatment of the problem, the electron and ion sheath heat flux transmission coefficients are $\gamma_e = 5.5$ and $\gamma_i = 3.5$. Other values can be more appropriate depending on the plasma parameters [9].

2.2.3 Sheath- and conduction-limited regimes

The sheath- and conduction-limited regimes describe two distinct scenarios of temperature variation in the direction parallel to the magnetic field. In the sheath-limited regime, virtually all power and particles enter at the top of a flux tube, the parallel flow is close to the sound speed along the length of the flux tube, $q_{\parallel\text{conv}}$ carries $\sim 6 k_B \overline{T}$ per ion-electron pair, and the sheath only removes $\sim 7 k_B T_t$ per ion-electron pair, where T_t is the temperature at the divertor target. Assuming volumetric power loss is not large, this situation results in little variation of T along a flux tube.

In the conduction-limited regime, virtually all power enters at the top of the flux tube, but the particle source is close to the divertor targets (also known as the high-recycling regime), so power is purely conducted out of the main plasma. In order for $q_{\parallel\text{cond}}$ to transport all the heat (equation 2.2), $\mathrm{d}T/\mathrm{d}s_\parallel$ may need to be large if $q_\parallel$ is

large and/or $\kappa_0 T^{5/2}$ is small.

Whether a plasma is in the sheath-limited or conduction-limited regime depends largely on the dimensionless plasma collisionality

$$\nu^*_{\rm SOL} \equiv L/\lambda_{ee\ ii} \approx 10^{-16}\frac{n_u L}{T_u^2}, \tag{2.6}$$

where L is the parallel connection length in meters between divertor target surfaces, $\lambda_{ee\ ii}$ is the electron/ion self-collisionality length in meters assuming $T_e = T_i$, n_u is the upstream density in units of m^{-3}, and T_u is the upstream temperature in units of eV. Plasmas tend to be in the sheath-limited regime when $\nu^*_{\rm SOL} \lesssim 10$ and are usually in the conduction-limited regime when $\nu^*_{\rm SOL} \gtrsim 15$ [9].

2.2.4 The heat flux width

The heat flux width λ_q is the radial decay length of the parallel heat flux at the outer midplane. Typically, the heat flux profile on a divertor target is measured and then that profile is magnetically mapped from the target to the outer midplane. Radial coordinates in the private flux region are mapped to midplane coordinates with equal normalized poloidal flux Ψ_N. An example of such a heat flux profile measured at the target and mapped to the midplane is shown in figure 2-2 (pink points). This is an Alcator C-Mod outer target profile measured by surface thermocouples. The part of the heat flux profile radially outward from the peak can typically be fit by a simple exponential decay function, thereby determining λ_q:

$$q_\parallel(\rho) = q_0 \exp(-\rho/\lambda_q), \tag{2.7}$$

where q_0 is the peak heat flux and $\rho = R_{\rm omp} - R_{\rm sep}$ is the radial coordinate at the outer midplane. The fit using this simple exponential decay function is shown in figure 2-2 over a width of one decay-length (black line).

In order to fit the entire heat flux profile, and not just a small region, more complicated functions are necessary. The most common such function is the convolution

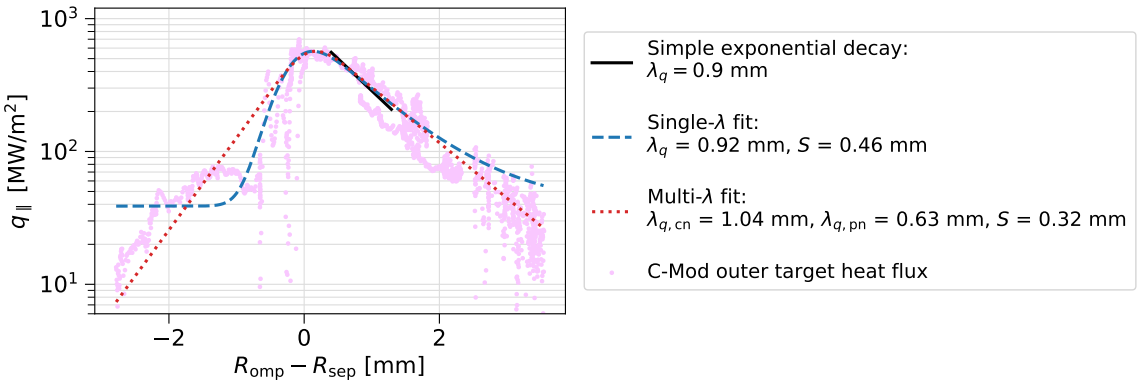

Figure 2-2: Parallel heat flux measured at the outer divertor target by surface thermocouples in Alcator C-Mod and mapped to the outer midplane. Fits to the heat flux profile using various formulas are shown.

of an exponential and a Gaussian of width S,

$$g(\rho) = \frac{1}{\sqrt{\pi}S} \exp(-\rho^2/S^2), \tag{2.8}$$

which yields

$$q_\parallel(\rho) = \frac{q_0}{2} \exp\left(\frac{S^2}{4\lambda_q^2} - \frac{\rho}{\lambda_q}\right) \operatorname{erfc}\left(\frac{S}{2\lambda_q} - \frac{\rho}{S}\right) + q_{\mathrm{BG}}, \tag{2.9}$$

where λ_q is again the exponential decay length, $q_0 + q_{\mathrm{BG}}$ is the peak heat flux as $S \to 0$, and q_{BG} is a constant background heat flux term. This functional form, also called the "single-λ" fit in this study, is usually found to fit experimental data from infrared thermography and follows the hypothesis that there is exponential falloff of heat flux in the common flux region and radial spreading of heat flux as it travels down the divertor leg [7]. However, the single-λ fit is not a very good match to the heat flux profile in Alcator C-Mod (dashed blue line in figure 2-2); the fit does not perform well in the private flux region and in the far scrape-off layer, where the assumption of a constant background heat flux q_{BG} is not well-supported by the data.

A different functional form, called the multi-λ fit, can better match the heat flux

data in Alcator C-Mod. It is based on a piecewise sum of exponentials:

$$q_{\parallel}(\rho) = \begin{cases} (q_{\mathrm{cn}} + q_{\mathrm{cf}}) \exp(\rho/\lambda_{q\,\mathrm{pn}}), & \rho < 0 \\ q_{\mathrm{cn}} \exp(-\rho/\lambda_{q\,\mathrm{cn}}) + q_{\mathrm{cf}} \exp(-\rho/\lambda_{q\,\mathrm{cf}}), & \rho \geq 0 \end{cases} \tag{2.10}$$

where $\lambda_{q\,\mathrm{cn}}$ is the heat flux width in the near common flux region, $\lambda_{q\,\mathrm{cf}}$ is that in the far common flux region, and $\lambda_{q\,\mathrm{pn}}$ is that in the near private flux region [8]. In order to fit the rounded shape of the heat flux at the target, the multi-λ function can be convolved with a Gaussian of width S, yielding

$$\begin{aligned} q_{\parallel}(\rho) = \frac{1}{2}\Bigg[& q_{\mathrm{cn}} \exp\left(\frac{S^2}{4\lambda_{q\,\mathrm{cn}}^2} - \frac{\rho}{\lambda_{q\,\mathrm{cn}}}\right) \mathrm{erfc}\left(\frac{S}{2\lambda_{q\,\mathrm{cn}}} - \frac{\rho}{S}\right) \\ & + q_{\mathrm{cf}} \exp\left(\frac{S^2}{4\lambda_{q\,\mathrm{cf}}^2} - \frac{\rho}{\lambda_{q\,\mathrm{cf}}}\right) \mathrm{erfc}\left(\frac{S}{2\lambda_{q\,\mathrm{cf}}} - \frac{\rho}{S}\right) \\ & + (q_{\mathrm{cn}} + q_{\mathrm{cf}}) \exp\left(\frac{S^2}{4\lambda_{q\,\mathrm{pn}}^2} + \frac{\rho}{\lambda_{q\,\mathrm{pn}}}\right) \mathrm{erfc}\left(\frac{S}{2\lambda_{q\,\mathrm{pn}}} + \frac{\rho}{S}\right)\Bigg]. \end{aligned} \tag{2.11}$$

The multi-λ fit in figure 2-2 maintains a good match to the data in both the far scrape-off layer and in the private flux region.

2.2.5 Detachment

Current empirical trends indicate that high fusion power production implies a challengingly large heat flux to the divertor that will cause unacceptable melting of plasma-facing components if unmitigated [7, 8]. Detachment is an important way to mitigate the heat flux to the divertor and can be compatible with a high-power core plasma. Detachment is typically achieved by supplying the plasma with an impurity gas such as nitrogen or neon. Figure 2-3 shows the multitude of reactions that occur near a detached divertor target (note that the figure shows detachment processes for a helium plasma, but these processes are also present in hydrogen plasmas). When a divertor target is detached, nearly all of the parallel heat flux from the main plasma is dissipated by impurity radiation before reaching the target surface. The momentum of ions incident on the surface and the static plasma pressure at the sur-

face are also significantly reduced. As detachment can also result in very low plasma temperatures, significant recombination can occur, raising the neutral density [12]. The degree of detachment cannot, however, be raised arbitrarily without risk: if the radiating region extends inside the separatrix, this can degrade the edge pedestal, and there is a danger of a so-called MARFE forming in the X-point region, further degrading the core plasma and even terminating the plasma [13]. Feedback control of detachment is therefore necessary [14].

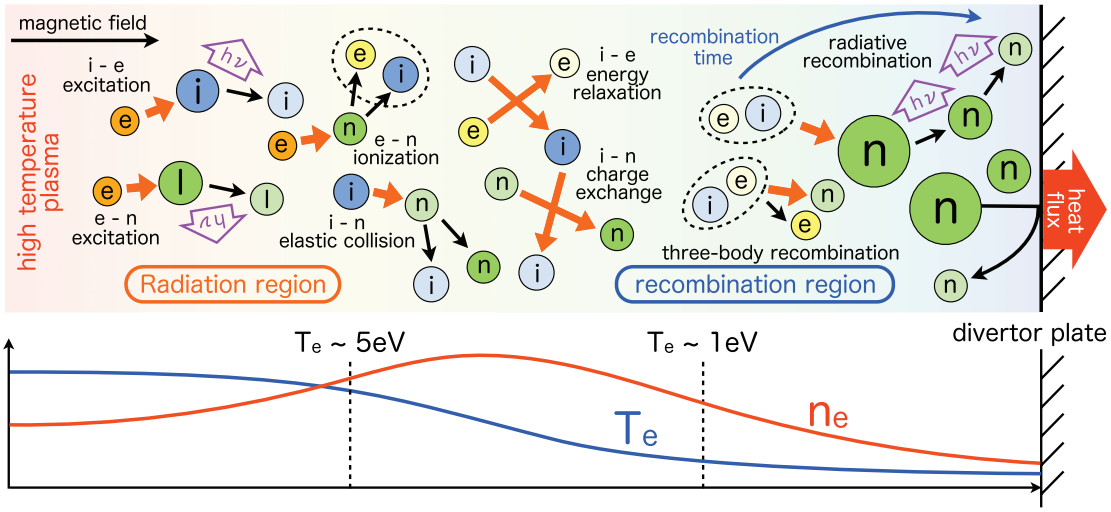

Figure 2-3: Reactions occurring near a detached divertor target. Abbreviations are e for electrons, i for helium ions, n for neutral helium atoms, I for impurity, and $h\nu$ for photons. Figure reproduced from [15].

2.2.6 Advanced divertor concepts

In addition to detachment, advanced divertor configurations may be able to safely handle large divertor heat fluxes by increasing the plasma wetted area and/or providing greater parallel distance for the heat flux to dissipate radially before reaching the target. This is an active area of research, and some concepts have few experimental results. The main concepts currently under investigation are the super-X divertor, the X-point target divertor, and the snowflake divertor (figure 2-4, table 2.1). The super-X divertor concept calls for a longer outer divertor leg (extending

to large R) and increased flux expansion [16]. In the snowflake divertor configuration, the poloidal field coils are used to produce a secondary X-point close to the primary X-point that results in the plasma having four strike-points (compared to two with a single X-point) [17]. The X-point target divertor combines the super-X and snowflake strategies, having a long outer divertor leg with a secondary X-point close to the target [18]. Other advanced divertor concepts under research include liquid-metal plasma-facing components [19] and the small-angle slot divertor [20].

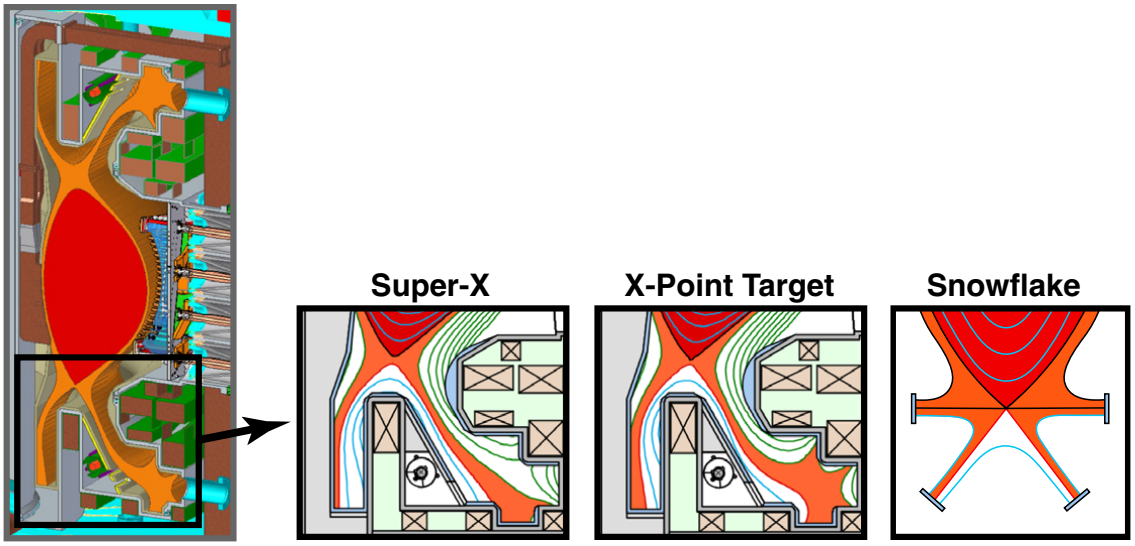

Figure 2-4: Super-X, X-point target, and snowflake divertors. Figure adapted from [18].

Concept	Design	Simulation	Experiment
Super-X	MAST-U [21], DTT [22], ADX [18], DEMO [23]	MAST-U [24–27], ADX [28], SPARC [29], ARC [30, 31]	TCV [32, 33]
Snowflake	MAST-U [21], NSTX-U [34], DTT [22], DEMO [23]	MAST-U [27, 35], NSTX-U [34], AUG [36]	DIII-D [34, 37, 38], NSTX [39], TCV [32, 40]
X-point target	MAST-U [21], ADX [18], SPARC [41]	ADX [28], ARC [30, 31]	TCV [32, 33]

Table 2.1: Overview of advanced divertor research.

2.3 Braginskii fluid equations

One of the most fundamental descriptions of a plasma is the kinetic one, in which each particle species in the plasma is characterized by a distribution function $f_s(\mathbf{x}, \mathbf{v}, t)$, where s denotes the species, $\mathbf{x}$ is the 3-dimensional position, $\mathbf{v}$ is the 3-dimensional velocity, and t is time. The Fokker-Planck equation describes the evolution of these distribution functions:

$$\frac{\partial f_s}{\partial t} + \mathbf{v} \cdot \nabla f_s + \frac{Z_s e}{m_s}(\mathbf{E} + \mathbf{v} \times \mathbf{B}) \cdot \nabla_v f_s = \sum_{s'} C_{ss'}\left[f_s, f_{s'}\right], \tag{2.12}$$

where Z_s is the atomic number of the species, m_s is the species mass, $\mathbf{E}$ and $\mathbf{B}$ are the local electric and magnetic field vectors, ∇_v is the gradient in velocity space, and $C_{ss'}$ is the collision operator between species s and s'. The Fokker-Planck equation is computationally challenging to use in tokamak plasma modeling. Taking moments of the Fokker-Planck equation (multiplying it by a function X and integrating over velocity) can yield a more tractable fluid description of the plasma. The choices of $X = 1$, $X = m_s\mathbf{v}$, and $X = m_s v^2/2$ yield the conservation equations for particles,

momentum, and energy, respectively.

The Braginskii fluid equations are derived assuming ions and electrons have comparable temperatures, $T_e \sim T_i$, and that average flows are of the order of the ion thermal speed v_{ti}:

$$\mathbf{u}_i \sim \mathbf{u}_e \sim v_{ti} \sim \sqrt{\frac{m_e}{m_i}} v_{te} \ll v_{te}. \tag{2.13}$$

The derivation is based on a particular set of orderings which relate the characteristic size of the system L (usually the length of a field line in the scrape-off layer) and the ion thermal gyroradius

$$\rho_i \sim \frac{v_{ti}}{\Omega_i} \sim \frac{\sqrt{m_i T_i}}{eB}, \tag{2.14}$$

to the mean free paths for electron-electron, electron-ion, and ion-ion collisions

$$\lambda_{ee} \sim \frac{v_{te}}{\nu_{ee}} \sim \frac{(4\pi\epsilon_0)^2 T_e^2}{e^4 n_e \ln\Lambda_{ee}}, \quad \lambda_{ei} \sim \frac{v_{te}}{\nu_{ei}} \sim \frac{(4\pi\epsilon_0)^2 T_e^2}{e^4 n_i \ln\Lambda_{ei}}, \quad \lambda_{ii} \sim \frac{v_{ti}}{\nu_{ii}} \sim \frac{(4\pi\epsilon_0)^2 T_i^2}{e^4 n_i \ln\Lambda_{ii}}, \tag{2.15}$$

where $\ln\Lambda$ is the Coulomb logarithm, with

$$\Lambda \approx \frac{12\pi\epsilon_0^{3/2} T_e^{3/2}}{n_e^{1/2} e^3}. \tag{2.16}$$

For ions, it is assumed that

$$\frac{\rho_i}{L} \sim \frac{\lambda_{ii}}{L} \sim \sqrt{\frac{m_e}{m_i}} \ll 1 \tag{2.17}$$

and

$$\frac{\rho_i}{\lambda_{ii}} \sim \frac{\nu_{ii}}{\Omega_i} \ll 1 \sim \frac{L}{\lambda_{ii}} \sqrt{\frac{m_e}{m_i}}. \tag{2.18}$$

For electrons, it is assumed that

$$\frac{\rho_e}{L} \sim \frac{\lambda_{ee}}{L} \sim \frac{\lambda_{ei}}{L} \sim \sqrt{\frac{m_e}{m_i}} \ll 1 \tag{2.19}$$

and

$$\frac{\rho_e}{\lambda_{ee}} \sim \frac{\nu_{ee}}{\Omega_e} \ll 1 \sim \frac{L}{\lambda_{ee}} \sqrt{\frac{m_e}{m_i}}. \tag{2.20}$$

These assumptions lead to the form of the Braginskii equations used in UEDGE and shown in section 2.4.1 [42, 43]. When the electron mean free path is greater than $\sim L/10$ in the scrape-off layer, discrepancies begin to arise between the fluid description and kinetic modeling [44]. Using conditions $\sim$0.1 mm outside the separatrix to evaluate L/λ_{ee}, we can assess the degree to which the discharges modeled with UEDGE in these chapters satisfy the Braginskii fluid criterion. The discharges in the C-Mod database modeled with UEDGE in chapter 4 have $0.6 < L/\lambda_{ee} < 6$. The C-Mod discharge modeled with UEDGE in chapter 5 has $L/\lambda_{ee} = 1.8$, and the SPARC discharge modeled with UEDGE in chapter 6 has $L/\lambda_{ee} = 2.0$. The choice to include flux limits in the UEDGE model, which approximate kinetic effects, was therefore a good one.

2.4 The UEDGE code

The UEDGE code [45–49] simulates ions, electrons, and neutrals as fluids in a 2D axisymmetric grid from inside the separatrix to the outer edge of the SOL. The model includes the Braginskii fluid equations, tabulated rates of radiation, ionization, recombination, and charge-exchange, adjustable cross-field particle and energy transport, and optional single-particle drifts and impurity physics. The equations are discretized on a spatial grid by a finite volume method and solved by fully implicit Newton-Krylov iterations to steady state, which is exact to machine precision [50].

A non-exhaustive selection of past work using the UEDGE code includes

- Investigating the L-H transition [51], inverse sheaths [52, 53], plasma-material interactions [54, 55], neutral models and molecular interactions [56, 57], detachment [58, 59], and ELMs [55, 60].
- Simulating existing tokamaks (C-Mod [61–66], DIII-D [61, 67–70], TCV [71], NSTX [61, 72]).
- Simulating future tokamaks, some with advanced divertors (ITER [73–75], ADX [28, 76, 77], SPARC [29], ARC [30, 31]).

2.4.1 UEDGE equations

In the UEDGE coordinate convention (figure 2-5), x and y refer to the poloidal and minor-radial directions, respectively. The poloidal direction is tangent to the flux surfaces, going clockwise from the inner divertor target to the outer target, and the radial direction is perpendicular to the flux surfaces in the direction of increasing Ψ_N. The z direction is toroidal and defined as $\hat{\mathbf{i}}_z = \hat{\mathbf{i}}_x \times \hat{\mathbf{i}}_y$. The $\|$ direction is that of the total magnetic field $\mathbf{B}$. The w direction, or $\perp$ direction, is perpendicular to $\mathbf{B}$ and tangent to the flux surfaces, having poloidal and toroidal components. Its unit vector is defined as $\hat{\mathbf{i}}_w = \hat{\mathbf{i}}_\| \times \hat{\mathbf{i}}_y = -(B_z/B)\,\hat{\mathbf{i}}_x + (B_x/B)\,\hat{\mathbf{i}}_z$ [49].

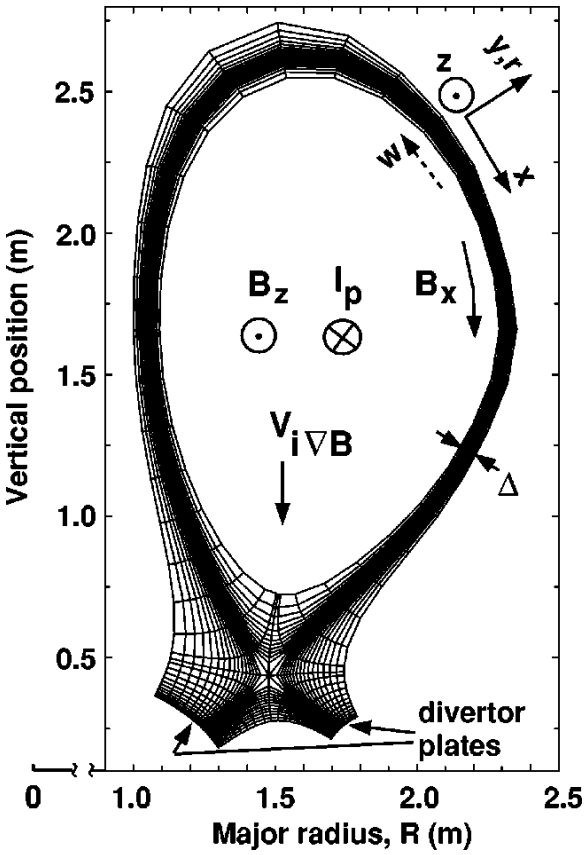

Figure 2-5: UEDGE coordinate conventions shown on an example grid in a case with the ion $\mathbf{B} \times \nabla \mathbf{B}$ drift directed down. Figure reproduced from [49].

Velocities in UEDGE include those due to classical drifts and anomalous (turbulence-driven, ambipolar) transport. $\mathbf{u}$ denotes the total velocity and v the components due

to classical drifts. The poloidal ion velocity is

$$u_{ix} = \frac{B_x}{B} v_{i\parallel} + v_{x,E} + v_{ix,\nabla B}, \tag{2.21}$$

where the first term is due to the parallel ion velocity and the second term is due to the $\mathbf{E} \times \mathbf{B}$ drift velocity. The third term includes the $\mathbf{B} \times \nabla \mathbf{B}$ and curvature drift velocities [78]:

$$\mathbf{v}_{\nabla B} = \pm \frac{B_z \left(2p_{i,e} + m_{i,e} n v_\parallel^2\right)}{enB^2 R} \left(\hat{\mathbf{i}}_R \times \hat{\mathbf{i}}_z\right), \tag{2.22}$$

where the upper and lower signs apply to ions and electrons, respectively. $p_{i,e}$ are the ion and electron pressures. This equation includes the approximations that in tokamaks, $B \approx B_0 R_0 / R$ and the $\mathbf{B} \times \nabla \mathbf{B}$ drift is entirely in the vertical direction [49].

The radial ion velocity is given by

$$u_{iy} = -\frac{D_a}{n_i} \frac{\partial n_i}{\partial y} + V_a + v_{y,E} + v_{iy,\nabla B} + v_{iy,vis}, \tag{2.23}$$

where the anomalous diffusivity D_a and anomalous convective velocity V_a are user-specified. $v_{y,E}$ and $v_{iy,\nabla B}$ are the radial components of the drift velocities. $v_{iy,vis}$ is a viscous drift velocity due to anomalous transport, which is non-ambipolar and connects the electrostatic potential across flux surfaces [78].

The electron velocity is given by

$$\mathbf{u}_e = \frac{n_i Z_i \mathbf{u}_i}{n_e} - \frac{\left(\mathbf{J}_\parallel + \mathbf{J}_{vis} + \mathbf{J}_{\nabla B}\right)}{e n_e}, \tag{2.24}$$

where the $\mathbf{J}$ terms are only those currents with non-zero divergence [49].

The ion continuity equation is

$$\frac{\partial}{\partial t} n_i + \frac{1}{V} \frac{\partial}{\partial x} \left(\frac{V}{h_x} n_i u_{ix}\right) + \frac{1}{V} \frac{\partial}{\partial y} \left(\frac{V}{h_y} n_i u_{iy}\right) = \langle \sigma_i v_{te} \rangle \, n_e n_n - \langle \sigma_r v_{te} \rangle \, n_i n_n, \tag{2.25}$$

where $\langle \sigma_i v_{te} \rangle$ is the rate coefficient for ionization and $\langle \sigma_r v_{te} \rangle$ is the rate coefficient

for recombination. $h_x \equiv 1/||\nabla x||$ and $h_y \equiv 1/||\nabla y||$ are the metric coefficients and $V = 2\pi R h_x h_y$ is the volume element in a torus with major radius R. The metric coefficients are ommitted in subsequent equations for brevity.

The equation for neutral continuity is

$$\frac{\partial}{\partial t} n_n + \frac{\partial}{\partial x}\left(n_n v_{nx}\right) + \frac{\partial}{\partial y}\left(n_n v_{ny}\right) = -\left\langle \sigma_i v_{te} \right\rangle n_e n_n + \left\langle \sigma_r v_{te} \right\rangle n_i n_n, \tag{2.26}$$

where the source terms have opposite sign compared to those of the ions.

The ion parallel momentum equation is

$$\begin{aligned} &\frac{\partial}{\partial t}\left(m_i n_i v_{i\parallel}\right) + \frac{\partial}{\partial x}\left(m_i n_i v_{i\parallel} u_{ix} - \eta_{ix}\frac{\partial v_{i\parallel}}{\partial x}\right) + \frac{\partial}{\partial y}\left(m_i n_i v_{i\parallel} u_{iy} - \eta_{iy}\frac{\partial v_{i\parallel}}{\partial y}\right) \\ &= \frac{B_x}{B}\left(-\frac{\partial p_p}{\partial x}\right) - m_i n_n \nu_{cx}\left(v_{i\parallel} - v_{n\parallel}\right), \end{aligned} \tag{2.27}$$

where $p_p = p_e + p_i$ is the total pressure. The poloidal viscosity $\eta_{ix} = (B_x/B)^2 \eta_{i\parallel}$ is classical [78], with $\eta_{i\parallel} = 0.96 n_i T_i \tau_i$ (the factor 0.96 is specific to atomic number $Z = 1$). τ_e and τ_i are the electron and ion collision times in seconds:

$$\tau_e = \frac{3\sqrt{m_e} T_e^{3/2}}{4\sqrt{2\pi} n_i Z^2 e^4 \ln\Lambda}, \tag{2.28}$$

$$\tau_i = \frac{3\sqrt{m_i} T_i^{3/2}}{4\sqrt{\pi} n_i Z^4 e^4 \ln\Lambda} \tag{2.29}$$

[43], where m_i is the mass of the ion and $\ln\Lambda$ usually has a value of 15–20 in tokamaks [1]. The radial viscosity $\eta_{iy} = m_i n_i \Upsilon_{a\parallel}$ is anomalous, with $\Upsilon_{a\parallel}$ being user-specified. $\nu_{cx} = n_i \left\langle \sigma_{cx} v_{ti} \right\rangle$ is the frequency of charge-exchange between hydrogen ions and neutral atoms. $u_{n\parallel}$ is the parallel velocity of the neutral atoms.

The equation for the neutral momentum in the parallel direction is

$$\begin{aligned} &\frac{\partial}{\partial t}\left(m_n n_n v_{n\parallel}\right) + \frac{\partial}{\partial x}\left(m_n n_n v_{n\parallel} u_{nx} - \eta_{nx}\frac{\partial v_{n\parallel}}{\partial x}\right) + \frac{\partial}{\partial y}\left(m_n n_n v_{n\parallel} u_{ny} - \eta_{ny}\frac{\partial v_{n\parallel}}{\partial y}\right) \\ &= \frac{B_x}{B}\left(-\frac{\partial p_n}{\partial x}\right) + m_i n_n \nu_{cx}\left(v_{i\parallel} - v_{n\parallel}\right), \end{aligned} \tag{2.30}$$

where η_{nx} and η_{ny} are the viscosities from charge-exchange collisions $\eta_n = T_n/(m_n\nu_{cx})$ and T_n is the neutral gas temperature. Neutrals also have velocities in the directions perpendicular to $\mathbf{B}$ due to charge-exchange and ionization:

$$\mathbf{v}_{\perp n} = -\frac{\nabla_\perp (n_n T_n)}{m_i n_n \left(n_i \langle \sigma_{cx} v_{ti} \rangle + n_e \langle \sigma_i v_{te} \rangle\right)}. \tag{2.31}$$

The total poloidal neutral velocity is then

$$u_{nx} = \frac{B_x}{B} v_{i\parallel} - \frac{B_z}{B} v_{nw}, \tag{2.32}$$

where v_{nw} is the component of $\mathbf{v}_{\perp n}$ in the w direction ($\hat{\mathbf{i}}_\parallel \times \hat{\mathbf{i}}_y$). The radial neutral velocity is $u_{ny} = \hat{\mathbf{i}}_y \cdot \mathbf{v}_{\perp n}$.

The electron energy equation is

$$\begin{aligned}
&\frac{\partial}{\partial t}\left(\frac{3}{2} n_e T_e\right) + \frac{\partial}{\partial x}\left(C_{ex} n_e u_{ex} T_e - \kappa_{ex}\frac{\partial T_e}{\partial x} - 0.71 n_e T_e \frac{B_x}{B}\frac{J_\parallel}{e n_e}\right) \\
&\qquad + \frac{\partial}{\partial y}\left(C_{ey} n_e u_{ey} T_e - \kappa_{ey}\frac{\partial T_e}{\partial y}\right) \\
&\qquad = \left(u_{ix}\frac{\partial p_e}{\partial x} - u_{iy}\frac{\partial p_i}{\partial y} - u_{iw}\frac{B_x}{B}\frac{\partial p_p}{\partial x}\right) + \mathbf{E}\cdot\mathbf{J} - K_q\left(T_e - T_i\right) + S_{Ee},
\end{aligned} \tag{2.33}$$

where $\kappa_{ex} = (B_x/B)^2 \kappa_\parallel^e$ is the classical poloidal heat conductivity [78] and $\kappa_\parallel^e = 3.16 n_e T_e \tau_e / m_e$ (the factor 3.16 is specific to atomic number $Z = 1$) [43]. $\kappa_{ey} = n_e \chi_e$ is the anomalous radial heat conductivity, where χ_e is user-specified. u_{iw} is the ion velocity in the $\hat{\mathbf{i}}_\parallel \times \hat{\mathbf{i}}_y$ direction and is only included when cross-field drifts are enabled. The convection coefficients $C_{ex,ey}$ typically have a value of 5/2 or 3/2. $\mathbf{E}\cdot\mathbf{J}$ is the Joule heating term. S_{Ee} represents the volume electron energy sources [78]. The term with the factor of 0.71 (which is specific to atomic number $Z = 1$) is the electron thermal force due to gradients in T_e that result in momentum transfer from the ions to the electrons by collisions, and

$$K_q = 3\frac{m_e}{m_i}\frac{n_e}{\tau_e} \tag{2.34}$$

is the collisional energy exchange coefficient [43].

The ion energy equation (where subscript j indicates summation over ion and neutral species and $T_i = T_n$) is

$$\frac{\partial}{\partial t}\left(\frac{3}{2}n_i T_i\right) + \frac{\partial}{\partial x}\left(C_{ix} n_i u_{ix} T_i - \kappa_{jx}\frac{\partial T_i}{\partial x}\right) + \frac{\partial}{\partial y}\left(C_{iy} n_i u_{iy} T_i - \kappa_{jy}\frac{\partial T_i}{\partial y}\right)$$
$$= \mathbf{u}_i \cdot \nabla p_i + \eta_{ix}\left(\frac{\partial v_{ij\|}}{\partial x}\right)^2 + \eta_{iy}\left(\frac{\partial v_{i\|}}{\partial y}\right)^2 + K_{qj}\left(T_e - T_i\right) + \frac{1}{2}m_i v_{i\|}^2 n_i \nu_{iz} + S_{Ej}, \tag{2.35}$$

where $\kappa_{ix} = (B_x/B)^2 \kappa_{\|}^i$ is the classical poloidal heat conductivity [78] and $\kappa_{\|}^i = 3.9 n_i T_i \tau_i / m_i$ (the factor 3.9 is specific to atomic number $Z = 1$) [43]. $\kappa_{iy} = n_i \chi_i$ is the anomalous radial heat conductivity, where χ_i is user-specified. The perpendicular viscosity $\eta_{iy} = m_i n_i \Upsilon_{a\perp}$ is anomalous, with $\Upsilon_{a\perp}$ being user-specified.

The potential equation is the result of subtracting the ion and electron continuity equations with $n_i = n_e$:

$$\nabla \cdot \mathbf{J}(\phi) = \frac{\partial}{\partial x}\left(J_x\right) + \frac{\partial}{\partial y}\left(J_y\right) = 0, \tag{2.36}$$

where $\mathbf{J}$ excludes the magnetization current, which has zero divergence due to being the curl of a vector. The components of $\mathbf{J}$ are

$$\mathbf{J} = \left[ne\left(\mathbf{v}_{i,\nabla B} - \mathbf{v}_{e,\nabla B}\right)\cdot \hat{\mathbf{i}}_x + J_{\|}\frac{B_x}{B}\right]\hat{\mathbf{i}}_x + ne\left(v_{i,y1} - v_{e,y1}\right)\hat{\mathbf{i}}_y. \tag{2.37}$$

Because terms due to the $\mathbf{B} \times \nabla \mathbf{B}$ drift do not depend on ϕ, they act as sources in equation 2.36. The equation for the parallel current $J_{\|}$ is obtained from the electron parallel momentum equation with $m_e \to 0$:

$$J_{\|} = \frac{en}{0.51 m_e \nu_e}\frac{B_x}{B}\left(\frac{1}{n}\frac{\partial p_e}{\partial x} - e\frac{\partial \phi}{\partial x} + 0.71\frac{\partial T_e}{\partial x}\right), \tag{2.38}$$

where ν_e is the electron collision frequency [78] and the numerical coefficients are for atomic number $Z = 1$ [43].

The two perpendicular velocities v_w and v_y due to drifts and currents are obtained

from the electron and ion momentum equations

$$\begin{aligned}&\frac{\partial n_{i,e} m_{i,e} \mathbf{v}_{i,e}}{\partial t} + \nabla \cdot (m_{i,e} n_{i,e} \mathbf{v}_{i,e} \mathbf{v}_{i,e}) \\ &= -\nabla p_{i,e} \pm e n_{i,e} (\mathbf{E} + \mathbf{v}_{i,e} \times \mathbf{B}) - \mathbf{F}_{i,e} - \mathbf{R}_{i,e} + \mathbf{S}^m_{i,e},\end{aligned} \tag{2.39}$$

where $\mathbf{F}_{i,e} = \nabla \cdot \mathbf{\Pi}_{i,e}$ is the viscous force, $\mathbf{R}_{i,e}$ is the friction force, and the source terms $\mathbf{S}^m_{i,e}$ describe external momentum exchange with neutrals. The perpendicular velocities are solved for iteratively, beginning with the $\mathbf{E} \times \mathbf{B}$ and diamagnetic drifts, which are dominant. Ion and electron velocities are denoted by the upper and lower signs, respectively:

$$v_{w0} = \frac{1}{B} \left(\frac{\partial \phi}{\partial y} \pm \frac{1}{en} \frac{\partial p_{i,e}}{\partial y} \right) \equiv v_{w,E} + v_{w,\nabla p}, \tag{2.40}$$

$$v_{y0} = -\frac{1}{B} \left(\frac{\partial \phi}{\partial w} \pm \frac{1}{en} \frac{\partial p_{i,e}}{\partial w} \right) - \frac{D_a}{n_{i,e}} \frac{\partial n_{i,e}}{\partial y} \equiv v_{y,E} + v_{y,\nabla p} + v_{y,a}. \tag{2.41}$$

With B constant, these velocities do not contribute to $\nabla \cdot \mathbf{J} = 0$, while the first-order corrections to v_y do. The corrections are given by

$$v_{i,y1} = \frac{1}{n\omega_{ci}} \frac{\partial}{\partial y} n \Upsilon_{a\perp} \frac{\partial}{\partial y} v_{w0} - \frac{v_{r0}}{\omega_{ci}} \frac{\partial}{\partial y} v_{w0} - \frac{(\nu_{cx} + \nu_{neo})}{\omega_{ci}} v_{w0} + \mathbf{v}_{i,\nabla B} \cdot \hat{\mathbf{i}}_y, \tag{2.42}$$

$$v_{e,y1} = \mathbf{v}_{e,\nabla B} \cdot \hat{\mathbf{i}}_y, \tag{2.43}$$

where $\omega_{ci} = eB/m_i$ is the ion cyclotron frequency. In order of appearance, the correction terms are due to the anomalous viscosity with diffusion coefficient $\Upsilon_{a\perp}$, inertia, neoclassical transport and charge-exchange, and the $\mathbf{B} \times \nabla \mathbf{B}$ and curvature drifts. The electron velocity correction is simpler due to small mass approximations. In the x-direction, the ion and electron velocity corrections are

$$v_{x1} \approx \mathbf{V}_{\nabla B} \cdot \hat{\mathbf{i}}_x \tag{2.44}$$

[49].

2.4.2 Boundary conditions

At the core boundary, UEDGE can have fixed temperatures T_e and T_i or fixed SOL-input powers P_e and P_i, defined independently for ions and electrons. Neutral/ion particle sources/sinks can be defined at boundaries and over volume regions. At all radial boundaries and at the targets, the neutral albedo and recycling coefficients can be specified. At all radial boundaries, the density, temperature, parallel velocity, and electric potential boundary conditions can generally be either fixed-value, extrapolated (e.g. $\nabla_y^2 T = 0$), gradient length-based (e.g. $T/\nabla_y T = 0.1$), or flux-based. More specialized boundary condition options also exist. At the targets, the parallel velocity can be set to the sound speed or allowed to be higher, flux limits can be configured with any value or disabled, and the values of the electron and ion sheath heat flux coefficients can be changed [78].

2.4.3 Anomalous transport

In UEDGE, the main transport coefficients that can be specified in each cell are the particle diffusivity D, convective velocity v_{conv}, and electron and ion thermal diffusivities χ_e and χ_i. The cross-field fluxes of particles (Γ_n) and energy (q_e and q_i) are largely determined by these transport coefficients, the density n, the electron and ion temperatures T_e and T_i, and the cross-field gradients:

$$\Gamma_n = -D\nabla n + v_{\text{conv}} n, \tag{2.45}$$

$$q_{e,i} = -\chi_{e,i} n \nabla T_{e,i} + \frac{5}{2}\Gamma_n T_{e,i}. \tag{2.46}$$

D, v_{conv}, χ_e, and χ_i are commonly set ad-hoc to replicate experimentally measured midplane profiles in UEDGE. Suitable profiles may be obtained with spatially uniform transport coefficients, but radial variations of the transport coefficients are typically employed in order to get a good match with measured profiles. To create a density pedestal, one common strategy is to include a radially varying profile of D with a transport barrier (reduced value) near the separatrix, where D goes to a minimum,

with uniform $v_{\text{conv}} = 0$. Another strategy is to have a uniform value of D with a radially varying profile of v_{conv} that is largely negative and reaches a minimum near the separatrix, "pinching" particles radially inward. To create a temperature pedestal, χ_e and χ_i usually have a transport barrier near the separatrix. These transport coefficient profiles can be tuned by hand or calculated iteratively.

Other anomalous transport parameters that can be specified are the radial diffusivity of toroidal momentum, which is a factor in the potential equation, and the radial diffusivity of parallel momentum. These parameters are spatially uniform but can be different for each ion species.

2.4.4 Atomic data

In the plasma edge, the balance of particles is governed by electron-impact ionization of neutrals and the recombination of ion-electron pairs into neutrals. At $n_e \geq 10^{19}\,\text{m}^{-3}$, the rates of electron excitation, de-excitation, and ionization collisions are similar to the rates of radiative decay for the excited states of hydrogen. Multi-step effects therefore become important to consider, including multi-step ionization ($\text{e}^- + \text{H} \rightarrow \text{e}^- + \text{H}^* \rightarrow 2\text{e}^- + \text{H}^+$) and (at $T_e \leq 3\,\text{eV}$) three-body recombination ($\text{e}^- + \text{e}^- + \text{H}^+ \rightarrow \text{e}^- + \text{H}$). This so-called collisional-radiative treatment is essential to accurately model hydrogen in tokamak divertors. UEDGE uses tabulated rates of hydrogen ionization and recombination from a collisional-radiative model [79, 80]. Figure 2-6 shows the rate coefficients in UEDGE for hydrogen ionization, recombination, and charge-exchange at various temperatures and densities.

While UEDGE simulations usually include neutral atoms, molecular interactions can also play an important role at high collisionality, especially near the onset of detachment. A molecular model has been implemented in UEDGE including electron-impact dissociation, elastic scattering, and energy equipartition. The molecular model was found to have a significant impact on solutions at high collisionality and to result in an earlier onset of detachment [56], but is not used in this study.

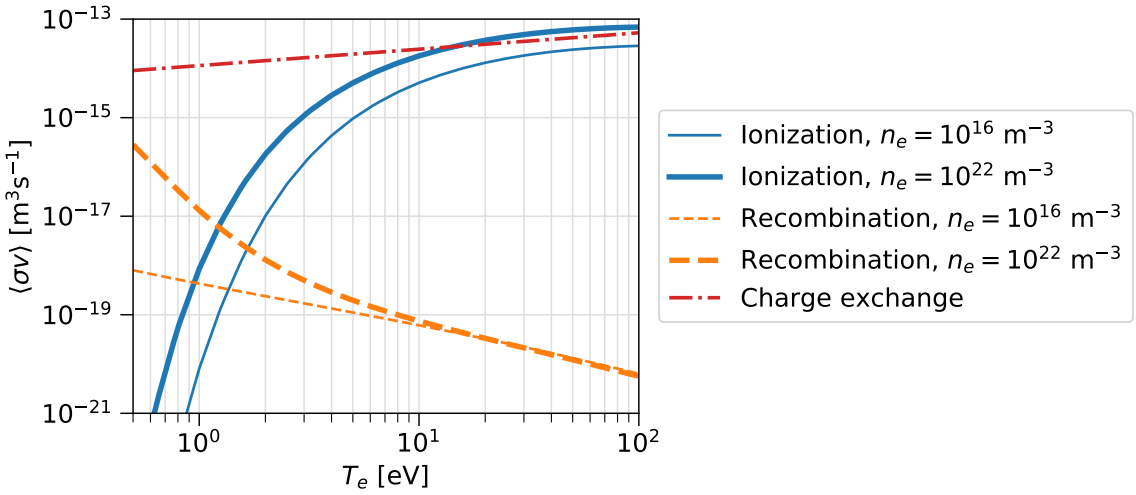

Figure 2-6: Ionization, recombination, and charge-exchange rate coefficients for deuterium in UEDGE at various electron temperatures and densities.

2.4.5 Fixed-fraction impurity model

In the fixed-fraction impurity model of UEDGE, the impurity density is a constant, user-specified fraction of the main ion density. This model reflects the assumption that the spatial transport of the various charge states is slow relative to the atomic-rate times that establish the equilibrium distribution of charge states [80]. The model uses impurity-specific look-up tables for radiation/cooling rates obtained from non-equilibrium coronal simulations using the MIST code [81]. The impurity emissivity is a function of the electron temperature, the charge-exchange recombination rate of neutral hydrogen, and the impurity lifetime due to convection. The impurity charge-exchange rate is calculated using the neutral density. The impurity lifetime is user-specified, with a default value of 1 second—solutions do not change significantly unless a much lower value is used. The impurity radiation energy is removed from the electron energy equation [78]. Figure 2-7 shows example cooling rate curves for various impurity elements when spatial transport is ignored.

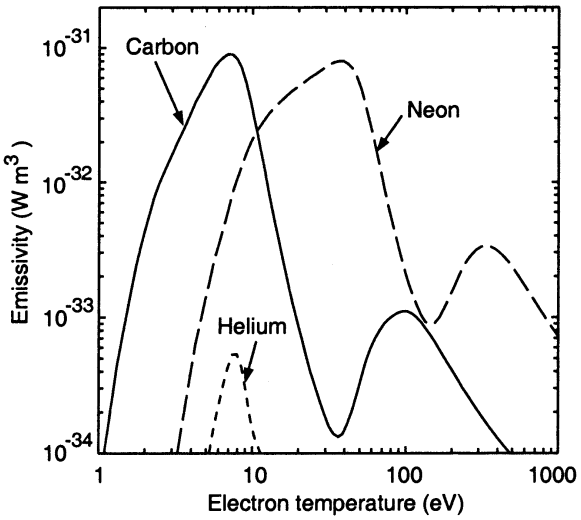

Figure 2-7: Cooling rates as a function of electron temperature for carbon, helium, and neon impurities when spatial transport is ignored. These rates must be multiplied by the impurity density and the electron density in order to obtain the radiated power density in units of W/m^3. Figure reproduced from [80].

2.4.6 Flux limiting

In the Spitzer-Härm model [82], the parallel conducted heat flux is

$$q_{\mathrm{SH}(e,i)} = -\kappa_{0(e,i)} T_{(e,i)}^{5/2} \frac{\mathrm{d}T_{(e,i)}}{\mathrm{d}s_{\|}}, \tag{2.47}$$

where κ_0 is the electron and ion thermal conductivity ($\kappa_{0e} \sim 2000\,\mathrm{W\,eV^{-7/2}\,m^{-1}}$ and $\kappa_{0i} \sim 60\,\mathrm{W\,eV^{-7/2}\,m^{-1}}$ for deuterium [9]). The Spitzer-Härm model is one of local transport (as it depends on the local temperature) and is valid at high collisionality. At low collisionality, however, the mean free path between collisions is comparable to the parallel connection length, and the character of transport is nonlocal, requiring kinetic simulations or an approximation thereof. In UEDGE, this approximation is accomplished through flux limiting.

Flux limits are imposed on parallel transport in UEDGE by harmonic averaging of the Spitzer-Härm heat flux and a fraction α of the free-streaming heat flux $q_{\mathrm{fs}(e,i)}$:

$$q_{\mathrm{fs}(e,i)} = n_{(e,i)} v_{\mathrm{t}(e,i)} k_B T_{(e,i)}, \tag{2.48}$$

$$\frac{1}{q_{\parallel(e,i)}} = \frac{1}{-\kappa_{0(e,i)} T_{(e,i)}^{5/2} \frac{\mathrm{d}T_{(e,i)}}{\mathrm{d}s_{\parallel}}} + \frac{1}{\alpha_{(e,i)} n v_{\mathrm{t}(e,i)} k_{\mathrm{B}} T_{(e,i)}}. \tag{2.49}$$

This can also be represented by an effective conductivity:

$$q_{\parallel} = \kappa_{\mathrm{eff}} q_{\mathrm{SH}}, \tag{2.50}$$

$$\kappa_{\mathrm{eff}} = \frac{\kappa_{\mathrm{SH}}}{1 + \left| \frac{q_{\mathrm{SH}}}{\alpha q_{\mathrm{fs}}} \right|}. \tag{2.51}$$

Flux limiting is effectively disabled by setting α to a very large value and usually enabled by setting $\alpha = 0.21$, which matches certain kinetic modeling results [78, 83–87]. The α coefficient is usually given the same value for ion and electron parallel heat flux. The ion parallel viscosity is similarly limited with a parameter which is usually set to 0.5 in the case of flux limiting. These flux limiting coefficient values result from fits to Monte Carlo and Fokker-Planck calculations, but can vary depending on plasma parameters. The default UEDGE flux limiter setting (used in this thesis) applies flux limiting only to the conducted heat flux, not the total conducted and convected heat flux.

Diffusive neutral fluxes are flux-limited in the radial and poloidal directions. The neutral viscosity and neutral fluxes driven by temperature gradients are also flux-limited. For neutrals, reasonable values of the flux-limiting coefficients are around 1. Flux limiting can cause computational difficulties when gradients are steep [78]. More sophisticated methods of flux limiting also exist and can be more accurate than the harmonic average scheme used in UEDGE [88].

2.5 Summary

This chapter has reviewed key concepts, e.g. tokamaks, divertors, exhaust heat flux, detachment, and flux limits, that will be explored in the following chapters. Of crucial importance for much of the work that follows was the introduction of the UEDGE simulation code, a powerful tool that will be used for analysis and prediction.

Chapter 3

Heat flux width studies in Alcator C-Mod

In tokamaks, the heat flux width λ_q describes the decay length of the parallel heat flux into the scrape-off layer (SOL). λ_q is typically inferred by analysis of the heat flux to the divertor target and subsequent magnetic mapping of the profile from the target to the outboard midplane. The target heat flux is obtained using infrared thermography, embedded thermocouples, or Langmuir probe measurements. The mapped profiles are fit with a parametric function. A small value of λ_q results in challengingly large heat fluxes to the divertor, which, if not mitigated, can result in unacceptable sputtering and melting of plasma-facing components. Empirical databases and power law fits are a common technique in fusion research to project parameters to new devices, lacking validated theoretical or first-principles ways of doing so. In this study, a C-Mod database is augmented with midplane electron density and temperature data to verify whether any edge local quantity or gradient is well-correlated with λ_q. The results of this study have been published in [89].

3.1 Previous heat flux width studies

A multi-machine study by Eich et al. [7] found that λ_q scales approximately as the inverse of the poloidal magnetic field B_P measured at the outer midplane separatrix

for plasmas with H-mode confinement and with the outer divertor "leg" attached to the divertor target. Data from C-Mod was included in that study and, because of its high field and small size, played a key role in the scaling. This scaling predicts $\lambda_q < 1\,\mathrm{mm}$ for ITER and SPARC [8, 41], for plasmas in which ∼100 MW (ITER) [7] and ∼28 MW (SPARC) of power is foreseen to reach the scrape-off layer [41]. A subsequent study of an extensive C-Mod database found that the average pressure from stored energy ($\overline{p} = 2/3\ W_{\mathrm{MHD}}/V_{\mathrm{LCFS}}$, where W_{MHD} is the plasma stored energy and V_{LCFS} is the plasma volume inside the magnetic separatrix, both calculated from EFIT magnetic reconstructions [90]) was an excellent predictor of λ_q, with a unified scaling across L-, I-, and H-mode confinement regimes [8]. Both of these empirical scalings imply that high-pressure, high-performance fusion plasmas with conventional magnetic divertor shapes (e.g. the single-null configuration) will likely produce unsustainably high heat flux densities if unmitigated, further motivating the development of solutions such as controlled detachment [12] and advanced divertor configurations such as the super-X [16, 21, 28, 32], X-point target [18, 21, 28, 32, 41], and snowflake divertor [17, 39, 40].

A 2020 study on ASDEX Upgrade (AUG) [91] found a correlation between λ_q and the average pressure, and a stronger correlation between λ_q and the edge electron pressure from Thomson scattering data at $\rho_{\mathrm{pol}} = 0.95$, where $\rho_{\mathrm{pol}} = \sqrt{\Psi_N}$ and $\Psi_N = (\Psi - \Psi_{\mathrm{axis}})/(\Psi_{\mathrm{sep}} - \Psi_{\mathrm{axis}})$ is the normalized poloidal flux. Furthermore, it found that λ_q scales with the electron pressure decay length at the separatrix, λ_{pe}, and that the data conformed to a relationship of $\lambda_q = 2/7\,\lambda_{Te}$ between the heat flux width and the separatrix electron temperature decay length as expected in the Spitzer-Härm electron heat conduction regime [91]. It is reasoned that the localized edge pressure and gradients are more directly correlated with the heat flux width than the average pressure. Earlier work on AUG has also verified that profile edge gradients are related to λ_q [92]. The main goal of the present study is to determine whether localized quantities and gradients also provide better scalings than the volume-averaged pressure in Alcator C-Mod.

The unified scalings with average pressure in C-Mod and with average/edge pressure in AUG differ from others in the literature, which tend to be developed for

individual confinement modes. Early multi-device studies focused on L-mode [93] and H-mode extrapolations of λ_q to ITER [7, 94]. The heuristic drift model performs well for H-modes across several devices but overpredicts λ_q in C-Mod [95, 96]. The C-Mod scaling with average pressure has also been tested on a multi-machine L-mode database, which found acceptable cross-device performance that was improved by the inclusion of the inverse aspect ratio a/R_0 and the plasma beta (the study also tested many other L-mode scalings) [97]. The critical gradient model, in which a ballooning instability sets an upper limit on the pressure gradient scale length that is related to the heat flux width, is satisfied in DIII-D discharges but does not provide as good a scaling for λ_q as the heuristic drift model [98, 99]. A theory-based scaling for the near SOL pressure decay length in L-mode, however, has been found to be a good predictor of the experimentally measured λ_q in a multi-machine database [100]. Recent studies in H-mode on AUG found that a turbulence control parameter is highly relevant [101] and that filament transport can have a strong impact on λ_q, an effect that is not captured by many of the existing scalings [102]. This underscores the importance of developing empirical scalings for λ_q from databases that cover a wide variety of plasma conditions.

3.2 The plasma edge database

The C-Mod heat flux width database [8] contains fits to the outer divertor heat flux profile measured through strike-point sweeping (figure 3-1) for around 300 discharges expressing no edge-localized modes (ELMs). In the present work, the original database was narrowed down to around 120 discharges that have good core and edge profile data from the Thomson scattering system and stationary plasma conditions over a period of at least 100 milliseconds, resulting in the parameter ranges shown in table 3.1. While the database covers a wide range of engineering parameters, the ranges of plasma triangularity and elongation are narrow due to the requirement to sweep the outer strike point over the Langmuir probes and surface thermocouples to measure heat flux profiles on the lower outer divertor target. As in the original

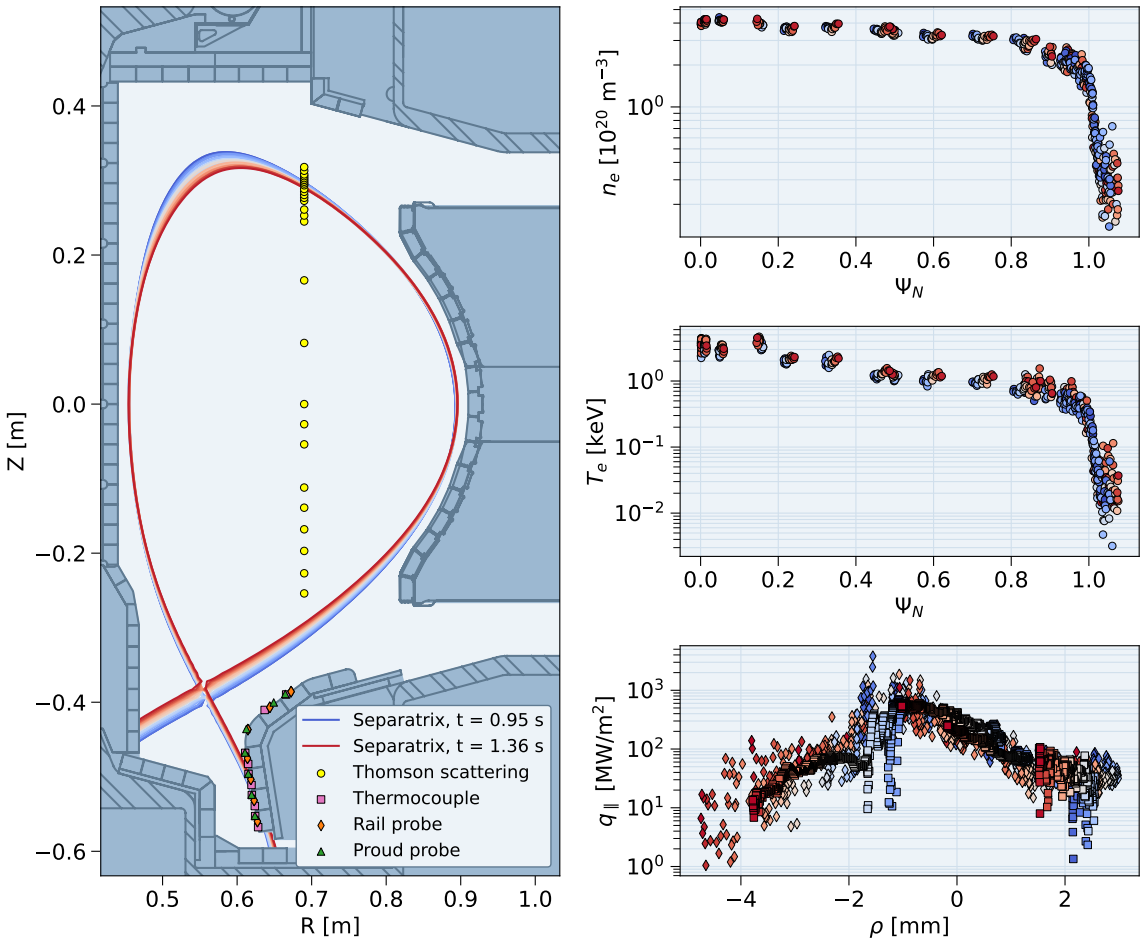

Figure 3-1: Overview of a strike-point sweep for an example discharge (1160718025) showing the change in separatrix location, Thomson scattering data for electron density and temperature, and parallel heat flux measured at the divertor surface by Langmuir probes and surface thermocouples. The profile data are colored according to the time of their measurement and correspond to the colors of the separatrix.

database, there are approximately equal proportions of L-mode, I-mode [11], and enhanced D-alpha (EDA) [103] H-mode discharges. Approximately half of the L-mode discharges are with "forward" toroidal field (i.e. with the ion $\mathbf{B} \times \nabla \mathbf{B}$ drift toward the X-point and lower divertor) and half are with "reversed" toroidal field. All of the I-mode discharges are with reversed field, and all of the EDA H-mode discharges are with forward field. No relationship is observed between the heat flux width and the toroidal field direction, all else being similar.

The target heat flux profiles are fit using a piecewise sum of exponentials called the multi-λ fit [8]:

$$q_{\parallel}(\rho) = \begin{cases} (q_0 - q_{\mathrm{pf}})\, e^{\rho/\lambda_{q\,\mathrm{pn}}}, & \rho < 0 \\ (q_0 - q_{\mathrm{cf}})\, e^{-\rho/\lambda_{q\,\mathrm{cn}}} + q_{\mathrm{cf}} e^{-\rho/\lambda_{q\,\mathrm{cf}}}, & \rho \geq 0 \end{cases} \tag{3.1}$$

where $\lambda_{q\,\mathrm{cn}}$ and $\lambda_{q\,\mathrm{cf}}$ describe the falloff in the near and far common flux region and $\lambda_{q\,\mathrm{pn}}$ describes the near private flux region (this equation was convolved with a Gaussian in order to better fit the data, as detailed in section 2.2.4). This function provides a well-matching shape over the large dynamic range of the probe and thermocouple data, rather than the original parametric single-λ fit that was used for fitting infrared measurements of divertor heat flux from multiple machines including C-Mod and AUG [7]. One of the quantities obtained from the multi-λ fit, $\lambda_{q\,\mathrm{cn}}$, describes the falloff in heat flux density in the near common flux region, just as λ_q in the single-λ fit does, so they can be treated the same despite originating from different parametric fits. In this work, the "λ_q" values from C-Mod are actually $\lambda_{q\,\mathrm{cn}}$.

The C-Mod and AUG databases have some notable differences. The C-Mod database includes higher average pressures and lower values of λ_q than the AUG database: C-Mod has $\overline{p}$ of 12–160 kPa and λ_q of 0.6–2.3 mm, while AUG has $\overline{p}$ of 3–35 kPa and λ_q of 0.8–5 mm. The C-Mod database also includes a larger range of average pressures for I- and H-mode discharges compared to AUG. The AUG database includes both inter-ELM periods from ELMy H-modes and ELM-free H-modes, while the H-modes in the C-Mod database are EDA H-modes, which have no ELMs but rather a quasi-coherent edge mode that flushes impurities and particles out of the

Parameter	Range
On-axis toroidal magnetic field B_T	5.1–7.9 T
Poloidal magnetic field B_P	0.42–1.3 T
Average electron density $\overline{n}_e$	4.4×10^{19}–$4.8 \times 10^{20}\,\mathrm{m}^{-3}$
Input power P_{in}	0.52–5.8 MW
Elongation κ	1.5–1.8
Triangularity δ	0.49–0.61

Table 3.1: Parameter ranges for the subset of the C-Mod heat flux width database with good profile data. The poloidal magnetic field is that calculated 1 mm outside the separatrix at the outer midplane.

confined plasma, thereby maintaining a steady-state H-mode [104, 105].

3.3 Profile fitting

The C-Mod core and edge Thomson scattering diagnostics were used to obtain electron density and temperature data [106]. Electron cyclotron emission (ECE) diagnostics (GPC1 and GPC2) were used to obtain additional electron temperature data [107]. Gaussian process regression (GPR) [108] was used to fit the profiles of density and temperature (figure 3.1). Confidence bounds resulting from this method are not rigorous because the Markov chain Monte Carlo (MCMC) method was not used; MCMC can require time-consuming fine tuning which was not feasible for 120 profiles.

In order to overcome uncertainty in the location of the separatrix in the Thomson scattering profiles [109, 110], the profiles of electron density and temperature obtained from GPR fitting were shifted to have a separatrix temperature consistent with the 2-point model [9]:

$$T_e^{\mathrm{sep}} \approx \left(\frac{7}{16} \frac{P_{\mathrm{sep}} q_{\mathrm{cyl}}^2 A}{\kappa_0^e \hat{\kappa} \lambda_q} \right)^{2/7} \tag{3.2}$$

as was done for the AUG profiles [91]. The power crossing the separatrix, P_{sep}, was approximated as $P_{\mathrm{ICRF}} + P_{\mathrm{OH}} - \mathrm{d}W/\mathrm{d}t - P_{\mathrm{rad\,core}}$, where the core radiated power is computed from a foil bolometer array. $q_{\mathrm{cyl}} = \frac{B_T \hat{\kappa}}{\langle B_P \rangle A}$ is the safety factor, where B_T is the toroidal magnetic field at the magnetic axis, $\langle B_P \rangle = \frac{\mu_0 I_P}{2\pi a \hat{\kappa}}$ is the average

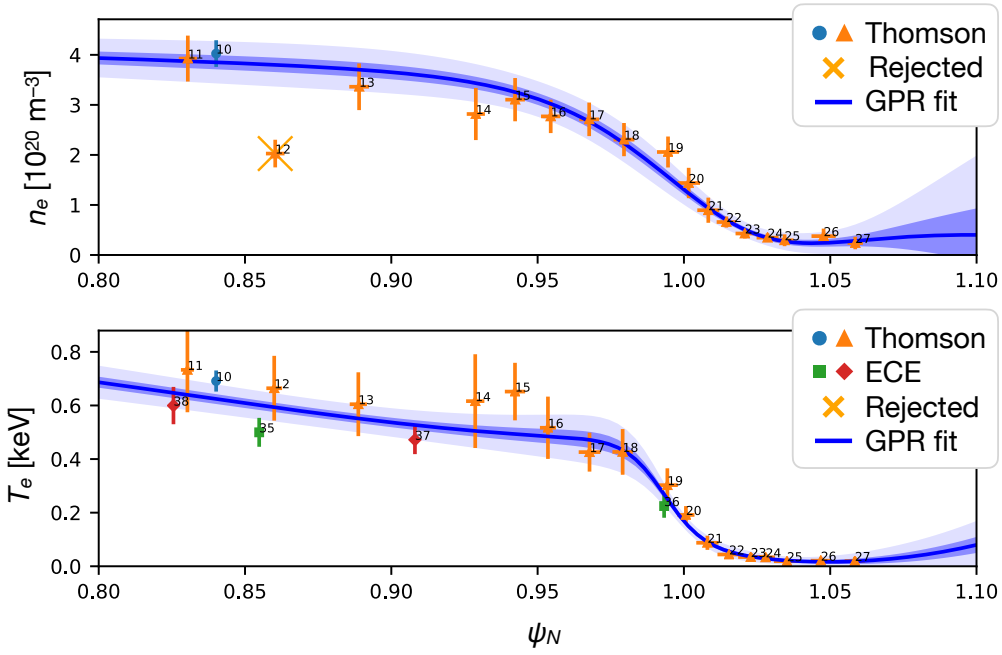

Figure 3-2: Example of electron temperature and density data and resulting fits from GPR for an H-mode discharge (1160729008). The light blue shaded region around the GPR fit shows the confidence bounds.

poloidal magnetic field, $A = R/a$ is the aspect ratio, and $\hat{\kappa} = \sqrt{1 + \kappa^2/2}$, where κ is the elongation. A value of $\kappa_0^e \approx 2000\,(\mathrm{eV})^{7/2}\,\mathrm{W\,m^{-1}}$ was used for the Spitzer-Härm electron conductivity. The values of λ_q were those from the experimental database, obtained from fits to the heat flux profile at the outer target. The values of T_e^{sep} obtained using this formalism ranged from 54 to 160 eV.

3.4 Heat flux width scalings with local quantities

Figure 3-3 compares the scaling of λ_q with the average pressure evaluated from the plasma stored energy (figure 3-3(a)), and the scaling with the electron pressure at $\rho_{\mathrm{pol}} = 0.95$ ($\Psi_N = 0.90$) from temperature and density profiles (figure 3-3(b)). The data are fit with scalings of the form $\lambda_q/\mathrm{mm} = A(p/\mathrm{kPa})^b$, with A and b being the two free parameters output by the fit. There is good agreement between C-Mod and AUG in the scaling of heat flux width with average pressure across all modes: the C-Mod scaling is $\lambda_q/\mathrm{mm} = (8.2 \pm 0.5)(\overline{p}/\mathrm{kPa})^{-0.48\pm0.02}$, while the AUG scaling is

$\lambda_q/\text{mm} = (7.6 \pm 0.25)(\overline{p}/\text{kPa})^{-0.52\pm0.01}$ [91]. Both fit factors are very similar, making this a remarkably good cross-regime and cross-device scaling. The fits with electron pressure at $\rho_{\text{pol}} = 0.95$, $\lambda_q/\text{mm} = (2.5 \pm 0.02)(p_e^{95}/\text{kPa})^{-0.34\pm0.01}$ (AUG) [91] and $\lambda_q/\text{mm} = (1.8 \pm 0.1)(p_e^{95}/\text{kPa})^{-0.26\pm0.03}$ (C-Mod) are quite similar. The absolute value of the edge pressure fit exponent is lower than that of the fit with average pressure. There is also considerably more scatter in the edge data, with lower coefficients of determination (R^2) in all cases. Finally, if data from L-, I-, and H-mode are fit separately as a function of p_e^{95}, the H-mode heat flux width scales as $(p_e^{95})^{-0.55}$, which is quite a different exponent compared to that of the L-modes (-0.27) and I-modes (-0.21). The AUG database has a smaller range of average and edge pressures in H-mode, making it difficult to say whether a separate trend for H-modes is observed in AUG.

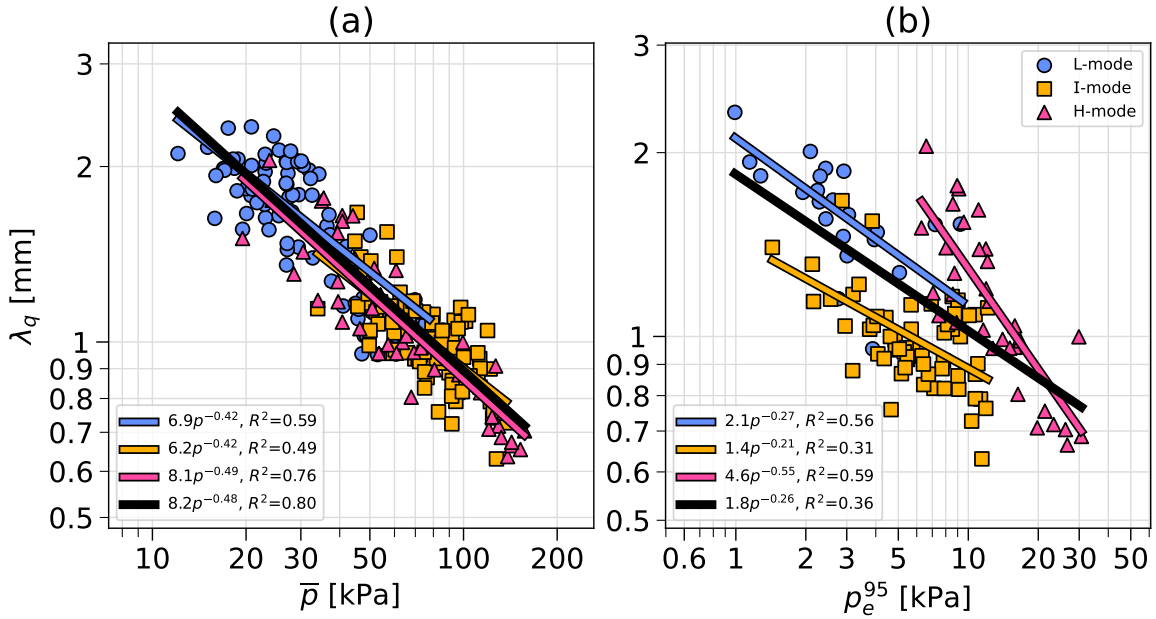

Figure 3-3: Scalings of the heat flux width with (a) average pressure from stored energy and (b) with electron pressure at $\rho_{\text{pol}} = 0.95$ fit with regressions of form $\lambda_q/\text{mm} = A(p/\text{kPa})^b$. Fits within individual confinement modes are shown by the correspondingly colored lines, and fits across all confinement modes are shown by black lines.

Figure 3-4(a) shows an approximately linear relationship between core ($\rho_{\text{pol}} \approx 0.1$) electron pressure and average pressure, with all confinement modes obeying a similar

trend, but in figure 3-4(b) H-modes have clearly higher edge pressure at $\rho_{\mathrm{pol}} = 0.95$ than L- and I-modes. This is expected due to the fact that the majority of H-modes do not have higher core pressure than L- and I-mode discharges, but have higher edge pressure due to their higher edge density. This explains why using the edge pressure for regressions in this database leads to different trends for different confinement modes.

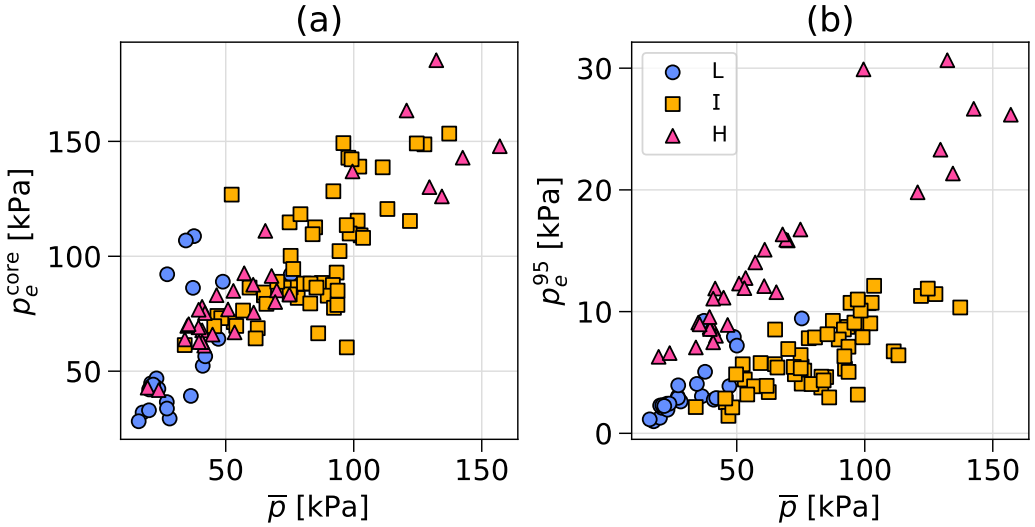

Figure 3-4: (a) Core ($\rho_{\mathrm{pol}} \approx 0.1$) electron pressure as a function of the average pressure from stored energy, and (b) electron pressure at $\rho_{\mathrm{pol}} = 0.95$ as a function of the average pressure.

The large range of average pressures in the C-Mod database across all confinement modes and the availability of profiles of n_e and T_e make it possible to exhaustively evaluate relationships between λ_q and local plasma parameters. Figure 3-5 shows regressions of the form $\lambda_q = AX^b$, where X is alternately p_e, n_e, and T_e, and fits are performed at every radial coordinate. Superimposed in dashed horizontal lines are the results of fits using volume-averaged quantities. $\overline{p}$ is obtained from the plasma stored energy while $\overline{n}_e$ and $\overline{T}_e$ are obtained by integrating profiles from Ψ_N of 0 to 1, with no T_e^{sep}-based shifting to avoid having to extrapolate profiles in case of an outward shift (note that the T_e^{sep}-based shifting impacts the average values much less than it does the local values). The graphs show Ψ_N up to 1.03, past which the experimental data can be scarce due to the T_e^{sep}-based shifting or have large error bars, and the value of R^2 is near zero.

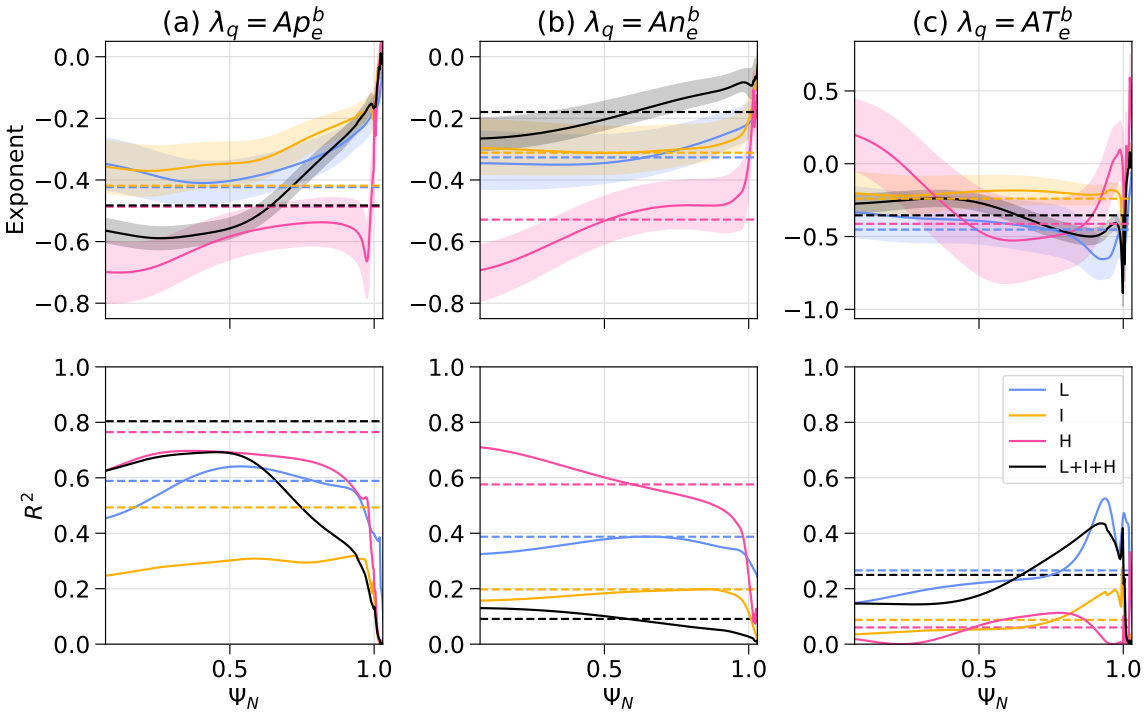

Figure 3-5: (top row) Exponent obtained from fitting a regression of form $\lambda_q = AX^b$ at each radial coordinate of normalized poloidal flux Ψ_N, with X being the electron pressure (column a), electron density (column b), and electron temperature (column c). (bottom row) Coefficient of determination R^2 for each regression. Colored lines show fits to individual confinement modes, and black lines show fits to all confinement modes. Dashed horizontal lines show exponents and R^2 values for fits to volume-averaged quantities: average pressure from stored energy (column a), average electron density from profiles (column b), and average electron temperature from profiles (column c).

The fits of λ_q with p_e, n_e, and T_e computed at every point along the profiles in figure 3-5 can be used to determine the local quantities most strongly correlated with λ_q for discharges in all confinement modes (L+I+H, black lines in figure 3-5). The scalings with p_e for all modes in the region of $\Psi_N < 0.5$ have the highest R^2 among the local quantity scalings, while the edge T_e at $\rho_{\text{pol}} = 0.95$ ($\Psi_N = 0.90$) somewhat exceeds the R^2 of the p_e fit at the same location. The local n_e fits for all modes have quite low R^2 over the entire profile due to the separate clustering of each confinement mode (not shown). Fits using the average quantities (dashed lines in figure 3-5) have higher R^2 than the local p_e fits but similar R^2 compared to those with n_e and T_e. It can therefore be concluded that the core pressure and to a lesser extent the edge temperature are most strongly correlated with λ_q across all confinement modes.

The scalings of λ_q in individual confinement modes in figure 3-5 show the complicated realities that underlie the scalings for L+I+H mode. The scaling with $\overline{p}$ is the most unified across modes, with the dashed lines in figure 3-5(a) showing exponents that are very similar in value. In scalings with n_e and p_e, H-modes have very different exponents compared to L- and I-modes. H-modes also have significantly poorer fits with T_e compared to L- and I-mode. This visualization shows that the scalings of λ_q with local quantities are in all cases less unified across confinement modes than those with average quantities: H-mode scalings with local quantities in particular stand out compared to L- and I-mode, warranting further investigation.

The importance of p_e^{95} in predicting λ_q is also tested using fits which allow for independent exponents of electron density and temperature:

$$\frac{\lambda_q}{\text{mm}} = A\left(\frac{n_e}{10^{20}\,\text{m}^{-3}}\right)^b\left(\frac{T_e}{\text{keV}}\right)^c. \tag{3.3}$$

The results of these fits are shown in figure 3-6. In the region of $\rho_{\text{pol}} \approx 0.1$, the n_e and T_e exponents are both around -0.6 (see figure 3-6(a) x-axis label), which is close to the $\overline{p}$ scaling exponent of -0.48 (figure 3-3(a)), and results in the same R^2 value as the fit with p_e^{core} alone. Further toward the edge, the fit exponent is larger in magnitude for T_e (-0.5) than n_e (-0.15). These two-parameter fits have a

higher R^2 in the edge than the fit with p_e^{95} alone (figure 3-5(a) black curve), but the low R^2 of the p_e^{95} fit is mainly due to the H-modes having a different slope and less overlap compared to L/I-mode (figure 3-3(b)). These fits with independent n_e and T_e exponents indicate that near the core, the *pressure* is indeed the important variable to predict λ_q, because n_e and T_e have similar exponents in the optimal fit, while near the edge, the temperature appears to be more important than the pressure.

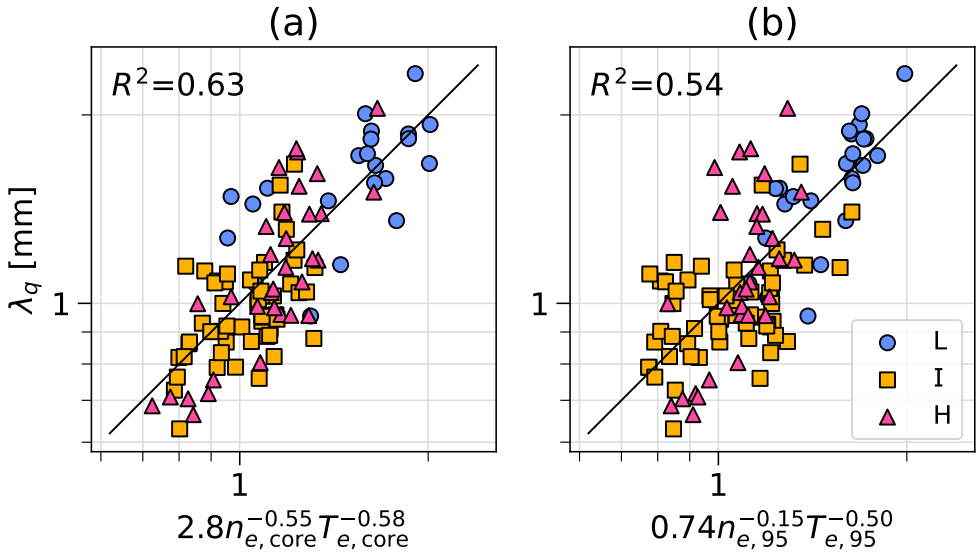

Figure 3-6: λ_q measurements compared to predictions from the regression $\lambda_q = An_e^bT_e^c$ fit from profiles (a) at $\rho_{\mathrm{pol}} \approx 0.1$ and (b) at $\rho_{\mathrm{pol}} = 0.95$. The identity line is shown in black.

Because the H-modes appear to follow quite a different scaling of λ_q with edge quantities compared to L/I-mode, another option is to abandon the unified scalings and use a different scaling for each confinement mode, i.e. $\lambda_q = A_m p_{e,95}^{b_m}$ where the index m indicates the confinement mode in which the fit was calculated (the values of A and b for each confinement mode are shown in the legend of figure 3-3(b)). This mode-dependent fit with $p_{e,95}$ (shown in figure 3-7(b)) results in an R^2 value of 0.71, approaching the quality of the $\overline{p}$ scaling (shown for comparison in figure 3-7(a)). A mode-dependent fit using independent exponents for n_e and T_e at $\rho_{\mathrm{pol}} = 0.95$ ($\lambda_q = A_m n_{e,95}^{b_m} T_{e,95}^{c_m}$) did not provide much improvement, achieving an R^2 value of 0.73. It is therefore possible to achieve accurate predictions of λ_q in C-Mod using edge p_e if the confinement mode is taken into account, and random error in the n_e and T_e

profiles does not appear to be entirely responsible for the significantly lower R^2 of the mode-independent p_e^{95} scaling.

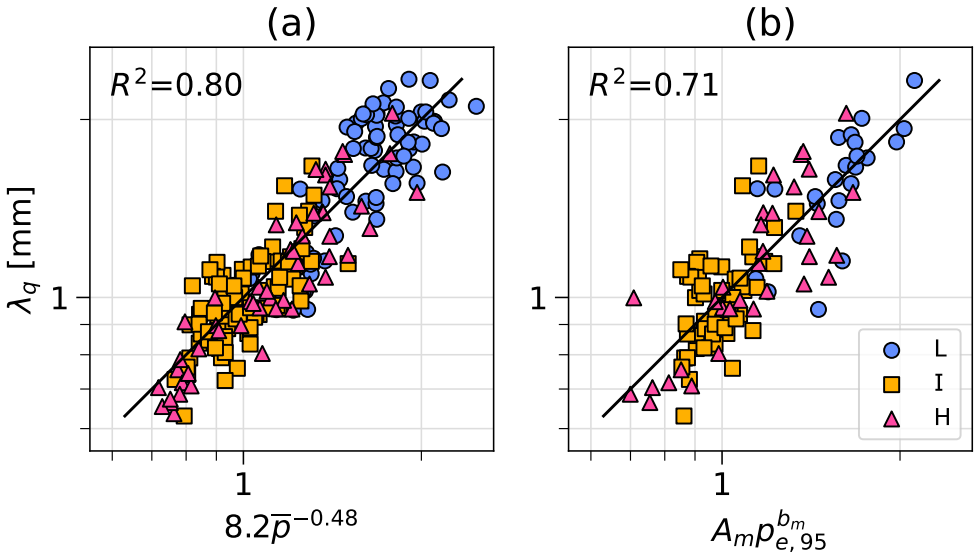

Figure 3-7: Comparison of the experimental λ_q with (a) λ_q predicted by the Brunner scaling with $\overline{p}$ and (b) λ_q predicted by a mode-dependent fit with p_e at $\rho_{\text{pol}} = 0.95$. The identity line is shown in black.

3.5 The heat flux width and edge gradients

In Alcator C-Mod, the heat flux width appears to be overall weakly correlated with separatrix gradient scale lengths (e.g. $L_{Te}^{\text{sep}} = T_e^{\text{sep}}/|\nabla T_e^{\text{sep}}|$), as shown in figure 3-8. No single gradient scale length variable appears to have a much stronger correlation with λ_q than the others. Comparing confinement modes, H-modes may have a strong correlation between λ_q and the pressure and density gradient lengths, but there is significant uncertainty in this statement due to the small range of H-mode gradient lengths. L- and I-modes cover a large range of all gradient lengths but show very little correlation with λ_q. The AUG database finds a strong cross-regime correlation between λ_q and λ_{Te}, which are well fit by $\lambda_q = 2/7\,\lambda_{Te}$, the scaling of the Spitzer-Härm electron heat conduction regime. Within individual confinement modes in the AUG database of [91], the Spitzer-Härm scaling is only evident for the L-mode points, but in a different database of AUG H-modes only, the Spitzer-Härm scaling is superior

to the flux-limited model [92]. This is different from what is found in the C-Mod database, where the Spitzer-Härm scaling does not adequately characterize any of the individual confinement modes. This may be due to the L-mode data in C-Mod having a maximum L_{Te}^{sep} of 10 mm, while the data in AUG with L_{Te}^{sep} between 10–15 mm are crucial to observe the Spitzer-Härm scaling [91]. H-modes in C-Mod also have smaller L_{Te}^{sep} in the range of 1–6 mm compared to 5–8 mm [91] and 4–11 mm [92] in AUG, and the Spitzer-Härm scaling underestimates λ_q in C-Mod while it overestimates it in AUG [91]. This may be due to C-Mod H-modes having lower collisionality, which would result in the Spitzer-Härm scaling being less adequate due to more important kinetic effects, nonlocal transport, and heat flux limiting. This could also explain why the AUG data is better fit by scalings with p_e^{95} and $\lambda_{pe}^{\text{SOL}}$ than the C-Mod data: if the AUG SOL is better characterized by local transport than the C-Mod SOL, AUG would see better correlations of λ_q with local quantities and gradients. One possible source of error in comparing C-Mod and AUG gradient scale lengths is that they are estimated differently. In the AUG analysis, a small region about the separatrix is fit by an exponential with decay length λ_{Te}, with $\lambda_{Te} = L_{Te}^{\text{sep}}$. In contrast, the gradient lengths in the C-Mod database are calculated from the full-profile GPR fits.

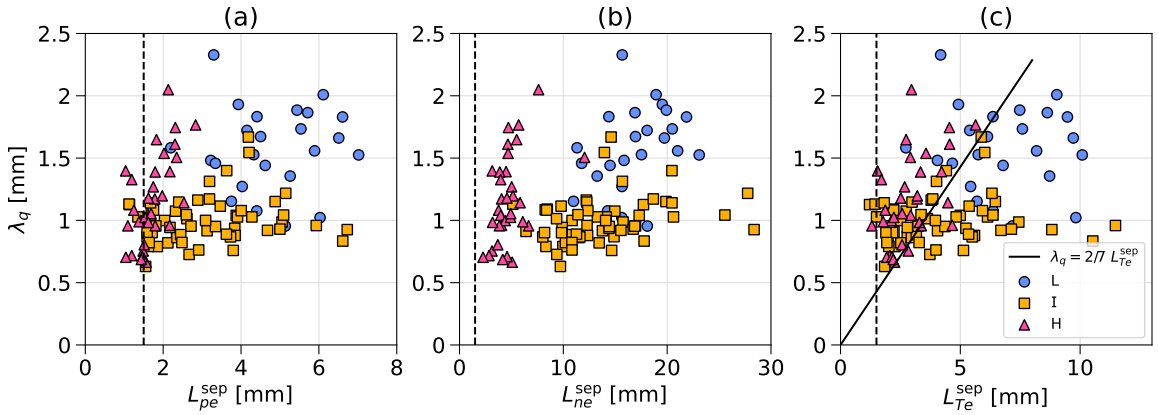

Figure 3-8: Heat flux width as a function of the gradient length evaluated at the separatrix for (a) electron pressure, (b) electron density, and (c) electron temperature. The solid black line in (c) shows λ_q assuming Spitzer-Härm electron heat conduction. The dashed black vertical lines show the smallest radial feature size of approximately 1.5 mm that can be resolved by Thomson scattering.

Finally, the relationship between λ_q and the pedestal pressure gradient length and

the relationship between the pedestal and separatrix pressure gradient lengths are examined (figure 3-9). The pressure gradient length at the pedestal is defined, for the purpose of comparison to AUG, by the same approximation of

$$L_{pe}^{\text{ped}} = -\frac{p_e}{\nabla p_e} \approx \frac{p_e^{95} + p_e^{\text{sep}}}{2} \cdot \frac{R^{\text{sep}} - R^{95}}{p_e^{95} - p_e^{\text{sep}}} \tag{3.4}$$

[91]. In figure 3-9(a) there is a somewhat unified trend between λ_q and L_{pe}^{ped} across all confinement modes, with a similar amount of scatter as in the AUG database. L_{pe}^{ped} appears to be a better predictor of λ_q in C-Mod than L_{pe}^{sep}, at least for L- and I-mode discharges (figure 3-9(a) compared to figure 3-8(a)). In figure 3-9(b) the inverse gradient length at the separatrix is compared to the approximate pedestal inverse gradient length, showing significantly greater spread in the data compared to AUG, with no clear unifying linear trend. This could be due to the much smaller range of R/L_{pe}^{ped} on C-Mod of ∼70 to ∼85, compared to ∼65 to ∼125 on AUG [91]. The fact that the pressure gradient in the SOL is somewhat independent of the weakly varying gradient in the pedestal region of the confined plasma may help explain why the scalings of λ_q with p_e^{95} and with L_{pe}^{sep} have more scatter than the scaling with average pressure.

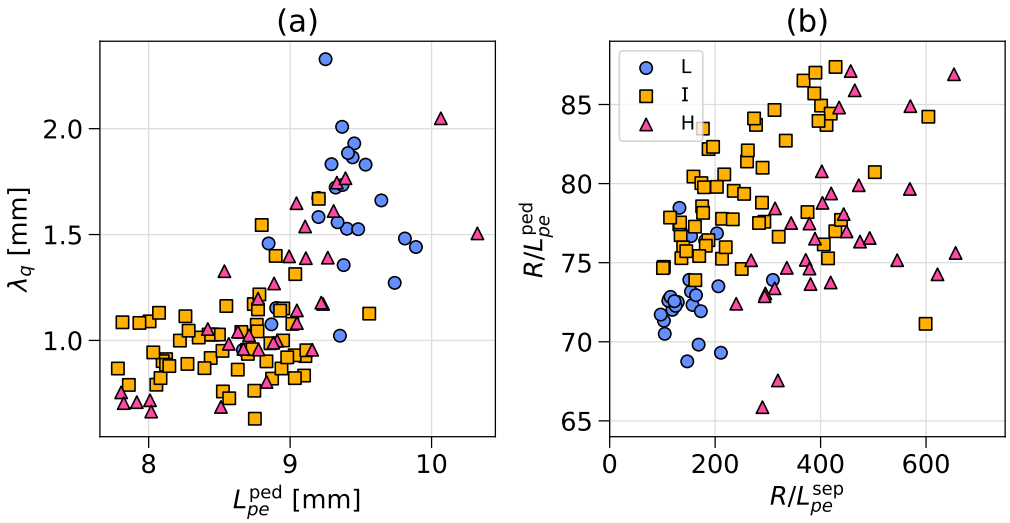

Figure 3-9: (a) Heat flux width as a function of pedestal electron pressure gradient length. (b) Inverse electron pressure gradient length at the pedestal as a function of inverse electron pressure gradient length at the separatrix, both normalized by major radius ($R = 0.68\,\mathrm{m}$ for C-Mod).

3.6 Sources of error

The finding that λ_q is better correlated with $\overline{p}$ in C-Mod than it is with p_e^{95} contrasts with theoretical expectations that cross-field turbulent transport (due to instabilities and modes that strongly depend on local plasma conditions) can broaden the heat load in the SOL [101], while there is as yet no theoretical justification for λ_q to instead be a strong function of the *average* pressure. Some possible reasons why the scaling with edge pressure in C-Mod is of reduced quality compared to the average pressure are listed:

- The average pressure, being an integrated quantity, can have lower random error than the localized pressure or its gradient.

- The edge ion temperature in C-Mod can be significantly higher than the electron temperature, especially at low collisionality [83], which implies that the electron pressure provides an incomplete description compared to the total pressure from stored energy.

- There is some error in the EFIT mappings, which use preset functional forms

of pressure and other profiles that can lead to inaccuracy in the pedestal top position. Kinetic EFITs, which take experimental profiles into account, could provide an improvement but are unlikely to have a significant impact on quantities other than L_{pe}^{ped}.

While the sources of error listed here may explain some differences in fit quality between AUG and C-Mod, they do not explain why H-modes in C-Mod have a clearly different scaling with p_e^{95} than L- and I-mode, which stands as a counterexample to the AUG observation that the scaling with p_e^{95} is universal across all confinement modes [91].

While the average pressure is a better predictor of the heat flux width in the C-Mod database and the edge pressure does a better job in the AUG database, both of these scalings show some limits: the C-Mod average pressure scaling still has room for improvement when used across different devices [97], and the AUG scaling with edge pressure can be a less good predictor when there is increased filament frequency [102]. Further work is therefore needed for a robust scaling of the heat flux width across different regimes in different devices.

3.7 Extrapolation to ITER and SPARC

The scalings with edge electron pressure from the C-Mod database can be used to obtain estimates for the heat flux width in ITER and SPARC (table 3.2). The ITER scenario considered here is the ITER baseline 15 MA, $Q = 10$, inductive H-mode

Scaling law	**ITER λ_q [mm]**	**SPARC λ_q [mm]**
$\lambda_q/\mathrm{mm} = 8.2(\overline{p}/\mathrm{kPa})^{-0.48}$	0.52	0.26
$\lambda_q/\mathrm{mm} = 1.8(p_e^{95}/\mathrm{kPa})^{-0.26}$	0.59	0.44 (0.38)
$\lambda_q/\mathrm{mm} = 4.6(p_e^{95}/\mathrm{kPa})^{-0.55}$ (H-mode)	0.44	0.23 (0.17)

Table 3.2: Extrapolations of λ_q for ITER and SPARC full-power H-mode scenarios using the C-Mod scalings with average pressure, electron pressure at $\rho_{\mathrm{pol}} = 0.95$, and electron pressure at $\rho_{\mathrm{pol}} = 0.95$ fitting only the H-mode discharges. λ_q values in parentheses indicate that the scaling law was evaluated using the upper limit of the pedestal pressure in SPARC.

scenario [111] and the SPARC scenario is the 8.7 MA, $Q \approx 11$ H-mode [112]. The predicted profiles for these scenarios are evaluated for the pressure at $\rho_{\text{pol}} = 0.95$ (equivalent to $\rho_{tor} \approx 0.87$ given the profiles of the rotational transform in the C-Mod database). Using the upper limit of the pedestal pressure in SPARC [113] can provide a lower bound on λ_q (table 3.2 values in parentheses). These extrapolations highlight the importance of preparing for challenging heat flux densities in SPARC and ITER. Results from these two devices should provide crucial data on which of these scalings is most relevant.

3.8 Summary of key findings

The Alcator C-Mod tokamak heat flux width database, augmented with core and edge electron density, temperature, and pressure profile data, displays a trend of decreasing heat flux width with increasing edge electron pressure, similar to results from the AUG tokamak [91]. Compared to the scaling of λ_q with the average pressure calculated from the total stored energy, however, the absolute value of the exponent is lower and depends on the plasma confinement regime (L-, I-, or H-mode). It is therefore concluded that the edge plasma pressure is a worse fit to the heat flux width in C-Mod than the average pressure. The results from the analysis of the augmented C-Mod database are now summarized:

- The scalings with average pressure $\lambda_q/\text{mm} = 8.2(\overline{p}/\text{kPa})^{-0.48}$ (C-Mod [8]) and $\lambda_q/\text{mm} = 7.6(\overline{p}/\text{kPa})^{-0.52}$ (AUG) show good agreement across devices.
- The scalings with edge pressure ($\rho_{\text{pol}} = 0.95$) $\lambda_q/\text{mm} = 1.8(p_e^{95}/\text{kPa})^{-0.26}$ (C-Mod) and $\lambda_q/\text{mm} = 2.5(p_e^{95}/\text{kPa})^{-0.34}$ (AUG) are also quite similar, but H-modes in C-Mod have a different trend compared to L- and I-mode.
- The core pressure is the local quantity with the highest R^2 when fit to λ_q using data from all confinement regimes.
- Fits using p_e^{95} that also depend on the confinement mode approach the high R^2 of the unified fit with $\overline{p}$.

- Gradient lengths of electron pressure, density, and temperature at the separatrix have a positive correlation with λ_q, as found in the AUG database, but the Spitzer-Härm scaling of $\lambda_q = 2/7\,\lambda_{Te}$ observed in AUG is not clearly followed in C-Mod.

- There is a positive correlation between λ_q and the pedestal pressure gradient length (using values at $\rho_{\mathrm{pol}} = 0.95$ and at the separatrix), as in the AUG database.

- There is little correlation between R/L_{pe}^{ped} and R/L_{pe}^{sep} in the C-Mod database, which is different from the strong correlation found in the AUG database.

Chapter 4

Automated modeling of the C-Mod database with UEDGE

The heat flux width database augmented with midplane profiles in chapter 3 was used to verify scalings of λ_q with local quantities. Some expected scalings were found, but were less robust and unified across confinement regimes than the scaling with volume-averaged pressure. As noted in chapter 3, all discharges in the database have an attached outer target with relatively low dissipation within the divertor. The extensive data for each discharge in the database and the relatively low computational resource requirements of the UEDGE code make it possible to attempt a full-fledged UEDGE simulation of each discharge. These circumstances provide an opportunity to answer several interesting questions:

1. How well does UEDGE estimate the heat flux width in the divertor when simulation midplane profiles are well-matched with experimentally measured midplane profiles?

2. How well are local quantities such as the separatrix pressure and the separatrix temperature gradient length, free of experimental uncertainty when simulated, really correlated with λ_q?

3. Can the heat flux width be calculated more accurately by a simple exponential fit to the parallel heat flux at the divertor entrance rather than a many-

parameter fit to the heat flux profile at the target?

4. What are the estimated heat flux width and total power at the inner divertor target, which were not measured in the original C-Mod heat flux width database?

5. Which model aspects in UEDGE (e.g. single-particle drifts, flux limiters) are crucial to match the experimental measurements of λ_q?

In the past, simple onion-skin models [114] and more advanced 2D heat conduction models [115] have been used to analyze large numbers of discharges in an automated way. The full UEDGE model has been used to manually simulate a small number of discharges from a database [116] and with automatic profile fitting to simulate several time-slices during the course of an ELM [60, 117] and to investigate parameter sensitivities [118, 119]. This is the first published study to use the full UEDGE model in an automated way to simulate a large number of discharges from a database to extract further information on scalings, estimate quantities that are difficult to measure experimentally, and determine which aspects of the UEDGE model are important to accurately estimate the divertor heat flux width. This will increase confidence in UEDGE predictions of λ_q for new scenarios and devices.

4.1 UEDGE setup

Each discharge was simulated through a series of automated steps:

1. Every simulation starts from the same base case with generic profiles of density and temperature that are the average of all experimental profiles in the database at each radial coordinate.

2. The equilibrium and grid are changed to those of the discharge to be modeled.

3. The fixed boundary condition values of power, temperature, and density are changed to values determined from the experimental midplane profiles of the discharge.

4. The anomalous transport coefficients are iteratively calculated to produce a good match to the experimental midplane profiles (T_e, n_e) of the discharge.

At each of these steps, a certain number of discharges can fail to converge. When aspects of the UEDGE model are changed (e.g. flux limits are removed), they are usually changed for the base case, and each step of this process is repeated.

4.1.1 Grid generation

Grids are generated for each discharge using the INGRID code [120] from an EFIT [90] equilibrium with a grid resolution of 129×129 cells. For all grids, the core and private flux region boundaries are set at $\Psi_N = 0.96$ and the common flux region outer boundary is at $\Psi_N = 1.04$. These boundary values were chosen in order to model as much of the SOL as possible while minimizing the number of grid generation failures. All grids have a resolution of 60 cells in the poloidal direction and 18 in the radial direction. Cells are non-orthogonal and of varying width, and are set to be thinner near the separatrix and the divertor plates in order to capture more detail. Two example grids are shown in figure 4-1.

4.1.2 The UEDGE model

For all discharges, UEDGE is configured with

- Deuterium ion and neutral particle species only, no impurities.
- Inertial neutrals with the neutral temperature defined as equal to the ion temperature.
- Flux limits with $\alpha = 0.21$ in equation 2.49.
- Only anomalous diffusive transport, no convective pinch velocity.
- Radial parallel momentum diffusion coefficient of $0.5\,\mathrm{m^2\,s^{-1}}$ and radial toroidal momentum diffusion coefficient of $1\,\mathrm{m^2\,s^{-1}}$.

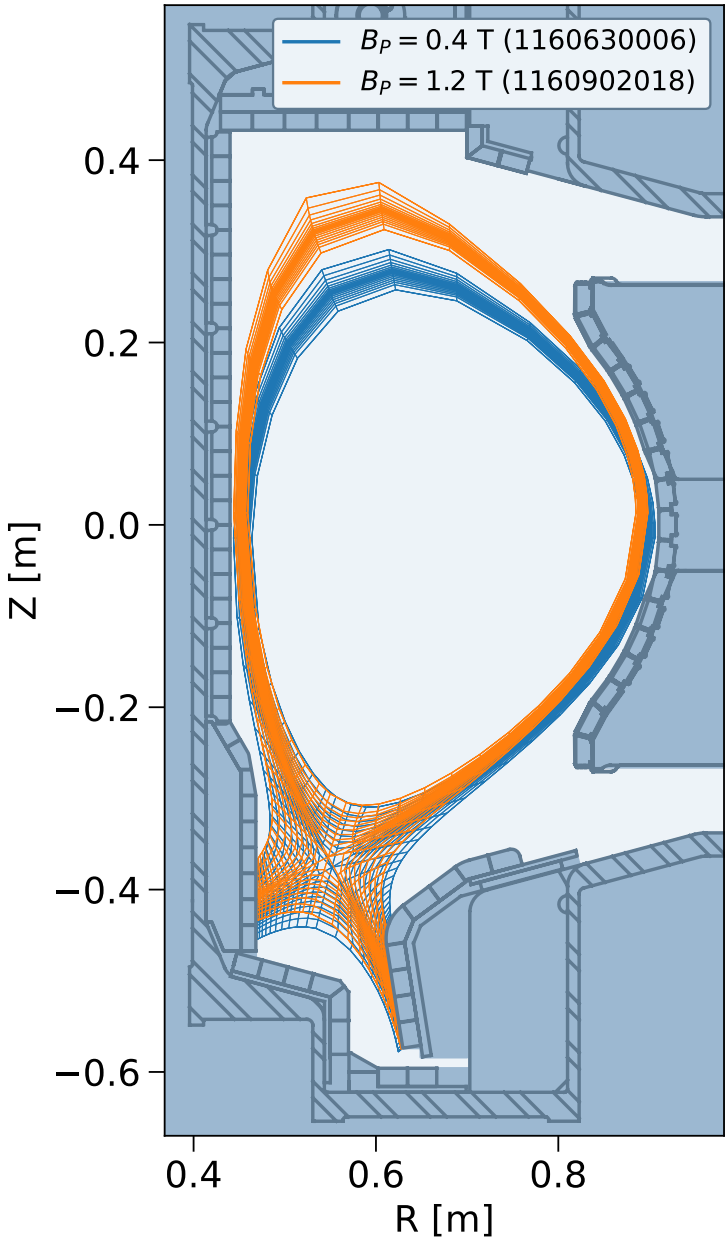

Figure 4-1: Grids of the discharges with lowest and highest poloidal field B_P among those modeled with UEDGE.

4.1.3 Boundary conditions

The boundary conditions common to all discharges are:

- Ion to neutral recycling coefficient of 0.98 at the outer boundaries and divertor targets (98% of ions flowing out the outer boundaries are reintroduced as neutrals).

- Neutral albedo of 1 (all outgoing neutral particles are reflected and there is zero neutral flux at the core and outer boundaries).

- Zero radial derivative of the parallel velocity at the core boundary, zero radial flux of the parallel momentum density at the common flux and private flux outer boundaries.

- Sheath boundary condition $v_{\|} = c_s$ at the divertor plates with an energy transmission factor of 4 for electrons and 2.5 for ions.

When the potential and current equations and single-particle drifts are enabled in UEDGE, there are new boundary conditions:

- Sheath boundary condition $v_{\|} = c_s$ at divertor plates, where the electron energy transmission factor is computed from the parallel current equation including the sheath potential contribution

- Constant potential and zero radial electric field at the core boundary; zero second derivative in the radial direction of the radial electric field at the outer midplane core boundary

- Zero radial derivative of the radial electric field at the common flux region and private flux region outer boundaries

Each discharge also has unique boundary conditions matching experimental values:

- Fixed power flowing from the core boundary into the SOL, divided equally between ions and electrons, calculated from the experimental power balance:

$$P_{\mathrm{SOL}} = P_{\mathrm{ICRF}} + P_{\mathrm{OH}} - \mathrm{d}W/\mathrm{d}t - P_{\mathrm{rad\,core}} \tag{4.1}$$

- Fixed ion density at the core boundary determined from the experimental n_e profile assuming $n_e = n_i$, and with ion flux into/out of the core boundary allowed

- Fixed ion density and equal ion and electron temperature at the outer common flux region boundary, determined from experimental profiles

- Fixed ion density and ion/electron temperature at the outer private flux region boundary, arbitrarily set to one tenth of the corresponding values at the outer common flux region boundary

4.1.4 Midplane profile fitting

The midplane profiles of density and temperature are matched in UEDGE assuming $T_e = T_i$. T_i is usually higher than T_e in the SOL, but their ratio can vary with factors such as density [83, 121]. The formula used to adjust the anomalous transport coefficients D and $\chi_{\mathrm{e,i}}$ so that the simulation profiles are a good match to the GPR-fit experimental profiles is

$$\begin{aligned} D^{\mathrm{new}} &= -\Gamma^{\mathrm{UEDGE}}/\nabla n^{\mathrm{expt}} \\ \chi_{\mathrm{e,i}}^{\mathrm{new}} &= -\left(q_{\mathrm{e,i}} - \frac{5}{2}\Gamma T_{\mathrm{e,i}}\right)^{\mathrm{UEDGE}} \Big/ n^{\mathrm{expt}} \nabla T_{\mathrm{e,i}}^{\mathrm{expt}} \end{aligned} \tag{4.2}$$

[122]. The coefficients are recalculated and the case is re-converged 10 times when adapting the base case to a specific discharge. The transport coefficients can be defined to vary poloidally, but in this method they are kept poloidally uniform. The transport coefficients in the private flux region are completely uniform and have the same value as just outside the separatrix. This fitting procedure can yield very good

matches to midplane profiles, especially when density gradients are not very steep, as in the L-mode example discharge shown in figure 4-2.

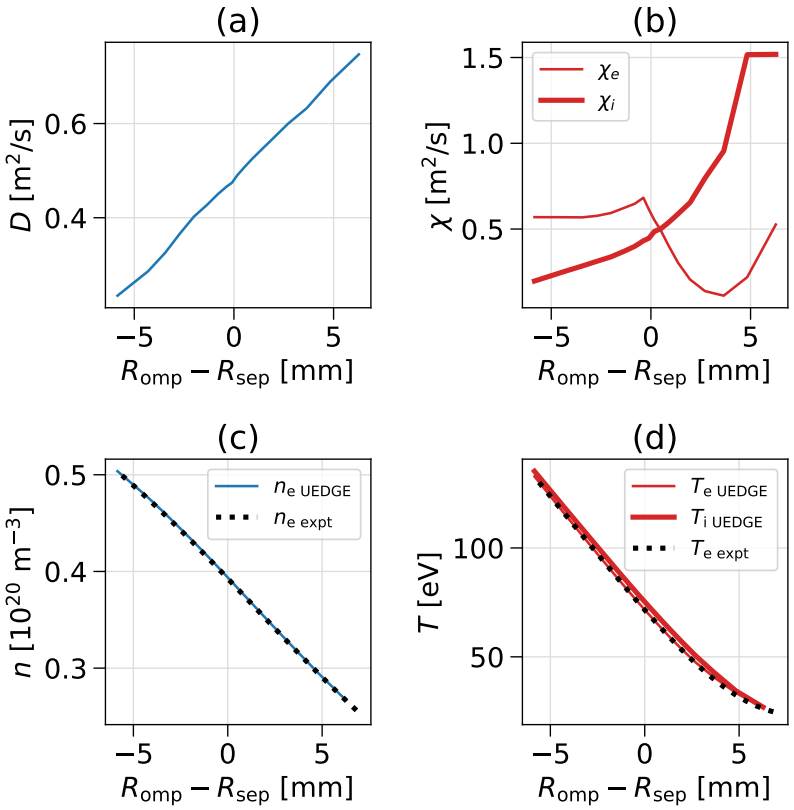

Figure 4-2: Outer midplane radial profiles of (a) the anomalous particle transport coefficient D, (b) the anomalous heat conduction coefficients $\chi_{e,i}$ and the resulting profiles of (c) density and (d) temperature (discharge 1160818008).

The quality of the midplane fits can be evaluated for all discharges by comparing the separatrix values in UEDGE and experiment (figure 4-3). The separatrix density is matched very well in all cases, while there are more significant discrepancies in the separatrix temperature. One possible explanation is that when density gradients are steep, the ion and electron temperatures inside the separatrix can be lower than the experimental values, as the fitting formula 4.2 reduces χ to decrease the conducted heat flux and create a steeper temperature gradient but can do nothing against the large convective heat flux due to the density gradient. This could explain why in figure 4-3(b), some H-modes have a poor match to the separatrix electron temperature, while I-modes do not: H-modes have a steeper density gradient than I-modes, which have

high energy confinement and low particle confinement.

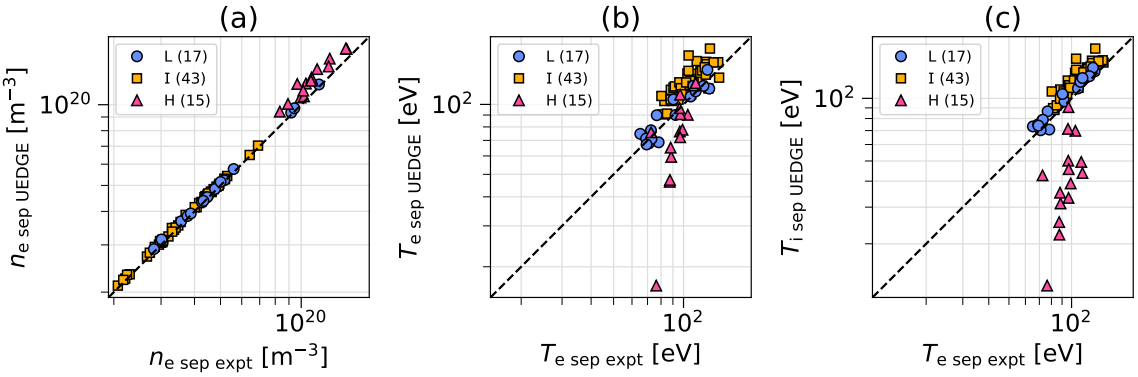

Figure 4-3: Comparison of UEDGE and experimental values of outer midplane separatrix (a) density and (b,c) temperature.

4.1.5 Subset of modeled discharges

Not all discharges with midplane profile data were successfully simulated. Some had grid generation problems, some failed to converge after the density and temperature boundary conditions were changed, and some failed to converge after the transport coefficients were changed. Overall, 75 of the 121 database discharges were modeled with UEDGE. Some key characteristics of the UEDGE-modeled subset are compared to the larger database in figure 4-4, showing that there is good UEDGE coverage of the original range of toroidal field B_T, poloidal field B_P, and separatrix density and temperature. The small number of L-mode and H-mode discharges relative to the I-mode discharges could be a focus for future work. This brief comparison of the simulated and experimental database parameters indicates that differences in parameter ranges are likely *not* responsible for differing trends in the simulated and experimental data.

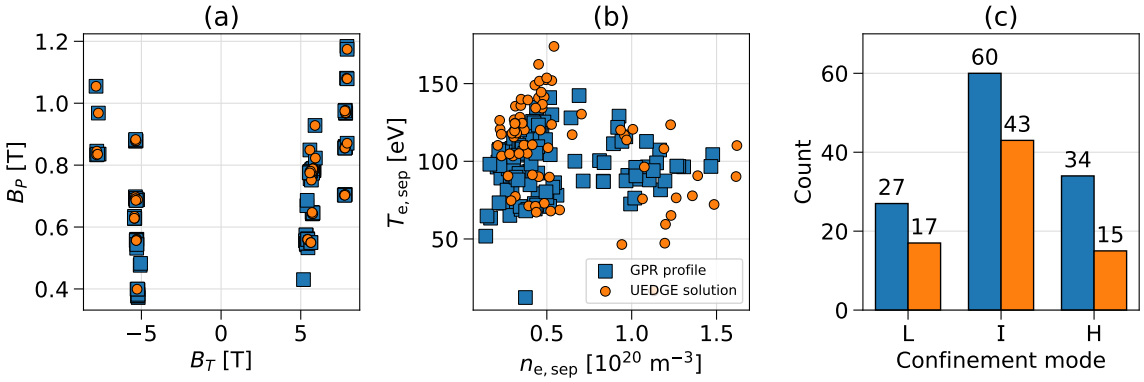

Figure 4-4: Comparison of database parameters between those discharges used in the heat flux width study that have GPR profile fits (blue squares) and the subset of discharges for which a UEDGE solution was obtained (orange circles). The parameters compared are (a) the poloidal and toroidal magnetic field, (b) the separatrix temperature and density, and (c) the confinement mode.

4.2 Comparison to experimental results

4.2.1 Heat flux width comparison to experiment

In order to verify the utility of the UEDGE configuration in this study to model modified scenarios such as detachment and future devices such as SPARC, we can test whether UEDGE accurately estimates the heat flux width for most discharges in the C-Mod database. In order to compare "apples to apples" as much as possible, the procedure to fit the heat flux profile in UEDGE was kept very similar to that used in the experimental database [8], with some improvements that resulted in better fits to the UEDGE data. The multi-λ function (section 2.2.4) was used with 3 decay length parameters ($\lambda_{q\,\mathrm{cn}}$ to fit the near common flux region, $\lambda_{q\,\mathrm{cf}}$ for the far common flux region, and $\lambda_{q\,\mathrm{pn}}$ for the near private flux region) and a Gaussian spreading parameter S. As in the original study, the logarithm of the heat flux data was fit using the Python library lmfit [123] with the same constraints on fit parameter values and ratios as were used to fit the experimental heat flux profiles. Changes that resulted in vastly improved fits to the UEDGE heat flux profiles included

- Ignoring data outside the region where the heat flux is monotonically decreasing in the radial directions compared to the peak heat flux.

- Linearly interpolating between UEDGE target heat flux data points, because fitting 7 parameters to a small number of data points (∼18) can result in bad fits.

- Weighting heat flux data by value, ensuring a good match to the data near the peak of the profile.

Figure 4-5 compares $\lambda_{q\,\mathrm{cn}}$ from fits to the heat flux profile at the outer divertor target in UEDGE to $\lambda_{q\,\mathrm{cn}}$ from experimental data, which are both referred to as λ_q going forward. A small number of discharges were removed due to having poor overall fits to the heat flux profile. The UEDGE heat flux widths are larger than the experimental values by an average factor of 1.8, with 95% of the UEDGE values being less than 3.1 times larger than the experimental values. This systematic overestimation appears to be uniform across confinement modes and over the full range of λ_q and is further investigated in this study.

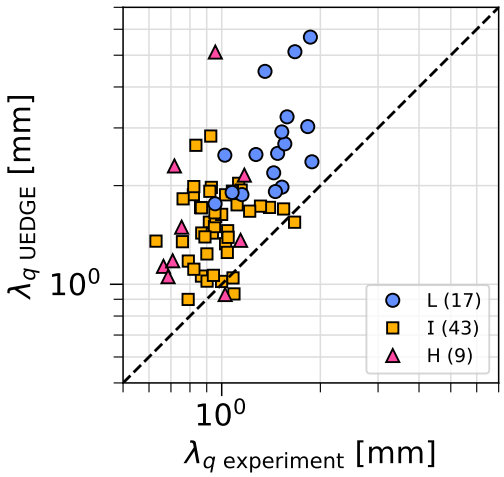

Figure 4-5: Heat flux width values from fits to the outer divertor target heat flux profile in UEDGE compared to those from experiment.

4.2.2 Heat flux width scalings

As in chapter 3, scalings of λ_q with local quantities and gradients can be examined. Figure 4-6 shows scalings with the local pressure and collisionality for identical sets

of discharges with experimental and UEDGE data. Figure 4-6(a) shows λ_q and the electron pressure at $\Psi_N = 0.96$, which is as close as possible to the chapter 3 scaling of λ_q with pressure at $\rho_{\rm pol} = 0.95$, i.e. $\Psi_N = 0.90$. The UEDGE points show λ_q decreasing more strongly with $p_{\rm e\,\Psi_N=0.96}$ in simulation compared to experiment, but this is mostly due to the overestimation of λ_q in the UEDGE cases. Figure 4-6(b) shows that the correlation between λ_q and the separatrix pressure $p_{\rm e\,sep}$ is less strong than that with $p_{\rm e\,\Psi_N=0.96}$ in both simulation and experiment. The fact that the simulation points do not have a strong correlation is in line with the finding in chapter 3 that the separatrix pressure is not well correlated with λ_q, and reduces the likelihood that the lack of correlation was entirely due to experimental measurement error.

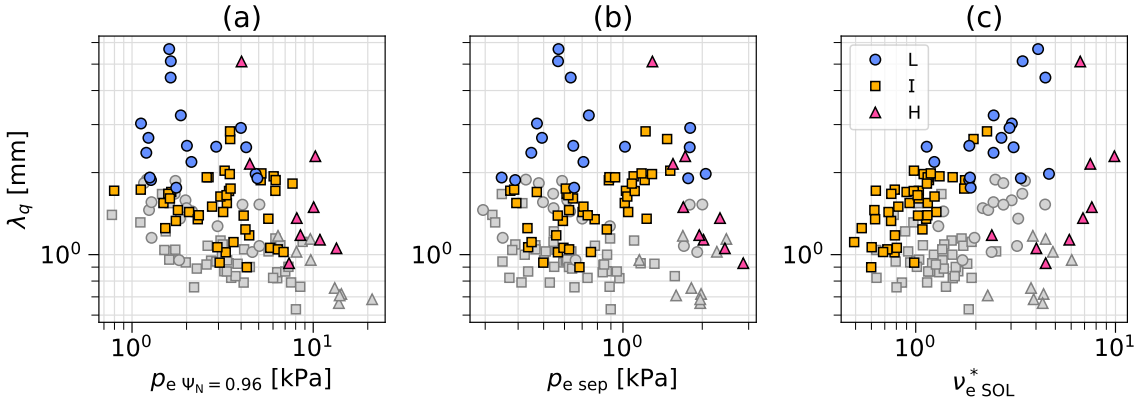

Figure 4-6: Relationship between the heat flux width and local plasma parameters. The colored points are UEDGE data and the gray points are experimental data. Scalings of λ_q are shown with (a) the electron pressure at the core boundary of the UEDGE simulation domain ($\Psi_N = 0.96$), (b) the electron pressure at the outer midplane separatrix, and (c) the dimensionless collisionality at the outer midplane separatrix.

The scaling of λ_q with plasma collisionality is shown in figure 4-6(c). The collisionality is defined as

$$\nu^*_{\rm eSOL} = \frac{L}{\lambda_{ee}} \approx 10^{-16}\frac{n_u L}{T_{eu}^2} \tag{4.3}$$

[9], where n_u is the upstream density at the outer midplane separatrix, T_{eu} is the upstream electron temperature at the outer midplane separatrix, and L is the parallel connection length between the outer midplane separatrix and the outer divertor target

(L from the UEDGE simulations was also used to calculate ν^*_{eSOL} for the experimental data points). A trend of increasing λ_q with increasing collisionality is only roughly evident in the experimental data (possibly due to random error in the measurements becoming significant in the n_u/T_{eu}^2 term), while it appears very clearly in the UEDGE data, except for the H-modes with high collisionality and low λ_q. This trend matches the predictions of the generalized heuristic drift model and experimental and simulation results [101, 124]. There are also significant differences in ν^*_{eSOL} between the simulation and experimental data, so this might be a case in which UEDGE reveals a trend that was not evident in the experimental data due to diagnostic measurement and EFIT mapping limitations.

The relationships between λ_q and edge gradient lengths in the UEDGE data are shown in figure 4-7. Trends of increasing λ_q with increasing gradient length are evident for the electron pressure, density, and temperature gradient lengths. In the case of the temperature gradient length (figure 4-7(c)), the data appears to follow the Spitzer-Härm scaling of $\lambda_q = 2/7\,\lambda_{Te}$, indicating that local transport is likely the dominant paradigm in these cases despite UEDGE being configured to include flux limits. Correlations between λ_q and gradient lengths are not as apparent in the experimental data (gray data points in figure 4-7), possibly due to the large uncertainty in the location of the separatrix and the calculated gradient length. Other studies investigating the relationships between the heat flux width and edge gradients might therefore benefit from UEDGE modeling to overcome some of the uncertainty in the experimental data.

4.2.3 Heat flux width overestimation in UEDGE

The systematic overestimation of λ_q in the UEDGE solutions compared to experiment (figure 4-5) is an unexpected result that merits further investigation. Figure 4-8 shows the ratio of the heat flux widths in simulation and experiment as a function of several variables for the subset of discharges with verified good fits to the outer target heat flux profile in UEDGE. The strongest correlation appears to be with the separatrix density (figure 4-8(a)), with high densities leading to high values of λ_q in UEDGE L-

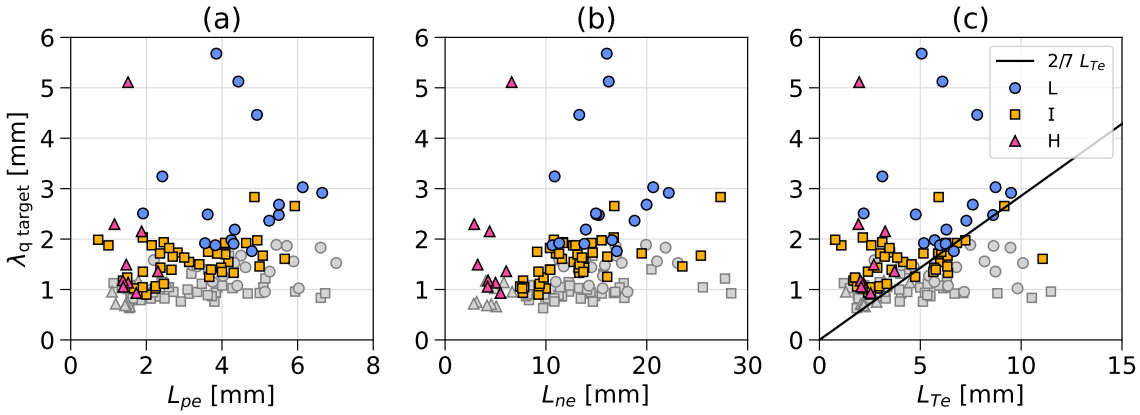

Figure 4-7: Relationship between the heat flux width and separatrix gradient lengths: (a) the electron pressure gradient length, (b) the electron density gradient length, (c) the electron temperature gradient length. The black line indicates the Spitzer-Härm scaling. The colored points are UEDGE data, and the gray points are experimental data.

and I-mode modeled discharges. This correlation could be due to the anomalous radial conducted heat flux $-\chi_{e,i} n \nabla T_{e,i}$ in equation 2.46 being proportional to the density, leading to greater heat flux broadening and therefore higher λ_q at high density. H-modes do not appear to follow this trend, possibly due to the steeper density gradient at the separatrix implying a large anomalous radial particle flux (Γ_n in equation 2.45) which would cause the convected heat flux term $5/2\,\Gamma_n T_{e,i}$ to dominate the total anomalous heat flux in equation 2.46. In such cases, the automated midplane profile fitting code often reduces the value of the anomalous heat conduction coefficient χ to very low values, leading to reduced heat flux broadening in proportion to temperature gradients and therefore lower λ_q for H-modes.

The next variable most strongly correlated with $\lambda_{q\,\mathrm{UEDGE}}/\lambda_{q\,\mathrm{expt}}$ is the ratio of the total power to the outer divertor target in UEDGE and experiment (figure 4-8(f)). The power to the outer target in experiment is estimated using the fit to the experimental heat flux profile, which is shifted in the radial direction such that its peak is at the same location as the peak heat flux in UEDGE; the experimental heat flux is then multiplied by the UEDGE outer target surface area along the profile and summed to give the total power. The positive correlation of the λ_q ratio with the modeled target power fraction is surprising because the UEDGE λ_q values appear to

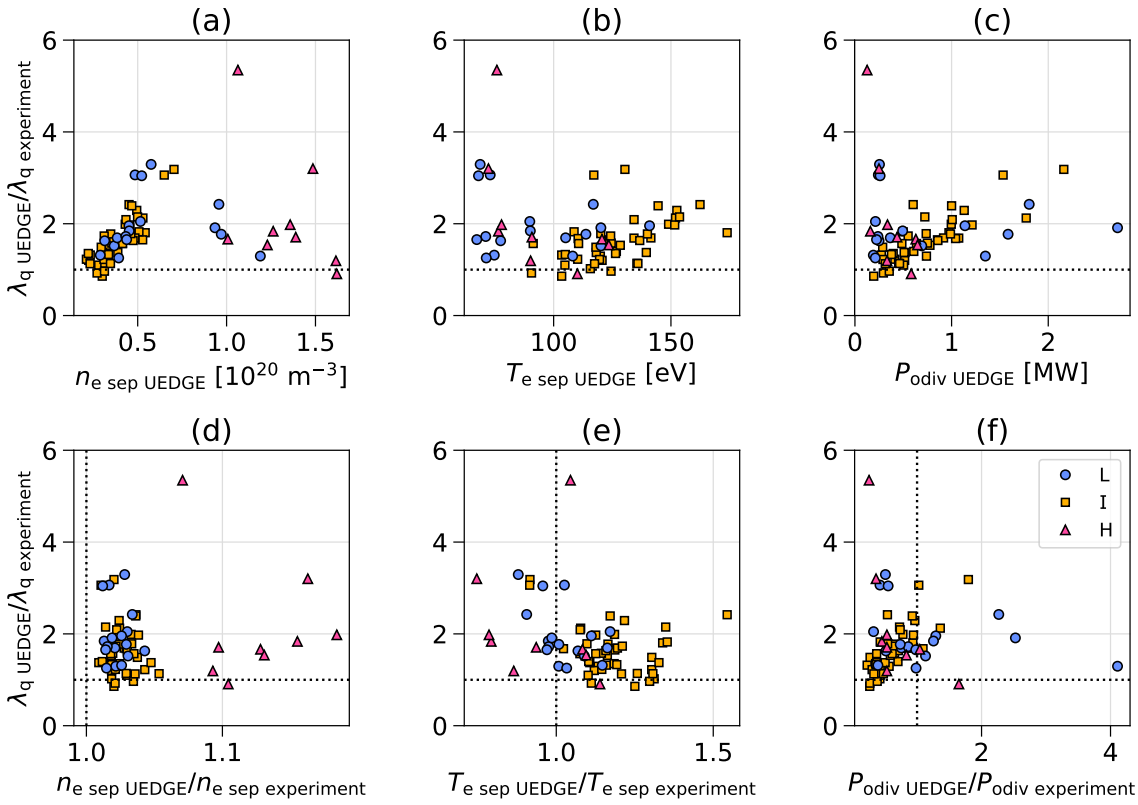

Figure 4-8: The ratio of the heat flux widths fit at the outer divertor target in UEDGE and experiment compared to (a) the separatrix density in UEDGE, (b) the separatrix temperature in UEDGE, (c) the total power to the outer divertor target in UEDGE, (d) the ratio of UEDGE to experimental separatrix density, (e) the ratio of UEDGE to experimental separatrix temperature, and (f) the ratio of UEDGE to experimental power to the outer divertor target. The horizontal dotted black lines mark values of 1, i.e. λ_q agreement. The vertical dotted black lines mark agreement between UEDGE and experiment for other parameters.

be closer to experiment when the power fraction is less than 1 and are a factor of ∼2 too high when the power fraction is near 1—when one quantity is closer to the experimental value, the other is not. It may be relevant that UEDGE systematically underestimates the power to the outer target in most cases (figure 4-22) and equation 4.1 may overestimate P_{SOL}.

Other variables correlated with $\lambda_{q\,\mathrm{UEDGE}}/\lambda_{q\,\mathrm{expt}}$ are the total power to the outer target and the separatrix temperature at values greater than 100 eV. In the experimental database, λ_q decreases with P_{SOL} and with separatrix temperature, so the positive correlations with these variables in UEDGE are unexpected.

Some UEDGE variables of interest do not appear to be strongly correlated with $\lambda_{q\,\mathrm{UEDGE}}/\lambda_{q\,\mathrm{expt}}$: the ratio of the UEDGE to experimental separatrix density and the ratio of the UEDGE to experimental separatrix temperature. These indicate that a mismatch in midplane profiles between UEDGE and experiment is likely not the source of the λ_q overestimation.

The heat flux width value can be tracked at several steps during the setup of the UEDGE solutions. Figure 4-9(a) shows that when cases have only the equilibrium corresponding to the discharge being modeled, and the boundary conditions and profiles have not yet been adjusted, $\lambda_q \approx 1.5$ mm for all cases. After the correct boundary conditions are set (figure 4-9(b)), a large number of discharges are close to the identity line in λ_q, while some discharges have $\lambda_{q\,\mathrm{UEDGE}} \approx 3\lambda_{q\,\mathrm{expt}}$. After the UEDGE midplane density and temperature profiles are adjusted to match experiment, however, the systematic overestimation of λ_q appears (figure 4-9(c)). This indicates that the midplane profile fitting procedure is responsible for the overestimation of λ_q.

The heat flux width is examined as a function of the anomalous transport coefficients D and $\chi_{\mathrm{e,i}}$ at the separatrix in figure 4-10. H-modes have distinctly lower D and χ than L- and I-mode. L- and I-mode have similar transport coefficients even though L-modes have higher λ_q than I-modes; this is likely due to different values of the P_{SOL} boundary condition, as the separation between L- and I-mode in λ_q is already evident in figure 4-9(b). Related to the anomalous transport coefficients are the anomalous radial fluxes of particles and energy (figure 4-11). Once again, H-modes appear dis-

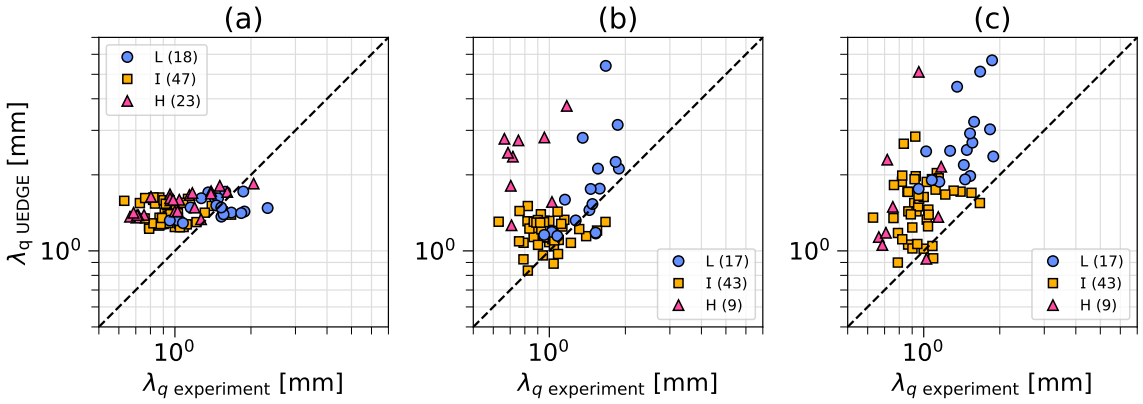

Figure 4-9: The heat flux width fit at the outer target in UEDGE compared to the experimental heat flux width for (a) UEDGE cases with equilibrium matching experiment but generic boundary conditions and profiles, (b) UEDGE cases with boundary conditions matching experiment, and (c) UEDGE cases with boundary conditions and profiles matching experiment.

tinct from L- and I-modes. H-modes have higher radial ion flux and therefore higher convected heat flux and lower conducted heat flux than L- and I-mode. For most discharges, the conducted power is greater than the convected power. The opposite is true for around half of the H-modes. These data support the hypothesis that the heat flux width is overestimated for the L- and I-mode cases simulated in UEDGE due to the fact that the midplane profile fitting method results in unrealistically high values of χ near the separatrix, increasing the conducted heat flux broadening and therefore increasing λ_q. Some potential solutions to this problem are (i.) to limit the maximum value of χ produced by the fitting formula, and (ii.) since the separatrix location in the profiles is still uncertain, to iteratively shift the profiles radially until a suitable value of n_{sep} and therefore a suitable λ_q at the outer target are obtained.

In conclusion, it appears that the heat flux width is on average overestimated in the UEDGE simulations because of the particular midplane profile fitting method used, and not because there is a poor match to the midplane profiles. Nevertheless, some discharges have λ_q quite close to the experimental value, so the fitting method can produce good outcomes in certain cases. The profiles of the transport coefficients that make UEDGE match the midplane profiles in experiment are not unique, so new methods to match the midplane profiles and heat flux width simultaneously should

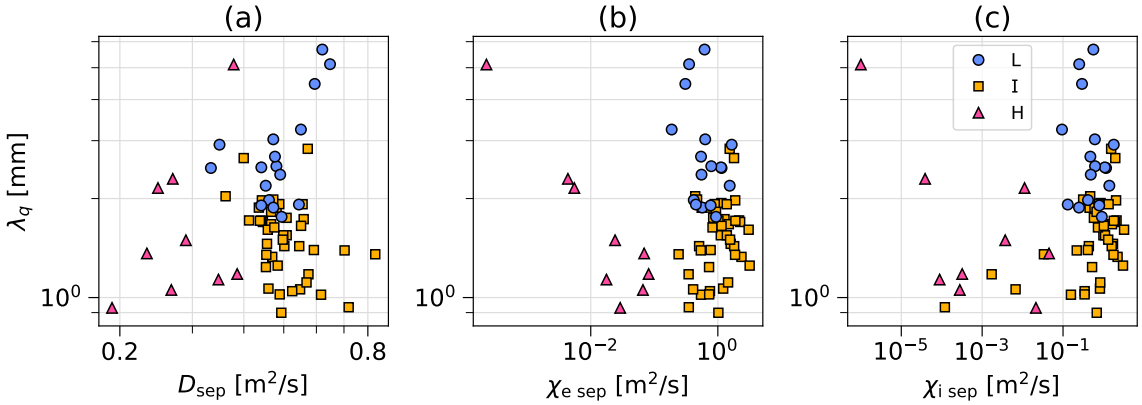

Figure 4-10: The heat flux width fit at the outer target in UEDGE as a function of the separatrix values of (a) the anomalous diffusive transport coefficient, (b) the anomalous electron conducted heat flux coefficient, and (c) the anomalous ion conducted heat flux coefficient.

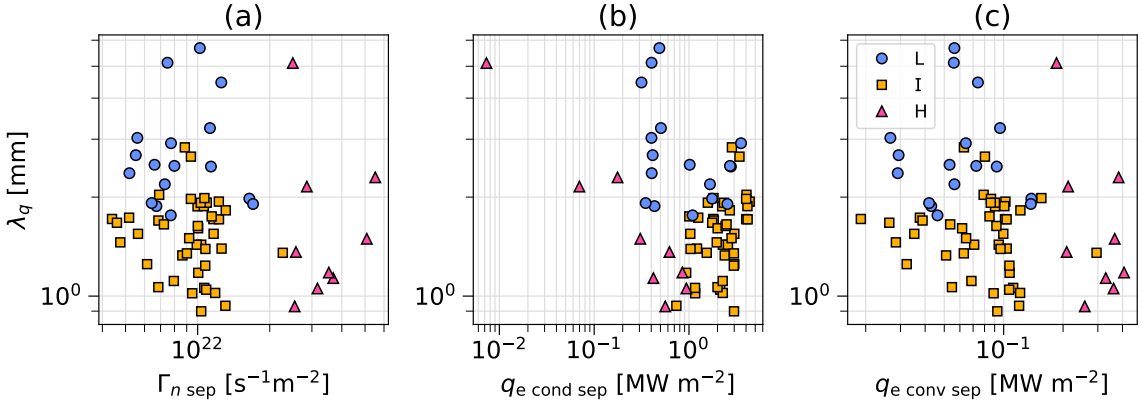

Figure 4-11: The heat flux width fit at the outer target in UEDGE as a function of the outer midplane separatrix values of (a) the radial ion flux, (b) the electron conducted heat flux, and (c) the electron convected heat flux.

be explored.

4.3 Beyond experimental measurements

The self-consistent solutions provided by UEDGE can be investigated in ways that experiments cannot. Some interesting aspects investigated here are the heat flux profiles at the divertor entrance and the inner divertor.

4.3.1 Heat flux width at the divertor entrance

In order to determine the impact of heat flux spreading along the outer divertor leg, the heat flux width at the outer divertor entrance (near the height of the X-point) can be obtained from UEDGE and compared to the heat flux at the target. Because the parallel heat flux at the X-point mapped to the outer midplane has a much simpler profile than the heat flux at the target, it can be fit with an exponential function with only two fit parameters, q_0 and λ_q:

$$q_{\parallel}(\rho) = q_0 e^{-\rho/\lambda_q}, \tag{4.4}$$

where ρ is the radial coordinate at the outer midplane. Figure 4-12(a) shows the heat flux width from fits at the X-point in UEDGE compared to the outer target λ_q in experiment. The X-point λ_q appears to exhibit the same overestimation of the experimental λ_q, being on average a factor of 1.8 times higher than experiment and with 95% of cases being less than 2.8 times higher than experiment. This indicates that the overestimation of λ_q in the UEDGE cases is not due to significant heat flux broadening along the divertor leg, and that changing the transport coefficients below the X-point would not yield better agreement with experiment. If better simultaneous matching of midplane and target profiles is desired for all cases, the midplane profile fitting method needs to be improved.

Figure 4-12(b) compares the heat flux width from fits at the X-point with λ_q fit at the target in UEDGE. This figure includes good and bad fits to the X-point and target heat flux profiles in order to show that the X-point fitting procedure is more robust due to the simpler shape and smaller number of fit parameters. It can be seen

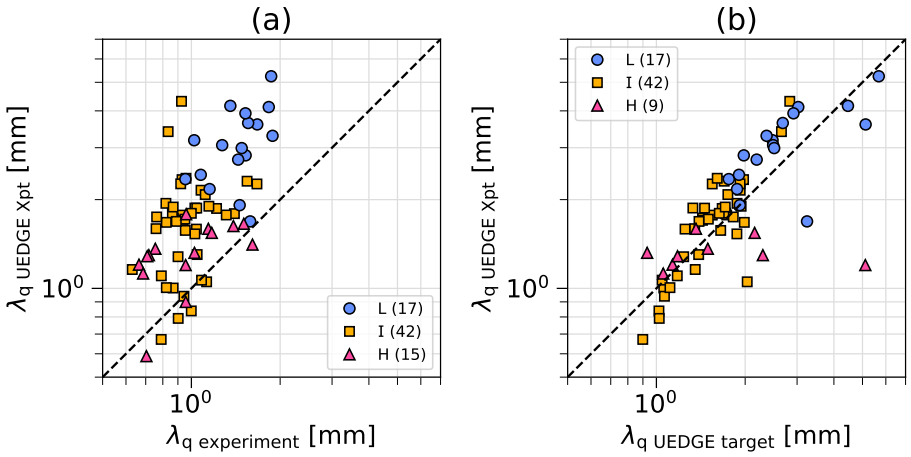

Figure 4-12: The heat flux width from fits at the outer X-point (divertor entrance) in UEDGE compared to (a) the heat flux width from fits at the outer target in experiment, and (b) the heat flux width from fits at the outer target in UEDGE.

that the variance of λ_q fit at the target is much greater than that of λ_q fit at the X-point, and the outliers are due to poor overall fits to the heat flux profile at the outer target. This is especially true for the H-mode discharges, which are much more tightly grouped when λ_q at the X-point is used. The heat flux width at the X-point can therefore be used to obtain more robust scalings of λ_q with parameters of interest as long as heat flux broadening below the X-point is not significant.

In figure 4-13, the heat flux width at the X-point is compared to the local values of electron pressure at $\Psi_N = 0.96$, electron pressure at the outer midplane separatrix, and dimensionless collisionality at the outer midplane separatrix. Compared to figure 4-6, which shows λ_q at the outer target as a function of the same local variables, only the scaling with pressure at $\Psi_N = 0.96$ is slightly improved by using λ_q at the X-point, and in fact the L- and I-mode points appear to have a better scaling with collisionality in 4-6(c) than in figure 4-13(c). While λ_q at the X-point may be a more robust parameter to fit than the outer target λ_q, it does not reveal a heightened dependence on local plasma quantities.

The scalings of λ_q with separatrix gradient lengths, however, are more clear when λ_q at the X-point is used (figure 4-14) rather than λ_q at the outer target (figure 4-7). Notably, with the X-point λ_q, the L-, I-, and H-mode discharges appear to follow

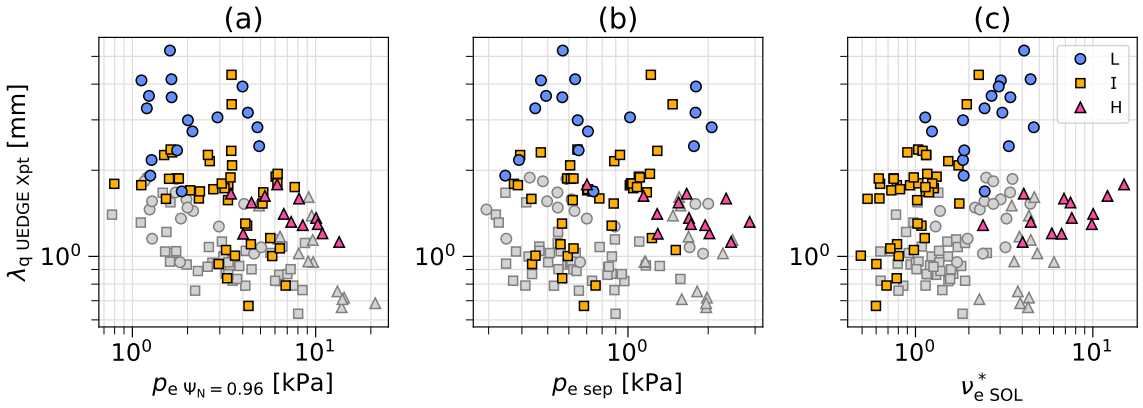

Figure 4-13: The heat flux width from fits at the outer X-point in UEDGE compared to (a) the electron pressure at $\Psi_N = 0.96$, (b) the electron pressure at the outer midplane separatrix, and (c) the dimensionless collisionality at the outer midplane separatrix. The colored points are UEDGE data and the gray points are experimental data, with the experimental λ_q obtained from fits at the outer target.

a unified scaling of increasing λ_q with increasing gradient length. Adherence to the Spitzer-Härm scaling is also more clear in figure 4-14(c) than when the outer target λ_q is used. The scaling of λ_q with the density gradient length (figure 4-14(b)), while still apparent, appears to be the least unified across confinement modes due to the H-mode cases having the lowest density gradient length but λ_q similar to that of many I-modes. Nevertheless, it appears that in these UEDGE cases, the heat flux width depends more clearly on local gradient lengths than on local plasma parameters. These results make sense considering that the dependence of λ_q on local gradients has some theoretical basis (e.g. the Spitzer-Härm scaling), while there is less theoretical basis for a relationship between λ_q and local quantities.

Some studies estimate that $\nu^*_{\mathrm{SOL}} \geq 100$ is required for the Spitzer-Härm scaling to be applicable, and the C-Mod heat flux width database has ν^*_{SOL} in the range of 0.5–20 (figure 4-13(c)). In order to identify which regime is more relevant in simulation and experiment, the UEDGE values of λ_q at the X-point can be compared to those estimated from the Spitzer-Härm scaling and those estimated in the flux-limited regime. In the Spitzer-Härm regime, $\lambda_{q\,\mathrm{SH}} = 2/7\,\lambda_{Te}$, while in the flux-limited regime,

$$\lambda_{q\,\mathrm{FL}} = \left(\frac{3/2}{\lambda_{Te}} + \frac{1}{\lambda_{ne}}\right)^{-1} \tag{4.5}$$

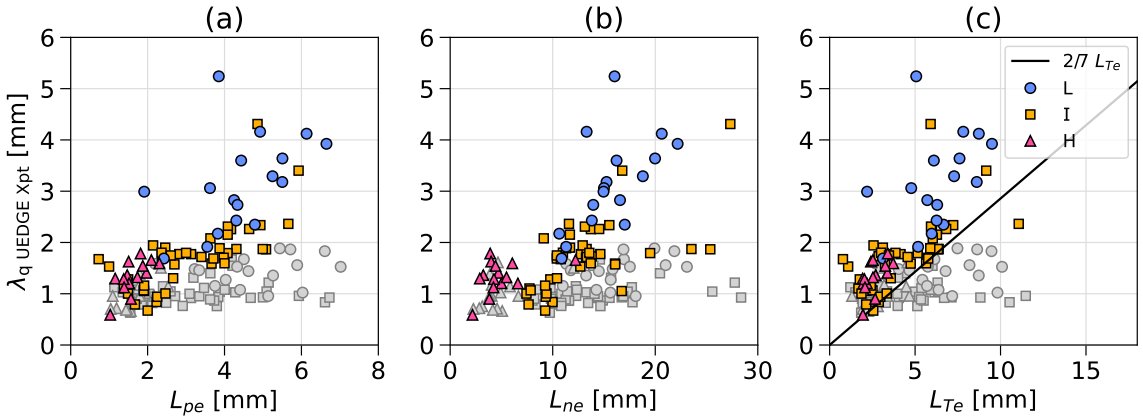

Figure 4-14: The heat flux width from fits at the outer X-point in UEDGE compared to (a) the electron pressure gradient length, (b) the electron density gradient length, (c) the electron temperature gradient length. The black line indicates the Spitzer-Härm scaling. The colored points are UEDGE data and the gray points are experimental data, with the experimental λ_q obtained from fits at the outer target.

[125]. A comparison of the Spitzer-Härm and flux-limited estimates of λ_q is shown for simulation and experimental data in figure 4-15. The Spitzer-Härm scaling tends to underestimate the UEDGE λ_q and only roughly matches the experimental λ_q, while the flux-limited regime scaling tends to overestimate the UEDGE λ_q as well as the experimental λ_q. It is not clear from this analysis which scaling is more applicable—it may be that the C-Mod heat flux width database discharges are in a somewhat intermediate regime.

The greater accuracy of the heat flux width fit at the X-point can also be used to repeat the analysis of the λ_q overestimation problem (figure 4-16). The results are mostly the same, except that a scaling with the separatrix temperature ratio between UEDGE and experiment is now evident (figure 4-16(e)). As with the ratio of UEDGE to experimental power to the outer target, the result is unusual in that λ_q in UEDGE is closer to experiment when the separatrix temperature in UEDGE is ∼25% higher than that in experiment; when the temperature in UEDGE best matches the experimental temperature, λ_q is overestimated by a factor of ∼2. For the L- and I-mode cases, there is a roughly negative correlation between separatrix χ_e and $T_{e\,\mathrm{UEDGE}}/T_{e\,\mathrm{expt}}$, so the cases that most overestimate λ_q have the highest χ_e. The H-mode cases, which have generally low χ_e, do a good job of matching the

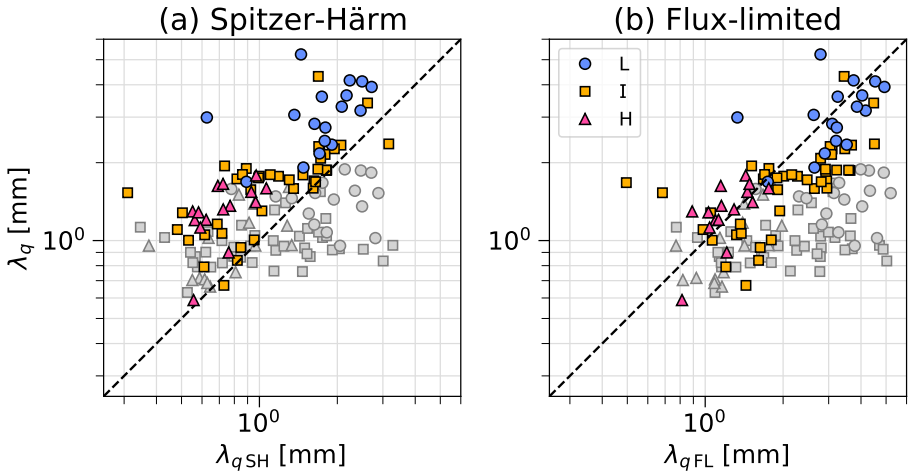

Figure 4-15: (a) Comparison of the UEDGE heat flux width at the X-point with the heat flux width estimated from the Spitzer-Härm scaling from midplane UEDGE gradient lengths (colored points) and comparison of the experimental heat flux width at the outer target with the Spitzer-Härm estimate from midplane experimental gradient lengths (gray points). (b) Same but using the flux-limited regime estimate of $\lambda_{q\,\mathrm{FL}}$.

experimental λ_q. These findings appear to confirm that large values of χ_e near the separatrix cause UEDGE to overestimate the heat flux width.

4.3.2 Inner divertor heat flux

UEDGE can also be used to examine the inner divertor heat flux profile. The inner divertor does have diagnostic capabilities in Alcator C-Mod but was not the focus of investigations during the creation of the heat flux width database. Figure 4-17 shows that the in:out total power ratio is close to 1:1.8 for all cases. Experiments on C-Mod found that I-modes have an in:out power sharing ratio of approximately 2:1 while H-modes instead have a ratio of 1:2 [126], so H-modes appear to be well-described but I-modes are not. This is likely due to the fact that single-particle drift effects are not included, as the I-mode discharges and H-mode discharges have oppositely directed toroidal field B_T. Half of the L-mode discharges also have the same toroidal field direction as the I-mode discharges.

The inner target heat flux width in UEDGE, like the outer target, matches λ_q at the inner X-point/divertor entrance (figure 4-18(a)). Compared to the outer target

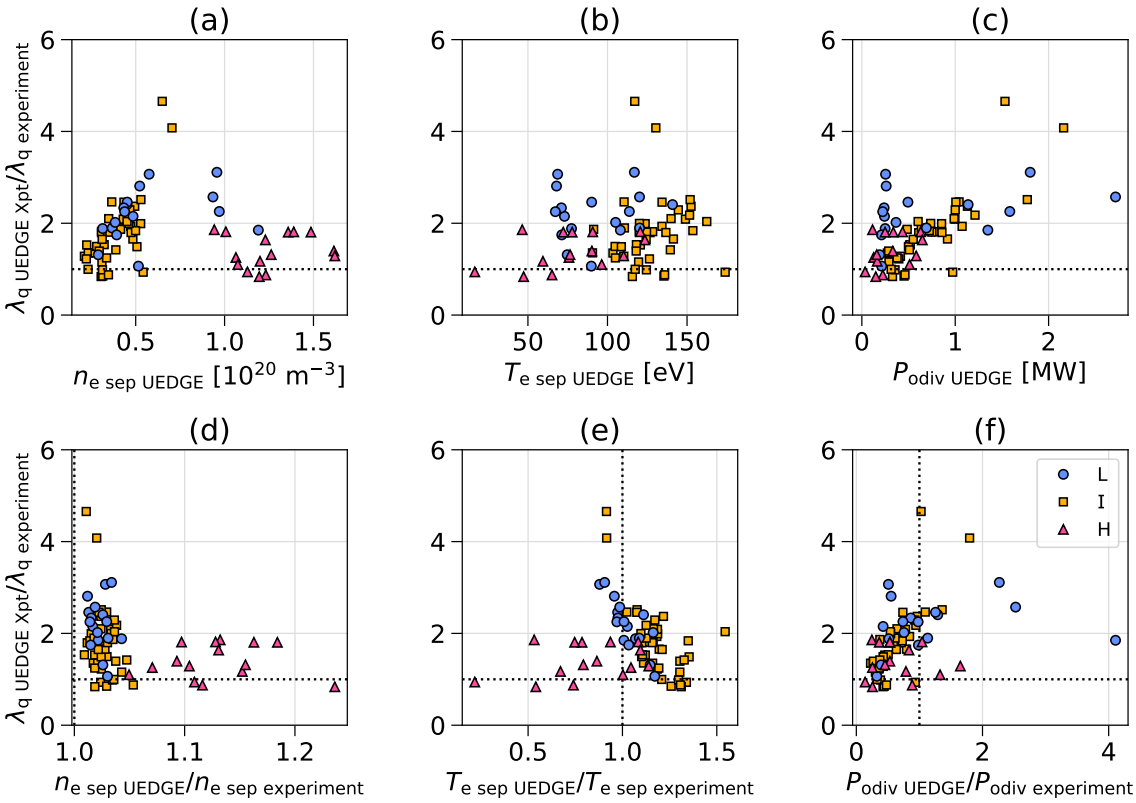

Figure 4-16: The ratio of the heat flux widths fit at the outer X-point in UEDGE and the outer target in experiment compared to (a) the separatrix density in UEDGE, (b) the separatrix temperature in UEDGE, (c) the total power to the outer divertor target in UEDGE, (d) the ratio of UEDGE to experimental separatrix density, (e) the ratio of UEDGE to experimental separatrix temperature, and (f) the ratio of UEDGE to experimental power to the outer divertor target. The dotted black horizontal and vertical lines mark values of 1.

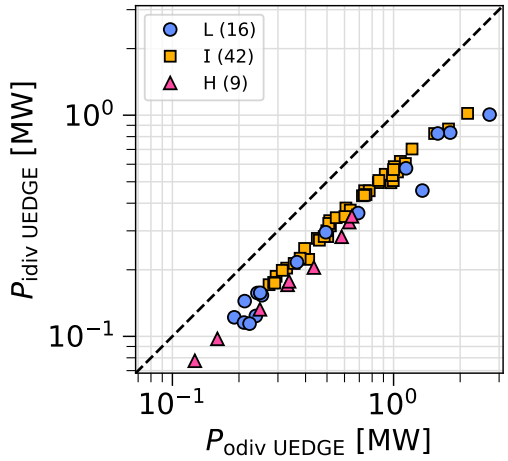

Figure 4-17: Comparison of the total power to the inner and outer divertor targets in UEDGE.

heat flux width, the inner target λ_q is usually equal or smaller (figure 4-18(b)). This is somewhat in line with experimental results on AUG which found a ratio $\lambda_q^{\text{in}}/\lambda_q^{\text{out}}$ of around 0.44 when the $\mathbf{B} \times \nabla \mathbf{B}$ drift is toward the primary X-point and around 0.85 in the opposite case [127].

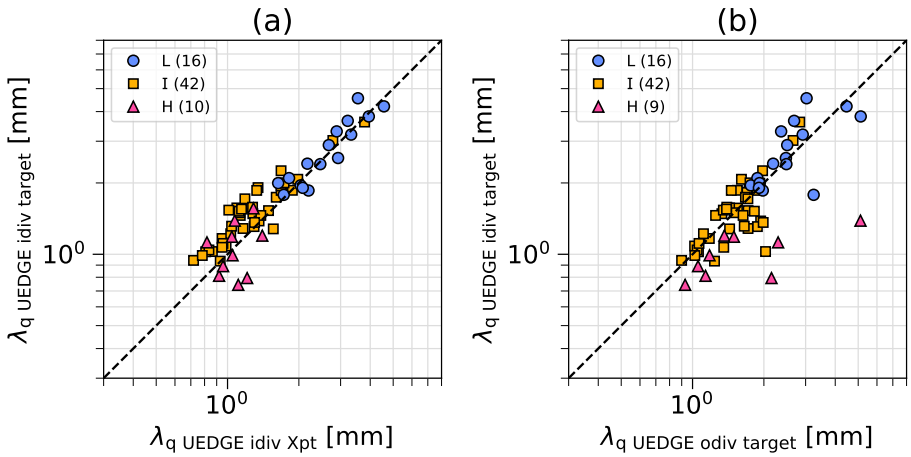

Figure 4-18: Comparison of the heat flux width fit at the inner target in UEDGE with (a) the heat flux width fit at the inner X-point (inner divertor entrance) in UEDGE, and (b) the heat flux width fit at the outer target in UEDGE.

4.4 Impact of changing model settings

The database of UEDGE solutions can be used to assess which components of the UEDGE model are important to reproduce scalings of the heat flux width. It has been established in this study that the midplane profile fitting method leads to overestimation of the experimental heat flux width. In a similar vein, the impact on λ_q of certain UEDGE model features can be investigated. In this study, the impact of enabling single-particle drifts and disabling flux limits are investigated separately. This exercise is meant as another step in moving toward more robust UEDGE modeling, where matching several midplane and target parameters simultaneously is less a matter of chance and more of a science.

4.4.1 Including single-particle drifts

Single-particle drifts ($\mathbf{B} \times \nabla \mathbf{B}$ and $\mathbf{E} \times \mathbf{B}$) were enabled using a procedure that has proved reliable to ensure convergence (described in section B.2.3), starting from the full solutions with drifts off (figure 4-19(a)). Around 55% of cases reached the final step of enabling full drift effects, of which 70% had good fits to the heat flux profile at the outer target, shown in figure 4-19(b).

The direction of the $\mathbf{B} \times \nabla \mathbf{B}$ drift is down (toward the active X-point) for negative ("normal") B_T and up (away from the X-point) for positive ("reversed") B_T. In the negative B_T cases, the $\mathbf{E}_r \times \mathbf{B}$ drift in the poloidal direction is directed away from the inner target and toward the outer target in the common flux region, and from the outer target toward the inner target in the private flux region. With negative B_T, the $\mathbf{E}_\theta \times \mathbf{B}$ drift is directed radially from the common flux region to the private flux region at the outer target, and from the private flux region to the common flux region at the inner target. When drifts are enabled, the negative B_T cases have a peak in ion density and a low temperature near the inner target; the positive B_T cases have high density and low temperature at the outer target.

Figure 4-19(b) shows that the manner in which drifts were enabled in this study caused λ_q to be a much worse match to experiment. The positive B_T cases in figure 4-19(b) are all I-modes, and of the negative B_T cases, two are L-modes and two are H-modes. To understand why this happens, it is instructive to look at the power to the divertor targets.

It can be seen that many of the positive B_T drifts-on cases in figure 4-20(a) have a total power to the outer target much lower than in experiment, as more power is directed by the $\mathbf{E} \times \mathbf{B}$ drift to the inner target. The power flows due to drifts are indeed significant: the parallel heat flux mapped to the poloidal direction near the X-point in UEDGE is often exceeded by the $\mathbf{E} \times \mathbf{B}$ heat flux in the poloidal direction at all but one or two cells with the highest parallel heat flux. These strong drift effects, almost causing detachment of the inner/outer target depending on the direction of B_T, help explain why there is such a large range of λ_q in figure 4-19(b).

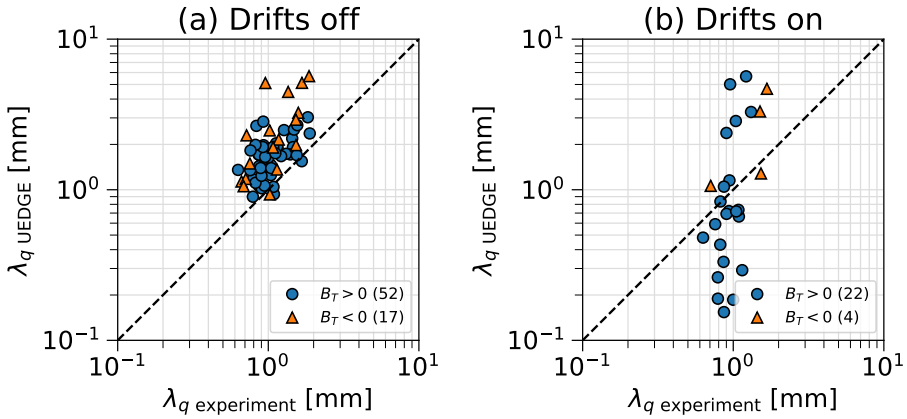

Figure 4-19: Heat flux width fit at the outer target in UEDGE compared to that from experiment for (a) UEDGE cases with single-particle drifts disabled, and (b) UEDGE cases with single-particle drifts enabled. The marker shape and color indicate the sign of the toroidal magnetic field.

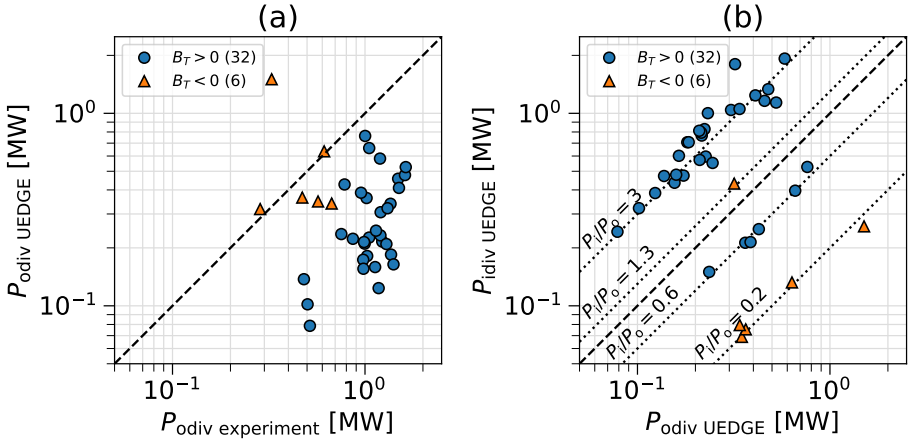

Figure 4-20: (a) Comparison of the total power to the outer target in (drifts-on) UEDGE to the same quantity in experiment. (b) Comparison of the total power to the inner and outer targets in UEDGE. The marker shape and color indicate the sign of the toroidal magnetic field. The dotted lines indicate inner to outer target power sharing ratios. There are more discharges displayed in this figure than in figure 4-19(b) because discharges with bad fits to the UEDGE target heat flux profile are included.

Figure 4-20(b) shows that several power sharing scenarios were obtained when drifts were enabled in UEDGE. It appears that for each toroidal field direction, there are at least two stable power sharing arrangements: for positive B_T, $P_\mathrm{i}/P_\mathrm{o} \approx \{0.6, 3\}$, and for negative B_T, $P_\mathrm{i}/P_\mathrm{o} \approx \{0.2, 1.3\}$. $P_\mathrm{i}/P_\mathrm{o} = 3$ in UEDGE is similar to $P_\mathrm{i}/P_\mathrm{o} = 2$ for I-modes in C-Mod (although figure 4-20(a) shows that the total power to the outer target is still too low in UEDGE) and $P_\mathrm{i}/P_\mathrm{o} = 0.2$ for the negative B_T cases in UEDGE is a little more extreme than $P_\mathrm{i}/P_\mathrm{o} = 0.5$ observed in experiments with the same B_T on C-Mod [126]. It appears that while not all UEDGE cases with drifts match experimental power sharing trends on C-Mod, they are much more realistic when B_T is positive than the cases with drifts disabled.

In this study, drifts in UEDGE appear to be a double-edged sword: they are essential to match the experimental power asymmetry in cases with positive B_T, but they can have such a strong effect that they completely change target conditions, making it challenging to match experiment. Drifts in UEDGE also clearly do not remedy whatever leads to the overestimation of λ_q. One solution that is often employed in modeling is to enable drifts at a reduced level: indeed, enabling drifts at 50% strength for the database cases results in more discharges having λ_q closer to experiment than with full-strength drifts, but with similar average overestimation of λ_q as in the cases with drifts off. Further work is needed to determine UEDGE procedures that make it possible to enable drifts and match midplane and target parameters simultaneously in all cases, but the impact of drifts should always be studied if possible.

4.4.2 Flux limits

The next aspect of the UEDGE model that was investigated is flux limiting. Figure 4-21(a) shows the base case with flux limiting of $\alpha = 0.21$ in equation 2.49 informed by kinetic modeling, and figure 4-21(b) shows the effect of removing the flux limits entirely. The overestimation of λ_q is somewhat reduced, with a mean ratio $\lambda_{q\,\mathrm{UEDGE}}/\lambda_{q\,\mathrm{expt}}$ of 1.5 and with 95% of cases having a ratio of less than 2.8 (compared to a mean of 1.8 and a 95% bound of 3.1 with flux limits enabled). This difference is fairly minor and not a strong motivator to disable flux limits.

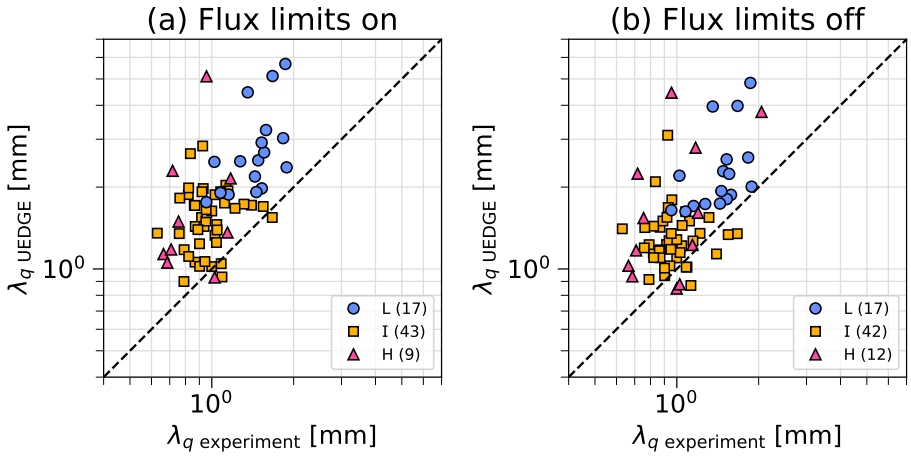

Figure 4-21: Heat flux width fit at the outer target in UEDGE compared to that from experiment for (a) UEDGE cases with flux limits on, and (b) UEDGE cases with flux limits off.

The most significant effect of disabling flux limits is the change in total power to the outer divertor. Figure 4-22 shows that when flux limits are off, the fraction of the UEDGE total power to the outer target compared to the experimental power is 20% higher than with flux limits off. This increase is fairly uniform, and the majority of discharges still have too little power to the outer target compared to experiment. In addition, figure 4-16 shows that the λ_q overestimation in UEDGE increases with $P_{\mathrm{odiv\,UEDGE}}$ and $P_{\mathrm{odiv\,UEDGE}}/P_{\mathrm{odiv\,expt}}$, so the fact that the λ_q in UEDGE is reduced when flux limits are disabled is surprising.

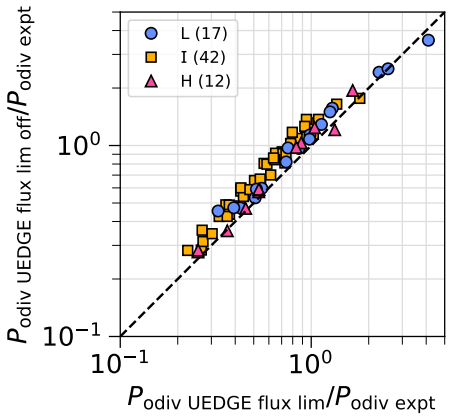

Figure 4-22: Comparison of the ratio of the power to the outer target in UEDGE and experiment with flux limits on and off.

Like drifts, flux limits are another important approximation of real physics in tokamaks. This study shows that in the edge plasma regimes of the C-Mod heat flux width database, flux limits can be disabled without causing the solution to change greatly. But including flux limits is not computationally burdensome and increases confidence when simulating plasma conditions beyond those included in the database.

4.4.3 Other attempts to understand overestimation of the heat flux width

Several modifications to the baseline UEDGE simulation were made in the hopes of resolving the λ_q overestimation issue in the C-Mod database (table 4.1). The fact that none of these changes has a huge impact on the model could mean that something more fundamental is responsible; two big unknowns are the ion temperature (which is usually larger than the electron temperature [83]) and the divertor neutral pressure. Going forward, simplifying the model may provide greater insights than modifying it or adding complexity; one way to do this would be to disable all equation terms other than 2D heat conduction.

The experimental heat flux profiles were also re-fit with the same code used to fit the UEDGE profiles, and it was thereby verified that the overestimation of λ_q is not due to the experimental profiles being fit with a very different method.

Change	**Impact on λ_q overestimation**
Use fixed core temperature boundary condition rather than fixed power, in case P_{SOL} underestimation was responsible for low separatrix temperatures in UEDGE.	Slightly lower overestimation. Fewer discharges converge.
Double the radial grid resolution to reduce the impact of numerical diffusion.	Similar overestimation.
Lower the maximum allowed value of χ, as large values produced by the fitting formula in the far SOL could be causing unrealistically large heat flux spreading in the divertor.	Similar overestimation.
Change the ion and electron convective heat flux coefficients from 5/2 to 3/2.	Similar overestimation.
Set $D = 0.5\,\mathrm{m}^2/\mathrm{s}$ over the entire domain and iteratively set the anomalous convective velocity to match the density profile.	Similar overestimation.
Set neutral temperature $T_n = 0.5T_i$.	Similar overestimation.
Set $\chi_i = \chi_e$, as χ_e can be calculated to match the T_e profile, but assuming $T_i = T_e$ is contrary to experimental findings.	Similar overestimation.
Set zero perpendicular convected heat flux for ions and electrons (neutral convected heat flux remains).	Similar overestimation.
Set zero parallel convected heat flux for ions, electrons and neutrals.	Similar overestimation.
Set $P_{i\,\mathrm{SOL}} = 2P_{e\,\mathrm{SOL}}$ and fit profiles aiming for $T_i = 2T_e$.	Slightly greater overestimation.
Use gradient-length boundary conditions at outer boundaries rather than fixed values.	Similar overestimation. H-mode cases don't converge.
Set constant $D = \chi_{e,i} = 0.02\,\mathrm{m}^2/\mathrm{s}$ in the divertor volume only.	Much reduced correlation between UEDGE and experimental λ_q, but a significant number of UEDGE cases have lower λ_q than experiment.

Table 4.1: Changes to the UEDGE baseline model made separately in hopes of resolving the λ_q overestimation issue in the C-Mod database. In each discharge, these changes can have a significant impact on the overall solution, the λ_q value, and the match to the midplane profiles; "similar overestimation" refers only to the average result across all discharges.

4.5 Conclusions

The simulation of 75 discharges with attached divertor conditions in the C-Mod heat flux width database with UEDGE is a first-of-its-kind achievement. This study has

- Evaluated the physical accuracy of a UEDGE configuration with a large number of discharges: UEDGE as configured underestimates the total power to the outer target and overestimates the experimental heat flux width by an average factor of 1.8.

- Demonstrated the potential of using UEDGE with midplane profiles matched to experiment in order to estimate the heat flux widths at divertor targets.

- Characterized issues with the midplane profile fitting procedure and simultaneous matching of the target heat flux width: the separatrix density and its gradient are found to have a significant impact on the convected and conducted heat flux and therefore the heat flux width.

- Examined scalings of the heat flux width with parameters that have significant measurement error in experiment, such as density and temperature gradient lengths at the separatrix: a stronger correlation is found between λ_q and edge gradients than between λ_q and edge absolute quantities, excepting an interesting new scaling with the dimensionless collisionality for L- and I-modes.

- Investigated parameters that cannot be easily measured in experiment, such as the heat flux width at the X-point, which can be determined more accurately than the heat flux width at the target and can also be used when targets are detached; and the inner target heat flux width, which was not the focus of the experimental database.

- Studied the impact of changes to the model such as adding drifts or removing flux limits and determined how they affect the match to experiment: drifts can result in more realistic inner/outer target power sharing but can completely

change conditions at the targets beyond what is observed in experiment, making heat flux width studies challenging; flux limits do not change solutions significantly but add some realism and increase confidence outside the database conditions at very little computational cost.

Chapter 5

Modeling detachment in C-Mod and extension to advanced divertor

The automated modeling of a large number of C-Mod discharges with UEDGE in chapter 4 showed the capability of the chosen UEDGE settings to adequately model the wide range of conditions covered in the C-Mod heat flux width database. By modeling an individual C-Mod EDA H-mode discharge with an attached outer divertor and modifying it to include an advanced divertor, further insights can be gained. The principal objectives of this study are to

- Simultaneously match several experimental measurements, which was not always possible in the automated modeling effort. This includes midplane profiles, target profiles, and both divertor and main-chamber neutral pressures.

- Examine the impact of single-particle drifts and anomalous transport in the simulation, and whether drifts can be used while matching midplane and target experimental data.

- Model the transition from a fully attached plasma to a fully detached plasma both with and without single-particle drifts turned on in the simulation by stepwise increasing the nitrogen fraction using the fixed-fraction nitrogen impurity model.

- Characterize the impact of a longer divertor leg on the ease of detachment in C-Mod, a high-field tokamak, starting from a robust match to an actual experimental scenario. This will make it possible to speculate on the ease of detachment in similar high-field, advanced-divertor tokamak concepts such as SPARC and ADX, which have little experimental basis for modeling.

5.1 Experimental basis for modeling

Data from C-Mod discharge 1160718025 between 0.95 and 1.36 seconds form the experimental basis of the UEDGE modeling in this study. This time period, shown by the blue highlighted area in figure 5-1, is an EDA H-mode with stationary, attached plasma conditions, a lower single null geometry, a toroidal field of $-5.23\,\mathrm{T}$, a plasma current of $1\,\mathrm{MA}$, and a total power to the scrape-off layer of

$$P_{\mathrm{SOL}} = P_{\mathrm{ICRF}} + P_{\mathrm{OH}} - \mathrm{d}W/\mathrm{d}t - P_{\mathrm{rad\,core}} = 2.9\,\mathrm{MW} \tag{5.1}$$

where $P_{\mathrm{ICRF}} = 3.7\,\mathrm{MW}$ is the power injected by ion-cyclotron resonance heating, $P_{\mathrm{OH}} = 0.65\,\mathrm{MW}$ is the power due to ohmic heating, $\mathrm{d}W/\mathrm{d}t = 0.16\,\mathrm{MW}$ is the rate of change of the plasma stored energy, and $P_{\mathrm{rad}} = 1.5\,\mathrm{MW}$ is the plasma radiated power measured by a bolometer, which is assumed here to be radiated in the core.

Experimental data available for this discharge includes:

- Midplane profiles of electron density and temperature from Thomson scattering (figure 3-1).
- Inner and outer target profiles of density, temperature, and ion saturation current from Langmuir probes.
- Outer target heat flux data from surface thermocouples. The discharge is part of the C-Mod heat flux width database described in Chapter 3 and has $\lambda_q = 0.91\,\mathrm{mm}$ at the outer target.
- Divertor neutral pressure of $4.36\,\mathrm{Pa}$ measured at a distance of around 1.5 meters

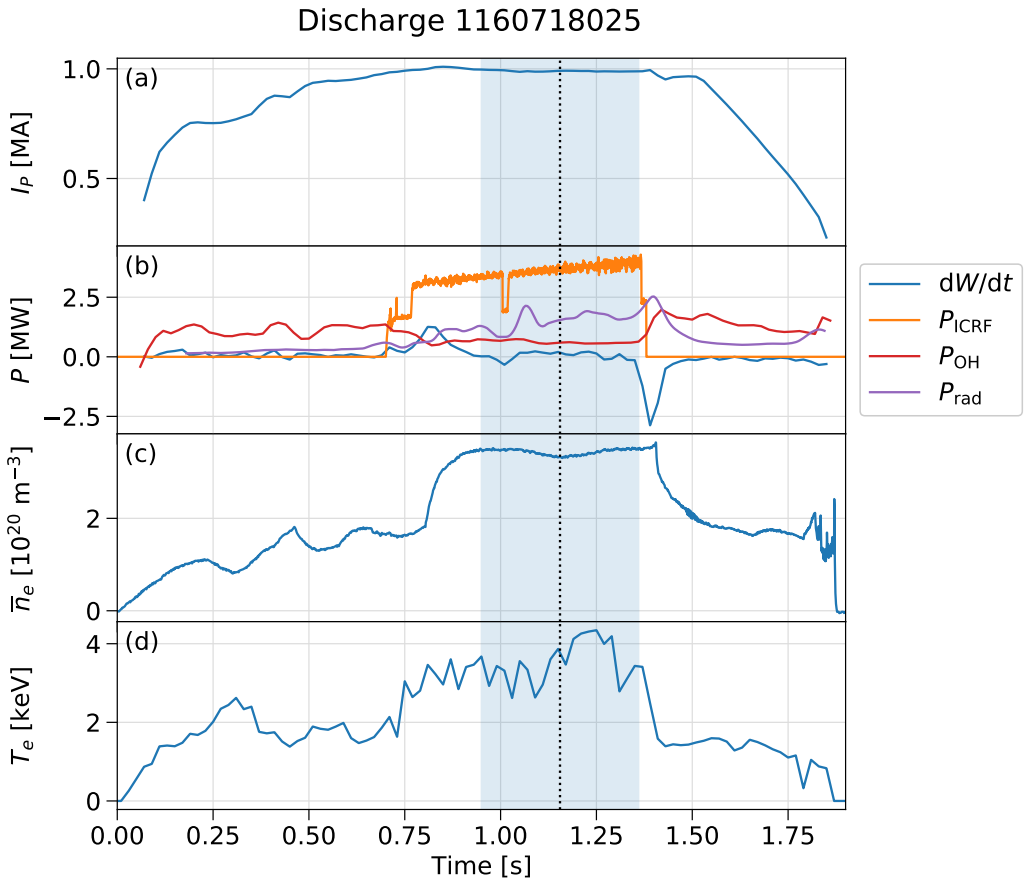

Figure 5-1: Time traces of discharge 1160718025, showing (a) the plasma current; (b) the power due to the change in plasma stored energy ($\mathrm{d}W/\mathrm{d}t$), the power injected by ion-cyclotron resonance heating (P_{ICRF}) and ohmic heating (P_{OH}), and the plasma power lost through radiation (P_{rad}); (c) the line-averaged electron density; and (d) the electron temperature near the core. The blue shaded region indicates the time period over which the experimental data used in UEDGE was averaged. The dotted black line indicates the time of the magnetic equilibrium used for modeling.

below the outer strike-point in a volume sampling the private flux region. The neutral pressure measured in the volume sampling the outer midplane region was 0.0467 Pa.

5.2 Equilibrium and grid geometry

The EFIT [90] magnetic equilibrium of C-Mod discharge 1160718025 at 1.2 seconds (indicated by the dotted black line in figure 5-1) was used to create a grid for UEDGE (figure 5-2) with the INGRID [120] grid generator. The radial extent of the grid corresponds to the normalized poloidal flux values of $\Psi_N = 0.9475$ at the core and PF region boundaries and $\Psi_N = 1.0525$ at the CF region outer boundary. The grid has increased concentrations of cells in the poloidal direction near the targets and X-points and in the radial direction near the separatrix in order to capture greater detail in these regions where steep gradients are expected.

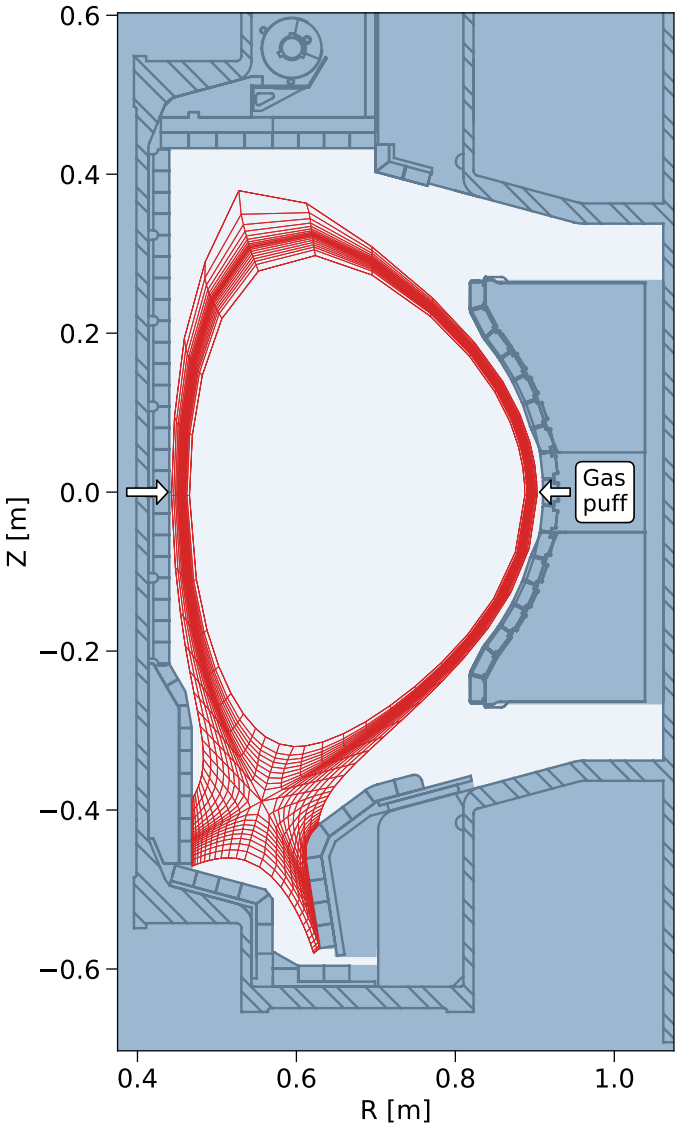

Figure 5-2: UEDGE grid (red) for C-Mod discharge 1160718025. The gas puff locations included in the UEDGE simulation are shown by white arrows. The surrounding machine geometry is not included in the simulation.

5.3 Setup

The UEDGE settings in this simulation are the same as those described in section 4.1.2 with the addition of gas puffs of 5.3 Torr L/s at the inner midplane and 7.1 Torr L/s at the outer midplane (as shown in figure 5-2), matching those in experiment. The gas puffs are modeled in UEDGE by specifying neutral fluxes at the outer radial boundary.

The boundary conditions of the UEDGE simulation are the same as those described in section 4.1.3, except that the fixed values of the density and temperature at the PF region boundary were set arbitrarily to values of $T_e = T_i = 1\,\mathrm{eV}$ and $n_i = 5 \times 10^{18}\,\mathrm{m}^{-3}$ based on early modeling results. With the 98% recycling condition and the gas puffs at the midplane, the ion flux out of the core is close to zero, as should be the case in steady state.

5.4 Base case

Because single-particle drifts can cause significant convergence difficulties, a "base case" was first obtained with drifts disabled using the grid shown in figure 5-2.

5.4.1 Match to midplane profiles

The anomalous transport coefficients were calculated iteratively using formula 4.2. A very good match to the experimental profiles was obtained (figure 5-3). The coefficients D and $\chi_{e,i}$ all have the same approximate shape, with reduced transport near the separatrix and high transport near the outer boundary, as is expected for C-Mod H-modes.

The different components of the radial transport that result from the chosen transport coefficients can be examined (figure 5-4). Particle and power fluxes are summed at each flux surface over the area of the flux surface above the X-point, so as to ignore divertor transport. Positive values indicate fluxes radially outward. The particle flux in this case is purely diffusive because the anomalous convective velocity was set to

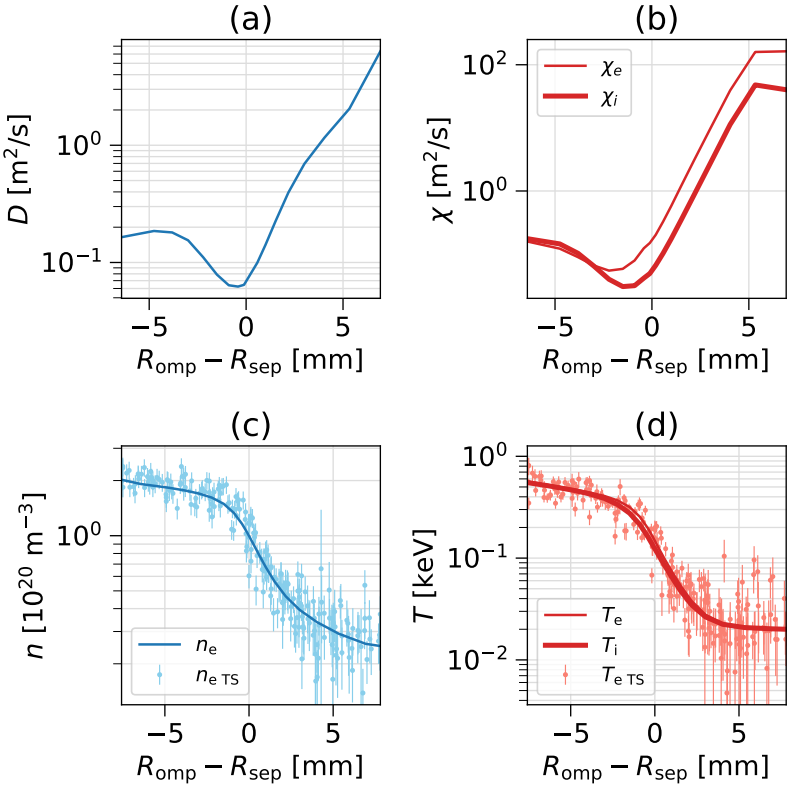

Figure 5-3: Anomalous transport coefficients and midplane profiles in UEDGE without single-particle drifts compared to experiment: (a) UEDGE anomalous radial particle diffusivity, (b) UEDGE anomalous electron and ion radial conductivity, (c) UEDGE density (line) and experimental density (points) at the outer midplane, and (d) UEDGE electron and ion temperatures (lines) and experimental temperature (points) at the outer midplane.

zero. There is a small net particle flux into the simulation domain from the core, which is required to maintain particle balance, as the simulation boundaries recycle only 98% of ions into neutrals and the midplane gas puffs are not sufficient to offset the losses fully. There is also a flux of neutrals toward the core that is approximately opposite to the flux of ions away from the core. The neutral flux through the core boundary is zero due to the boundary condition.

Figure 5-4 also shows the various radial power flux channels. While the total electron and ion power fluxes are approximately equal close to the core boundary, most of the radial power flux in the SOL is carried by electrons. Electron and ion convection of power is most significant in the core and diminished in the SOL. Ion conduction is greater in the core than in the SOL. Electron conduction is greater in the SOL than in the core, and dominates over other power flux channels. The power flux due to neutrals is small compared to the other power fluxes, but is opposite in sign, as neutrals carry some energy radially inward.

5.4.2 Match to target profiles

After obtaining a good match to the experimental midplane profiles in UEDGE, divertor target conditions were compared (figure 5-5). At the outer target, UEDGE has a good match to the experimental electron density and temperature, with peaks within an order of magnitude of the experimental values. The UEDGE outer target density has a higher peak and steeper radial gradient in the CF region than in experiment. The UEDGE outer target electron temperature is within a factor of 2 of experiment in the CF region. At the inner target, near the separatrix, the electron temperature and density in UEDGE have a slightly worse match to the experimental values.

In this analysis, the ion saturation current in UEDGE is calculated as

$$j_{\mathrm{sat}} = I_x/A \tag{5.2}$$

where I_x is the ion poloidal current and A is the surface area of each UEDGE cell at the

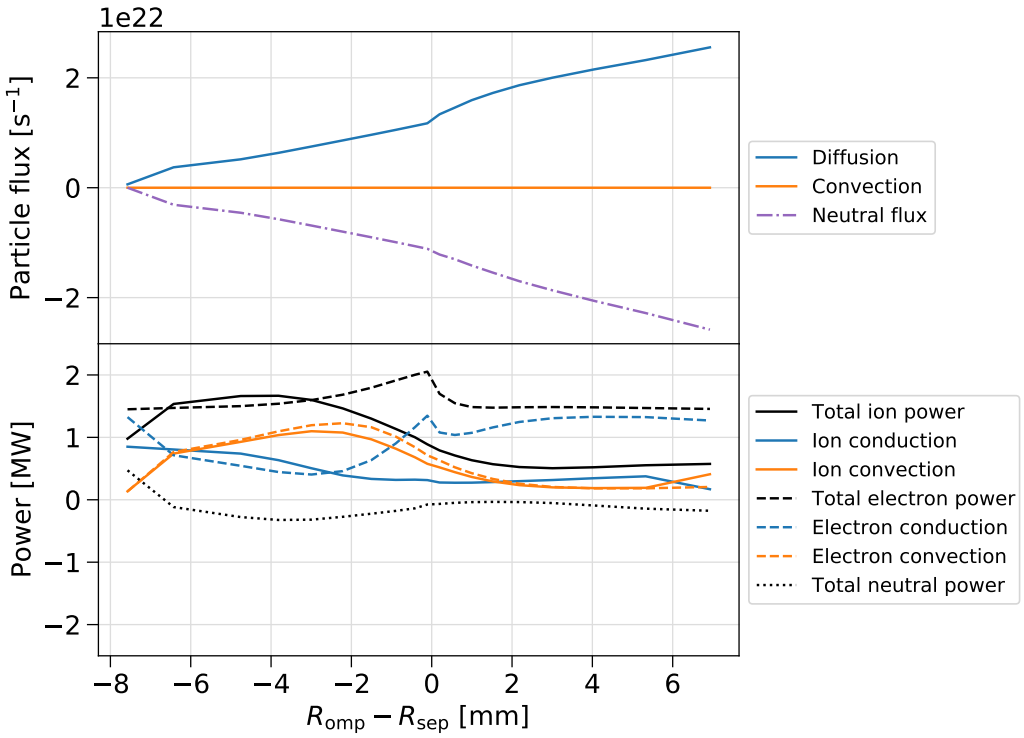

Figure 5-4: Radial fluxes of particles and power after adjustment of transport coefficients to match midplane profiles. Particle and power fluxes are summed at each flux surface over the area of the flux surface above the X-point, so as to ignore divertor transport. Positive values indicate fluxes radially outward.

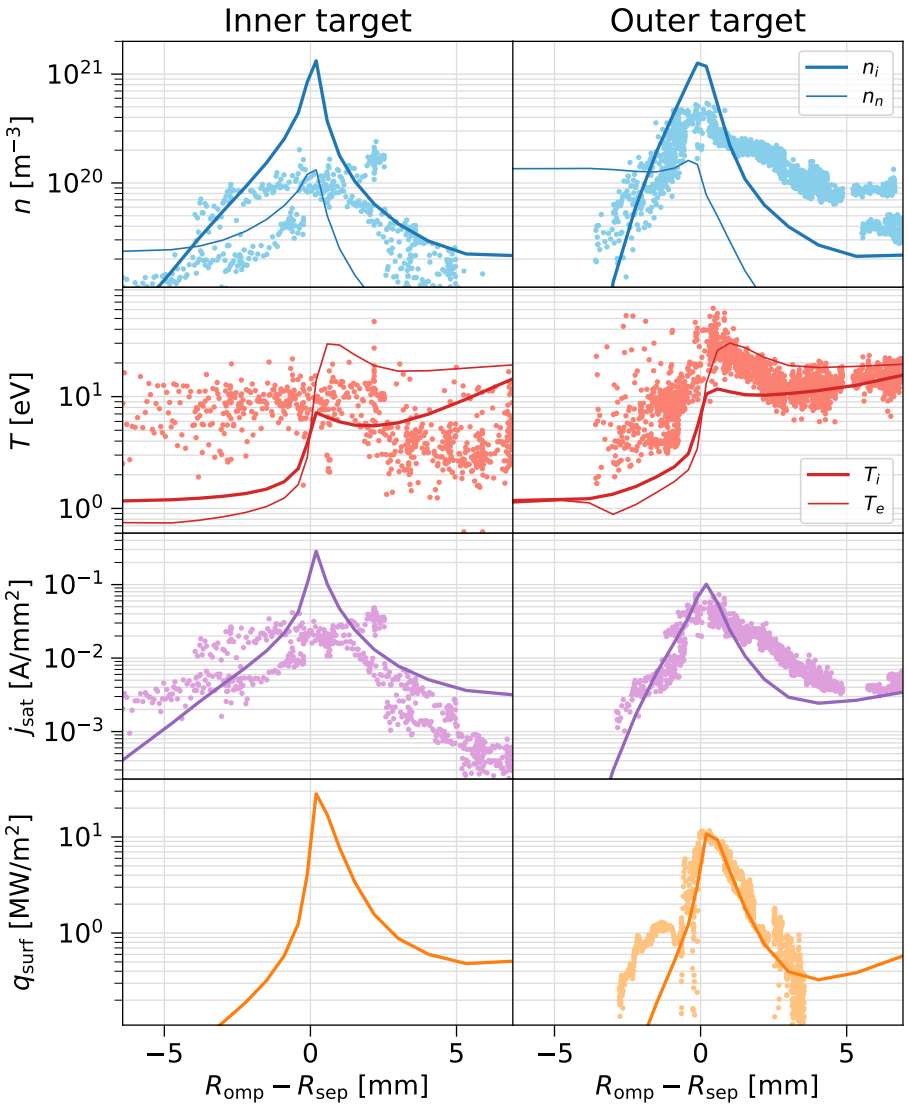

Figure 5-5: Comparison of UEDGE values and experimental measurements at the inner and outer targets: the UEDGE ion/electron density and neutral density are compared to the electron density from Langmuir probes; the UEDGE electron and ion temperatures are compared to the electron temperature from Langmuir probes; the ion saturation current in UEDGE is compared to that measured by Langmuir probes; the UEDGE surface heat flux is compared to measurements from surface thermocouples.

target. This value of j_{sat} from UEDGE is compared to the experimentally measured j_{sat} assuming an axisymmetric surface (the real Langmuir probes are situated on a toroidally asymmetric surface, so a correction factor is applied). At the outer target, UEDGE matches the ion saturation current well in the PF region and near the separatrix, but has a steeper radial gradient than the experimental j_{sat} in the CF region. At the inner target, UEDGE has j_{sat} around an order of magnitude higher than in experiment.

In this analysis, the heat flux in UEDGE is calculated as

$$q_{\text{surf}} = P_x/A \tag{5.3}$$

where P_x is the total power in the poloidal direction (including plasma convected and conducted power, surface recombination, and radiation) and A is the surface area of each UEDGE cell at the target. An experimental heat flux profile from surface thermocouples is available at the outer target. The heat flux at the outer target in UEDGE is a particularly good match to experiment in the peak value and the radial gradients near the peak.

In the UEDGE case, a total power of 0.44 MW is incident on the inner target and 0.77 MW is incident on the outer target. Using the experimental heat flux measurements and the UEDGE cell surface areas at the target, the real power to the outer target is estimated to be 0.89 MW, so UEDGE slightly underestimates this quantity. The inner:outer target power sharing ratio of 1:1.8 in UEDGE closely matches the experimental finding of 1:2 for H-modes in C-Mod [126]. The neutral density at the inner and outer target is around 10 times lower than the ion density, confirming that that plasma is attached at both targets.

The heat flux width fit with the multi-λ function at the outer target in UEDGE is 0.63 mm, which is close to the experimental value of 0.91 mm. The fact that λ_q is lower in UEDGE than in experiment for this case is a somewhat surprising result after the finding in chapter 4 that the ratio of λ_q in UEDGE to that found from experiment should be around 2 for a discharge with a separatrix density of $n_{e\,\text{sep}} = 10^{20}\,\text{m}^{-3}$ and

a power to the outer target of $P_{\text{odiv}} = 0.77\,\text{MW}$ (figure 4-8).

Figure 5-6 shows the poloidal variation of the density and temperature at the separatrix in UEDGE. The divertor targets have a plasma density around 10 times higher and a temperature around 10 times lower than the plasma above the X-point, indicating that the plasma is in the conduction-limited regime. The variation of the neutral density, which increases by 5 orders of magnitude from the X-point to the targets, and by 2 orders of magnitude from the X-point to the midplane, shows that recycling at the targets has a much greater impact than the midplane gas puffs.

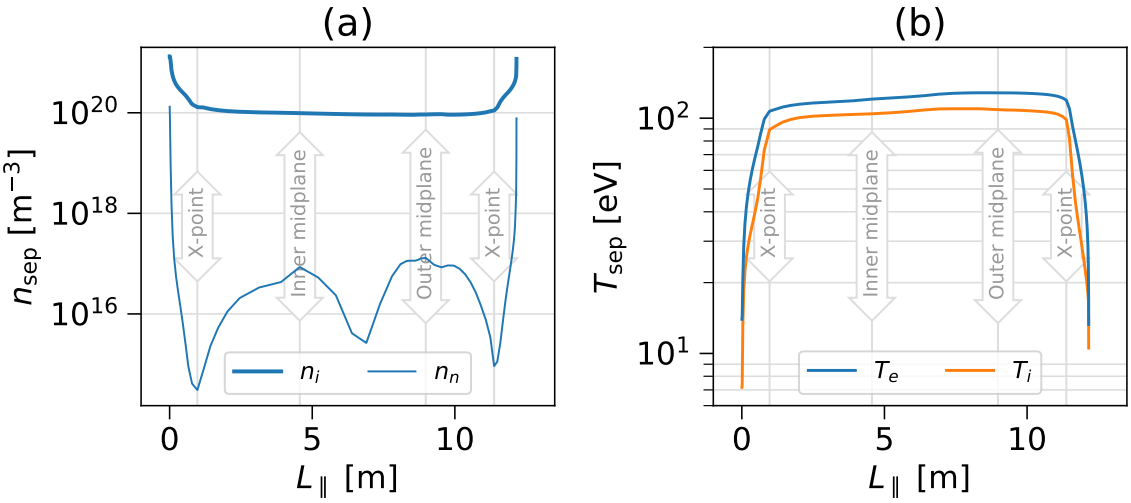

Figure 5-6: Separatrix values of (a) the plasma and neutral density and (b) the electron and ion temperature as a function of the distance parallel to the magnetic field starting at the inner target and ending at the outer target.

5.4.3 Neutral pressure

The neutral pressure is an important quantity to match to experiment as it affects the degree of detachment of the divertor. Experimental measurements of the neutral pressure in C-Mod are available from a gauge connected to the PF region situated around 1.5 meters below the outer strike-point and a gauge at the outer midplane recessed in the vessel wall. The neutral pressure in UEDGE is calculated using the neutral density and the ion temperature, as the neutral and ion temperatures are defined as equal with the current UEDGE settings. Figure 5-7(a) shows the overall

variation of the neutral pressure, with the highest pressures near the targets due to recycling and the inner and outer midplane due to the gas puffs. Figure 5-7(b) shows the profiles of neutral pressure compared to the experimental measurements. The measured neutral pressure at the midplane is much lower than the UEDGE value in the midplane far SOL, which could be acceptable because there would be steep gradients in neutral density and temperature between the UEDGE outer boundary and the location of the pressure gauge. The neutral pressure measured by the divertor gauge is much lower than the UEDGE value at the outer target PF region boundary, but is close to the value at the inner target. Again, due to gradients in density and temperature between the UEDGE locations and the gauge location, the measured divertor neutral pressure can be seen as an upper bound that UEDGE should not exceed in order to accurately model divertor conditions. The UEDGE case therefore appears to have an acceptable divertor neutral pressure.

The discharge modeled in UEDGE in this study was previously modeled using the SOLPS code with a more advanced kinetic neutral model [128], which allows comparison with the simpler neutral model in UEDGE. The SOLPS simulation had a 30% higher neutral pressure than the experimental value in the divertor and was 3 times higher than experiment at the outer midplane [128]. The UEDGE simulation in this study has neutral pressures around an order of magnitude greater than measured at both locations. It is therefore possible that a more advanced neutral model could improve the fidelity of these UEDGE simulations.

The neutral density at the midplane can also be assessed in the context of experimental studies of this quantity in C-Mod. The neutral density of $n_n = 6.6 \times 10^{16}\,\mathrm{m}^{-3}$ at 2 mm inside the separatrix at the midplane in UEDGE is high compared to an experiment that found $n_n = 0.7 \times 10^{16}\,\mathrm{m}^{-3}$ at $\overline{n}_e = 3.1 \times 10^{20}\,\mathrm{m}^{-3}$ [129] (the discharge modeled in UEDGE has $\overline{n}_e = 3.4 \times 10^{20}\,\mathrm{m}^{-3}$). This discrepancy could be due to the midplane gas puffs in UEDGE being closer to the separatrix than in experiment and the fact that the C-Mod neutral pressure study did not have local puffing while the UEDGE-modeled discharge did.

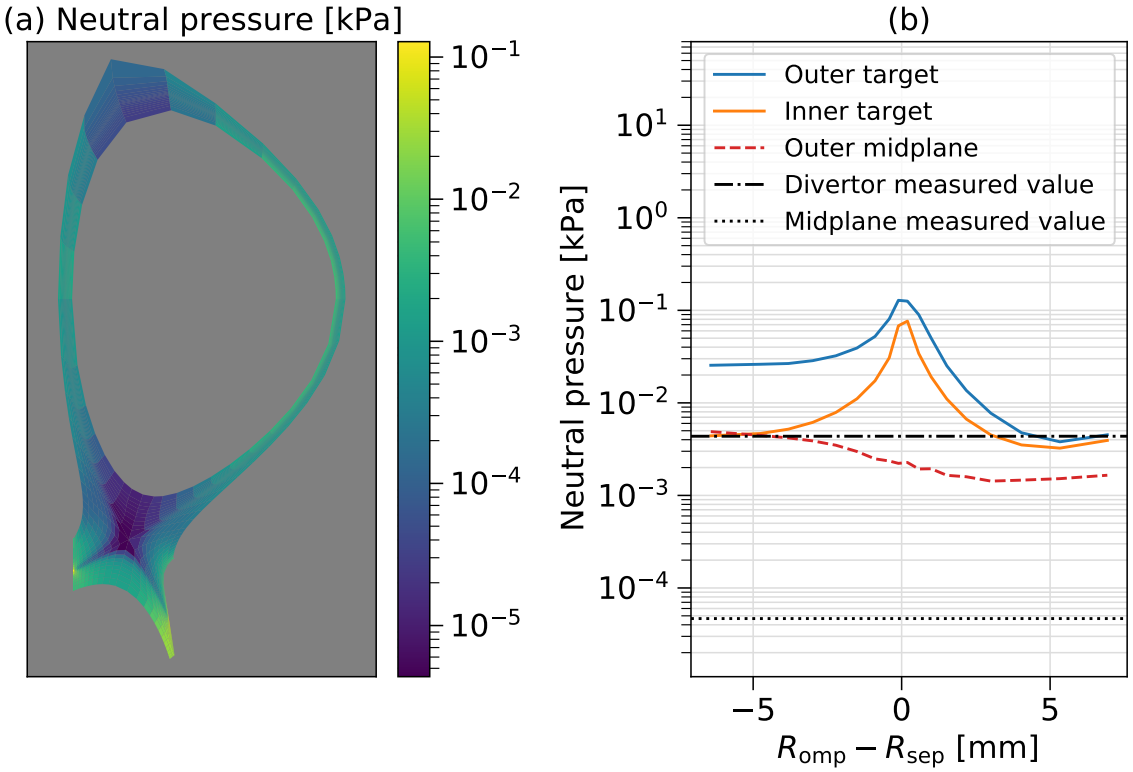

Figure 5-7: (a) Neutral pressure over the entire UEDGE grid, and (b) neutral pressure profiles at various locations in UEDGE compared to neutral pressures measured in experiment.

5.4.4 Midplane and target pressure balance

An important aspect of detachment is plasma pressure loss between the midplane and divertor target. To ensure that the attached plasma conditions in experiment are accurately modeled, the pressure balance can be examined. In attached conditions, a simple two-point model of pressure balance between the static (nT) and dynamic (nmv^2) pressure along a flux surface and the sheath boundary condition result in an expected relationship of

$$2n_tT_t = n_uT_u, \tag{5.4}$$

where the subscript t denotes the target and the subscript u denotes the upstream plasma [9]. This relationship can also be verified in UEDGE: figure 5-8 shows the total (static+dynamic) plasma pressure and static pressure alone in UEDGE compared to the static pressure at the target measured by Langmuir probes (with the approximation $T_e = T_i$). The total pressure in UEDGE at the midplane and target should be approximately equal, but just outside the separatrix (at $R_{\text{omp}} - R_{\text{sep}} \approx 0.2\,\text{mm}$), the UEDGE total pressure is larger than the midplane value by close to a factor of 3. This is mainly due to the dynamic pressure in UEDGE, as the total pressure is a factor of around 2 higher than the static pressure alone. Since UEDGE is more advanced than the two-point model, this discrepancy is not a major cause for concern, and the fact that the UEDGE total pressure is not significantly lower at the target compared to upstream confirms that the plasma is attached over the entire CF profile. Beyond 2 mm outside the separatrix, the two-point model relationship between upstream and target pressure is observed.

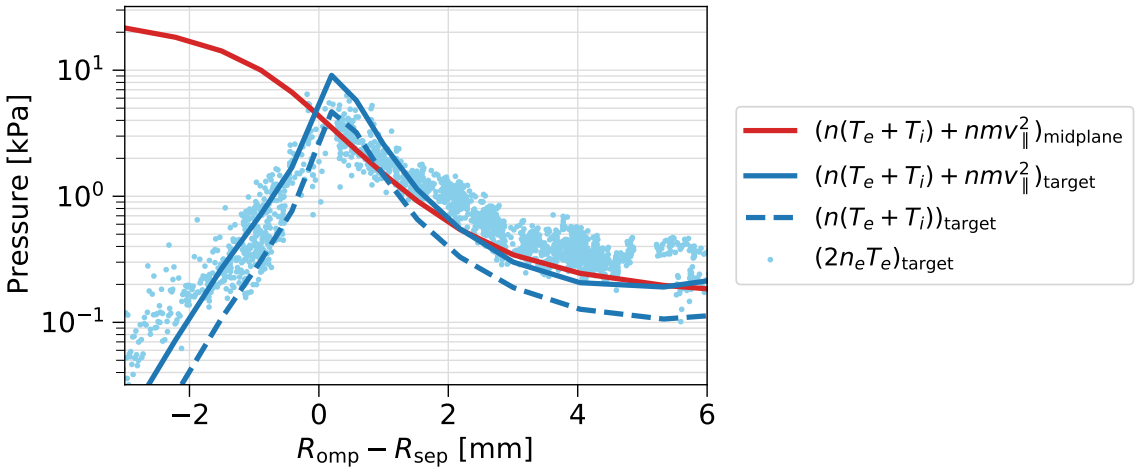

Figure 5-8: Comparison of the total (static+dynamic) plasma pressure at the midplane and outer divertor target in UEDGE, the static pressure at the target in UEDGE, and the static pressure at the target measured by Langmuir probes.

5.5 Drifts

Very good matches to the midplane and target profiles were obtained without single-particle drifts, but drift effects were included in order to have more confidence in the model when adding impurities or changing the length of the outer divertor leg.

5.5.1 Drift directions

In the discharge under consideration, the ion $\mathbf{B} \times \nabla\mathbf{B}$ drift is directed downward. The net direction of the $\mathbf{E} \times \mathbf{B}$ drift velocity projected into the poloidal plane is shown in figure 5-9. The $\mathbf{E} \times \mathbf{B}$ drift velocity is generally much larger than the ion $\mathbf{B} \times \nabla\mathbf{B}$ drift velocity over the entire grid. In the PF region and near the separatrix in the CF region, the dominant poloidal flow direction is from the outer target to the inner target. Further out in the SOL, the poloidal flow is from the inner target to the outer target, and even further out, the direction is once again from the outer target to the inner. The expected poloidal direction of the $\mathbf{E} \times \mathbf{B}$ drift in the CF region in this magnetic configuration is from the inner target to the outer target. The reversal of the poloidal direction of the drift in UEDGE is due to the radial electric field changing sign, which may be due to $\nabla_r T_e$ changing sign at the last few cells

radially near the CF region outer boundary at the outer divertor target. The change in sign of $\nabla_r T_e$ is likely due to the fixed $T_e = 20\,\mathrm{eV}$ boundary condition at the outer CF region boundary, while the divertor targets usually have lower T_e, especially some distance away from the strike-point.

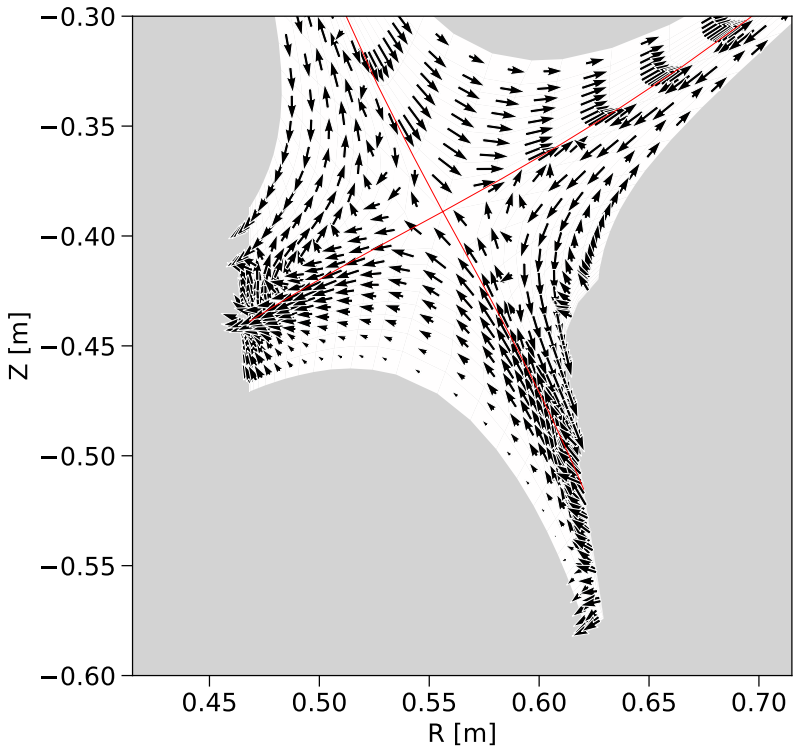

Figure 5-9: Directions and magnitudes (sizes of arrows) of the $\mathbf{E} \times \mathbf{B}$ drift velocities near the lower X-point.

Figure 5-10 shows that the radial velocity of the $\mathbf{E} \times \mathbf{B}$ drift is from the PF region to the CF region at the inner target, and from the CF region to the PF region at the outer target, with some exceptions near the separatrix just above the outer target. The radial velocity due to the $\mathbf{E} \times \mathbf{B}$ drift is therefore mostly in line with expectations for the given magnetic configuration. The magnitude of the $\mathbf{E} \times \mathbf{B}$ drift in the poloidal direction reaches a maximum fraction of around half the sound speed. The radial velocity is generally lower than the poloidal velocity, reaching a maximum fraction of around 7% of the sound speed.

When drifts are enabled, the spatial profile of the radiation due to ionization in UEDGE roughly matches D-α profile measurements in Alcator C-Mod (figure 5-

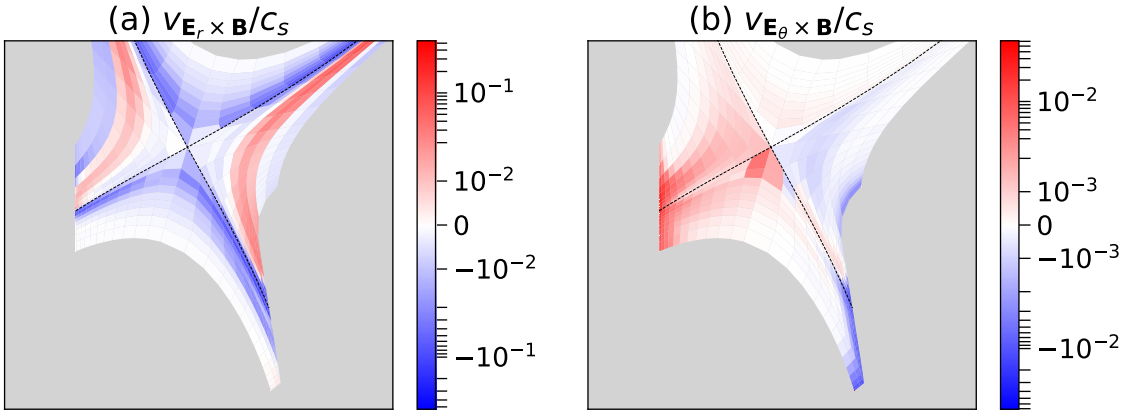

Figure 5-10: $\mathbf{E} \times \mathbf{B}$ drift velocities as a fraction of the sound speed for (a) the drift velocity in the $\hat{\mathbf{i}}_w = \hat{\mathbf{i}}_\parallel \times \hat{\mathbf{i}}_y$ direction (mostly poloidal), where positive values indicate a clockwise poloidal direction in the SOL; and (b) the drift velocity in the radial direction, where positive values indicate a direction radially outward from the core in the CF region and toward the separatrix in the PF region.

11(a)). In experiment, the peak D-α power density was found to occur upstream of the inner target in a discharge with a toroidal field direction matching that in the UEDGE case, and close to the outer target in a discharge with reversed toroidal field [130]. The toroidal field in UEDGE can be controlled by a scalar factor for the purpose of setting the drift velocities, and when the toroidal field was reversed in UEDGE, the region of highest power density was instead upstream of the outer target, again matching the C-Mod experimental results (figure 5-11(b)). The experimental result from C-Mod, however, was for discharges at relatively low line-averaged density ($\overline{n}_e = 0.8 \times 10^{20}\,\mathrm{m}^{-3}$) while a change in spatial distribution was less clear for discharges with $\overline{n}_e = 1.8 \times 10^{20}\,\mathrm{m}^{-3}$ (the discharge modeled here has $\overline{n}_e = 3.4 \times 10^{20}\,\mathrm{m}^{-3}$) [130]. In another study, drifts were found to be important to include in UEDGE in order to more accurately model the divertor impurity radiation profile in DIII-D [131].

5.5.2 Midplane profiles

After the base case was modified to include single-particle drifts, the ion and electron temperature inside the separatrix were too low by a factor of around 2. Adjustments to anomalous transport coefficients using equation 4.2 improved the match to the

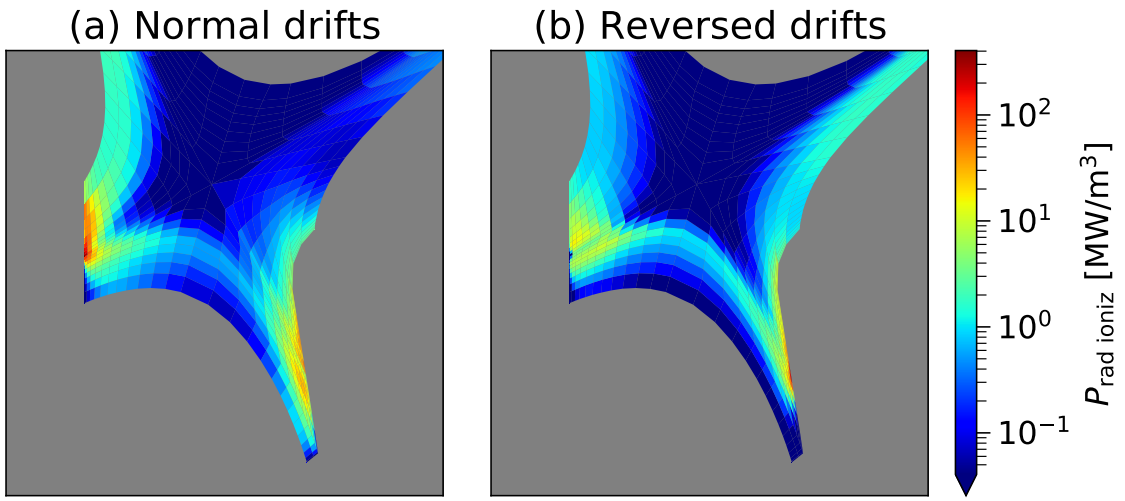

Figure 5-11: Power density due radiation from ionization in the UEDGE cases with (a) drift directions matching experiment (b) drifts assuming an oppositely directed toroidal field.

density profile but not the match to the temperature profile (figure 5-12).

The low ion and electron temperatures inside the separatrix appear to be due to the increase in convective heat flux inside the separatrix compared to the case without single-particle drift effects (figure 5-13). This explains why using equation 4.2 to lower the anomalous conduction coefficients did not improve the profiles, as the amount of conductive heat flux was low to begin with. The increased convective heat flux is mostly due to the $\mathbf{B} \times \nabla \mathbf{B}$ particle convection radially outward inside the separatrix, which is greater than the anomalous diffusive particle flux in that region. The $\mathbf{B} \times \nabla \mathbf{B}$ particle flux inside the separatrix is countered by a flux of particles radially inward due to the $\mathbf{E} \times \mathbf{B}$ drift, but the $\mathbf{B} \times \nabla \mathbf{B}$ particle flux is generally greater.

Many modifications to the UEDGE settings were tried in order to raise the low temperatures inside the separatrix, but none helped other than to change the convective heat flux factor of 5/2 in equation 2.46 to 3/2, with which an excellent match to the experimental temperature profile was restored after adjusting D and χ. The 5/2 coefficient appears to be appropriate for the form of the energy equation used in UEDGE, while the 3/2 factor should be used in a different but equivalent form of the

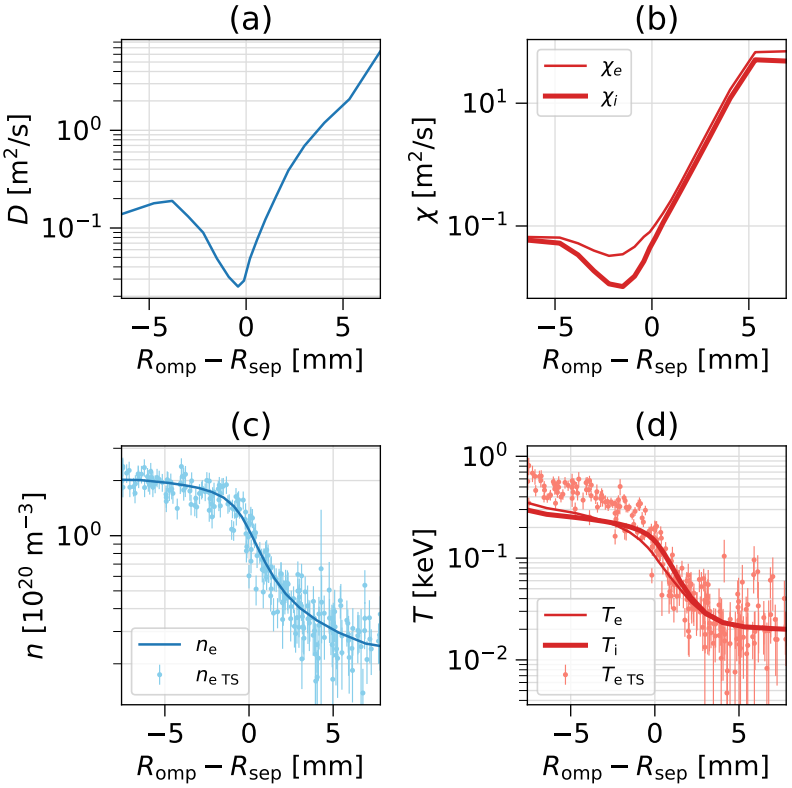

Figure 5-12: Anomalous transport coefficients and midplane profiles in UEDGE with single-particle drifts enabled compared to experiment: (a) UEDGE anomalous radial particle diffusivity, (b) UEDGE anomalous electron and ion radial conductivity, (c) UEDGE density (line) and experimental density (points) at the outer midplane, and (d) UEDGE electron and ion temperatures (lines) and experimental temperature (points) at the outer midplane. (To compare to the drifts-off case, see figure 5-3.)

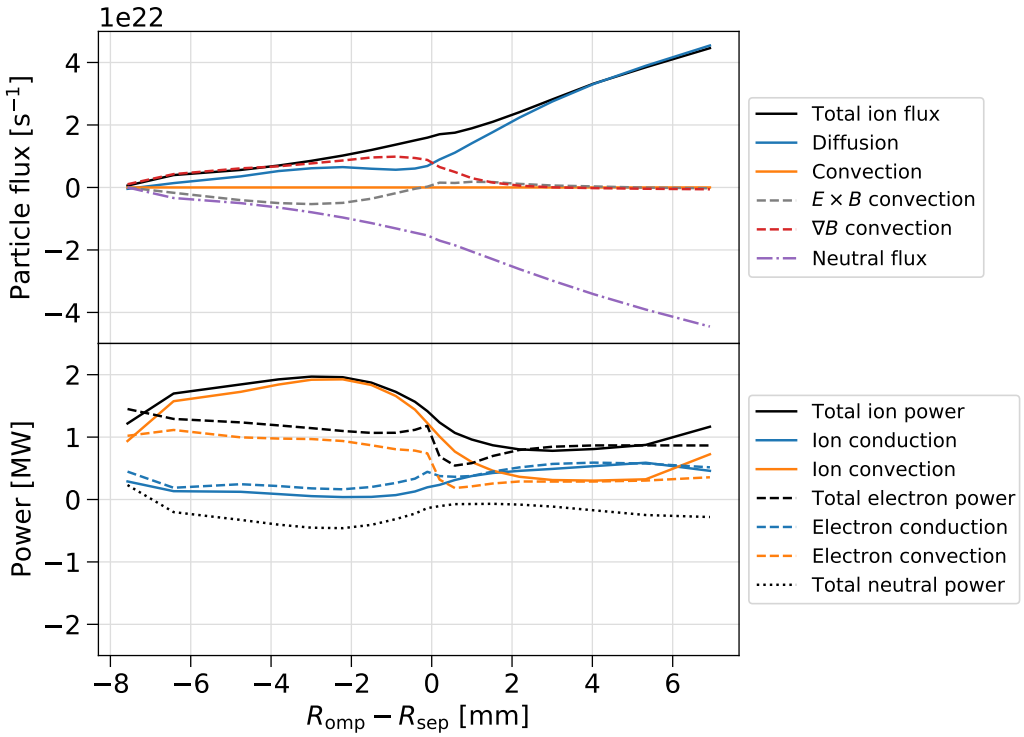

Figure 5-13: Radial fluxes of particles and power in UEDGE with single-particle drifts enabled after the adjustment of transport coefficients to match the midplane profiles. Particle and power fluxes are summed at each flux surface over the area of the flux surface above the X-point, so as to ignore divertor transport. Positive values indicate fluxes radially outward.

energy equation, which happens to be that used by the SOLPS code [9, 78, 132–136]. Therefore, despite the promising result, the 3/2 factor was deemed inappropriate to use in this case. Other modifications were also tried, including using central differencing rather than the upwind method and increasing the grid resolution, but these did not have a significant impact on the core temperatures. This imperfect simulation with low temperatures inside the separatrix should nevertheless be useful because SOL conditions are well-modeled and the discrepancy inside the separatrix should not have a large impact on the SOL.

5.5.3 Target profiles

Single-particle drifts have a strong effect on target conditions in this UEDGE case (figure 5-14). Drifts decrease the peak density at the outer target by an order of magnitude and shift the peak into the PF region, while the density at the inner target is increased in the CF region. With the $\mathbf{B} \times \nabla \mathbf{B}$ drift toward the lower X-point, the $\mathbf{E} \times \mathbf{B}$ drift poloidal flow should redistribute particles from the inner target to the outer target. This effect appears to be less important than the process of (1.) $\mathbf{E} \times \mathbf{B}$ radial flow of particles near the outer target from the CF region into the PF region, (2.) $\mathbf{E} \times \mathbf{B}$ poloidal flow from the outer target to the inner target through the PF region, and (3.) $\mathbf{E} \times \mathbf{B}$ radial flow near the inner target from the PF region into the CF region. The $\mathbf{E} \times \mathbf{B}$ poloidal flow in the CF region may not redistribute particles from the inner to the outer divertor as significantly as it should due to the change in sign of $v_{\mathbf{E}_r \times \mathbf{B}}$ in the far SOL, which has been speculated in this study to be due to the relatively high fixed temperature boundary condition on the CF region wall. Another possible explanation for the density imbalance between the inner and outer target that defies experimental measurements can be seen in figure 5-15(a, b), which shows that despite the poloidal $\mathbf{E} \times \mathbf{B}$ drift velocity pointing away from the inner target strike-point in the radial region of high parallel heat flux, the net flux of particles there is toward the inner target. This makes it difficult for the poloidal $\mathbf{E} \times \mathbf{B}$ flow in the CF region SOL to distribute particles from the inner target to the outer target. Overall, including drifts in UEDGE does not appear to significantly improve

or worsen the match to the density at the target measured by Langmuir probes, as there are significant discrepancies in both cases.

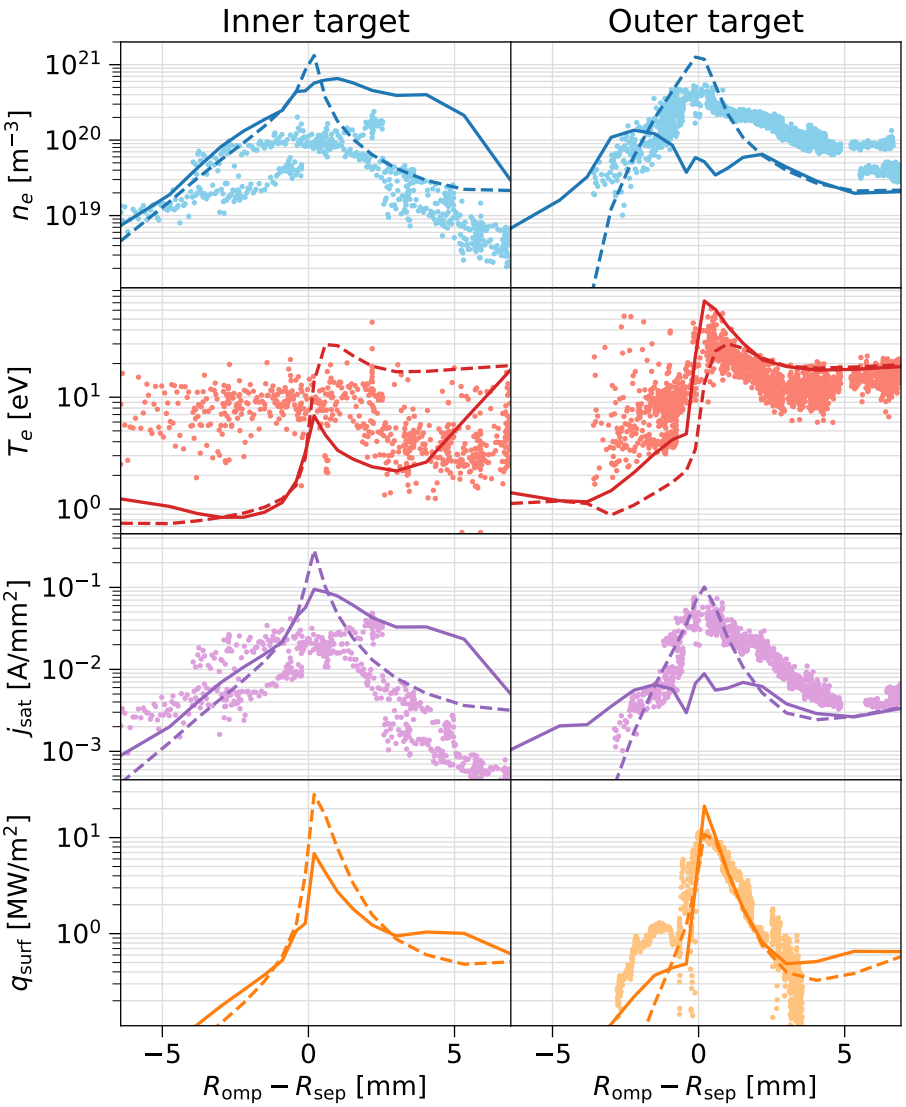

Figure 5-14: UEDGE plasma parameters before (dashed lines) and after (solid lines) enabling single-particle drifts: the UEDGE ion/electron density is compared to the electron density from Langmuir probes; the UEDGE electron temperature is compared to the electron temperature from Langmuir probes; the ion saturation current in UEDGE is compared to that measured by Langmuir probes; the UEDGE surface heat flux is compared to measurements from surface thermocouples.

Figure 5-14 also shows that the peak temperature increases at the outer target and decreases at the inner target when drifts are enabled in UEDGE, possibly due to the approximate conservation of pressure along flux tubes and the general decrease

and increase, respectively, of the density at outer and inner targets. Relative to the Langmuir probe measurements of the electron temperature, the UEDGE target temperatures do not significantly improve or worsen at the inner target, and at the outer target the peak temperature is slightly too high but agreement with experiment is improved in the PF region.

The ion saturation current at the targets in UEDGE behaves very similarly to the density at the targets after enabling drifts (figure 5-14). The peak j_{sat} at the outer target matched the experimental peak very well without drifts, and became too low by an order of magnitude when drifts were enabled. The match at the inner target is also slightly worsened by enabling drifts, which raise j_{sat} in the CF region.

The heat flux profiles at the targets in UEDGE are also changed by the inclusion of drifts (figure 5-14). This is most pronounced at the inner target, where the peak heat flux decreases significantly. At the outer target, the peak heat flux increases by around a factor of 2, and the decay length changes from 0.63 mm to 0.49 mm, straying a little further from the experimental value of 0.91 mm. Nonetheless, the match with experiment on either side of the peak remains quite good. The total power to the inner and outer target are 0.44 MW and 0.77 MW (1:1.8) without drifts and 0.24 MW and 1 MW (1:4.2) with drifts. The case without drifts is closer to the 1:2 ratio expected for H-modes [126] but the case with drifts has an acceptable total power to the outer target (estimated to be 0.89 MW in experiment). This appears to be due at least in part to the poloidal component of the $\mathbf{E} \times \mathbf{B}$ drift bringing more power from the inner target to the outer target through the CF region and to a lesser degree from the outer target to the inner target in the PF region (figure 5-15(a, c)).

The variation of plasma quantities in UEDGE in the parallel direction along the separatrix can once again be examined with drifts enabled (figure 5-16). All profiles change significantly compared to figure 5-6. One notable change is that the ion density at the outer target decreases going from the X-point to the outer target, whereas before, it increased. The neutral density at the outer target is also an order of magnitude lower than in the case without drifts. The higher electron and ion temperatures at the outer target are also apparent in figure 5-16(b). The ion temperature in par-

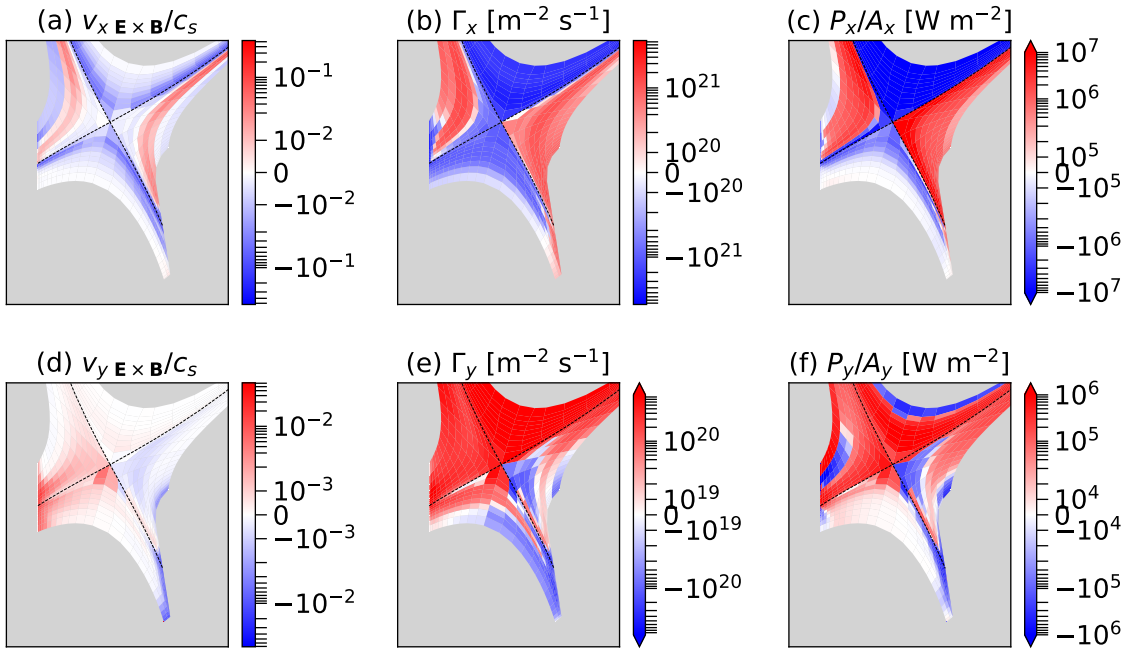

Figure 5-15: Poloidal and radial transport in the UEDGE case with single-particle drifts enabled: (a) the $\mathbf{E}\times\mathbf{B}$ poloidal velocity as a fraction of the sound speed, (b) the total poloidal particle flux, (c) the total poloidal power flux, (d) the $\mathbf{E}\times\mathbf{B}$ radial velocity as a fraction of the sound speed, (e) the total radial particle flux, and (f) the total radial power flux.

ticular varies strongly from one side of the X-point to the other. This was verified to be mostly due to the ion $\mathbf{B} \times \nabla \mathbf{B}$ velocity by using the radial component of the $\mathbf{B} \times \nabla \mathbf{B}$ drift velocity as the user-defined anomalous convective velocity in the case with no drifts and recovering the shape of the $T_{i\,\mathrm{sep}}(L_\parallel)$ profile. It can be seen that where the $\mathbf{B} \times \nabla \mathbf{B}$ drift directs high-temperature ions out of the core, between the X-point and the inner midplane and between the outer midplane and the X-point, $T_{i\,\mathrm{sep}}$ is increased. Between the inner and outer midplane, the $\mathbf{B} \times \nabla \mathbf{B}$ drift directs low-temperature ions from the SOL toward the core, and $T_{i\,\mathrm{sep}}$ is decreased. The electron temperature does not vary as much over $L_\parallel$ as the ion temperature, possibly due to the higher conductivity of electrons.

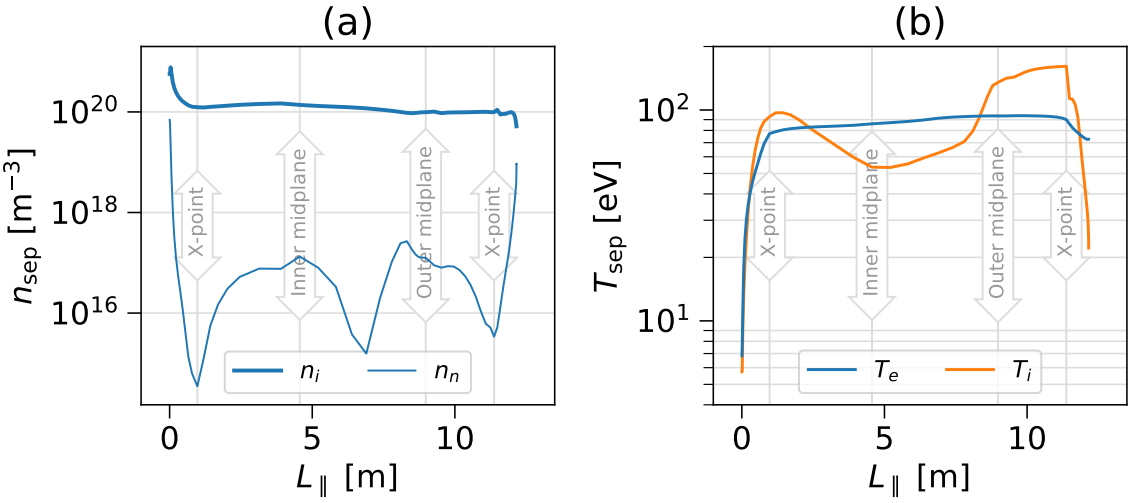

Figure 5-16: Separatrix plasma parameters with single-particle drifts enabled in UEDGE: (a) the plasma and neutral density and (b) the electron and ion temperature as a function of the distance parallel to the magnetic field starting at the inner target and ending at the outer target.

The pressure balance between the outer midplane and target can also be re-examined with drifts enabled (figure 5-17). Unlike the case without drifts (figure 5-8), the total (static+dynamic) pressure at the target just outside the separatrix is reduced compared to the midplane total pressure. This coincides with a rise in the PF region pressure at the target, likely due to the radial component of the $\mathbf{E} \times \mathbf{B}$ drift transporting ions from the CF region to the PF region along the outer divertor leg. The static pressure at the target in UEDGE can also be compared to the exper-

imental data from Langmuir probes. Without drifts, the peak static pressure at the target in UEDGE was quite close to the peak experimental value, while with drifts the peak static pressure is too low by a factor of around 4.

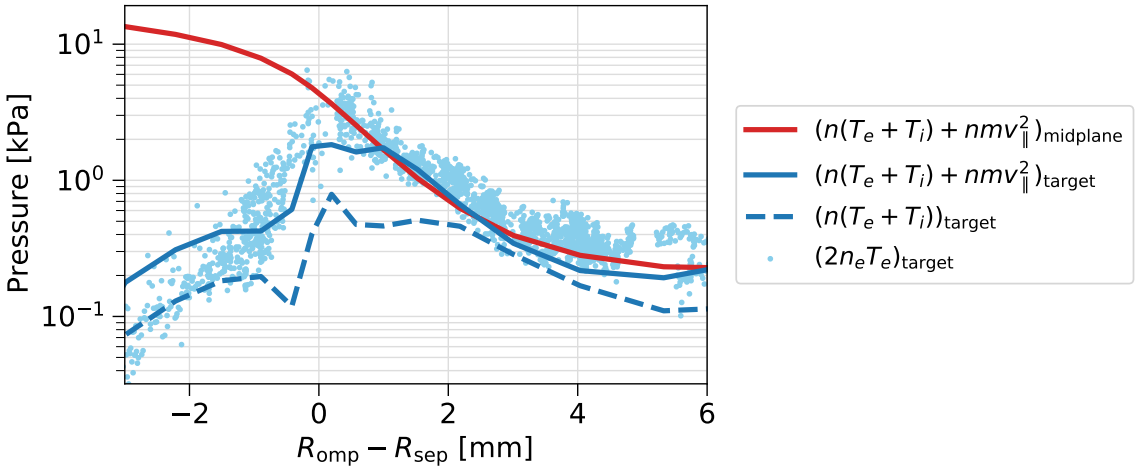

Figure 5-17: Pressure balance with single-particle drifts enabled in UEDGE: the total (static+dynamic) plasma pressure at the midplane and outer divertor target in UEDGE, the static pressure at the target in UEDGE, and the static pressure at the target measured by Langmuir probes.

Another metric of interest with drifts enabled is the neutral pressure. The neutral pressure at the divertor target PF corners is around a factor of 2 higher than the experimental measurement, while the neutral pressure in the far SOL of the outer midplane is more than an order of magnitude greater than the pressure measured there in experiment. In this respect, the cases with and without drifts are similar.

In conclusion, enabling drifts in this simulation of a particular C-Mod discharge has a significant impact on target conditions, in some respects for the worse. Most concerning is the worse match to j_{sat} at the outer target, which is a robust measurement from the Langmuir probes. Some of the most important metrics, however, such as the heat flux profile at the outer target, are still a good match to experiment with drifts enabled, giving confidence in the utility of this case. Further work is needed to determine whether certain UEDGE settings could be modified to enable drifts while avoiding some of the adverse effects observed. This study confirms, however, that drifts play an important role in the SOL of C-Mod, and that including them will

enable more robust predictions of the impact of impurities and changes in divertor leg geometry.

5.6 Impurities

Impurity puffing is one way to induce detachment and protect the divertor targets from the high heat flux of a high-performance plasma. The fixed-fraction impurity model in UEDGE (section 2.4.5) was used to examine the effect of nitrogen impurity puffing. In this model, the impurity density is a user-specified fraction of the ion density at each cell in the grid. Single-particle drift effects are enabled unless otherwise noted. A nitrogen impurity is used in this study due to its history in target heat flux reduction experiments in Alcator C-Mod [137–139].

The effects of a small and large impurity fraction on the outer target heat flux are shown in figure 5-18. At 0.1% nitrogen, the dominant component of the heat flux is the convected and conducted power due to ions, electrons, and neutrals. There is also significant heat flux due to the ion kinetic energy and surface recombination, while hydrogen photons and impurity photons contribute very little. When the impurity fraction is increased to 3.5% nitrogen, causing the outer target to fully detach, the peak heat flux to the outer target is reduced by approximately 2 orders of magnitude, and the dominant component of the heat flux is that due to impurity photons, which radiate most of the power in the SOL evenly before it can travel to the outer target along magnetic field lines. It must be noted that in order for the UEDGE case to converge with a fully detached outer target and with drifts enabled, the poloidal resolution of the outer leg had to be reduced from 14 cells to 7 cells between the X-point and the outer target. The grid used is shown in blue in figure 5-20.

Another hallmark of detachment is significant pressure loss along a flux tube, which can be verified in UEDGE (figure 5-19). It can be seen that near the separatrix, the UEDGE total pressure (static+dynamic) drops by more than an order of magnitude between the outer midplane and the outer target. This increases confidence that the full effects of detachment are being modeled.

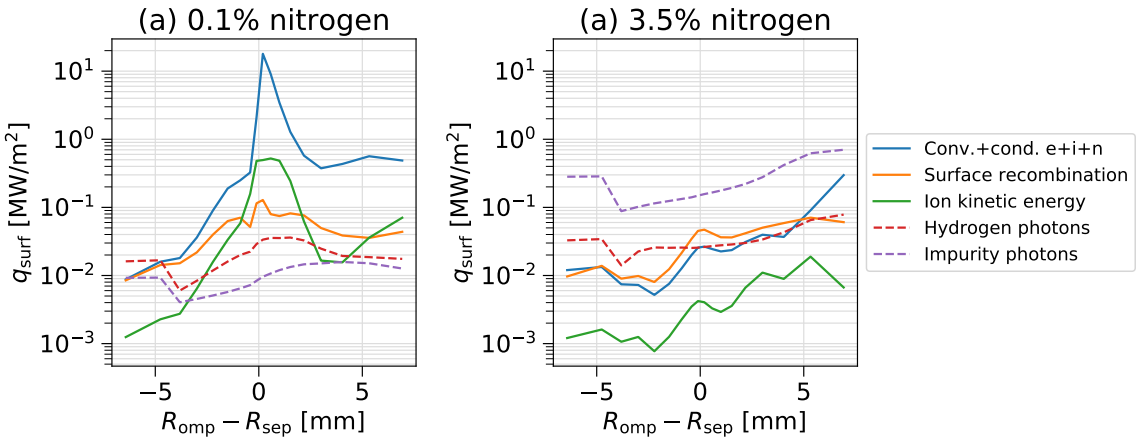

Figure 5-18: Components of the total heat flux to the outer target with (a) 0.1% nitrogen and (b) 3.5% nitrogen. The first component listed in the legend is the total convected and conducted heat flux due to electrons, ions, and neutrals.

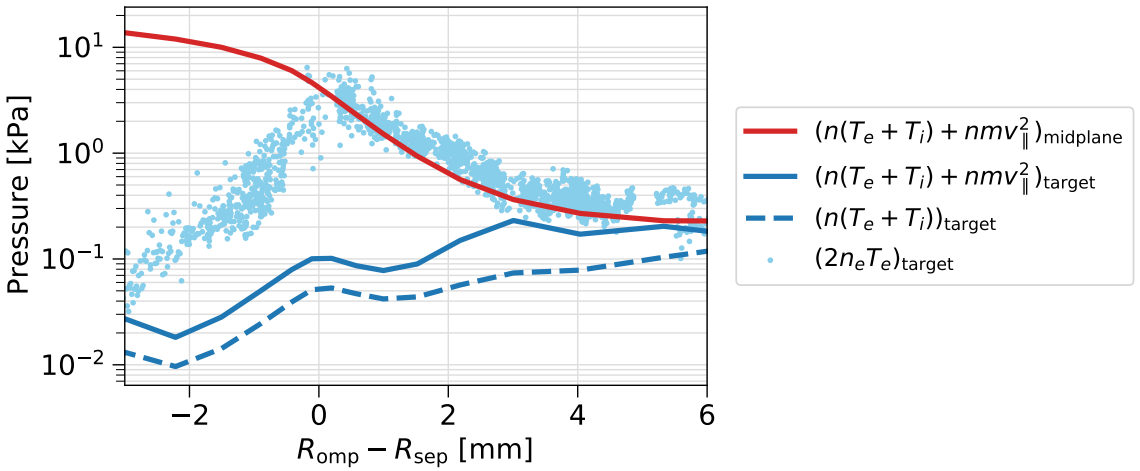

Figure 5-19: Pressure balance with single-particle drifts enabled and a spatially uniform fraction of 3.5% nitrogen impurity in UEDGE: the total (static+dynamic) plasma pressure at the midplane and outer divertor target in UEDGE, the static pressure at the target in UEDGE, and the static pressure at the target measured by Langmuir probes.

5.7 Long outer leg

Modeling Alcator C-Mod with a long outer divertor leg is a way to bridge simulations that closely track a real high-power H-mode experimental discharge with simulations of new high-field advanced-divertor devices such as ADX, SPARC, and ARC, in which plasma profiles and other real-world effects can only be roughly predicted. The results of the C-Mod long-leg modeling effort will give a sense of the impact of an advanced divertor in a high-field device, and will provide increased confidence when modeling future devices. It should be kept in mind that detaching such a C-Mod H-mode without degrading core performance was difficult and a major research goal for the program [140] and it is of interest to provide insight from modeling about whether a relatively minor change in the divertor geometry could have made the desired detachment significantly easier. This modeling effort will also be one of very few SOL fluid simulations of advanced divertor concepts to include single-particle drift effects.

5.7.1 Grid

The grid for the long outer divertor leg geometry is shown compared to the grid based on the real C-mod geometry in figure 5-20. Because the angle of incidence of the field line on the outer target is an important factor in the heat flux profile on the plate, care was taken to rotate the plate such that the total angle between the field line and the target near the separatrix was the same as in the real C-Mod geometry case. It can be seen in figure 5-20 that the outer target in the long leg case is closer to vertical than in the real geometry. This was also the maximum leg length possible within the boundaries of the available EFIT equilibrium. The poloidal distance from the X-point to the outer target is increased by 77% with the long leg. The parallel distance from the X-point to the outer target along the first cell outside the separatrix is increased by 130% with the long leg, but the parallel distance from the inner target to the outer target is only increased by 5.3%.

The poloidal resolution of the grid in the outer divertor leg for the real C-Mod geometry is decreased from 14 cells to 7 cells because higher-resolution grids had

trouble converging near detachment with drifts and impurities. In the long-leg grid, there are 14 cells poloidally between the X-point and outer target, to maintain a poloidal resolution similar to that in the real geometry grid.

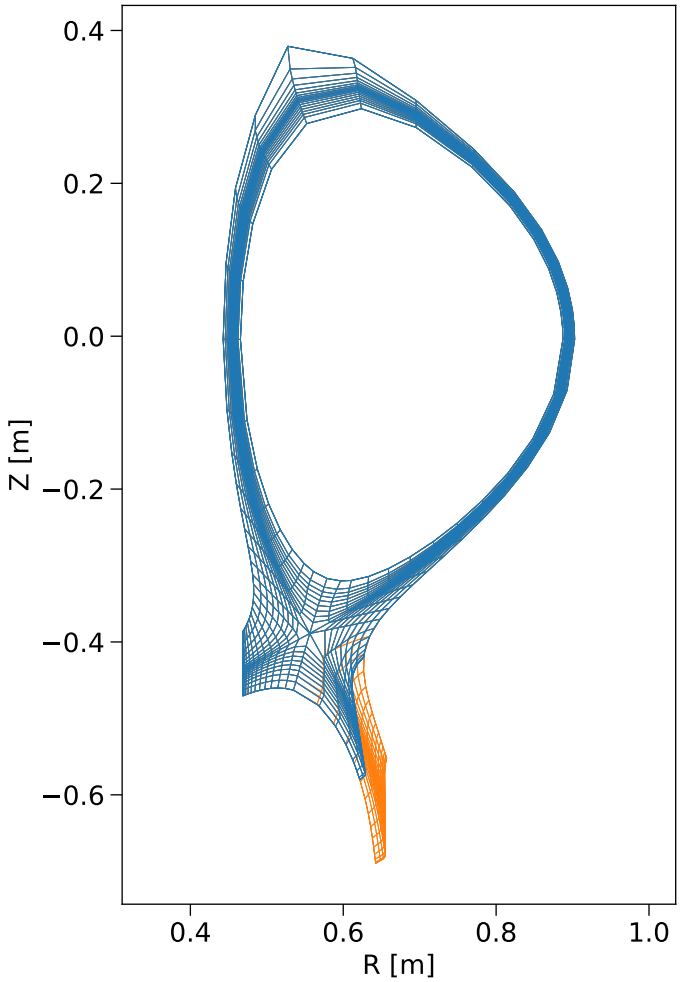

Figure 5-20: Grid based on the real Alcator C-Mod geometry (blue), and grid with a long outer divertor leg (orange).

5.7.2 Impact on target conditions

With drifts enabled, the impact of the long leg geometry on target conditions is shown compared to the real geometry in figure 5-21. The effect of the long leg appears to be subtle in most cases. Most importantly, the peak heat flux at the outer target barely changes at all. One change is in the peak temperature at the inner target, which is decreased by a factor close to 2 with the long leg, and the peak heat flux

there decreases slightly as well. The density at the outer target in the PF region is greater in the long leg geometry, likely due to the radial component of the $\mathbf{E} \times \mathbf{B}$ drift having more opportunity to transport ions from the CF to the PF region over the longer parallel distance between the X-point and the outer target.

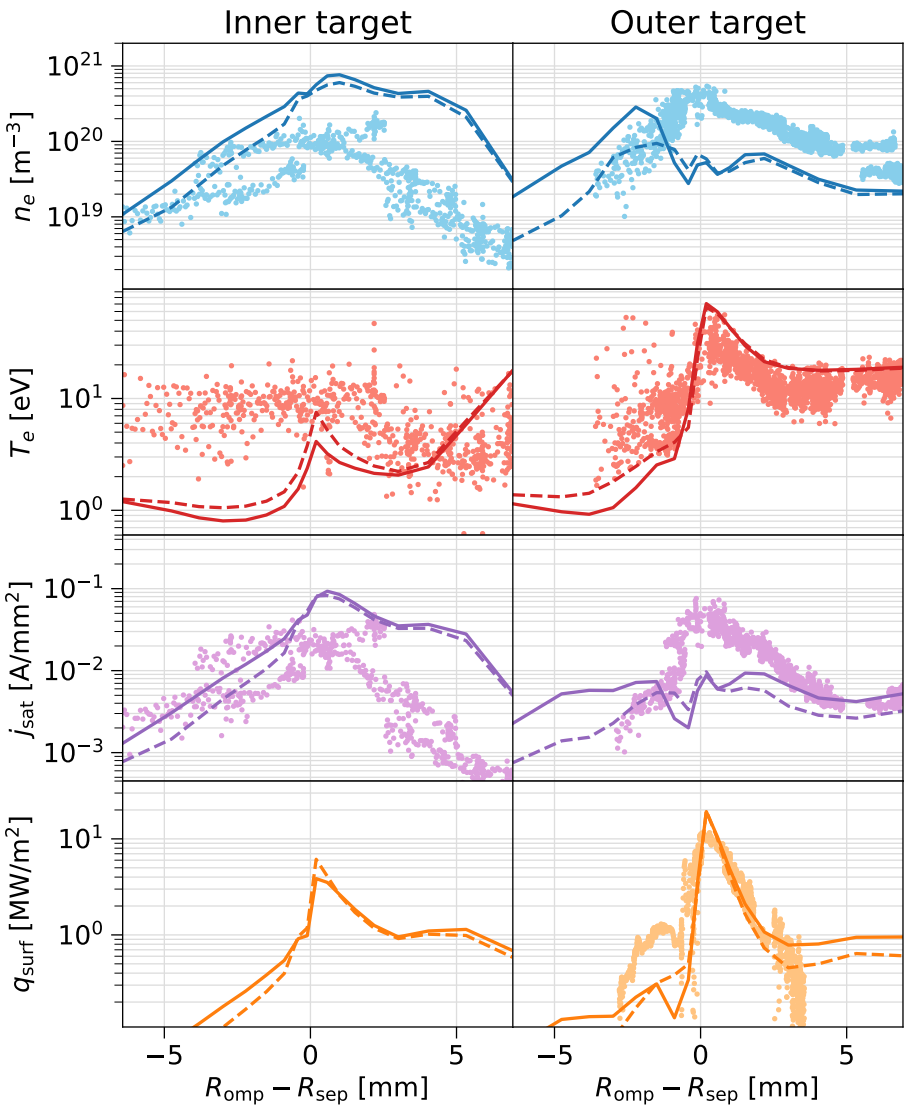

Figure 5-21: UEDGE plasma parameters using the real C-Mod outer leg geometry (dashed lines) and with a long leg (solid lines), with single-particle drifts enabled and no impurities: the UEDGE ion/electron density is compared to the electron density from Langmuir probes; the UEDGE electron temperature is compared to the electron temperature from Langmuir probes; the ion saturation current in UEDGE is compared to that measured by Langmuir probes; the UEDGE surface heat flux is compared to measurements from surface thermocouples.

With drifts disabled, the biggest change between the real and long-leg geometries is in the heat flux at the outer target, with the peak heat flux decreasing by a factor of almost 2 in the long-leg case. The fact that with drifts enabled, the peak heat flux does not change when going from the real geometry to the long leg means that expectations for advanced-divertor heat flux reduction should be tempered if drifts are not included in the simulation.

5.8 Detachment studies

One of the most important processes to investigate with these UEDGE cases is that of impurity-induced detachment. In this study, the nitrogen fraction was increased up to 5% in steps of 0.1%. Higher than 5% (and in some cases slightly lower), there can be unphysical power balance issues in these C-Mod scenarios (e.g. more power radiated than the power specified at the core boundary). Figure 5-22 shows key detachment metrics as a function of the nitrogen fraction in UEDGE, for the cases with and without drifts in the real C-Mod geometry and the case with drifts and the long leg geometry.

Most importantly, figure 5-22 shows that the detachment threshold is reduced from 3.5% nitrogen in the real geometry to 2.4% nitrogen with the long leg. Long-leg advanced divertor designs should therefore make detachment easier in high-field devices such as ADX, SPARC, and ARC. This result includes drift effects and is firmly grounded in C-Mod experimental data, increasing confidence in this general prediction.

In figure 5-22, the cases with drifts appear to have a much stronger detachment "cliff" behavior than the case without drifts, which appears to decrease more gradually even at higher nitrogen fractions. Although all cases up to at least 1% nitrogen show an approximately linear decrease in heat flux, dynamic pressure, and temperature, the cases without drifts have a step-like transition to values consistent with detachment. Furthermore, the step-like transition with drifts enabled affects all detachment metrics simultaneously. When drifts are disabled, these metrics progress toward their fully detached values at different rates: the dynamic pressure and the neutral to ion density

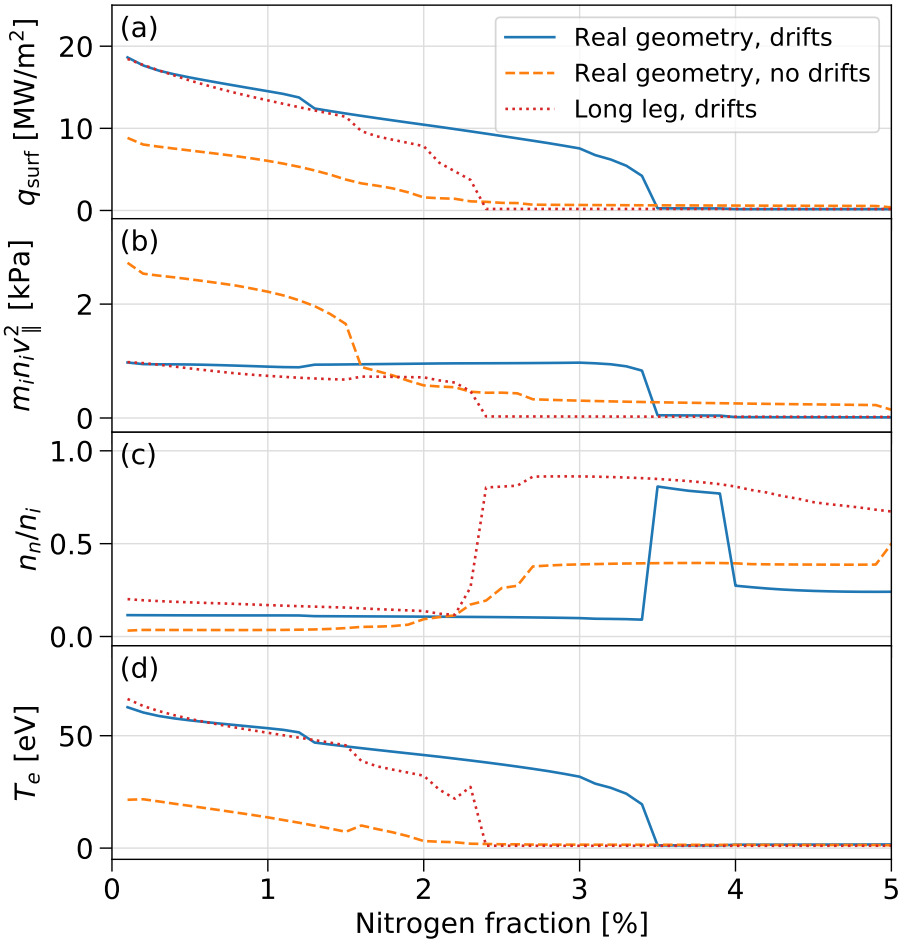

Figure 5-22: Key metrics of detachment at the outer target strike-point for various UEDGE cases: (a) the surface heat flux, (b) the dynamic pressure, (c) the ratio of the neutral density to the ion density, and (d) the electron temperature.

ratio take longer to reach a steady, detached value than the surface heat flux and the electron temperature. It can be noted that the peak heat flux in the case without drifts is around half that of the cases with drifts, somewhat muddying the comparison, but the more gradual transition to detachment when drifts are ignored is clear enough that it should be unlikely to change in higher heat flux conditions. Finally, the rise and unexpected fall of the neutral to ion density ratio in figure 5-22 for the case with the real geometry and drifts enabled is another interesting phenomenon that is further examined in this study.

Figure 5-23 shows the change in the peak heat flux and the total power to the surface for the inner and outer targets. Interestingly, at low nitrogen fractions, during the linear decrease in peak heat flux at the outer target that precedes the detachment cliff, the total power to the inner target actually increases, before suddenly decreasing and remaining constant after the detachment cliff. This phenomenon is observed in the long leg as well. In the real C-Mod geometry, this is not a cause for concern, as the peak heat flux at the inner target decreases to a very low value at greater than 1.5% nitrogen. In the long leg geometry, however, the peak heat flux at the inner target remains somewhat high even at high nitrogen fractions. This could be due to the $\mathbf{E} \times \mathbf{B}$ drift transporting energy from the outer divertor leg to the inner divertor leg through the PF region. This result means that in some cases, special care may be needed to avoid exceeding heat flux tolerances for the inner target when impurities are introduced to induce detachment.

In order to better understand why the case with the long leg geometry has a lower detachment threshold, it is instructive to look at the total power due to impurity radiation in the inner and outer divertor legs, the main chamber SOL (above the X-point), and the core (figure 5-24). In the real geometry case, detachment is due to a sudden rise in the radiated power in the outer leg and main chamber SOL (just above the outer divertor leg entrance). Figures 5-25(A, B) show that this is due to an increase in radiation near and above the X-point at the outer divertor entrance. In case B, there is still some radiation near the outer target, but when the nitrogen fraction is increased to 4% in figure 5-25(C), the peak radiated power density is in a

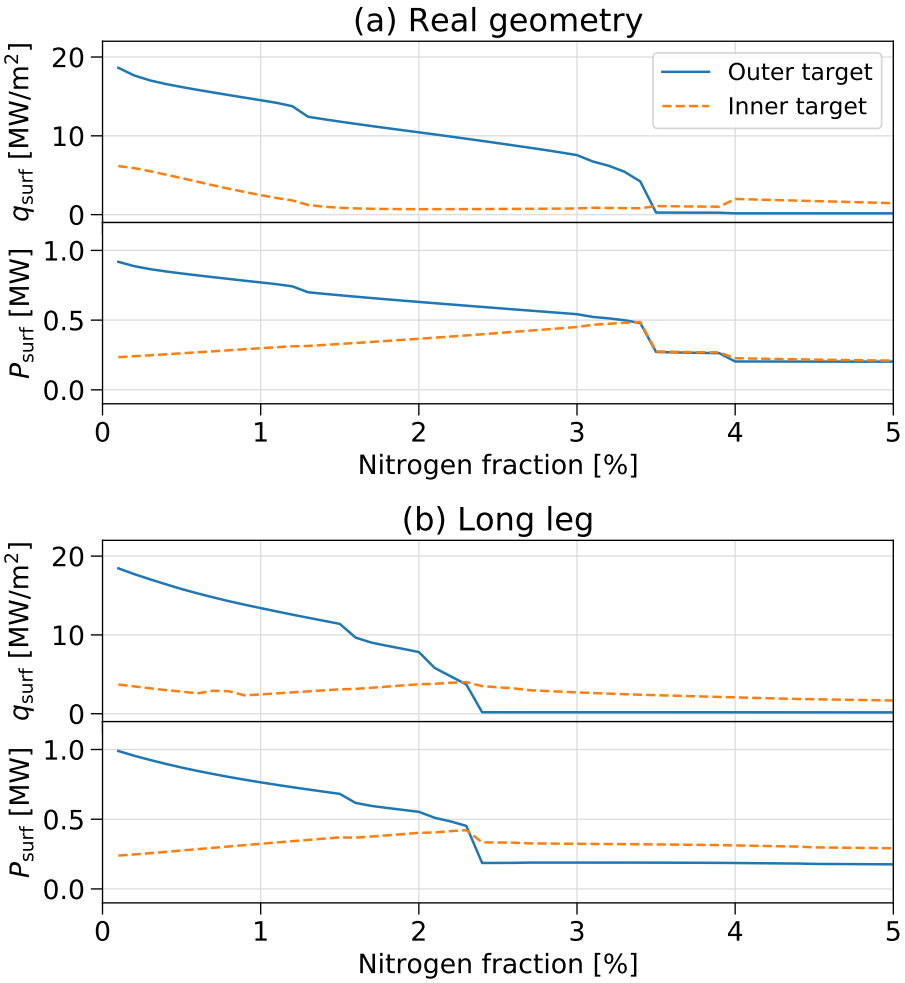

Figure 5-23: The heat flux at the strike-point and total power to the inner and outer target surfaces for cases with drifts enabled in (a) the real C-Mod geometry, and (b) the long outer divertor leg.

cell well above the X-point, and there is very little radiation along the outer divertor leg near the separatrix. The transition from B to C is also when the neutral to ion density ratio decreases markedly in figure 5-22—the ion and neutral density both decrease, but the neutral density decreases more. Case C appears to be in a slightly different detachment regime compared to case B (the total radiated power does not increase very significantly), and it does not appear to be a MARFE, as the highly radiating volume above the X-point is still outside the separatrix.

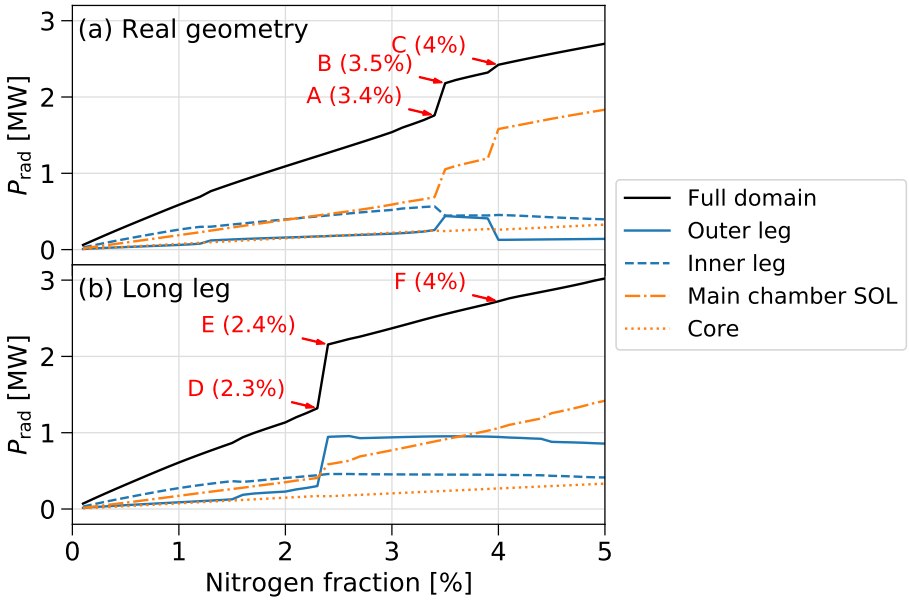

Figure 5-24: Total power due to impurity radiation in various parts of the simulation domain as a function of nitrogen fraction for (a) the real geometry and (b) the long leg geometry. The impurity radiation over the grid is shown in figure 5-25 for the points marked A, B, C, D, E, F.

In both the real geometry and long leg cases in figure 5-24, before and after the sudden rise in total radiated power due to detachment, the total radiated power rises gradually. This is due to a gradual increase in radiated power in the main chamber SOL. Before the detachment jump in radiated power, the radiated power in the inner leg also appears to be increase gradually. In the long leg geometry, when the outer leg detaches, the high radiated power in the outer leg remains approximately constant while the radiation front moves further up the leg as the nitrogen fraction is increased to 4% (figure 5-25(E, F)). This is different from the real geometry case, where the

radiation in the outer leg decreases significantly as the radiation front moves to above the X-point (figure 5-25(C)). Having the region of strong radiation in the divertor leg rather than the main chamber is desirable in order to avoid MARFEs, so this is another advantage of the long-leg configuration.

The jump in radiated power due to detachment can be seen in figure 5-24 to not only occur at lower nitrogen fraction in the long leg case compared to the real geometry case, but also to be a much larger jump in power than in the real geometry case. This is likely due to the greater volume of the outer leg and greater parallel distance between the X-point and outer target in the long-leg case.

The dependence of the radiated power density on the poloidal position and the impurity fraction are visualized simultaneously in figure 5-26. The radiated power density is averaged at each poloidal index over the cells at that index in the SOL, ignoring the core and PF regions as they would result in unusual V-shaped averaging volumes due to the non-orthogonal grids. Figure 5-26(a) shows that the C-Mod real geometry case really does appear to undergo two detachment transitions. Before the first transition at 3.5% nitrogen, the radiation front makes its way up the inner leg toward the X-point, and radiation in the outer leg remains fixed in position but increases in power density. After the transition at 3.5% nitrogen, the power density in the inner divertor leg drops while the power density between inner divertor entrance and the inner midplane increases. The radiation front that was around halfway between the X-point and outer target also moves up to the X-point. In the second transition at 4% nitrogen, the regions of highest radiated power density move from at or just below the X-point to just above the X-point on both the inner and outer target sides. Interestingly, the radiating region between the X-point and inner midplane also appears to move further up, into the region between the inner midplane and the plasma crown (top of the plasma).

Figure 5-26(b) shows that the case with the longer outer divertor leg behaves very differently. Before the transition to detachment at 2.4% nitrogen, the highly radiating region moves steadily from the inner and outer targets toward the X-point, while continuing to radiate strongly close to the target. After detachment, the highly

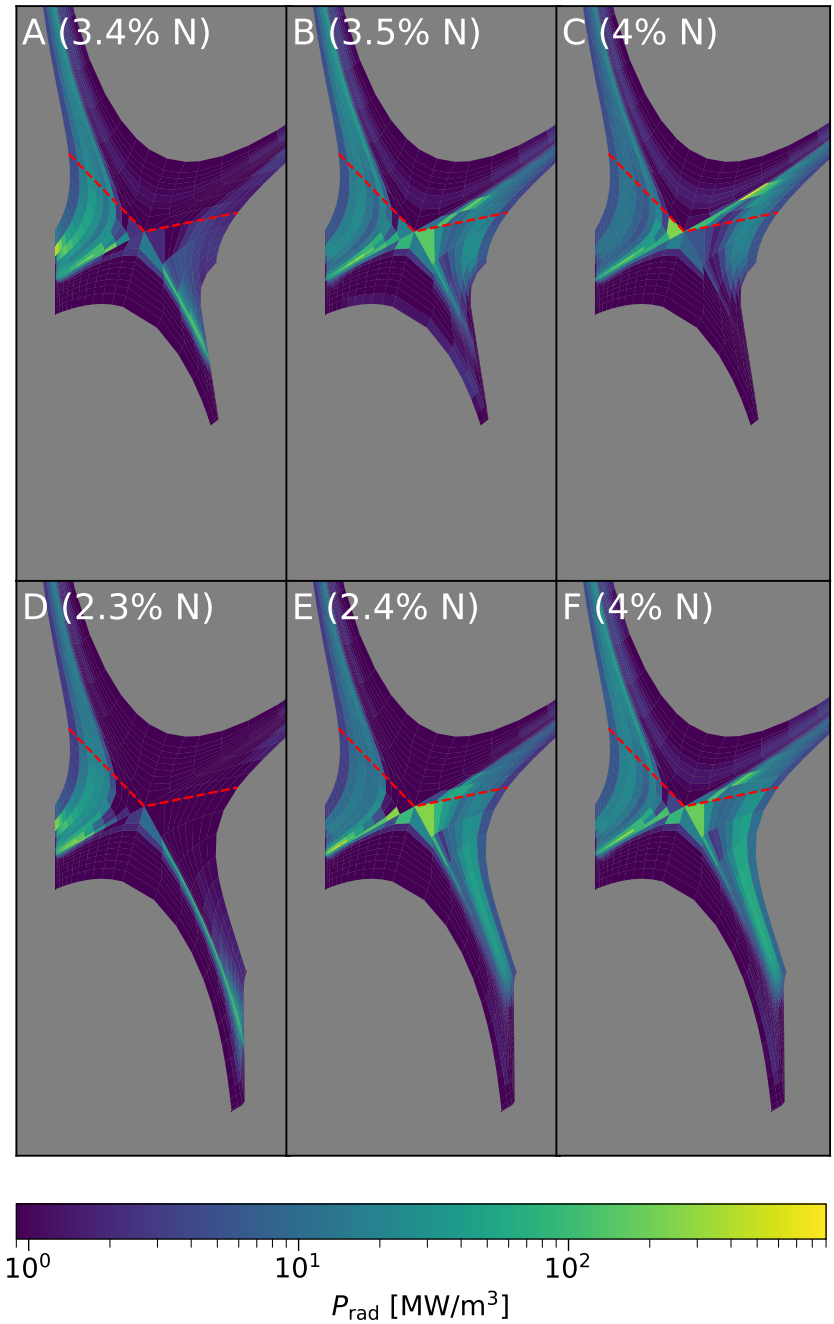

Figure 5-25: Power density due to impurity radiation over the grid for the UEDGE cases marked with points A, B, C, D, E, F in figure 5-24. The red lines show the boundary between the divertor and main chamber in the nomenclature of figure 5-24 and the locations of the X-point poloidal indices in the nomenclature of figure 5-26.

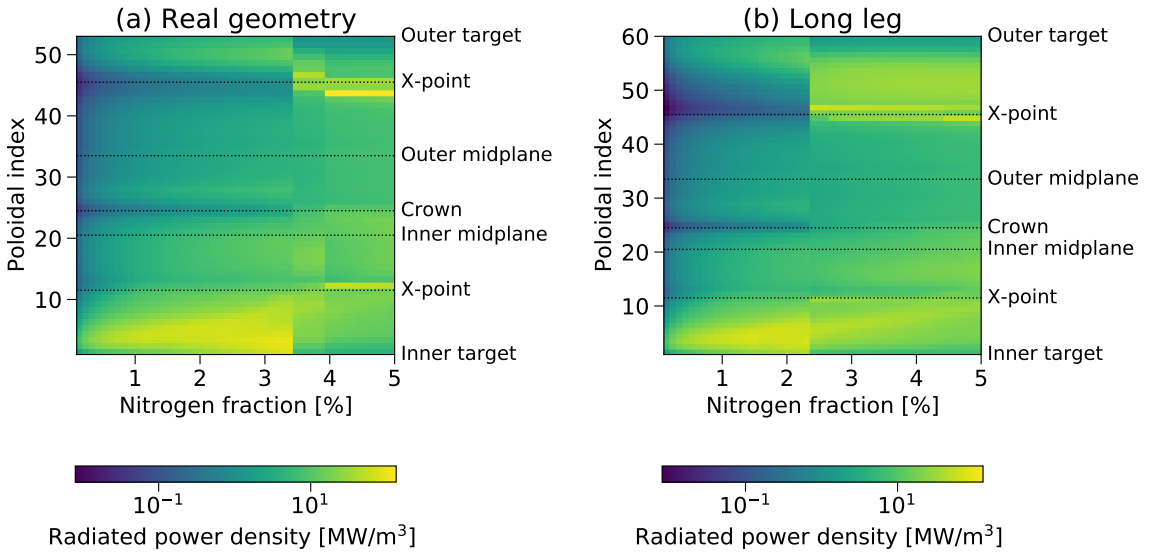

Figure 5-26: SOL-averaged impurity radiation power density for (a) the real C-Mod geometry and (b) the long-leg geometry. Only the volume outside the separatrix is considered, including in the divertor legs.

radiating region is closer to the X-point, and there is markedly less radiation just above either target. This is desirable, as a strong source of radiated power right above a divertor target could also result in challenging heat fluxes. As the nitrogen fraction is further increased after detachment, the highly radiating regions continue moving upstream, toward the X-point at the inner target and above the X-point at the outer target.

5.9 Conclusions

This effort to model a discharge in Alcator C-Mod with drifts and impurities achieves a good match to experimental midplane and target SOL measurements, and may be the first published UEDGE simulation of an advanced divertor concept modeled with drifts and impurities (SOLPS and UEDGE advanced divertor simulations without drifts include [24–28, 30, 31, 34, 35, 77], and [36] is a SOLPS simulation of an advanced divertor with drifts). This study has produced a number of important and interesting results:

- Profiles of midplane density and temperature and target heat flux can be matched

simultaneously with the iterative calculation of anomalous transport coefficients using formula 4.2.

- Drifts significantly change the detachment process in UEDGE and are therefore necessary to accurately determine a detachment threshold.
- Drifts result in a depressed temperature profile inside the separatrix in UEDGE compared to experiment, and do not improve the match to the experimental density and temperature at the divertor targets.
- Drifts allow UEDGE to better match the location of the region of peak D-α emission in C-Mod experiments in positive and negative toroidal field directions.
- Before full detachment, the total power to the inner target can increase as the impurity concentration is increased.
- The long outer leg geometry does not necessarily result in additional anomalous heat flux spreading, but enables detachment at a significantly lower impurity fraction.

Chapter 6

Modeling the SPARC tokamak

In the previous chapters, UEDGE simulations were "tuned to" and compared with actual profiles from Alcator C-Mod. This chapter details how UEDGE was used to simulate edge and divertor conditions that are foreseen in a new, possibly game-changing tokamak presently under construction: SPARC [6]. This modeling was undertaken during the design phase of the device in order to characterize attached and detached plasma conditions, informing divertor design decisions. Such studies are necessary because the device will operate at magnetic fields 1.5x larger than have ever been used in a tokamak and face extreme challenges for heat and particle exhaust. The results of this study are also published in [29].

6.1 Overview of the SPARC tokamak

The SPARC tokamak is currently being designed as a compact device with a magnetic field of 12 T targeting a fusion gain of $Q > 2$ [6]. The SPARC scenario of primary interest in this study is one for which 13 MW of external radiofrequency and ohmic heating is supplied, 20–28 MW of fusion alpha power and 113 MW of neutron power is produced, and 10–13 MW is radiated from the core. The amount of power crossing the separatrix and entering the scrape-off layer (SOL) is therefore taken to be $P_{\mathrm{SOL}} = 28$ MW at "full power" for the purpose of simulation with UEDGE. This scenario is at the L-H threshold power, though a maximum of 25 MW of external heating power

is available to provide some margin [41].

In the absence of significant dissipation in the SOL upstream, for example via radiation, the majority of the 28 MW of power into the SOL will be directed into the divertor legs, and the divertor surfaces may experience very high heat fluxes. Well-documented empirical scalings for the SOL heat flux width predict a narrow width between 0.18 and 0.4 mm, leading to an expected peak parallel heat flux greater than 10 GW/m^2 [41]. Full-power operation will be attempted with both single- and double-null equilibria. In a double-null equilibrium, power sharing between the inner and outer divertor is expected to have a ratio of 1:4 [141], resulting in a peak perpendicular heat flux of 25 MW/m^2 to the inner divertor target and 70 MW/m^2 to the outer target assuming a shallow incident field line angle and 50% radiation fraction (figure 6-1).

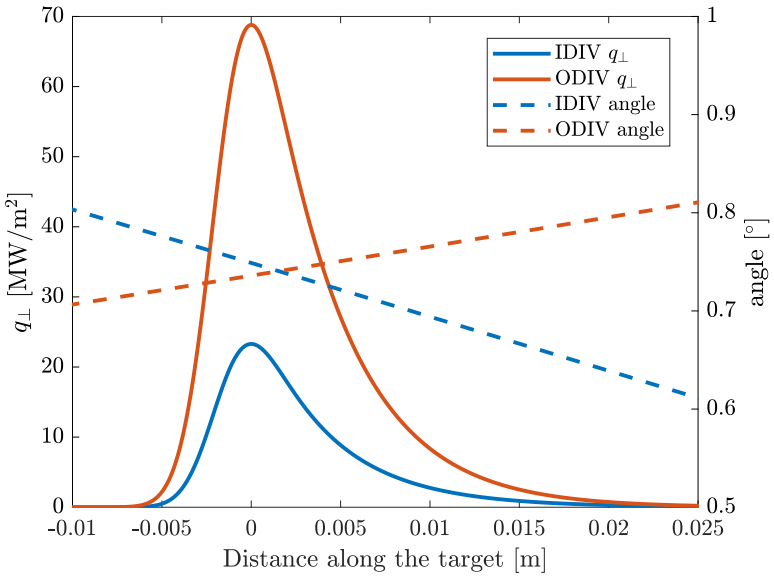

Figure 6-1: Prediction from empirical scalings of the perpendicular heat flux along the inner and outer divertor targets in a SPARC double-null configuration assuming a 50% radiation fraction. Courtesy Adam Kuang.

Due to the high heat fluxes expected in the inertially cooled SPARC divertor, the tokamak is being designed with several heat flux mitigation measures: plasma pulses will be kept short (under 10 seconds), the incident field line angles in the divertor are designed to be under 1° (assuming toroidal symmetry—fish-scaling may be required to hide leading edges), and the strike-point on each target surface will be swept at a

rate of $\sim$1 Hz over 30–40 cm of poloidal arc length [41].

Beyond these baseline strategies, SPARC will also attempt to take advantage of divertor detachment, in which interactions of plasma with neutral hydrogen and impurity atoms result in volumetric energy losses, reducing plasma momentum, heat flux, and temperature at the divertor targets. Detachment is usually induced by puffing gases containing low-Z impurity atoms such as nitrogen or neon. In SPARC, if the plasma-facing components are made of a graphite-based material, sputtered carbon atoms could cause detachment.

A previous analysis estimated the impurity density as a fraction of the main ion density required to achieve detachment in tokamaks, including a SPARC-like device. The 0-D model used empirical scalings for the heat flux width and L-H threshold power and a simple SOL radiation model, and found that for the divertor to detach in a SPARC-like device ($B_T = 12\,\mathrm{T}$, $R = 1.65\,\mathrm{m}$, $P_{\mathrm{SOL}} = 48\,\mathrm{MW}$, and an upstream density of $6 \times 10^{20}\,\mathrm{m}^{-3}$), the required impurity fraction is 11% using nitrogen, 4% using neon, and 3% using argon [142]. The SPARC design as of late 2020 had $B_T = 12.2\,\mathrm{T}$, $R = 1.85\,\mathrm{m}$, $P_{\mathrm{SOL}} = 30\,\mathrm{MW}$, and an upstream density of $1 \times 10^{20}\,\mathrm{m}^{-3}$ [6].

The estimates of the 0-D model serve as a starting point for more advanced studies that take into account the SOL geometry and plasma profiles. In this work, the UEDGE code [45] is used to examine SOL plasma dynamics and detachment in SPARC in greater detail. UEDGE has recently been used to model advanced-divertor configurations, in particular the SOL of the ADX and ARC tokamak concepts [28, 30]. Before this study, it was uncertain whether UEDGE would be able to model SPARC without issues due to the extremely small heat flux width and extremely large average plasma pressure and parallel heat flux density expected for SPARC [8, 41].

6.2 SPARC UEDGE simulation setup

6.2.1 Equilibrium and grid geometry

The SPARC SOL is modeled in a double-null equilibrium assuming up-down symmetry for geometry and physics (figure 6-2). The radial extent of the domain is $\Psi_N \approx 0.98 - 1.04$ in units of standard normalized poloidal magnetic flux, and grid cells are aligned with the flux surfaces. In the simplified model considered here, the target plates are normal to flux surfaces at the strike points, while plates tilted at a shallow angle are planned in the actual SPARC design (a factor of 0.39 at the inboard target separatrix and 0.16 at the outer target separatrix can be applied to convert from the perpendicular heat flux density in the UEDGE geometry to the perpendicular heat flux density in the SPARC design). The grid target surfaces are angled in the far SOL and private flux region in order to alleviate a numerical performance issue with corner cells. The much more open divertor in the UEDGE grid geometry compared to the real SPARC design is a large source of uncertainty due to neutral baffling effects [143].

6.2.2 UEDGE physics model

UEDGE is used in this study to solve for the plasma and neutral densities n_i and n_n (plasma quasineutrality is assumed), electron and ion/neutral temperatures T_e and $T_{i,n}$, and parallel velocities $u_{\parallel i}$ and $u_{\parallel n}$. No single-particle drifts or plasma potential effects are included in this study, due to the up-down symmetry of the setup. The impurity used in this study is carbon, with a concentration specified as a fixed fraction of the main ion density and radiation rates obtained from a non-equilibrium coronal model assuming an impurity lifetime of 1 second (the impurity lifetime setting was found in this study to cause no noticeable change in the UEDGE solutions unless set to a value less than 10 milliseconds). A fluid model is used for the neutral atoms, as the neutral mean free path is expected to be small in the SPARC divertor (in a typical simulation, the neutral charge-exchange mean free path is found in most of

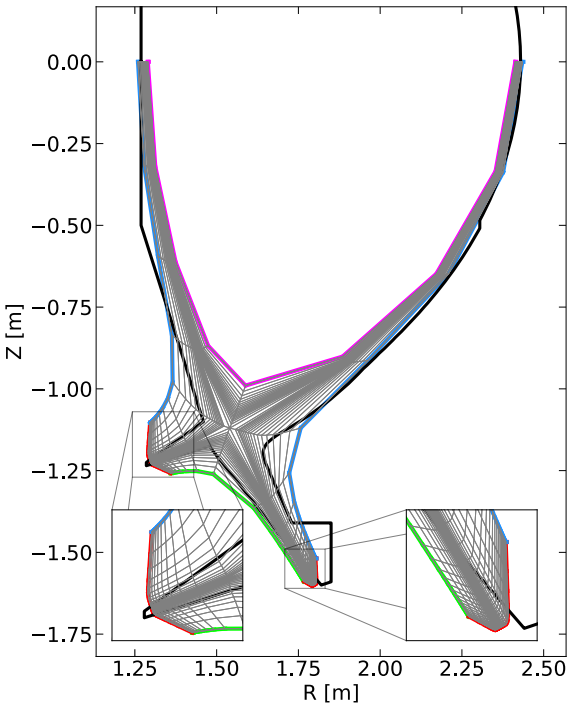

Figure 6-2: The 2D axisymmetric grid used in this study is shown in gray, and the SPARC first wall geometry is shown in black (the first wall geometry is not included in the simulation). The colored lines are the core boundary (magenta), side wall boundaries (blue), private flux region boundary (green) and target plate boundaries (red).

the divertor volume to be less than 1 centimeter, which is small compared to any connection length). The fluid neutral model in UEDGE includes inertial effects in the direction parallel to B, to account for strong parallel flows.

6.2.3 Boundary conditions

The boundary conditions at the core interface are a fixed ion density, zero gradient in parallel velocity, zero neutral flux, and a fixed power divided equally between the ions and electrons. At the target plate boundaries, $v_{\parallel} = c_s$, and the sheath energy transmission coefficients are $\gamma_e = 4$ and $\gamma_i = 2.5$ (informed by kinetic simulations). Sputtering effects are not included. At the side wall and private flux wall boundaries, the ion density and electron and ion temperature are extrapolated ($\partial^2/\partial r^2 = 0$), with a minimum temperature limit of 0.1 eV. The ion recycling coefficient for all side walls and targets is 1 (appropriate for modeling an experiment in steady state [28]), and the neutral albedo is 1 on all side walls and targets. This means no pumping effects are included in the model. Finally, a heat flux limiter value of 0.21 is used as the fraction of the free-streaming flux that the maximum thermal conduction is limited to. This value is informed by kinetic-fluid modeling [87] and is found to improve agreement between simulation and experiment in Alcator C-Mod [83].

6.2.4 Base case setup

The cross-field transport coefficients in UEDGE were tuned to match several parameters predicted for SPARC using empirical scalings, summarized in table 6.1. The transport coefficients satisfying these interrelated constraints were a particle diffusivity of $D = 0.1\,\mathrm{m}^2/\mathrm{s}$ and the spatially varying convective velocity v_{conv} and thermal diffusivity $\chi_{e,i}$ shown in figure 6-3. These values were tuned using a case with $P_{\mathrm{SOL}} = 10\,\mathrm{MW}$ in the full domain and no impurity. The spatial profile of v_{conv} is informed by experiment [144]. The spatial profile of $\chi_{e,i}$ reflects assumptions of reduced energy transport on the high-field side and a transport barrier on the low-field side that strongly affects the outer target heat flux width. The heat flux width in each

	Expected in SPARC	Achieved in UEDGE	UEDGE controlling variables
Midplane separatrix density	$1 \times 10^{20}\,\mathrm{m}^{-3}$ [145]	$0.7 \times 10^{20}\,\mathrm{m}^{-3}$	D, v_{conv}, n_{core}
Heat flux width λ_q	0.18–0.4 mm [41]	0.23 mm	D, v_{conv}, $\chi_{e,i}$
Heat flux width spreading factor S	$0.5\lambda_q$ [41]	$0.7\lambda_q$	D, v_{conv}, $\chi_{e,i}$
Inner/outer divertor power sharing	1:4 [141]	1:4	D, v_{conv}, $\chi_{e,i}$

Table 6.1: Parameters predicted for SPARC and targeted in UEDGE.

simulation was measured by fitting a simple exponential curve to the parallel heat flux density at the outer side of the X-point mapped to the outer midplane, and the heat flux spreading factor was obtained from an Eich fit [7] to the total surface heat flux density at the outer target mapped to the outer midplane. The inner/outer divertor power sharing was calculated by comparing the total power crossing the separatrix on the inboard side to that crossing the separatrix on the outer side.

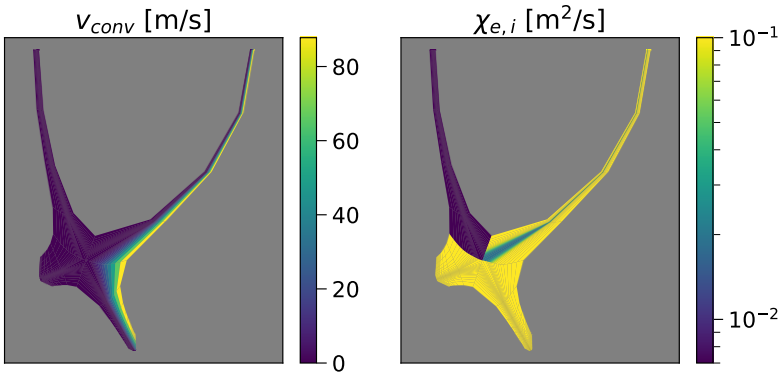

Figure 6-3: Spatially varying profiles of convective velocity v_{conv} and thermal diffusivity $\chi_{e,i}$ used in this study.

The case with $P_{\mathrm{SOL}} = 10\,\mathrm{MW}$ and no impurity, which was used to tune the transport coefficients, has suitable profiles of parallel heat flux density (due to convection and conduction of electrons, ions, and neutrals) at the outer divertor entrance, as well as midplane profiles of T_i, T_e, n_i, and n_n (figure 6-4). The portions of the profiles inside the separatrix are not fit to any particular targets and may not be represen-

tative of conditions in that region. One interesting feature is the high ion density in the far SOL, where the particle balance is dominated by a radial transport sink and an ionization source at the wall. A flat, high-density "shoulder" is sometimes seen in experiment due to convective radial transport [146], but the high and rising density in the far SOL of these UEDGE simulations appears to be an artifact of the recycling boundary condition that provides a large source of neutrals to be ionized.

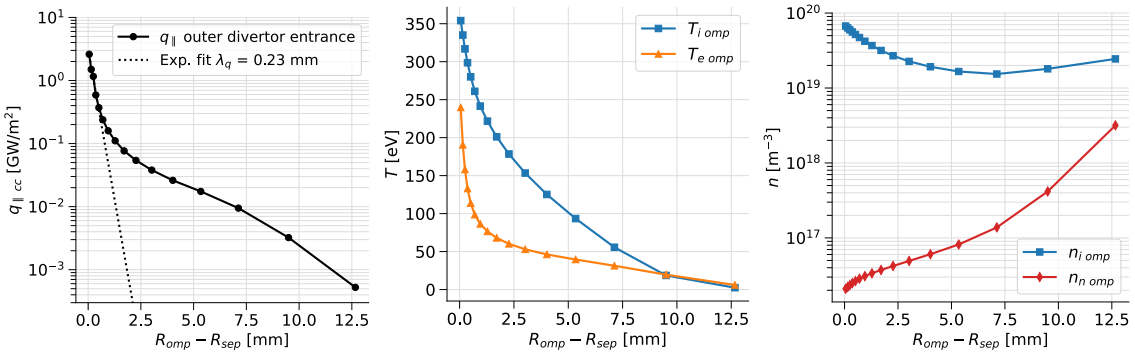

(a) (b) (c)

Figure 6-4: For the case with $P_{\mathrm{SOL}} = 10\,\mathrm{MW}$ and 0% carbon fraction, (a) the parallel heat flux density due to convected and conducted power at the outer divertor leg entrance (solid line) and a fit to the data with a simple exponential curve (dotted line), (b) temperature of the ions (blue) and electrons (orange) at the outer midplane, and (c) density of the ions (blue) and neutrals (red) at the outer midplane.

6.3 Survey of detachment access conditions

For computational efficiency, the simulations shown in this study are evolved from sequential changes in carbon fraction and input power starting from a single "ancestor" solution rather than each starting from UEDGE's default profiles of density, temperature, and parallel velocity. The "ancestor" solution was started on a crude grid with the transport coefficients set to large values, then changed to the grid and transport coefficients shown in figure 6-3. It is important to consider the history of each simulation because solutions can bifurcate [30, 75]. The final result of a UEDGE run depends on both the setup parameters and the starting solution. For example, the case with both legs detached at $P_{\mathrm{SOL}} = 28\,\mathrm{MW}$ and 1% carbon is obtained start-

ing from the case with only the inner leg detached at $P_{\mathrm{SOL}} = 28\,\mathrm{MW}$ and 1% carbon by lowering the power to 16 MW and raising the carbon fraction to 1.4% (at which point both legs are detached) then returning to $P_{\mathrm{SOL}} = 28\,\mathrm{MW}$ and 1% carbon while remaining in this new detachment regime. Notably, this means that the UEDGE model used in this study cannot be used to predict a detachment threshold.

6.3.1 Scan of power and carbon fraction

The SOL input power and carbon fraction were varied in order to characterize a wide range of attached and detached target conditions. One scan began from a solution with the inner target detached and the outer target attached (circles in figure 6-5(a)), while the second scan began from the solution with both targets detached (diamonds in figure 6-5(a)). A large region of overlap can be seen (diamonds superimposed on circles), where both of the bifurcated solutions are possible at identical P_{SOL} and carbon fraction. The scans were started from an outer-attached and an outer-detached case at $P_{\mathrm{SOL}} = 28\,\mathrm{MW}$ and 1% carbon fraction. The power was decreased in steps of 4 MW, and the carbon fraction was raised and lowered in steps of 0.1%. The outer-detached case at $P_{\mathrm{SOL}} = 28\,\mathrm{MW}$ and 1% carbon fraction originated from a case following the transition of an outer-attached case at $P_{\mathrm{SOL}} = 16\,\mathrm{MW}$: when the carbon impurity fraction was raised from 1.3% to 1.4%, there was a sudden drop in the target temperature, total pressure, heat flux density, and ratio of ion to neutral density at the outer target. These values remained low over the large range of P_{SOL} and carbon fraction values shown by the diamonds in figure 6-5(a).

Simulations with lower or higher carbon fraction than those shown by either scan in the figure either failed to converge or transitioned to a different detachment state and are not shown when redundant (e.g. if during the attached scan, a case became detached at high carbon fraction, but a case in the detached scan had also converged at the same power and impurity fraction, only a diamond would be shown). Convergence failures were due to certain cells at the divertor targets reaching negative ion densities because of numerical issues in balancing large fluxes in and out of the cells. These convergence failures arise at low and high carbon fraction, where changes in de-

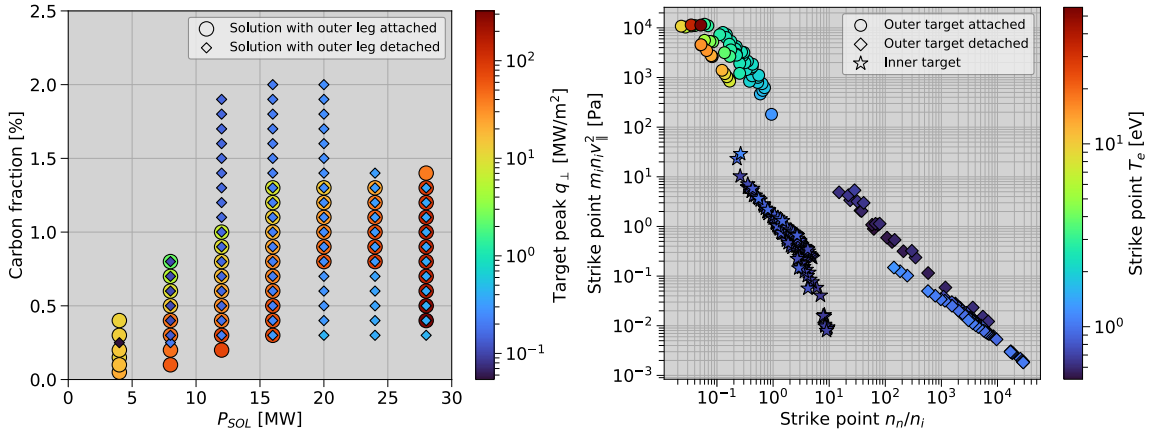

(a) (b)

Figure 6-5: (a) Peak total heat flux density perpendicular to the outer target (due to convection, conduction, ion parallel kinetic energy, surface recombination, and radiation) as a function of the SOL input power and carbon fraction. (b) Key metrics of detachment measured at the strike points: ratio of neutral to ion density, dynamic pressure, and electron temperature.

tachment regime or radiative collapse might be expected, but it is unknown whether the large fluxes at the target cells that cause the numerical issues are physically justified or themselves also due to numerical issues. In light of this uncertainty, these scans can be viewed as a limited window indicating conditions under which detached (or attached) conditions can exist in SPARC. Of course, the existence of detached regimes is of greater interest for power handling considerations. However, the upper and lower carbon fraction limits of the scans cannot yet indicate the true operating window for each detachment regime.

Key metrics of detachment are shown in figure 6-5(b) for cases in the scan of power and impurity fraction. The dynamic pressure $m_i n_i v_\parallel^2$ at the strike point serves as an indicator of ion momentum removal, which is one aspect of total pressure removal along a field line (due to neutral interactions, radial convection, and viscous dissipation [147]), a key marker of detachment [9]. The ratio of neutral density to ion density characterizes plasma particle loss, and the strike point temperature and peak $q_\perp$ can be used to assess energy detachment. The correlations between the parameters in figure 6-5(b) show that momentum removal and energy removal go hand in hand.

Attached and detached target conditions have non-overlapping ranges of target peak $q_\perp$ and strike point dynamic pressure but have some overlap in the ranges of strike point n_n/n_i and T_e. The highest values of n_n/n_i around 10^4 are due to very low ion density rather than very high neutral density. The conditions at the inner target (stars in figure 6-5(b), which are from both sets of cases with the outer leg attached/detached) are similar to those at the detached outer target, indicating that the inner target remains detached throughout the scans. One notable difference between the inner target and detached outer target conditions is in n_n/n_i, which is due to higher average n_i at the inner strike point when the outer leg is detached.

Importantly for the plasma-facing components, the detached targets all have peak $q_\perp < 1\,\mathrm{MW/m^2}$, not including factors coming from the real geometry with tilted target plates. Of course, the scan also shows that lowering P_{SOL}, for example through increased core radiation, can lower the peak $q_\perp$. Finally, the peak heat flux density to the targets can vary significantly in the attached regime for the same P_{SOL}. For example, in the case at full power with the inner leg detached, the peak $q_\perp$ at the outer target is $324\,\mathrm{MW/m^2}$ at 0.4% carbon but drops to $39\,\mathrm{MW/m^2}$ at 1.4% carbon, without having fully transitioned to a detached outer leg.

6.3.2 Comparison of attached and detached target conditions

When the outer leg is attached at full power and 1% carbon fraction, the outer target has a peak $q_\perp \approx 63\,\mathrm{MW/m^2}$ due to convection and conduction of electrons, ions, and neutrals, $T_{e,i\,\mathrm{max}} \approx 4\,\mathrm{eV}$, $n_{i\,\mathrm{max}} \approx 10^{22}\,\mathrm{m^{-3}}$, and $n_{n\,\mathrm{max}} \approx 10^{21}\,\mathrm{m^{-3}}$ (figure 6-6). The power delivered to the target due to surface recombination (not shown) is similar in profile and magnitude to the convected and conducted heat flux density, and the power due to impurity radiation reaches a peak of $q_\perp \approx 11\,\mathrm{MW/m^2}$, as the volume just upstream of the strike-point is highly radiating (figure 6-7(a)). A total of 4.2 MW of power is lost due to impurity radiation in the cells near the X-point, while 5.2 MW is radiated in the volume of the outer leg and only 0.12 MW is radiated in the inner leg. This difference in radiation power loss between the legs is likely due to a difference in temperature, since the maximum temperature is 2.5 eV in the volume of the inner

leg and 100 eV in the volume of the outer leg, and the peak in the radiated power cooling rate coefficient for carbon is about 10 eV [148].

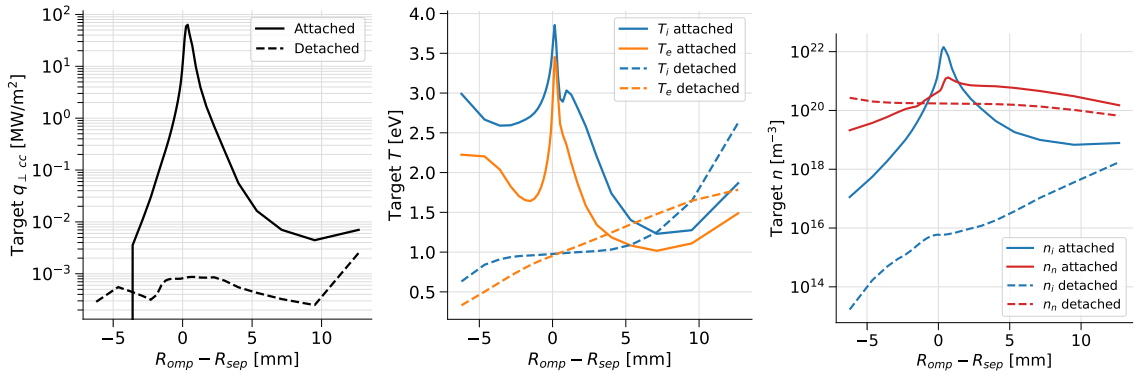

(a) (b) (c)

Figure 6-6: Comparison of plasma parameters at the outer target mapped to the outer midplane for the attached case (solid lines) and detached case (dashed lines) at $P_{\mathrm{SOL}} = 28\,\mathrm{MW}$ and 1% carbon fraction, showing (a) the convected and conducted heat flux density perpendicular to the target, (b) the temperature of the ions (blue) and electrons (orange), and (c) the density of the ions (blue) and neutrals (red).

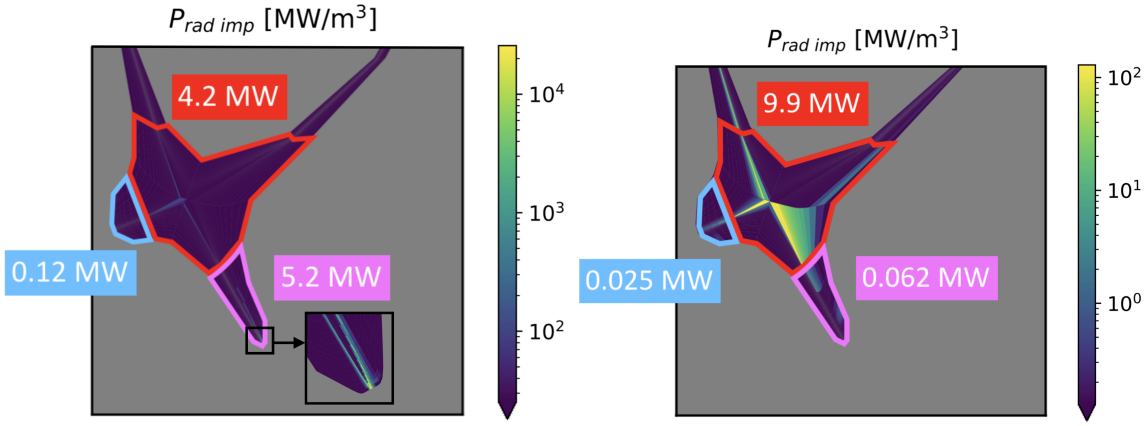

(a) (b)

Figure 6-7: Carbon impurity radiation at $P_{\mathrm{SOL}} = 28\,\mathrm{MW}$ and 1% carbon fraction in (a) the case with the inner leg detached and outer leg attached and (b) the case with both legs detached. The total power loss due to impurity radiation is indicated in red for cells adjacent to the X-point, blue for cells in the inner divertor leg, and magenta for cells in the outer divertor leg.

The solution with a detached outer leg at full power and 1% carbon fraction shows a peak $q_\perp \approx 2.5\,\mathrm{kW/m^2}$ due to convection and conduction, $T_{e,i\,\max} \approx 2.5\,\mathrm{eV}$,

$n_{i\,\max} \approx 10^{18}\,\mathrm{m}^{-3}$, and $n_{n\,\max} \approx 2 \times 10^{20}\,\mathrm{m}^{-3}$ (figure 6-6). In this scenario, impurity radiation produces a peak of only $q_\perp \approx 0.32\,\mathrm{MW/m^2}$ at the outer target, as 9.9 MW of power is lost due to radiation near the X-point and only negligible amounts are lost in the volume of either leg (figure 6-7(b)). Core performance is unaffected, however, as only 0.12 MW of power is lost to radiation inside the separatrix. In both cases with and without detachment of the outer leg, the total power lost due to deuterium radiation is 1–1.4 MW from ionization and 1.4–1.6 MW from recombination.

6.3.3 Sensitivity to boundary conditions

In order to determine the sensitivity of the solutions to various aspects of the simulation setup, certain assumptions were varied to note the effect on the convected and conducted heat flux density at the outer target (figure 6-8(a)). The original case, with an attached outer leg, had extrapolated values of temperature T_i in the range of 0.1–4 eV for the common flux region radial boundary and 1–5 eV for the private flux region boundary. When the extrapolation boundary conditions were all changed to gradient-length type with an infinite gradient length, the outer leg became fully detached. This result held for gradient lengths as low as 1 centimeter. Changing from the extrapolation boundary condition to a fixed value similarly upended the original result. Setting a fixed boundary value of 2 eV for the ion temperature on the radial boundary of the common flux region caused a large increase in heat flux to the outer leg, while doing so instead on the private flux region boundary had the opposite effect, causing the outer leg to completely detach. For the private flux boundary, a threshold was observed: the outer leg would detach if the boundary temperature was fixed to less than 2.3 eV and would remain attached if the boundary temperature was fixed to a higher value (while still having a noticeable effect on the peak heat flux density). This sensitivity to different values of the fixed boundary condition shows the importance of the extrapolation boundary conditions in allowing the absolute value and gradient to float.

The outer strike plate geometry was also found to have a large impact on the overall solution (figure 6-8(a,b)) at $P_{\mathrm{SOL}} = 28\,\mathrm{MW}$ and 1% carbon fraction. A grid

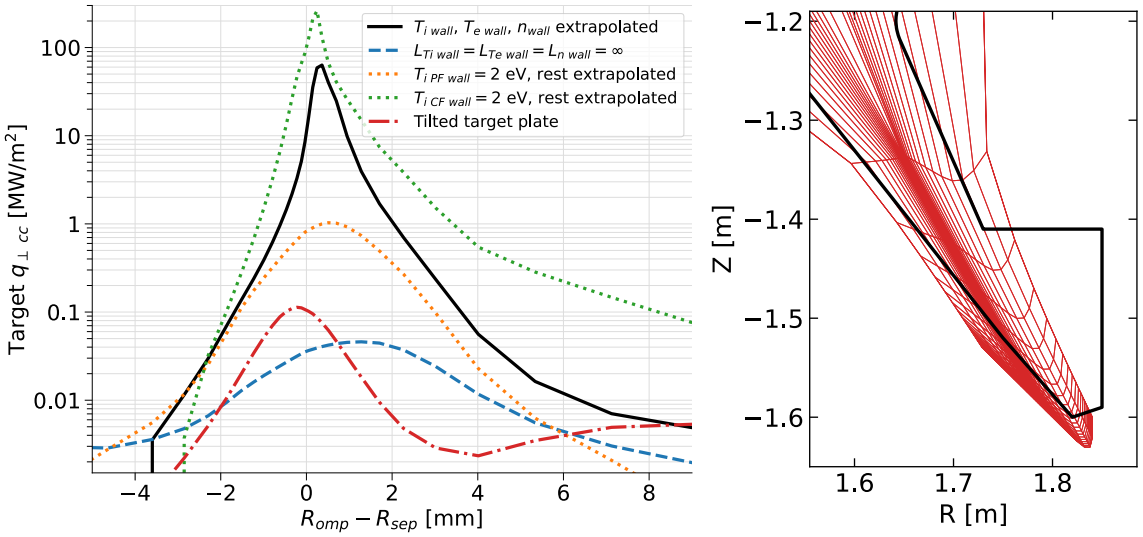

(a) (b)

Figure 6-8: (a) Heat flux density due to convection and conduction perpendicular to the outer target mapped to the outer midplane. The original case with $P_{\mathrm{SOL}} = 28\,\mathrm{MW}$ and 1% carbon fraction is shown in black and has extrapolated density and temperature values on the radial boundaries. The dashed blue line shows the result of setting all radial boundary values based on an infinite gradient length ($L_T = T/\nabla T = \infty$). The dotted orange line shows the result of changing the ion temperature boundary condition on the private flux region radial boundary to be fixed at 2 eV rather than extrapolated. The dotted green line shows the result of fixing the ion temperature to 2 eV on the common flux region radial boundary. The red dash-dotted line shows the result of changing the outer target plate geometry to that shown in subfigure (b). (b) (Red) Detail of the UEDGE mesh with an outer target geometry better matching the tilt of the as-designed SPARC divertor geometry (black).

was produced in which the outer divertor strike plate was tilted to more closely match the as-designed SPARC divertor surfaces. The new target geometry still does not match the SPARC design perfectly due to grid generator issues encountered when attempting to further increase fidelity. There are also fundamental limitations in UEDGE which make it impossible to include the shadowed corner volume in the bottom right. The new grid target plate has a slightly less grazing angle than the SPARC design, with slopes differing by 5.5° in the poloidal plane. The incident field line angle at the separatrix is 1.66° in the new grid (compared to 6.36° in the grid shown in figure 6-2 used in the rest of this study), which is close to the target value of 1° and less than the 2° upper limit considered in the SPARC design [41]. In the simulation with the new grid, a factor of 3.9 reduction in the peak heat flux density at the outer target was expected due to the increase in surface area at the strike plate near the separatrix, but a much larger degree of power detachment is instead observed: the peak heat flux density is three orders of magnitude smaller than in the case where the plate was not tilted. At the outer target separatrix, the electron temperature is 1.2 eV, and the ratio of neutral to ion density is 4.8. These values are similar to those of the detached inner target, but the ratio of neutral to ion density is lower than that at the outer target in cases where the outer leg is fully detached (figure 6-5). In light of these results, the grid with non-tilted target plates that was used throughout this work appears to overestimate the carbon fraction required to detach, though the present study cannot predict absolute detachment thresholds that would apply to the experiment. Finally, it must be noted that there are still differences in baffling between the real SPARC geometry and the grid with tilted targets that will influence the absolute thresholds.

In all cases where the boundary conditions were changed or the target plate was tilted, the heat flux width measured at the outer divertor entrance remained in the range of 0.2–0.3 millimeters. While the degree of detachment changes significantly with the boundary conditions, it is reassuring that the heat flux width does not.

6.3.4 Sensitivity to the neutral fraction

In addition to the carbon fraction, the neutral fraction is an important factor in simulation results. The neutral fraction is defined here as the total number of neutrals in the full domain divided by the total number of ions. A case at $P_{\mathrm{SOL}} = 10\,\mathrm{MW}$ and 0% carbon with both legs attached has a ∼5% neutral fraction. At $P_{\mathrm{SOL}} = 28\,\mathrm{MW}$ and 1% carbon fraction, the case with only the inner leg detached has a neutral fraction of ∼10%, and the case with both legs detached has a neutral fraction of ∼20%. In order to determine whether neutral sources or sinks would have a significant effect on the $P_{\mathrm{SOL}} = 28\,\mathrm{MW}$ cases, a neutral pumping/puffing surface was defined on the outer leg common flux region boundary, with user-specified neutral throughput. The neutral pumping or puffing rate can change the neutral fraction by a few percent before solutions begin to have trouble converging (figure 6-9(a)). Raising the neutral fraction results in a lower peak convected and conducted heat flux density on the outer target (figure 6-9(b)). This trend holds when both legs are detached and when only the inner leg is detached. For the case with only the inner leg detached, the fact that the highest pumping rate results in a neutral fraction around 5% might lead one to expect that the inner leg would reattach, however it remains detached. The neutral fraction therefore does not perfectly determine each detachment regime, but it may partially explain why different solutions are possible at the same P_{SOL} and carbon fraction.

6.3.5 Comparison to SOLPS

SOLPS-ITER [149] simulations of SPARC [150] have been developed alongside UEDGE ones in a parallel, independent effort. The SOLPS simulations use more sophisticated neutral and impurity models and a more realistic geometry, while the UEDGE cases are simpler in most respects. The UEDGE setup has been convenient for large parameter scans like the ones in this study, and the more detailed SOLPS cases can be useful to roughly check the validity of certain simplifying assumptions in UEDGE. Due to the large differences in setup between the codes, this comparison cannot serve

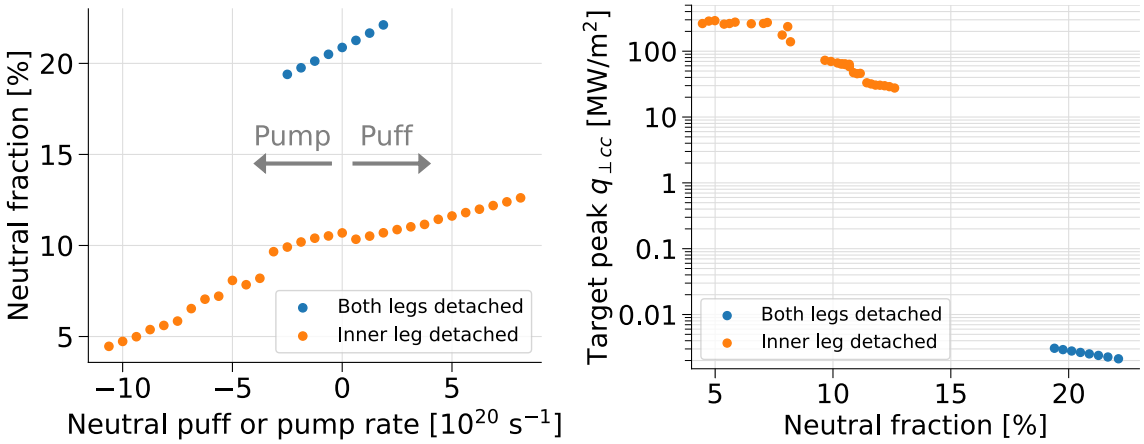

(a) (b)

Figure 6-9: All cases have $P_{\mathrm{SOL}} = 28\,\mathrm{MW}$ and 1% carbon fraction. (a) The total neutral fraction as a function of the neutral puff or pump rate in the outer leg. (b) Peak heat flux density due to convection and conduction to the outer divertor target as a function of the total neutral fraction.

as a verification exercise. Table 6.2 summarizes the differences in setup between a UEDGE case with no pumping and the most comparable SOLPS case (found by lowering the pumping rate in the SOL volume in SOLPS). The cases have similar peak $q_{\parallel}$ and have peak densities at the outer target within a factor of 3.

The fixed carbon fraction used in UEDGE can be compared to the spatial distribution of carbon resulting from the transported impurity model with multiple charge states in the SOLPS case. In the UEDGE case, the carbon density is defined everywhere as 1% of the ion density. In the SOLPS case, the carbon released from sputtering and transported in the model results in a carbon fraction as low as 0.3% and as high as 40% in a small number of cells, with more typical values in the SOL in the range of 1–4 %, resulting in an average of 1.7% over the entire domain. The charge states of carbon that reach the highest densities in the divertor legs are C^{+} and C^{2+}, reaching peaks of $10^{20}\,\mathrm{m}^{-3}$ while other charge states have peak densities of $10^{19}\,\mathrm{m}^{-3}$ or lower. While the discrepancy in carbon fraction between SOLPS is on the order of a few percent in most of the cells, highly radiating cells near the targets can account for a large fraction of the power dissipated through impurity radiation (see figure 6-7(a)). The SOLPS impurity transport model therefore offers much more

	UEDGE	**SOLPS**
Magnetic configuration	Double null	Single null
Target plates	Not tilted	Tilted
Simulation domain	Near SOL	Near SOL (+far SOL for neutrals)
Neutral model	Fluid neutrals	Kinetic neutrals
Impurity model	Fixed fraction	Transported impurities
Pumping	No	Yes
Carbon chemical sputtering	0%	2%
Carbon fraction	1%	1.7%
Outer target peak $q_\parallel$	$0.57\,\mathrm{GW/m^2}$	$0.42\,\mathrm{GW/m^2}$
Outer target peak n_i	$1.4 \times 10^{22}\,\mathrm{m^{-3}}$	$0.57 \times 10^{22}\,\mathrm{m^{-3}}$

Table 6.2: Comparison of UEDGE and SOLPS simulations of SPARC at $P_{\mathrm{SOL}} = 28\,\mathrm{MW}$.

detail than the fixed impurity fraction model and could have a large impact on the UEDGE solutions. An impurity transport model is available in UEDGE but has so far caused convergence difficulties when enabled.

The UEDGE case uses a fluid neutral model with inertia but assumes that the neutral temperature is equal to the ion temperature everywhere. In reality, the neutral temperature could be much lower than the ion temperature near the walls before the two equilibrate through charge-exchange collisions. In the SOLPS case, the kinetic neutral model provides some indication of the variation in neutral temperature to be expected. The ratio of neutral to ion temperature ranges between 0.5–1 in most of the domain, with values close to 2 occurring in the divertor regions where the plasma temperature is low. The charge-exchange and ionization mean free paths for deuterium atoms near the Franck-Condon energy in the SOLPS case are less than 1 centimeter in most of the domain except the very far SOL where they can be greater than 1 meter. These neutral temperature and mean free path results from SOLPS indicate that the UEDGE fluid neutral model is not an egregious simplification.

Like the UEDGE case, the SOLPS case is also sensitive to neutral pumping rates, especially when the pumping rate in the outer divertor is varied. This has a large impact on $q_\parallel$ and the average carbon fraction: in the original SOLPS case, the average carbon fraction was 5% and the peak $q_\parallel$ was around $4\,\mathrm{GW/m^2}$, which changed to

1.7% and $0.57\,\mathrm{GW/m^2}$ as the pumping rate in the outer divertor was decreased. The average carbon fraction in SOLPS is more a function of the overall plasma and neutral density (which affect the carbon sputtering source) than a function of the carbon being directly pumped out. In any case, the sensitivity of both UEDGE and SOLPS to the neutral pumping rate underscores the importance of this quantity in the predictions of both codes.

6.4 Discussion

UEDGE simulations yielding detached divertor target conditions in a SPARC double-null equilibrium with $P_{\mathrm{SOL}} = 28\,\mathrm{MW}$ show markedly low target temperatures, ion densities, and heat fluxes. This result shows that planned "full-power" SPARC operation could be compatible with plasma-facing components (PFCs) even without strike-point sweeping. Peak heat flux densities from detached plasmas are typically around $q_\perp \approx 0.8\,\mathrm{MW/m^2}$, dominated by impurity radiation. Cases at "full power" with the inner leg or both legs detached are obtained with a carbon fraction between 0.3–1.4 %. This study cannot predict a definitive value of the carbon fraction required to detach due to the simplifications in the model and convergence difficulties at high and low carbon fraction.

The small carbon fraction at which detachment may be possible could have advantages and disadvantages. The detrimental effect of around 1% carbon on core performance due to increased Z_{eff} is small: a 1% carbon fraction, fully ionized, results in $Z_{\mathrm{eff}} = 1.3$, and TRANSP simulations predict that SPARC should be able to maintain $Q > 2$ up to $Z_{\mathrm{eff}} = 3.4$ [112]. The stability and control of detachment, however, are of some concern, as it may be difficult to avoid detachment if graphite is chosen as a divertor material and enough carbon is released through sputtering. Furthermore, in the regime where both legs are detached, the radiation pattern concentrated near the X-point is similar to an X-point MARFE, which can terminate the discharge [151]. Stable operation in this regime is not impossible, however, as demonstrated by experiments on the AUG tokamak with a tungsten wall and neon

impurity seeding [152].

The results of this study indicate that detachment through impurity seeding in SPARC may provide significant benefits in the divertor heat flux handling challenge. Future work is planned to refine these results by modeling realistic tilted target plates and neutral baffles, using a multi-fluid impurity model rather than the fixed-fraction model, seeding with other impurities such as neon (which would likely be used if a tungsten-based material is chosen for the plasma-facing components), and modeling electric fields, drifts, and currents. The present results will serve as starting points and points of comparison for additional UEDGE simulations of the single-null and X-point target [18] configurations that are also planned for SPARC.

6.5 Summary of key findings

Key findings from the UEDGE simulations of the SPARC boundary and divertor are summarized:

- Scenarios in which both targets are detached are likely possible even under the high power and extremely narrow heat exhaust channel conditions that are expected in SPARC—this was not known before this work was done.
- However, the attached/detached solutions do depend on "ancestor" conditions from which the simulation started, as seen in other studies [30, 75].
- The detached targets all have peak $q_\perp < 1\,\mathrm{MW/m^2}$, even without expected reductions that come from the real geometry with more tilted target plates.
- The UEDGE results are roughly similar to those obtained by a different group modeling SPARC using the SOLPS code with greater realism compared to the UEDGE simulation in several respects. The similarity of the results obtained with the different codes increases confidence in the UEDGE results.

Chapter 7

Conclusion

7.1 Summary

As research on tokamaks approaches breakeven and net fusion energy is on the horizon, it is crucial to address the heat flux handling challenge. A better understanding of this issue will make fusion power plants more resilient against accidental self-damage, and therefore more economically attractive. This study uses the valuable tools of empirical database scalings and edge simulations to better understand the heat flux width challenge in current and future tokamaks and to assess different mitigation strategies including detachment and advanced divertors. This study also attempts to bridge these different tools in a novel way by using the experimental database to verify the advantages and limitations of the chosen edge model.

Chapter 3 examines the relationship between the heat flux width and edge quantities. Relationships between λ_q and the edge pressure are observed, but a different trend is observed for H-mode compared to L/I-mode. The relationships between λ_q and edge gradients of temperature, density, and pressure are less clear. The Spitzer-Härm scaling of $\lambda_q = 2/7\,\lambda_{Te}$ is not evident. These relationships between λ_q and edge quantities/gradients were also not as clear and unified across confinement regimes as the relationship between λ_q and the average pressure. Nevertheless, this study made it possible to predict the heat flux width in SPARC and ITER based on the scaling with edge pressure in Alcator C-Mod, finding agreement with predictions using other

variables and therefore increasing confidence in the overall heat flux width predictions for these devices.

Chapter 4 details the use of UEDGE to model 75 discharges in the C-Mod heat flux width database in an automated manner. This is a significant achievement because UEDGE cases can be difficult to reliably converge (past studies normally involve only a handful of cases) and UEDGE cases greatly augment the available data for each discharge in the database, enabling new studies of SOL dynamics over a wide range of conditions. By modeling a large number of discharges, this study verified that UEDGE was able to replicate the experimental scaling of λ_q after algorithmically setting the transport coefficients so that the midplane profiles of $n_e(r)$ and $T_e(r)$ were matched, albeit while overestimating experimental λ_q by a factor of $\sim$1.8. This demonstrates that UEDGE can be reliably used to model experimental discharges with simultaneous matching (to an extent) of λ_q and midplane profiles, without a large number of custom settings applied ad-hoc for each discharge. The source of the factor 1.8 discrepancy is as yet not fully understood, but further study could lead to more robust modeling with UEDGE. This study also investigates the impact of certain model settings on the agreement between the UEDGE and experimental values of λ_q. Including drift effects in UEDGE results in a better match of the experimental power balance between the inner and outer divertor targets with that found in the simulation, but makes UEDGE estimates of λ_q vary wildly. Disabling flux limits results in slightly better agreement between the UEDGE and experimental λ_q values. The overestimation of λ_q and the overall negative impact of including drift effects indicate that as yet, UEDGE does not fully capture the physics of the SOL in C-Mod. While this may seem a disappointing observation to the modeling community, it is an important realization going forward. Nevertheless, this chapter bridges experimental database analysis and edge simulation in a novel way that provides insights into the credibility and generality of the UEDGE model and provides a path forward to improve the accuracy of the model by benchmarking against experiment.

Chapter 5 uses the UEDGE model verified in chapter 4 to study a particular C-Mod high-performance attached H-mode discharge in depth. The UEDGE simulation

has excellent agreement with the experimental SOL midplane profiles and with the heat flux profile at the outer target. Furthermore, single-particle drift effects are enabled at full strength, which is often a challenging feat in UEDGE. This case with a strong experimental basis is then used to investigate the advantages of a common feature in advanced divertors: increased length of the outer leg. It is found that a longer leg enables detachment at a lower impurity fraction than that of the non-extended leg and keeps the detachment front further away from the main plasma. Drift effects are also found to have a significant impact on the detachment process. Thus this chapter uses modeling to predict what might have been needed to detach this plasma if C-mod had had a ∼2x longer leg. This chapter also bridges the UEDGE modeling of C-Mod, which has an abundance of experimental data, to the UEDGE modeling of SPARC, which has a long outer leg but no experimental data.

Chapter 6 uses UEDGE to model the SPARC tokamak, finding that detachment should be possible even at the high power and small λ_q expected in SPARC. The possibility of detachment in SPARC and the capability of UEDGE to model plasma conditions in SPARC were previously unknown. Detachment is found to significantly reduce the peak heat flux to the targets, indicating that this is a valid strategy to deal with high heat fluxes even in next-generation devices.

7.2 Physics roadmap

Data from an AUG database clearly obey the relationship of $\lambda_q = 2/7\,\lambda_{Te}$ expected in the high-collisionality Spitzer-Härm regime [91]. Data in the C-Mod database do not clearly adhere to this trend (figure 3-8(c)), but appear to follow it when modeled with UEDGE (figure 4-14(c)). The difference in experimental results between AUG and C-Mod could be due to either error in measurement or different heat transport physics, e.g. differences in the ion channel, which is measured in neither device. It is also possible that some of the C-Mod discharges are not deep enough in the Spitzer-Härm regime. The trend in the C-Mod UEDGE simulations, which somewhat follows the Spitzer-Härm relationship, may simply mean that most of the heat flux in UEDGE is

due to conduction, and that the included flux limiting and convective heat flux have little impact.

The steps below detail a roadmap to understanding the possibly different SOL physics in C-Mod and AUG:

1. Recalculate the temperature decay length λ_{Te} in C-Mod using the same method as in AUG, by fitting an exponential decay function to the raw Thomson scattering data about the separatrix [91], and observe whether this reveals a trend of $\lambda_q = 2/7\,\lambda_{Te}$.

2. Investigate scalings with turbulence parameters in C-Mod, as was done with the AUG database [101].

3. Compare the SOL collisionality in C-Mod and AUG. The AUG study in [91] used a subset of the data in [101] which has $2 < \nu^*_{\mathrm{e\,SOL}} < 50$, while the C-Mod data has $0.6 < \nu^*_{\mathrm{e\,SOL}} < 6$. By some estimates, $\nu^*_{\mathrm{e\,SOL}} \gtrsim 100$ may be required for Spitzer-Härm heat conductivity to fully hold [125]. It is therefore possible that more of the AUG data are in the Spitzer-Härm regime, while the C-Mod data are in a more flux-limited regime.

4. Compare reciprocating probe studies of SOL density, temperature, and heat flux profiles on Alcator C-Mod [153] and AUG at similar collisionality.

5. Augment the C-Mod database with higher-collisionality discharges to see if these more clearly follow the trend of $\lambda_q = 2/7\,\lambda_{Te}$.

6. Model the discharges in the AUG database using the same automated UEDGE procedure as used for C-Mod discharges in this thesis.

   (a) Compare the convected and conducted heat fluxes in the parallel and perpendicular directions in AUG and C-Mod to understand their relative importance, and look for systematic differences between the two devices in the ratio of convected to conducted heat flux.

(b) Investigate ion physics in both devices: in addition to experimental studies of the ion to electron temperature ratio in C-Mod [83] and AUG [154], it may be possible to use UEDGE to infer the average ion/electron temperature ratio by finding the ratio which produces the best match to the experimental heat flux width for each discharge.

(c) The AUG database study [91] used an "integrated data analysis" system to reduce uncertainty in midplane profile measurements [155], while no such system was used for the C-Mod database. In both the AUG and C-Mod studies, profiles were shifted such that separatrix temperatures were consistent with 2-point model predictions. UEDGE could be used to more accurately determine the midplane profile separatrix location producing the best match to the experimental target heat flux profile. A similar procedure was recently used in a SOLPS simulation of an AUG discharge, in which the midplane profiles were shifted to produce the separatrix density and temperature most consistent with experiment [156].

7.3 Future work

This thesis makes strides in bridging experimental database studies and edge modeling and applies these tools to simulate the SPARC tokamak. In the future, the C-Mod heat flux width database could be greatly expanded by automated analysis over entire operation campaigns, with multiple time segments in each discharge, as was done to study the 1-2 kHz mode in the W7-X stellarator [157]. Building on the automated UEDGE modeling of 75 discharges in this study, UEDGE could be used to model thousands of different time segments to ensure data quality: for example, UEDGE could verify whether midplane profiles and the total power to the outer divertor are mutually compatible, and a scaling analysis would include only such high-quality time segments. The possibility of inferring the heat flux width at the outer divertor entrance in UEDGE would also make it possible to include detached plasmas in such an analysis, which has not been done before.

Another important issue to investigate is the overestimation of the experimental heat flux width by an average factor of 1.8 in the UEDGE database study. The power balance should be further analyzed, including parallel as well as perpendicular heat flux. The model could be made more accurate by targeting experimentally informed values of the SOL ion/electron temperature ratio and divertor neutral pressure. Simplifying the model, rather than modifying it or adding complexity, could also provide insights: one option would be to eliminate heat convection effects, leaving only heat conduction, and to see whether the heat flux width is still overestimated by an average factor of 1.8. The result that drift effects do not lead to better estimation of the heat flux width in the C-Mod database should also be explored. Modifications to the profile fitting procedure could also be investigated: the anomalous heat conduction coefficient could be fit to ensure a match between the heat flux width at the divertor entrance in UEDGE and that measured in experiment, and the resulting UEDGE midplane profiles could be compared to experimental profiles. More advanced approaches that match midplane and divertor profiles simultaneously could also be used [158].

The detachment threshold investigation using a particular C-Mod discharge in this study could be expanded to the 75 UEDGE cases modeling the heat flux width database. The resulting range of detachment thresholds would provide a more general understanding of the detachment process. While the detachment threshold investigation in this study was already rather advanced thanks to the inclusion of full drift effects and the fixed-fraction impurity model, the more advanced, but difficult to implement, multi-species impurity model in UEDGE could be used to provide deeper insight.

For the SPARC simulations in this study, developing a grid with higher resolution near the X-point and more realistic target geometry would be beneficial. Including drifts effects and using the multi-species impurity model in UEDGE could also improve confidence in predictions. SPARC is also being designed to support the advanced X-point target divertor configuration, and UEDGE could be used to investigate detachment and drift effects in that configuration.

Appendix A

UEDGE code utilities

Over the course of this thesis work, relatively general utilities were created that could be of interest to the wider UEDGE user community. These have been made available on the web at https://github.com/sballin/UEDGE_utils. Any filenames mentioned in this section can be found in this repository.

A.1 Result overview

The `plotall` method in `plot.py` generates an extensive overview PDF showing various plots of interest for a UEDGE case, including boundary conditions, midplane vs. target pressure and power balance, and radial particle and power transport analysis (figure A-1).

Run label bl10_nwalli5e18
Path cmod/25
Plots created 03:15 PM Fri 18 Feb 2022
UEDGE version 7.0.9.2.2

Grid nx = 60, ny = 18, 0 cells are invalid polygons
Core n_i fixed uniform 2.02e+20 m^{-3}
Core n_n set loc flux = -(1-albedoc)*ng*vtg/4
Core T_e, T_i or P_e, P_i fixed P_e = 1.45 MW, P_i = 1.45 MW
Core ion $v_\parallel$ (up) d(up)/dy = 0 at core boundary
Uniform coeffs D = 0 m^2/s, χ_e = 0 m^2/s, χ_i = 0 m^2/s
CF wall T_e fixed 20 eV
PF wall T_e fixed 1.11 eV
CF wall T_i fixed 20 eV
PF wall T_i fixed 1.17 eV
CF wall n_i fixed 2.5e+19 m^{-3}
PF wall n_i fixed 5e+18 m^{-3}
Flux limits on
Recycling coefficient 0.98 (plates), 0.98 (walls)
Neutral model inertial neutrals
Impurity model no impurity
Potential equation off

Converged yes, sim. time 0.112 s
Field line angle 2.41° inner target, 0.916° outer target
Separatrix n_i = 9.8e+19 m^{-3}, n_n = 1.2e+17 m^{-3}, T_i = 121 eV, T_e = 144 eV
Outer PF corner p_n 25.5 Pa
Power sharing 1:3.5, $P_{LCFS\ inboard}$ = 0.64 MW, $P_{LCFS\ outboard}$ = 2.2 MW
Power balance P_{loss} = 3 MW = P_{core}+4.7%
(P_{IT} = 0.43 MW, P_{OT} = 0.75 MW, P_{CFW} = 1.9 MW, P_{PFW} = 0.0092 MW, P_H = 0.077 MW, P_I = 0 MW)
Density balance $\Sigma_{xy}|\Sigma_s(\Delta n)_s^{xy}|/\Sigma_{xy}\Sigma_s|(\Delta n)_s^{xy}|$ = 5.8e-08%

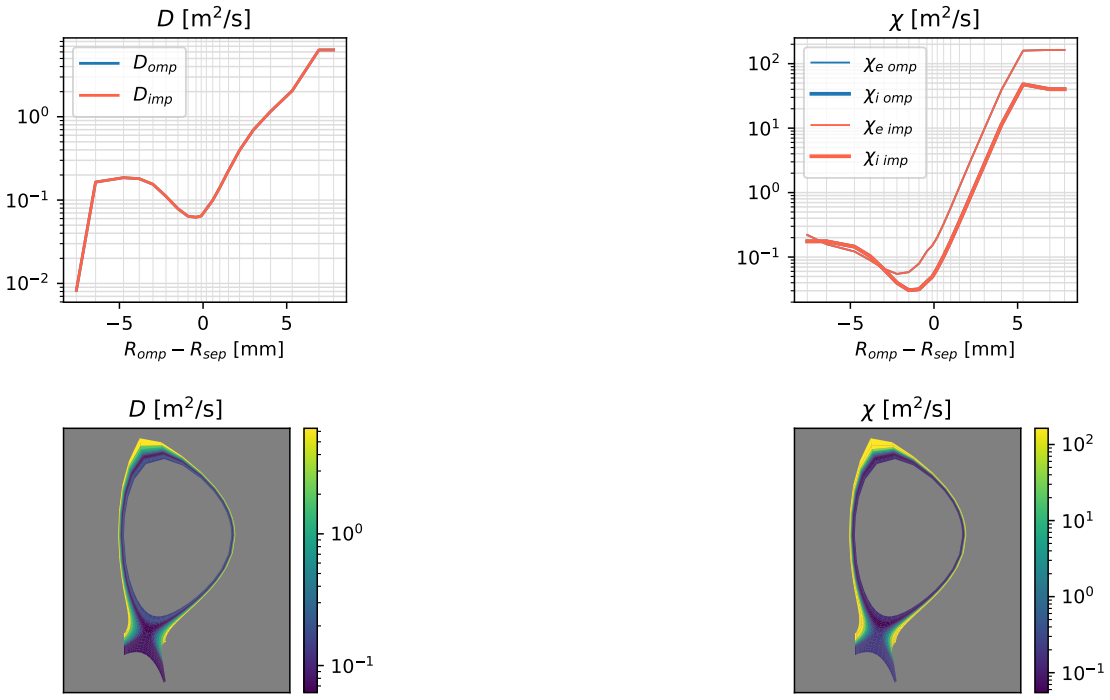

Figure A-1: Example first page of UEDGE result overview PDF showing configuration settings and anomalous transport coefficients.

A.2 Diagnosing runs

UEDGE runs can fail to converge after certain settings are changed. To understand why failures occur, it can be helpful to look at the evolution of temperatures and densities in certain cells over the course of the run. The file `Diagnose run.ipynb` provides an example of such a diagnostic workflow. It was originally developed to investigate certain negative density errors encountered early in the UEDGE modeling effort. It stores the density, temperature, particle poloidal/radial flows, and particle ionization/recombination rates for every cell in the grid after each UEDGE run time-step. This makes it possible to look at not only how the density is changing in each cell, but also which components are driving the changes. This tool requires the `rundtp` method in `run.py` (a fork of the `rundt` method in the main UEDGE repository with a few additional features added) to be used with the keyword argument `storeExt=True` to store extended information about the run.

A.3 Saving and restoring full solutions

The `fsave` and `frest` methods in `run.py` save and restore every UEDGE variable and the grid geometry using hdf5. This provides some advantages over the standard UEDGE save/restore workflow, which is concerned only with the main solution variables `ni, ng, te, ti, tg, up, phi`—to fully restore such cases requires running a solution step in UEDGE that requires all non-default settings (e.g. boundary conditions) to be correctly defined, which is usually done using a python/BASIS setup file. This made it difficult to share cases with collaborators. The full-save and full-restore functionality in these methods makes solutions self-contained hdf5 files. This code could be used as the basis of a system that stores full UEDGE cases in MDSplus for analysis and collaboration.

Appendix B

Workflow details

B.1 Midplane profile fitting with GPR

GPR fits were created using the profiletools GUI, which is available at https://github.com/markchil/profiletools/blob/master/profiletools/gui.py.

B.2 UEDGE workflows for automated modeling

The code to simultaneously run UEDGE for all available discharges in the C-Mod heat flux width database is on the PSFC Engaging cluster at the path

```
/home/sballinger/share/uedge_db
```

where each discharge has a folder with its discharge number containing the appropriate equilibrium, grid, and past run save-files. Each discharge folder also has a file named `targetData_[discharge].h5` which contains midplane and target profiles that are used to adjust the UEDGE transport coefficients and for visual comparison to UEDGE profiles in the result summary PDF files. The file named `run` is used to submit job arrays where each job runs the file `CMod.py` that changes the directory to that of the discharge to model, restores the requested save-file for that discharge, and executes any requested changes to the model.

In the PSFC MFE filesystem, the code to analyze the UEDGE automated modeling is in

```
/home/sballinger/share/uedge_cmod/Analyze edgedb.ipynb
```

B.2.1 EFIT equilibria

INGRID requires EFIT equilibrium files to generate grids. In the PSFC MFE filesystem folder

```
/home/sballinger/share/uedge_db/notebooks
```

an IDL script can be run with the command

```
idl efit.pro -args [discharge_number] [time_milliseconds]
```

to generate the aeqdsk and geqdsk EFIT files from the EFIT20 tree. These have the same timebase as the Thomson scattering system and have a spatial resolution of 129×129 cells.

B.2.2 Grid generation

On the PSFC Engaging cluster, the file

```
/home/sballinger/share/uedge_db/notebooks/make_grids.py
```

generates the grid for each discharge using INGRID. This takes several minutes for each grid at the current resolution and all discharge grids can be generated in parallel using code in

```
/home/sballinger/share/uedge_db/CMod.py
```

B.2.3 Enabling single-particle drifts

This recipe to enable single-particle drifts in UEDGE has proved reliable when starting from the settings used in the C-Mod UEDGE models:

1. Enable the old potential equation.

2. Enable the new potential equation with core boundary condition of constant potential and zero radial electric field.

3. Enable drifts with a toroidal field scaling factor of 100 (a larger magnetic field results in reduced drift velocities).

4. Slowly change the toroidal field scaling factor to 2.

5. Re-fit anomalous transport coefficients as necessary to match midplane profiles, which may have changed.

6. Change the toroidal field scaling factor to 1 (usually the longest step to converge).

7. Re-fit anomalous transport coefficients as necessary to match midplane profiles, which may have changed.

B.3 UEDGE workflows for C-Mod detachment and long leg modeling

The UEDGE models of C-Mod discharge 1160718025, including detachment and long leg studies, are in the PSFC MFE filesystem folder

```
/home/sballinger/share/uedge_1160718025
```

where most of the code to run the available cases is contained in the file `CMod.py`. The baseline cases of interest are described in table B.1.

Save-file	Description
`bl10.h5`	Real C-Mod geometry without drifts
`bl10_e4.h5`	Long leg geometry without drifts
`bl10a.h5`	Real C-Mod geometry with drifts
`bl10a_e4.h5`	Long leg geometry with drifts

Table B.1: Main UEDGE cases for C-Mod discharge 11601718025.

B.3.1 Impurity scans

Example code to perform an impurity scan is given in the method `impurityScan` in `CMod.py`. The code to analyze the completed detachment scans is in

`/home/sballinger/share/uedge_1160718025/notebooks/Analyze 25.ipynb`

B.4 UEDGE workflows for SPARC modeling

The code to analyze the completed impurity scans is in

`/home/sballinger/share/uedge_sparc/NF 2021 paper figures.ipynb`

Bibliography

[1] J. P. Freidberg, *Plasma Physics and Fusion Energy*. Cambridge University Press, 2008.

[2] U.S. Energy Information Administration. (2022). "Short-Term Energy Outlook," [Online]. Available: https://www.eia.gov/outlooks/steo/report/electricity.php (visited on 04/14/2022).

[3] R. P. White, "Regulatory Frameworks and Evaluation Methodologies for the Licensing of Commercial Fusion Reactors," 2021.

[4] J. Wesson and D. J. Campbell, *Tokamaks*, 3rd ed, ser. Oxford Science Publications 118. Oxford : New York: Clarendon Press ; Oxford University Press, 2004.

[5] H. Fountain, "A Dream of Clean Energy at a Very High Price," *The New York Times*, 2017.

[6] A. J. Creely, M. J. Greenwald, S. B. Ballinger, D. Brunner, J. Canik, J. Doody, T. Fülöp, D. T. Garnier, R. Granetz, T. K. Gray, C. Holland, N. T. Howard, J. W. Hughes, J. H. Irby, V. A. Izzo, G. J. Kramer, A. Q. Kuang, B. LaBombard, Y. Lin, B. Lipschultz, N. C. Logan, J. D. Lore, E. S. Marmar, K. Montes, R. T. Mumgaard, C. Paz-Soldan, C. Rea, M. L. Reinke, P. Rodriguez-Fernandez, K. Särkimäki, F. Sciortino, S. D. Scott, A. Snicker, P. B. Snyder, B. N. Sorbom, R. Sweeney, R. A. Tinguely, E. A. Tolman, M. Umansky, O. Vallhagen, J. Varje, D. G. Whyte, J. C. Wright, S. J. Wukitch, J. Zhu, and t. S. Team, "Overview of the SPARC tokamak," *Journal of Plasma Physics*, vol. 86, no. 5, 2020.

[7] T. Eich, A. W. Leonard, R. A. Pitts, W. Fundamenski, R. J. Goldston, T. K. Gray, A. Herrmann, A. Kirk, A. Kallenbach, O. Kardaun, A. S. Kukushkin, B. Labombard, R. Maingi, M. A. Makowski, A. Scarabosio, B. Sieglin, J. Terry, and A. Thornton, "Scaling of the tokamak near the scrape-off layer H-mode power width and implications for ITER," *Nuclear Fusion*, vol. 53, no. 9, 2013.

[8] D. Brunner, B. Labombard, A. Q. Kuang, and J. L. Terry, "High-resolution heat flux width measurements at reactor-level magnetic fields and observation of a unified width scaling across confinement regimes in the Alcator C-Mod tokamak," *Nuclear Fusion*, vol. 58, no. 9, 2018.

[9] Stangeby, *The Plasma Boundary of Magnetic Fusion Devices*. Bristol: Institute of Physics Publishing, 2000.

[10] J. W. Conner and H. R. Wilson, "Survey of theories of anomalous transport," *Plasma Physics and Controlled Fusion*, vol. 36, no. 5, pp. 719–795, 1994.

[11] D. Whyte, A. Hubbard, J. Hughes, B. Lipschultz, J. Rice, E. Marmar, M. Greenwald, I. Cziegler, A. Dominguez, T. Golfinopoulos, N. Howard, L. Lin, R. McDermott, M. Porkolab, M. Reinke, J. Terry, N. Tsujii, S. Wolfe, S. Wukitch, Y. Lin, and the Alcator C-Mod Team, "I-mode: An H-mode energy confinement regime with L-mode particle transport in Alcator C-Mod," *Nuclear Fusion*, vol. 50, no. 10, p. 105 005, 2010.

[12] A. W. Leonard, "Plasma detachment in divertor tokamaks," *Plasma Physics and Controlled Fusion*, vol. 60, no. 4, 2018.

[13] B. Meerson, "Nonlinear dynamics of radiative condensations in optically thin plasmas," *Reviews of Modern Physics*, vol. 68, no. 1, pp. 215–257, 1996.

[14] A. Kallenbach, R. Dux, V. Mertens, O. Gruber, G. Haas, M. Kaufmann, W. Poschenrieder, F. Ryter, H. Zohm, M. Alexander, K. H. Behringer, M. Bessenrodt-Weberpals, H.-S. Bosch, K. Buchl, A. R. Field, J. C. Fuchs, O. Gehre, A. Herrmann, S. Hirsch, W. Koppendorfer, K. Lackner, K. F. Mast, G. Neu, J. Neuhauser, S. D. P. Hempel, G. Raupp, K. Schonmann, A. Stabler, K.-H. Steuer, O. Vollmer, M. Weinlich, W. P. West, and T. Zehetbauer, "H mode discharges with feedback controlled radiative boundary in the ASDEX Upgrade tokamak," *Nuclear Fusion*, vol. 35, no. 10, pp. 1231–1246, 1995.

[15] Y. Hayashi, K. Ješko, H. van der Meiden, J. Vernimmen, T. Morgan, N. Ohno, S. Kajita, M. Yoshikawa, and S. Masuzaki, "Plasma detachment study of high density helium plasmas in the Pilot-PSI device," *Nuclear Fusion*, vol. 56, no. 12, p. 126 006, 2016.

[16] P. M. Valanju, M. Kotschenreuther, S. M. Mahajan, and J. Canik, "Super-X divertors and high power density fusion devices," *Physics of Plasmas*, vol. 16, no. 5, p. 056 110, 2009.

[17] D. D. Ryutov and V. A. Soukhanovskii, "The snowflake divertor," *Physics of Plasmas*, vol. 22, no. 11, p. 110 901, 2015.

[18] B. LaBombard, E. Marmar, J. Irby, J. L. Terry, R. Vieira, G. Wallace, D. G. Whyte, S. Wolfe, S. Wukitch, S. Baek, W. Beck, P. Bonoli, D. Brunner, J. Doody, R. Ellis, D. Ernst, C. Fiore, J. P. Freidberg, T. Golfinopoulos, R. Granetz, M. Greenwald, Z. S. Hartwig, A. Hubbard, J. W. Hughes, I. H. Hutchinson, C. Kessel, M. Kotschenreuther, R. Leccacorvi, Y. Lin, B. Lipschultz, S. Mahajan, J. Minervini, R. Mumgaard, R. Nygren, R. Parker, F. Poli, M. Porkolab, M. L. Reinke, J. Rice, T. Rognlien, W. Rowan, S. Shiraiwa, D. Terry, C. Theiler, P. Titus, M. Umansky, P. Valanju, J. Walk, A. White, J. R. Wilson, G. Wright, and S. J. Zweben, "ADX: A high field, high power density, advanced divertor and RF tokamak," *Nuclear Fusion*, vol. 55, no. 5, 2015.

[19] S. V. Mirnov, V. N. Dem'yanenko, and E. V. Murav'ev, "Liquid-metal tokamak divertors," *Journal of Nuclear Materials*, Plasma-Surface Interactions in Controlled Fusion Devices, vol. 196–198, pp. 45–49, 1992.

[20] H. Y. Guo, C. F. Sang, P. C. Stangeby, L. L. Lao, T. S. Taylor, and D. M. Thomas, "Small angle slot divertor concept for long pulse advanced tokamaks," *Nuclear Fusion*, vol. 57, no. 4, p. 044 001, 2017.

[21] W. Morris, J. R. Harrison, A. Kirk, B. Lipschultz, F. Militello, D. Moulton, and N. R. Walkden, "MAST Upgrade Divertor Facility: A Test Bed for Novel Divertor Solutions," *IEEE Transactions on Plasma Science*, vol. 46, no. 5, pp. 1217–1226, 2018.

[22] R. Ambrosino, "DTT - Divertor Tokamak Test facility: A testbed for DEMO," *Fusion Engineering and Design*, vol. 167, p. 112 330, 2021.

[23] N. Asakura, K. Shinya, K. Tobita, K. Hoshino, K. Shimizu, H. Utoh, Y. Someya, M. Nakamura, N. Ohno, M. Kobayashi, and H. Tanaka, "Investigation of Advanced Divertor Magnetic Configuration for DEMO Tokamak Reactor," *Fusion Science and Technology*, vol. 63, pp. 70–75, 1T 2013.

[24] E. Havlíčková, J. Harrison, B. Lipschultz, G. Fishpool, A. Kirk, A. Thornton, M. Wischmeier, S. Elmore, and S. Allan, "SOLPS analysis of the MAST-U divertor with the effect of heating power and pumping on the access to detachment in the Super-x configuration," *Plasma Physics and Controlled Fusion*, vol. 57, no. 11, p. 115 001, 2015.

[25] E. Havlíčková, M. Wischmeier, B. Lipschultz, and G. Fishpool, "The effect of the Super-X divertor of MAST Upgrade on impurity radiation as modelled by SOLPS," *Journal of Nuclear Materials*, PLASMA-SURFACE INTERACTIONS 21, vol. 463, pp. 1209–1213, 2015.

[26] D. Moulton, J. Harrison, B. Lipschultz, and D. Coster, "Using SOLPS to confirm the importance of total flux expansion in Super-X divertors," *Plasma Physics and Controlled Fusion*, vol. 59, no. 6, p. 065 011, 2017.

[27] V. A. Soukhanovskii, A. I. Khrabryi, H. A. Scott, T. D. Rognlien, D. Moulton, and J. R. Harrison, "Modeling of deuterium and carbon radiation transport in Super-X and snowflake divertor plasmas in MAST-U tokamak," presented at the 28th IAEA Fusion Energy Conference (FEC2020), 2021, p. 10.

[28] M. V. Umansky, M. E. Rensink, T. D. Rognlien, B. LaBombard, D. Brunner, J. L. Terry, and D. G. Whyte, "Assessment of X-point target divertor configuration for power handling and detachment front control," *Nuclear Materials and Energy*, pp. 1–6, 2017.

[29] S. B. Ballinger, A. Q. Kuang, M. V. Umansky, D. Brunner, J. M. Canik, M. J. Greenwald, J. D. Lore, B. LaBombard, J. L. Terry, and M. Wigram, "Simulation of the SPARC plasma boundary with the UEDGE code," *Nuclear Fusion*, 2021.

[30] M. R. Wigram, B. Labombard, M. V. Umansky, A. Q. Kuang, T. Golfinopoulos, J. L. Terry, D. Brunner, M. E. Rensink, C. P. Ridgers, and D. G. Whyte, "Performance assessment of long-legged tightly-baffled divertor geometries in the ARC reactor concept," *Nuclear Fusion*, vol. 59, no. 10, 2019.

[31] M. Wigram, B. LaBombard, M. V. Umansky, A. Q. Kuang, D. Brunner, J. L. Terry, T. Golfinopoulos, M. E. Rensink, and D. G. Whyte, "UEDGE modelling of detached divertor operation for long-leg divertor geometries in ARC," *Contributions to Plasma Physics*, vol. 58, no. 6-8, pp. 791–797, 2018.

[32] H. Reimerdes, B. P. Duval, J. R. Harrison, B. Labit, B. Lipschultz, T. Lunt, C. Theiler, C. K. Tsui, K. Verhaegh, W. A. J. Vijvers, J. A. Boedo, G. Calabro, F. Crisanti, P. Innocente, R. Maurizio, V. Pericoli, U. Sheikh, M. Spolare, N. Vianello, and and, "TCV experiments towards the development of a plasma exhaust solution," *Nuclear Fusion*, vol. 57, no. 12, p. 126 007, 2017.

[33] C. Theiler, B. Lipschultz, J. Harrison, B. Labit, H. Reimerdes, C. Tsui, W. A. J. Vijvers, J. A. Boedo, B. P. Duval, S. Elmore, P. Innocente, U. Kruezi, T. Lunt, R. Maurizio, F. Nespoli, U. Sheikh, A. J. Thornton, S. H. M. van Limpt, K. Verhaegh, and N. Vianello, "Results from recent detachment experiments in alternative divertor configurations on TCV," *Nuclear Fusion*, vol. 57, no. 7, p. 072 008, 2017.

[34] V. A. Soukhanovskii, S. L. Allen, M. E. Fenstermacher, C. J. Lasnier, M. A. Makowski, A. G. McLean, E. T. Meier, W. H. Meyer, T. D. Rognlien, D. D. Ryutov, F. Scotti, E. Kolemen, R. E. Bell, A. Diallo, S. Gerhardt, R. Kaita, S. Kaye, B. P. LeBlanc, R. Maingi, J. E. Menard, M. Podesta, A. L. Roquemore, R. J. Groebner, A. W. Hyatt, A. W. Leonard, T. H. Osborne, T. W. Petrie, J.-W. Ahn, R. Raman, and J. G. Watkins, "Snowflake Divertor Experiments in the DIII-D, NSTX, and NSTX-U Tokamaks Aimed at the Development of the Divertor Power Exhaust Solution," *IEEE Transactions on Plasma Science*, vol. 44, no. 12, pp. 3445–3455, 2016.

[35] A. I. Khrabry, V. A. Soukhanovskii, T. D. Rognlien, M. V. Umansky, D. Moulton, and J. R. Harrison, "Modeling snowflake divertors in MAST-U Tokamak," *Nuclear Fusion*, vol. 62, no. 1, p. 016 007, 2021.

[36] O. Pan, T. Lunt, M. Wischmeier, D. Coster, and U. Stroth, "SOLPS-ITER modeling with activated drifts for a snowflake divertor in ASDEX Upgrade," *Plasma Physics and Controlled Fusion*, vol. 62, no. 4, p. 045 005, 2020.

[37] V. A. Soukhanovskii, S. L. Allen, M. E. Fenstermacher, D. N. Hill, C. J. Lasnier, M. A. Makowski, A. G. McLean, W. H. Meyer, E. Kolemen, R. J. Groebner, A. W. Hyatt, A. W. Leonard, T. H. Osborne, and T. W. Petrie, "Radiative snowflake divertor studies in DIII-D," *Journal of Nuclear Materials*, Plasma-Surface Interactions 21, vol. 463, pp. 1191–1195, 2015.

[38] V. A. Soukhanovskii, S. L. Allen, M. E. Fenstermacher, C. J. Lasnier, M. A. Makowski, A. G. McLean, W. H. Meyer, D. D. Ryutov, E. Kolemen, R. J. Groebner, A. W. Hyatt, A. W. Leonard, T. H. Osborne, T. W. Petrie, and J. Watkins, "Developing physics basis for the snowflake divertor in the DIII-D tokamak," *Nuclear Fusion*, vol. 58, no. 3, p. 036 018, 2018.

[39] V. A. Soukhanovskii, R. E. Bell, A. Diallo, S. Gerhardt, S. Kaye, E. Kolemen, B. P. LeBlanc, A. G. McLean, J. E. Menard, S. F. Paul, M. Podesta, R. Raman, T. D. Rognlien, A. L. Roquemore, D. D. Ryutov, F. Scotti, M. V. Umansky, D. Battaglia, M. G. Bell, D. A. Gates, R. Kaita, R. Maingi, D. Mueller, and S. A. Sabbagh, "Snowflake divertor configuration studies in National Spherical Torus Experiment," *Physics of Plasmas*, vol. 19, no. 8, p. 082 504, 2012.

[40] H. Reimerdes, G. P. Canal, B. P. Duval, B. Labit, T. Lunt, W. A. J. Vijvers, S. Coda, G. D. Temmerman, T. W. Morgan, F. Nespoli, and B. T. and, "Power distribution in the snowflake divertor in TCV," *Plasma Physics and Controlled Fusion*, vol. 55, no. 12, p. 124 027, 2013.

[41] A. Q. Kuang, S. Ballinger, D. Brunner, J. Canik, A. J. Creely, T. Gray, M. Greenwald, J. W. Hughes, J. Irby, B. LaBombard, B. Lipschultz, J. D. Lore, M. L. Reinke, J. L. Terry, M. Umansky, D. G. Whyte, S. Wukitch, and the SPARC Team, "Divertor heat flux challenge and mitigation in SPARC," *Journal of Plasma Physics*, vol. 86, no. 5, p. 865 860 505, 2020.

[42] F. I. Parra. (2019). "Braginskii fluid equations," [Online]. Available: `http://www-thphys.physics.ox.ac.uk/people/FelixParra/CollisionalPlasmaPhysics/notes/lecIV_braginskii.pdf` (visited on 04/13/2022).

[43] S. Braginskii, "Transport processes in a plasma," *Reviews of Plasma Physics*, vol. 1, 1965.

[44] R. H. Cohen and T. D. Rognlien, "Finite Mean-Free-Path Effects in Tokamak Scrape-Off Layers," *Contributions to Plasma Physics*, vol. 34, no. 2-3, pp. 198–203, 1994.

[45] T. D. Rognlien, J. L. Milovich, M. E. Rensink, and G. D. Porter, "A fully implicit, time dependent 2-D fluid code for modeling tokamak edge plasmas," *Journal of Nuclear Materials*, vol. 196–198, no. C, pp. 347–351, 1992.

[46] T. D. Rognlien, P. N. Brown, R. B. Campbell, T. B. Kaiser, D. A. Knoll, P. R. McHugh, G. D. Porter, M. E. Rensink, and G. R. Smith, "2-D Fluid Transport Simulations of Gaseous/Radiative Divertors," *Contributions to Plasma Physics*, vol. 34, no. 2-3, pp. 362–367, 1994.

[47] G. R. Smith, P. N. Brown, R. B. Campbell, D. A. Knoll, P. R. McHugh, M. E. Rensink, and T. D. Rognlien, "Techniques and results of tokamak-edge simulation," *Journal of Nuclear Materials*, Plasma-Surface Interactions in Controlled Fusion Devices, vol. 220–222, pp. 1024–1027, 1995.

[48] T. D. Rognlien, B. J. Braams, and D. A. Knoll, "Progress in Integrated 2-D Models for Analysis of Scrape-Off Layer Transport Physics," *Contributions to Plasma Physics*, vol. 36, no. 2-3, pp. 105–116, 1996.

[49] T. D. Rognlien, D. D. Ryutov, N. Mattor, and G. D. Porter, "Two-dimensional electric fields and drifts near the magnetic separatrix in divertor tokamaks," *Physics of Plasmas*, vol. 6, no. 5, pp. 1851–1857, 1999.

[50] D. A. Knoll and D. E. Keyes, "Jacobian-free Newton–Krylov methods: A survey of approaches and applications," *Journal of Computational Physics*, vol. 193, no. 2, pp. 357–397, 2004.

[51] T. D. Rognlien, X. Q. Xu, and R. H. Cohen, "Simulation of edge-plasma profiles and turbulence related to L-H transitions in tokamaks," *Plasma Physics and Controlled Fusion*, vol. 42, A271–A276, 5A 2000.

[52] R. Masline, R. D. Smirnov, and S. I. Krasheninnikov, "Simulations of divertor plasmas with inverse sheaths," *Physics of Plasmas*, vol. 27, no. 9, p. 092 505, 2020.

[53] R. Masline, R. D. Smirnov, and S. I. Krasheninnikov, "Influence of the inverse sheath on divertor plasma performance in tokamak edge plasma simulations," *Contributions to Plasma Physics*, vol. 60, no. 5-6, e201900097, 2020.

[54] M. V. Umansky, R. D. Smirnov, W. R. Elwasif, and S. I. Krasheninnikov, "Modelling of edge plasma dynamics with active wall boundary conditions," *Contributions to Plasma Physics*, e202100156, 2022.

[55] A. Y. Pigarov, S. I. Krasheninnikov, T. D. Rognlien, C. J. Lasnier, and E. Unterberg, "Dynamic plasma-wall modeling of ELMy H-mode with UEDGE-MB-W," *Journal of Nuclear Materials*, Plasma-Surface Interactions 21, vol. 463, pp. 705–708, 2015.

[56] A. Holm, T. Rognlien, and W. Meyer, "Implementation and assessment of an extended hydrogenic molecular model in UEDGE," *Contributions to Plasma Physics*, vol. 60, no. 5-6, e201900150, 2020.

[57] A. Holm, P. Börner, T. D. Rognlien, W. H. Meyer, and M. Groth, "Comparison of a collisional-radiative fluid model of H2 in UEDGE to the kinetic neutral code EIRENE," *Nuclear Materials and Energy*, vol. 27, p. 100 982, 2021.

[58] A. E. Jaervinen, S. L. Allen, D. Eldon, M. E. Fenstermacher, M. Groth, D. N. Hill, A. W. Leonard, A. G. McLean, G. D. Porter, T. D. Rognlien, C. M. Samuell, and H. Q. Wang, "E×B Flux Driven Detachment Bifurcation in the DIII-D Tokamak," *Physical Review Letters*, vol. 121, no. 7, p. 75 001, 2018. pmid: 30169054.

[59] M. Groth, A. Mahdavi, G. Porter, and T. Rognlien, "Study of Plasma Detachment in a Simplified 2D Geometry using UEDGE," *Contributions to Plasma Physics*, vol. 42, no. 2-4, pp. 389–394, 2002.

[60] A. O. Nelson, Z. A. Xing, O. Izacard, F. M. Laggner, and E. Kolemen, "Interpretative SOL modeling throughout multiple ELM cycles in DIII-D," *Nuclear Materials and Energy*, vol. 26, p. 100 883, 2021.

[61] A. Y. Pigarov, S. I. Krasheninnikov, T. D. Rognlien, W. P. West, B. LaBombard, B. Lipschultz, R. Maingi, and V. Soukhanovskii, "Multi-fluid code simulations including anomalous non-diffusive transport of plasma and impurities in the tokamak SOL," *Contributions to Plasma Physics*, vol. 44, no. 1-3, pp. 228–234, 2004.

[62] G. D. Porter, "UEDGE Simulations of CMOD Discharge 1100212014," Lawrence Livermore National Lab. (LLNL), Livermore, CA (United States), LLNL-TR-457951, 2010.

[63] M. V. Umansky, S. I. Krasheninnikov, B. LaBombard, and J. L. Terry, "Comments on particle and energy balance in the edge plasma of Alcator C-Mod," *Physics of Plasmas*, vol. 5, no. 9, pp. 3373–3376, 1998.

[64] M. V. Umansky, S. I. Krasheninnikov, B. LaBombard, B. Lipschultz, and J. L. Terry, "Modeling of particle and energy transport in the edge plasma of Alcator C-Mod," *Physics of Plasmas*, vol. 6, no. 7, pp. 2791–2796, 1999.

[65] M. Umansky, "Transport of particles and energy in the edge plasma of the Alcator C-Mod tokamak," MIT Plasma Science and Fusion Center, 2000.

[66] F. Wising, D. A. Knoll, S. I. Krasheninnikov, T. D. Rognlien, and D. J. Sigmar, "Simulation of the Alcator C-Mod Divertor with an Improved Neutral Fluid Model," *Contributions to Plasma Physics*, vol. 36, no. 2-3, pp. 136–139, 1996.

[67] G. D. Porter, R. Isler, J. Boedo, and T. D. Rognlien, "Detailed comparison of simulated and measured plasma profiles in the scrape-off layer and edge plasma of DIII-D," *Physics of Plasmas*, vol. 7, no. 9, pp. 3663–3680, 2000.

[68] A. E. Jaervinen, S. L. Allen, M. Groth, A. G. McLean, T. D. Rognlien, C. M. Samuell, A. Briesemeister, M. Fenstermacher, D. N. Hill, A. W. Leonard, and G. D. Porter, "Interpretations of the impact of cross-field drifts on divertor flows in DIII-D with UEDGE," *Nuclear Materials and Energy*, Proceedings of the 22nd International Conference on Plasma Surface Interactions 2016, 22nd PSI, vol. 12, pp. 1136–1140, 2017.

[69] A. E. Jaervinen, S. L. Allen, A. W. Leonard, A. G. McLean, A. L. Moser, T. D. Rognlien, and C. M. Samuell, "Role of poloidal E × B drift in divertor heat transport in DIII-D," *Contributions to Plasma Physics*, vol. 60, no. 5-6, e201900111, 2020.

[70] T. D. Rognlien, A. G. McLean, M. E. Fenstermacher, M. Groth, A. E. Jaervinen, I. Joseph, C. J. Lasnier, W. Meyer, A. Moser, G. D. Porter, and M. V. Umansky, "Comparison of 2D simulations of detached divertor plasmas with divertor Thomson measurements in the DIII-D tokamak," *Nuclear Materials and Energy*, vol. 12, pp. 44–50, 2017.

[71] N. Christen, C. Theiler, T. Rognlien, M. Rensink, H. Reimerdes, R. Maurizio, and B. Labit, "Exploring drift effects in TCV single-null plasmas with the UEDGE code," *Plasma Physics and Controlled Fusion*, vol. 59, no. 10, p. 105 004, 2017.

[72] V. A. Soukhanovskii, "A review of radiative detachment studies in tokamak advanced magnetic divertor configurations," *Plasma Physics and Controlled Fusion*, vol. 59, no. 6, 2017.

[73] M. E. Rensink and T. D. Rognlien, "Edge plasma modeling of limiter surfaces in a tokamak divertor configuration," *Journal of Nuclear Materials*, vol. 266–269, pp. 1180–1184, 1999.

[74] T. Rognlien, R. Bulmer, M. Rensink, and J. Brooks, "Scrape-off layer plasmas for ITER with 2nd X-point and convective transport effects," *Journal of Nuclear Materials*, vol. 363–365, pp. 658–663, 2007.

[75] F. Wising, D. A. Knoll, S. I. Krasheninnikov, T. D. Rognlien, and D. J. Sigmar, "Simulation of Detachment in ITER-Geometry Using the UEDGE Code and a Fluid Neutral Model," *Contributions to Plasma Physics*, vol. 36, no. 2-3, pp. 309–313, 1996.

[76] M. Umansky, B. LaBombard, D. Brunner, T. Golfinopoulos, A. Kuang, M. Rensink, J. Terry, M. Wigram, and D. Whyte, "Study of passively stable, fully detached divertor plasma regimes attained in innovative long-legged divertor configurations," *Nuclear Fusion*, vol. 60, no. 1, p. 016 004, 2020.

[77] M. V. Umansky, B. LaBombard, D. Brunner, M. E. Rensink, T. D. Rognlien, J. L. Terry, and D. G. Whyte, "Attainment of a stable, fully detached plasma state in innovative divertor configurations," *Physics of Plasmas*, vol. 24, no. 5, 2017.

[78] T. Rognlien and M. Rensink, "Users Manual for the UEDGE Edge-Plasma Transport Code," 2015.

[79] D. Post, "A review of recent developments in atomic processes for divertors and edge plasmas," *Journal of Nuclear Materials*, vol. 220–222, pp. 143–157, 1995.

[80] T. D. Rognlien and M. E. Rensink, "Edge-plasma models and characteristics for magnetic fusion energy devices," *Fusion Engineering and Design*, vol. 60, no. 4, pp. 497–514, 2002.

[81] R. A. Hulse, "Numerical Studies of Impurities in Fusion Plasmas," *Nuclear Technology - Fusion*, vol. 3, no. 2, pp. 259–272, 1983.

[82] L. Spitzer and R. Härm, "Transport Phenomena in a Completely Ionized Gas," *Physical Review*, vol. 89, no. 5, pp. 977–981, 1953.

[83] D. Brunner, B. Labombard, R. M. Churchill, J. Hughes, B. Lipschultz, R. Ochoukov, T. D. Rognlien, C. Theiler, J. Walk, M. V. Umansky, and D. Whyte, "An assessment of ion temperature measurements in the boundary of the Alcator C-Mod tokamak and implications for ion fluid heat flux limiters," *Plasma Physics and Controlled Fusion*, vol. 55, no. 9, 2013.

[84] A. Froese, T. Takizuka, and M. Yagi, "Kinetic Particle Simulation Study of Parallel Heat Transport in Scrape-off Layer Plasmas over a Wide Range of Collisionalities," *Plasma and Fusion Research*, vol. 5, pp. 026–026, 2010.

[85] W. Fundamenski, "Parallel heat flux limits in the tokamak scrape-off layer," *Plasma Physics and Controlled Fusion*, vol. 47, no. 11, R163–R208, 2005.

[86] A. Loarte, B. Lipschultz, A. Kukushkin, G. Matthews, P. Stangeby, N. Asakura, G. Counsell, G. Federici, A. Kallenbach, K. Krieger, A. Mahdavi, V. Philipps, D. Reiter, J. Roth, J. Strachan, D. Whyte, R. Doerner, T. Eich, W. Fundamenski, A. Herrmann, M. Fenstermacher, P. Ghendrih, M. Groth, A. Kirschner, S. Konoshima, B. LaBombard, P. Lang, A. Leonard, P. Monier-Garbet, R. Neu, H. Pacher, B. Pegourie, R. Pitts, S. Takamura, J. Terry, E. Tsitrone, and t. I. S.-o. L. a. D. Group, "Chapter 4: Power and particle control," *Nuclear Fusion*, vol. 47, no. 6, S203–S263, 2007.

[87] Z. Abou-Assaleh, J. P. Matte, T. W. Johnston, and R. Marchand, "Fokker-Planck Modelling of Edge Plasma Near the Neutralizer Plate in a Tokamak," *Contributions to Plasma Physics*, vol. 32, no. 3-4, pp. 268–272, 1992.

[88] M. R. K. Wigram, "Modelling tokamak power exhaust and scrape-off-layer thermal transport in high-power fusion devices," 2019.

[89] S. Ballinger, D. Brunner, A. Hubbard, J. Hughes, A. Kuang, B. LaBombard, J. Terry, and A. White, "Dependence of the boundary heat flux width on core and edge profiles in Alcator C-Mod," *Nuclear Fusion*, vol. 62, no. 7, p. 076 020, 2022.

[90] L. L. Lao, H. S. John, R. D. Stambaugh, A. G. Kellman, and W. Pfeiffer, "Reconstruction of current profile parameters and plasma shapes in tokamaks," *Nuclear Fusion*, vol. 25, no. 11, pp. 1611–1622, 1985.

[91] D. Silvagni, T. Eich, M. Faitsch, T. Happel, B. Sieglin, P. David, D. Nille, L. Gil, U. Stroth, the ASDEX Upgrade team, and the EUROfusion MST1 team, "Scrape-off layer (SOL) power width scaling and correlation between SOL and pedestal gradients across L, I and H-mode plasmas at ASDEX Upgrade," *Plasma Physics and Controlled Fusion*, vol. 62, no. 4, p. 045 015, 2020.

[92] H. J. Sun, E. Wolfrum, T. Eich, B. Kurzan, S. Potzel, U. Stroth, and the ASDEX Upgrade Team, "Study of near scrape-off layer (SOL) temperature and density gradient lengths with Thomson scattering," *Plasma Physics and Controlled Fusion*, vol. 57, no. 12, p. 125 011, 2015.

[93] A. Scarabosio, T. Eich, A. Herrmann, and B. Sieglin, "Outer target heat fluxes and power decay length scaling in L-mode plasmas at JET and AUG," *Journal of Nuclear Materials*, vol. 438, S426–S430, 2013.

[94] M. A. Makowski, D. Elder, T. K. Gray, B. Labombard, C. J. Lasnier, A. W. Leonard, R. Maingi, T. H. Osborne, P. C. Stangeby, J. L. Terry, and J. Watkins, "Analysis of a multi-machine database on divertor heat fluxes," *Physics of Plasmas*, vol. 19, no. 5, 2012.

[95] R. J. Goldston, "Heuristic drift-based model of the power scrape-off width in low-gas-puff H-mode tokamaks," *Nuclear Fusion*, vol. 52, no. 1, p. 013 009, 2011.

[96] ——, "Theoretical aspects and practical implications of the heuristic drift SOL model," *Journal of Nuclear Materials*, Plasma-Surface Interactions 21, vol. 463, pp. 397–400, 2015.

[97] J. Horacek, J. Adamek, M. Komm, J. Seidl, P. Vondracek, A. Jardin, C. Guillemaut, S. Elmore, A. Thornton, K. Jirakova, F. Jaulmes, G. Deng, X. Gao, L. Wang, R. Ding, D. Brunner, B. LaBombard, J. Olsen, J. Rasmussen, A. Nielsen, V. Naulin, M. Ezzat, K. Camacho, M. Hron, G. Matthews, EUROfusion MST1 Team, JET Contributors, and MAST-U Team, "Scaling of L-mode heat flux for ITER and COMPASS-U divertors, based on five tokamaks," *Nuclear Fusion*, vol. 60, no. 6, p. 066 016, 2020.

[98] M. Makowski, C. Lasnier, A. Leonard, T. Osborne, M. Umansky, J. Elder, J. Nichols, P. Stangeby, D. Baver, and J. Myra, "Models of SOL transport and their relation to scaling of the divertor heat flux width in DIII-D," *Journal of Nuclear Materials*, vol. 463, pp. 55–60, 2015.

[99] M. A. Makowski, C. J. Lasnier, A. W. Leonard, and T. H. Osborne, "Analysis of edge stability for models of heat flux width," *Nuclear Materials and Energy*, Proceedings of the 22nd International Conference on Plasma Surface Interactions 2016, 22nd PSI, vol. 12, pp. 1010–1014, 2017.

[100] M. Giacomin, A. Stagni, P. Ricci, J. Boedo, J. Horacek, H. Reimerdes, and C. Tsui, "Theory-based scaling laws of near and far scrape-off layer widths in single-null L-mode discharges," *Nuclear Fusion*, vol. 61, no. 7, p. 076 002, 2021.

[101] T. Eich, P. Manz, R. Goldston, P. Hennequin, P. David, M. Faitsch, B. Kurzan, B. Sieglin, E. Wolfrum, ASDEX, and EUROfusion b, "Turbulence driven widening of the near-SOL power width in ASDEX Upgrade H-Mode discharges," *Nuclear Fusion*, vol. 60, no. 5, p. 056 016, 2020.

[102] M. Faitsch, T. Eich, G. Harrer, E. Wolfrum, D. Brida, P. David, M. Griener, and U. Stroth, "Broadening of the power fall-off length in a high density, high confinement H-mode regime in ASDEX Upgrade," *Nuclear Materials and Energy*, vol. 26, p. 100 890, 2021.

[103] M. Greenwald, R. Boivin, P. Bonoli, R. Budny, C. Fiore, J. Goetz, R. Granetz, A. Hubbard, I. Hutchinson, J. Irby, B. LaBombard, Y. Lin, B. Lipschultz, E. Marmar, A. Mazurenko, D. Mossessian, T. Sunn Pedersen, C. S. Pitcher, M. Porkolab, J. Rice, W. Rowan, J. Snipes, G. Schilling, Y. Takase, J. Terry, S. Wolfe, J. Weaver, B. Welch, and S. Wukitch, "Characterization of enhanced Dα high-confinement modes in alcator *C*-mod," *Physics of Plasmas*, vol. 6, no. 5, pp. 1943–1949, 1999.

[104] J. A. Snipes, B. LaBombard, M. Greenwald, I. H. Hutchinson, J. Irby, Y. Lin, A. Mazurenko, and M. Porkolab, "The quasi-coherent signature of enhanced Dα H-mode in Alcator C-Mod," *Plasma Physics and Controlled Fusion*, vol. 43, no. 4, pp. L23–L30, 2001.

[105] B. LaBombard, T. Golfinopoulos, J. L. Terry, D. Brunner, E. Davis, M. Greenwald, and J. W. Hughes, "New insights on boundary plasma turbulence and the quasi-coherent mode in Alcator C-Mod using a Mirror Langmuir Probe," *Physics of Plasmas*, vol. 21, no. 5, p. 056 108, 2014.

[106] J. W. Hughes, D. Mossessian, K. Zhurovich, M. DeMaria, K. Jensen, and A. Hubbard, "Thomson scattering upgrades on Alcator C-Mod," *Review of Scientific Instruments*, vol. 74, no. 3, pp. 1667–1670, 2003.

[107] N. P. Basse, A. Dominguez, E. M. Edlund, C. L. Fiore, R. S. Granetz, A. E. Hubbard, J. W. Hughes, I. H. Hutchinson, J. H. Irby, B. LaBombard, L. Lin, Y. Lin, B. Lipschultz, J. E. Liptac, E. S. Marmar, D. A. Mossessian, R. R. Parker, M. Porkolab, J. E. Rice, J. A. Snipes, V. Tang, J. L. Terry, S. M. Wolfe, S. J. Wukitch, K. Zhurovich, R. V. Bravenec, P. E. Phillips, W. L. Rowan, G. J. Kramer, G. Schilling, S. D. Scott, and S. J. Zweben, "Diagnostic Systems on Alcator C-Mod," *Fusion Science and Technology*, vol. 51, no. 3, pp. 476–507, 2007.

[108] M. A. Chilenski, M. Greenwald, Y. Marzouk, N. T. Howard, A. E. White, J. E. Rice, and J. R. Walk, "Improved profile fitting and quantification of uncertainty in experimental measurements of impurity transport coefficients using Gaussian process regression," vol. 55, no. 2, p. 023 012, 2015.

[109] J. W. Hughes, D. A. Mossessian, A. E. Hubbard, E. S. Marmar, D. Johnson, and D. Simon, "High-resolution edge Thomson scattering measurements on the Alcator C-Mod tokamak," *Review of Scientific Instruments*, vol. 72, no. 1, pp. 1107–1110, 2001.

[110] J. W. Hughes, D. A. Mossessian, A. E. Hubbard, B. LaBombard, and E. S. Marmar, "Observations and empirical scalings of the high-confinement mode pedestal on Alcator C-Mod," *Physics of Plasmas*, vol. 9, no. 7, pp. 3019–3030, 2002.

[111] T. Casper, Y. Gribov, A. Kavin, V. Lukash, R. Khayrutdinov, H. Fujieda, C. Kessel, ITER Organization, and ITER Domestic Agencies, "Development of the ITER baseline inductive scenario," *Nuclear Fusion*, vol. 54, no. 1, p. 013 005, 2014.

[112] P. Rodriguez-Fernandez, N. T. Howard, M. J. Greenwald, A. J. Creely, J. W. Hughes, J. C. Wright, C. Holland, Y. Lin, and F. Sciortino, "Predictions of core plasma performance for the SPARC tokamak," *Journal of Plasma Physics*, pp. 1–24, 2020.

[113] J. W. Hughes, N. T. Howard, P. Rodriguez-Fernandez, A. J. Creely, A. Q. Kuang, P. B. Snyder, T. M. Wilks, R. Sweeney, and M. Greenwald, "Projections of H-mode access and edge pedestal in the SPARC tokamak," *Journal of Plasma Physics*, vol. 86, no. 5, p. 865 860 504, 2020.

[114] P. C. Stangeby, J. D. Elder, J. A. Boedo, B. Bray, N. H. Brooks, M. E. Fenstermacher, M. Groth, R. C. Isler, L. L. Lao, S. Lisgo, G. D. Porter, D. Reiter, D. L. Rudakov, J. G. Watkins, W. P. West, and D. G. Whyte, "Interpretive modeling of simple-as-possible-plasma discharges on DIII-D using the OEDGE code," *Journal of Nuclear Materials*, Plasma-Surface Interactions in Controlled Fusion Devices 15, vol. 313–316, pp. 883–887, 2003.

[115] M. V. Umansky and B. LaBombard, "Empirical scalings of cross-field heat diffusivities in the scrape-off layer of Alcator C-Mod from a 2-D interpretive model," *Journal of Nuclear Materials*, vol. 266, pp. 721–725, 1999.

[116] M. A. Makowski, C. J. Lasnier, A. W. Leonard, J. Boedo, J. G. Watkins, and D. N. Hill, "Comparison of upstream Te profiles with downstream heat flux profiles and their implications on parallel heat transport in the SOL in DIII-D," *Journal of Nuclear Materials*, Proceedings of the 19th International Conference on Plasma-Surface Interactions in Controlled Fusion, vol. 415, S357–S359, 1, Supplement 2011.

[117] O. Izacard, E. Kolemen, O. Meneghini, D. Eldon, and M. Umansky, "Automatic UEDGE simulations of a large series of time-slices for tokamak discharges," in *Bulletin of the American Physical Society*, vol. 2018, 2018, UP11.027.

[118] Z. Xing, A. O. Nelson, O. Izacard, M. E. Austin, A. Marinoni, A. Jarvinen, M. Umansky, and E. Kolemen, "Automating Interpretive Edge Transport Modeling on DIII-D with UEDGE," in *Bulletin of the American Physical Society*, vol. 2020, 2020, TP15.020.

[119] Z. Xing, A. Nelson, O. Izacard, A. Jarvinen, M. Umansky, D. Humphreys, and E. Kolemen, "Sensitivity analysis of cross-field transport coeffcients with autoUEDGE," in *Bulletin of the American Physical Society*, vol. 2021, 2021, UP11.094.

[120] B. M. Garcia, M. V. Umansky, J. Watkins, J. Guterl, and O. Izacard, "INGRID: An interactive grid generator for 2D edge plasma modeling," 2021.

[121] M. Kočan, J. P. Gunn, S. Carpentier-Chouchana, A. Herrmann, A. Kirk, M. Komm, H. W. Müller, J. .-Y. Pascal, R. A. Pitts, V. Rohde, and P. Tamain, "Measurements of ion energies in the tokamak plasma boundary," *Journal of Nuclear Materials*, Proceedings of the 19th International Conference on Plasma-Surface Interactions in Controlled Fusion, vol. 415, S1133–S1138, 1, Supplement 2011.

[122] J. M. Canik, R. Maingi, V. A. Soukhanovskii, R. E. Bell, H. W. Kugel, B. P. Leblanc, and T. H. Osborne, "Measurements and 2-D modeling of recycling and edge transport in discharges with lithium-coated PFCs in NSTX," *Journal of Nuclear Materials*, vol. 415, S409–S412, 1 SUPPL 2011.

[123] M. Newville, R. Otten, A. Nelson, A. Ingargiola, T. Stensitzki, D. Allan, A. Fox, F. Carter, Michał, R. Osborn, D. Pustakhod, Lneuhaus, S. Weigand, Glenn, C. Deil, Mark, A. L. R. Hansen, G. Pasquevich, L. Foks, N. Zobrist, O. Frost, A. Beelen, Stuermer, Azelcer, A. Hannum, A. Polloreno, J. H. Nielsen, S. Caldwell, A. Almarza, and A. Persaud, *Lmfit/lmfit-py: 1.0.3*, version 1.0.3, Zenodo, 2021.

[124] N. M. Li, X. Q. Xu, R. J. Goldston, J. Z. Sun, and D. Z. Wang, "Impact of plasma density/collisionality on divertor heat flux width," *Nuclear Fusion*, vol. 61, no. 2, p. 026 005, 2020.

[125] P. C. Stangeby, J. M. Canik, and D. G. Whyte, "The relation between upstream density and temperature widths in the scrape-off layer and the power width in an attached divertor," *Nuclear Fusion*, vol. 50, no. 12, p. 125 003, 2010.

[126] J. L. Terry, B. LaBombard, D. Brunner, J. W. Hughes, M. L. Reinke, and D. G. Whyte, "Heat-flux footprints for I-mode and EDA H-mode plasmas on Alcator C-Mod," *Journal of Nuclear Materials*, Proceedings of the 20th International Conference on Plasma-Surface Interactions in Controlled Fusion Devices, vol. 438, S212–S215, 2013.

[127] M. Faitsch, B. Sieglin, T. Eich, H. J. Sun, and A. Herrmann, "Change of the scrape-off layer power width with the toroidal B-field direction in ASDEX upgrade," *Plasma Physics and Controlled Fusion*, vol. 57, no. 7, p. 075 005, 2015.

[128] R. Reksoatmodjo, S. Mordijck, J. W. Hughes, J. D. Lore, and X. Bonnin, "The role of edge fueling in determining the pedestal density in high neutral opacity Alcator C-Mod experiments," *Nuclear Materials and Energy*, vol. 27, p. 100 971, 2021.

[129] R. L. Boivin, J. Goetz, A. Hubbard, J. W. Hughes, J. Irby, B. LaBombard, E. Marmar, D. Mossessian, and J. L. Terry, "High resolution measurements of neutral density and ionization rate in the main chamber of the Alcator C-Mod tokamak," *Journal of Nuclear Materials*, 14th Int. Conf. on Plasma-Surface Interactions in Controlled Fusion D Evices, vol. 290–293, pp. 542–545, 2001.

[130] I. H. Hutchinson, B. LaBombard, J. A. Goetz, B. Lipschultz, G. M. McCracken, J. A. Snipes, and J. L. Terry, "The effects of field reversal on the Alcator C-Mod divertor," *Plasma Physics and Controlled Fusion*, vol. 37, no. 12, pp. 1389–1406, 1995.

[131] C. M. Samuell, A. G. Mclean, S. L. Allen, M. E. Fenstermacher, C. J. Lasnier, G. D. Porter, T. D. Rognlien, F. Scotti, V. Soukhanovskii, W. H. Meyer, A. E. Jaervinen, A. Holm, M. Groth, D. A. Ennis, C. A. Johnson, F. Glass, H. Guo, A. W. Leonard, A. L. Moser, D. Thomas, H. Q. Wang, J. D. Watkins, J. Boedo, E. M. Hollmann, and R. S. Wilcox, "Advancements in Understanding the 2-D Role of Impurity Radiation for Dissipative Divertor Operation on DIII-D," in

28th IAEA Fusion Energy Conference (Proc. Int. Conf. Nice, France, 2021), IAEA, Vienna, 2021, p. 8.

[132] D. P. Coster, O. Wenisch, A. S. Kukushkin, M. Stanojevic, and X. Bonnin. (2013). "SOLPS 5.0," [Online]. Available: http://solps-mdsplus.aug.ipp.mpg.de:8080/solps/Documentation/solps.pdf (visited on 04/04/2022).

[133] S. Krasheninnikov, A. Smolyakov, and A. Kukushkin, *On the Edge of Magnetic Fusion Devices*. Springer, 2020.

[134] A. I. Smolyakov and A. Hirose, "On energy transport equations for turbulent magnetized plasma," *Plasma Physics and Controlled Fusion*, vol. 35, no. 12, pp. 1765–1776, 1993.

[135] B. Scott, "The character of transport caused by E×B drift turbulence," *Physics of Plasmas*, vol. 10, no. 4, pp. 963–976, 2003.

[136] T. E. Stringer, "Different forms of the plasma energy conservation equation," *Plasma Physics and Controlled Fusion*, vol. 33, no. 14, pp. 1715–1722, 1991.

[137] J. A. Goetz, B. LaBombard, B. Lipschultz, C. S. Pitcher, J. L. Terry, C. Boswell, S. Gangadhara, D. Pappas, J. Weaver, B. Welch, R. L. Boivin, P. Bonoli, C. Fiore, R. Granetz, M. Greenwald, A. Hubbard, I. Hutchinson, J. Irby, E. Marmar, D. Mossessian, M. Porkolab, J. Rice, W. L. Rowan, G. Schilling, J. Snipes, Y. Takase, S. Wolfe, and S. Wukitch, "High confinement dissipative divertor operation on Alcator C-Mod," *Physics of Plasmas*, vol. 6, no. 5, pp. 1899–1906, 1999.

[138] B. Lipschultz, B. LaBombard, J. L. Terry, C. Boswell, and I. H. Hutchinson, "Divertor physics research on alcator C-Mod," *Fusion Science and Technology*, vol. 51, no. 3, pp. 369–389, 2007.

[139] M. L. Reinke, J. W. Hughes, A. Loarte, D. Brunner, I. H. Hutchinson, B. LaBombard, J. Payne, and J. L. Terry, "Effect of N2, Ne and Ar seeding on Alcator C-Mod H-mode confinement," *Journal of Nuclear Materials*, Proceedings of the 19th International Conference on Plasma-Surface Interactions in Controlled Fusion, vol. 415, S340–S344, 1, Supplement 2011.

[140] A. Loarte, J. W. Hughes, M. L. Reinke, J. L. Terry, B. LaBombard, D. Brunner, M. Greenwald, B. Lipschultz, Y. Ma, S. Wukitch, and S. Wolfe, "High confinement/high radiated power H-mode experiments in Alcator C-Mod and consequences for International Thermonuclear Experimental Reactor (ITER) $Q_{DT} = 10$ operation," *Physics of Plasmas*, vol. 18, no. 5, p. 056 105, 2011.

[141] D. Brunner, A. Q. Kuang, B. Labombard, and J. L. Terry, "The dependence of divertor power sharing on magnetic flux balance in near double-null configurations on Alcator C-Mod," *Nuclear Fusion*, vol. 58, no. 7, 2018.

[142] M. L. Reinke, "Heat flux mitigation by impurity seeding in high-field tokamaks," *Nuclear Fusion*, vol. 57, no. 3, 2017.

[143] A. Loarte, "Effects of divertor geometry on tokamak plasmas," *Plasma Physics and Controlled Fusion*, vol. 43, no. 6, R183–R224, 2001.

[144] B. Lipschultz, D. Whyte, and B. LaBombard, "Comparison of particle transport in the scrape-off layer plasmas of Alcator C-Mod and DIII-D," *Plasma Physics and Controlled Fusion*, vol. 47, no. 10, pp. 1559–1578, 2005.

[145] A. S. Kukushkin, G. Janeschitz, A. Loarte, H. D. Pacher, D. Coster, D. Reiter, and R. Schneider, "Critical issues in divertor optimisation for ITER-FEAT," *Journal of Nuclear Materials*, vol. 290–293, pp. 887–891, 2001.

[146] B. LaBombard, J. W. Hughes, D. Mossessian, M. Greenwald, B. Lipschultz, and J. L. Terry, "Evidence for electromagnetic fluid drift turbulence controlling the edge plasma state in the Alcator C-Mod tokamak," *Nuclear Fusion*, vol. 45, no. 12, pp. 1658–1675, 2005.

[147] M. V. Umansky, D. Brunner, B. LaBombard, and T. D. Rognlien, "Modeling of Local Edge Plasma Perturbations Induced by a Biased Probe," *Contributions to Plasma Physics*, vol. 52, no. 5-6, pp. 417–423, 2012.

[148] P. G. Carolan and V. A. Piotrowicz, "The behaviour of impurities out of coronal equilibrium," *Plasma Physics*, vol. 25, no. 10, pp. 1065–1086, 1983.

[149] S. Wiesen, D. Reiter, V. Kotov, M. Baelmans, W. Dekeyser, A. S. Kukushkin, S. W. Lisgo, R. A. Pitts, V. Rozhansky, G. Saibene, I. Veselova, and S. Voskoboynikov, "The new SOLPS-ITER code package," *Journal of Nuclear Materials*, vol. 463, pp. 480–484, 2015.

[150] J. Lore, J. M. Canik, A. Q. Kuang, B. LaBombard, B. Lipschultz, and M. L. Reinke, "Predictive modeling of SPARC divertor conditions using SOLPS-ITER," in *Bulletin of the American Physical Society*, APS, 2020.

[151] B. Lipschultz, J. L. Terry, C. Boswell, J. A. Goetz, A. E. Hubbard, S. I. Krasheninnikov, B. LaBombard, D. A. Pappas, C. S. Pitcher, F. Wising, and S. Wukitch, "The role of particle sinks and sources in Alcator C-Mod detached divertor discharges," *Physics of Plasmas*, vol. 6, pp. 1907–1916, 5 I 1999.

[152] F. Reimold, M. Wischmeier, M. Bernert, S. Potzel, A. Kallenbach, H. W. Müller, B. Sieglin, and U. Stroth, "Divertor studies in nitrogen induced completely detached H-modes in full tungsten ASDEX Upgrade," *Nuclear Fusion*, vol. 55, no. 3, 2015.

[153] B. LaBombard, J. L. Terry, J. W. Hughes, D. Brunner, J. Payne, M. L. Reinke, I. Cziegler, R. Granetz, M. Greenwald, I. H. Hutchinson, J. Irby, Y. Lin, B. Lipschultz, Y. Ma, E. S. Marmar, W. L. Rowan, N. Tsujii, G. Wallace, D. G. Whyte, S. Wolfe, S. Wukitch, G. Wurden, and A. C.-M. Team, "Scaling of the power exhaust channel in Alcator C-Mod," *Physics of Plasmas*, vol. 18, no. 5, p. 056 104, 2011.

[154] J. Adamek, J. Horacek, H. W. Müller, R. Schrittwieser, M. Tichy, and A. H. Nielsen, "Fast ion temperature measurements using ball-pen probes in the SOL of ASDEX Upgrade during L-mode," presented at the 38th EPS Conference on Plasma Physics, European Physical Society, 2011, p. 4.

[155] R. Fischer, C. J. Fuchs, B. Kurzan, W. Suttrop, E. Wolfrum, and ASDEX Upgrade Team, "Integrated Data Analysis of Profile Diagnostics at ASDEX Upgrade," *Fusion Science and Technology*, vol. 58, no. 2, pp. 675–684, 2010.

[156] A. Zito, M. Wischmeier, D. Carralero, P. Manz, I. P. Pérez, and M. Passoni, "Numerical modelling of an enhanced perpendicular transport regime in the scrape-off layer of ASDEX Upgrade," *Plasma Physics and Controlled Fusion*, vol. 63, no. 7, p. 075 003, 2021.

[157] S. B. Ballinger, J. L. Terry, S. G. Baek, M. Beurskens, K. J. Brunner, G. Fuchert, J. Knauer, C. Killer, E. Pasch, K. Rahbarnia, J. Schilling, E. Scott, A. von Stechow, H. Thomsen, O. Grulke, G. Wurden, G. Kocsis, T. Szepesi, and L. Zsuga, "Dynamics and dependencies of the configuration-dependent 1–2 kHz fluctuation in W7-X," *Nuclear Materials and Energy*, vol. 27, p. 100 967, 2021.

[158] C. Furia and M. Churchill, "Likelihood-free inference using normalizing flows for experiment and simulation comparison," in *Bulletin of the American Physical Society*, vol. 66, APS, 2021.